PEPTIDE-BASED SUPRAMOLECULAR NANOSTRUCTURES FOR CANCER DIAGNOSTICS AND THERAPEUTICS

by

Lye Lin Lock

A dissertation submitted to Johns Hopkins University in conformity with the
requirements for the degree of Doctor of Philosophy

Baltimore, Maryland

August, 2015

Abstract

Years of dedicated research and billions of dollars of investment made in cancer research have significantly increased our understanding of cancer biology. Yet, converting this knowledge to more sensitive diagnostics and more effective therapeutics is limited by several challenges. For example, in cancer diagnostics, optical-based activatable probes such as molecular beacons have been devised to detect protease activities of cancer relevant enzymes, but the unwanted degradation of the designed linker by non-specific enzymes could result in false signals and thereby limit diagnostic accuracy. Additionally, the efficacy of current cancer therapeutics, such as small molecule anticancer drugs, are challenged by their hydrophobic nature, as well as their non-specific delivery to normal cells which causes side effects as commonly seen in cancer chemotherapy.

The aim of this thesis is to develop a new class of peptide-based supramolecular nanostructures with the potential to advance both cancer diagnostics and therapeutics. In the first part of this thesis, we designed a series of self-assembling molecular probes with an activatable linker embedded within the core of a nanostructure. This particular design shields the linker from any non-specific enzymatic degradation prior to reaching the targeted site. In the second part, we harnessed the hydrophobic nature of anticancer drugs by coupling them to a short peptide with overall hydrophilicity to create self-assembling drug conjugates. This conjugation strategy addresses not only the low solubility issue of typical hydrophobic drugs, but also the multidrug resistance that cancer cells may have developed during the course of chemotherapy. More importantly, these self-assembled nanostructures with diagnostic and therapeutic agents have the potential to increase tumor specificity through the enhanced permeability and retention (EPR) effect.

In the first example, we develop a diagnostic probe system, peptide-based molecular beacon, to detect the activities of the target enzyme in cancer cells. A green fluorophore reporter was covalently linked to a quencher that effectively reduces the reporter's fluorescence, but could resume its fluorescence upon enzymatic activation. We found that the degradable linker is inaccessible to the enzyme in its self-assembled state (nanostructure) for protection, but can be activated in its monomeric state to report enzymatic activity. Next, we further investigate the effect of shape and charge of self-assembling molecular beacons in regulating cellular uptake. With the incorporation of a *β*-sheet forming sequence, the beacon molecule can be directed to form both spherical and cylindrical nanostructures by controlling self-assembly parameters such as temperature and aging time. Furthermore, the surface charges of the nanostructure can be altered by customizing the peptide sequences. We found that cancer cells have difficulties internalizing negatively charged monomeric molecular beacons as well as extremely high-aspect ratio cylindrical nanobeacons. However, cancer cells could rapidly internalize positively charged spherical nanobeacons. Following the beacon concept, we introduce a fluorescent anticancer drug doxorubicin that gives rise to both therapeutic and diagnostic functionalities. This integrated enzymatic-responsive feature enables intracellular drug release and fluorescence detection upon linker degradation by the specific enzyme. *In vitro* studies suggest that the drug beacon with a cell penetrating peptide can circumvent non-desirable drug resistance response in ovarian cancer cells, where higher cell cytotoxicity is observed compared to cells treated with free drug.

To explore a different imaging modality, we investigate a new MRI platform, chemical exchange saturation transfer (CEST), using self-assembling drug nanofibers as a potential image-guided drug delivery system. CEST enables anticancer drugs with exchanging protons to serve as a modality reporter, thereby exhibiting both therapeutic and imaging capabilities. To increase retention time at the targeted site upon local injection, a customized peptide sequence was covalently linked to the anticancer drug, forming cylindrical nanofibers with hydrogel characteristics. Employing an anticancer drug with intrinsic CEST MRI signals, *in vitro* and *in vivo* studies show that real-time monitoring of drug distribution is feasible.

To further demonstrate the prospect of anticancer drugs as a molecular building unit, we study the self-assembly behavior of natural and synthetic drug amphiphiles into discrete nanostructures. We showed the direct assembly of two amphiphilic drug molecules, methotrexate and folic acid, in different solvent conditions. Interestingly, folic acid exhibits stronger self-assembly behavior via Hoogsteen hydrogen bonding while methotrexate was unable to assemble into any well-defined nanostructures, despite their similarity in chemical structure.

These findings demonstrate the feasibility and potential of utilizing peptide-based systems to transform anticancer drugs and imaging agents into discrete nanostructures with customizable properties. While the rational design of molecular amphiphilicity is essential in governing the self-assembly process, the selection of peptide sequences, as well as the processing conditions, is equally crucial in defining the final self-assembled morphology. The systems studied in this thesis open up innovative opportunities to exploit new functional and structural features of anticancer drugs and diagnostic probes.

Advisor

Honggang Cui, Ph.D.

Assistant Professor of Chemical & Biomolecular Engineering, Johns Hopkins University

Committee Members

John D. Tovar, Ph.D.

Associate Professor of Chemistry, Johns Hopkins University

Martin G. Pomper, M.D., Ph.D.

Professor of Radiology, Johns Hopkins University

Michael A. Bevan, Ph.D

Professor of Chemical & Biomolecular Engineering, Johns Hopkins University

Sharon Gerecht, Ph.D.

Associate Professor of Chemical & Biomolecular Engineering, Johns Hopkins University

Acknowledgements

This thesis has been made possible by the incredible support and contribution from numerous amazing individuals. I am genuinely thankful for their impact in this thesis.

I would like to express my deepest appreciation and gratitude to my advisor, Dr. Honggang Cui. His passion for science and fascination over new discoveries has created the utmost environment for me to pursue my research endeavor in the past five years. He always challenged us to think critically and exploring science under his guidance has been an exciting and fun journey. I am grateful for this research experience and sincerely thank Dr. Cui for this opportunity.

I appreciate the collaboration experiences and invaluable discussions with Dr. Guanshu Liu and Dr. Yuguo Li whom have taught me so much about CEST MRI, Dr. Qingguo Xu for sharing his knowledge in ocular drug delivery, Dr. Michael McCaffery and Ms. Erin Pryce for their guidance in TEM and confocal microscope and Dr. Phil Mortimer for his help in mass spectrostropy

Specifically, I would like to thank my GBO committee members, Dr. Martin Pomper, Dr. John Tovar, Dr. Michael Bevan, and Dr. Sharon Gerecht. Their feedback and advice were insightful and valuable in refining this thesis. I truly appreciate their time, participation and contribution.

I am very grateful to Dr. Andrew Cheetham for his mentorship in research, especially peptide chemistry. From basic experimental techniques to fundamental theories, he had shown great patience and enthusiasm to newcomers like me in the lab. I

would like to thankfully acknowledge Dr. Pengcheng Zhang for the research discussions, training in cell culture and his guidance in several research projects. His dedication, patience and selflessness in helping others have been an inspiration to me. I am also grateful to our past and current lab members, Dr. Shuang Liu, Dr. Yi-an Lin, Ran Lin, Hao Su, Yang Hu, Zidu Tang, Claudia Reyes, Michelle LaComb, and Kelly Schwarz. I appreciate our fruitful discussion in the lab and the friendly working environment that we have fostered over the years. In particular, I would like to thank Xinpei Mao for her great contribution and dedication to the projects that we have been working closely together.

I am truly grateful and thankful to have met some of the lifelong friends here in Hopkins. From the coffee breaks, dinner get-together, sports time to a random walk in campus, these moments have made this journey more fun and meaningful to me. A special thanks to Dheeraj, Jude, Sarita, Yi-An, the Robotics group – Paul, Xing Chi, Min Yang, Sue Sue and Wen Pei for all the quality conversations and friendships.

I would also like to thank my friends who has always been there and supportive to my career and my life, Sin Yee, Grace, Cheng Yee, Kit Toong, Chew Ling, Zho Yin, Yee Von, Lai Yeng, Merry, Yuet Ling, Chyi Chin, Chih Yong, and the S.K. Jun family. It is the memories that we shared in Malaysia, Buffalo and Indiana that drives me forward.

Most importantly, I am truly grateful to my family, especially my parents, for their unconditional love and continuous support to my education and career. I would also like to thank my brother-in-law for his guidance, directly and indirectly. A special thanks and appreciation to my sister, for her support in my higher education and sharing her experiences unreservedly.

Dedication

To all cancer patients, who had fought or still fighting.
You are not alone.

Table of Contents

List of Figures

1 Introduction

1.1 Background and motivation

Cancer is a category of diseases that comprises of one major characteristic, the uncontrollable growth and spread of mutated abnormal cells. It can be caused by internal factors such as inherited genetic mutations, hormones, immune conditions and external factors such as tobacco, infectious organisms, and unhealthy diet. For example, women with a family history of breast cancer possess higher risk to develop breast cancer throughout their life time and smokers are 25 times more likely to develop lung cancer compared to nonsmokers. In 2015, the estimated death caused by cancer in US alone is 589,430 people, or about 1,615 American per day. On top of this, there are approximately 1,658,370 new cancer cases expected to be diagnosed in 2015.[1]

Although years of dedicated research and billions of dollars of investment have significantly increased our understanding on the cause and biology of cancer, the development in cancer diagnostics and therapeutics is still limited by several challenges. For example, in cancer diagnostics, optical-based activatable molecular probes, such as molecular beacons with peptide degradable linkers have been devised to detect the overexpression of cancer protease activity.[2,3] However, the peptide linkers which are crucial in reporting signal, typically are exposed to the physiological environment and their facile degradation by non-specific enzymes often give rise to an undesired false signal, thus limiting the accuracy of enzyme detection. Apart from that, cancer therapeutics also faces challenges in achieving high therapeutic effect. Small molecule anticancer drugs are generally hydrophobic in nature, resulting in poor solubility of drug in aqueous environment.[4] In addition, non-specific delivery of these anticancer drugs to both normal and cancer cells is the major cause for drug's side effects. Although numerous nanoparticulate systems have been established in an attempt to address these challenges, their drug loading capacity and encapsulation efficiency are still limited in this technology.[5]

The objective of this work was to develop a versatile system to address the issues stated above for cancer diagnostic and cancer therapeutics. Our approach was to incorporate a peptide-based system to existing anticancer drugs and imaging modalities that ultimately transforms molecular system to nanostructure, harnessing some of the advantages offered in the realm of nano-scale. Specifically, nanostructure enables passive targeting through enhanced permeability and retention effect as well as cargo protection by embedding molecules of interest within the core of nanostructure.

1.2 Nanomedicine for diagnostic and drug delivery applications

1.2.1 The emergence of nanomedicine

Nanomedicine, a term that first emerged in the year 2000, focuses on using nanotechnology approaches for medical applications. By definition, nanotechnology comprises of objects in the dimension of nanometer, ranging from 1 nm to 100 nm. At this nanometer and atomic level scale, materials could exhibit enhanced properties due to the increased surface area and quantum effects, which is otherwise unattainable at the larger scale.[6] For example, quantum dots (QDs) fluorescence emission wavelength can be tuned from blue to near infrared by manipulating the particle's diameter as a result of the usually high surface-to-volume ratio and quantum confinement.[7] QDs with 4 nm in diameter will fluoresce green while 6.5 nm QDs fluoresce red[8], and they have shown greater photostability than traditional fluorescence dyes.[9] On the other hand, iron oxide nanocrystals were found to exhibit superparamagnetic properties that can be used as contrast agents for magnetic resonance imaging (MRI). With an iron core of approximately 4-5nm, its induced magnetic disturbance causes a reduction in T2 relaxation time of nearby water protons resulting in a loss of local signal intensity.[10] Another example of utilizing nanotechnology in diagnostic applications is the gold nanoparticle, which has the ability to serve as a quencher in Förster resonance energy transfer measurement studies. With this approach, researchers were able to evaluate the binding event of DNA-conjugated gold nanoparticles and its complementary sequence.[11,12]

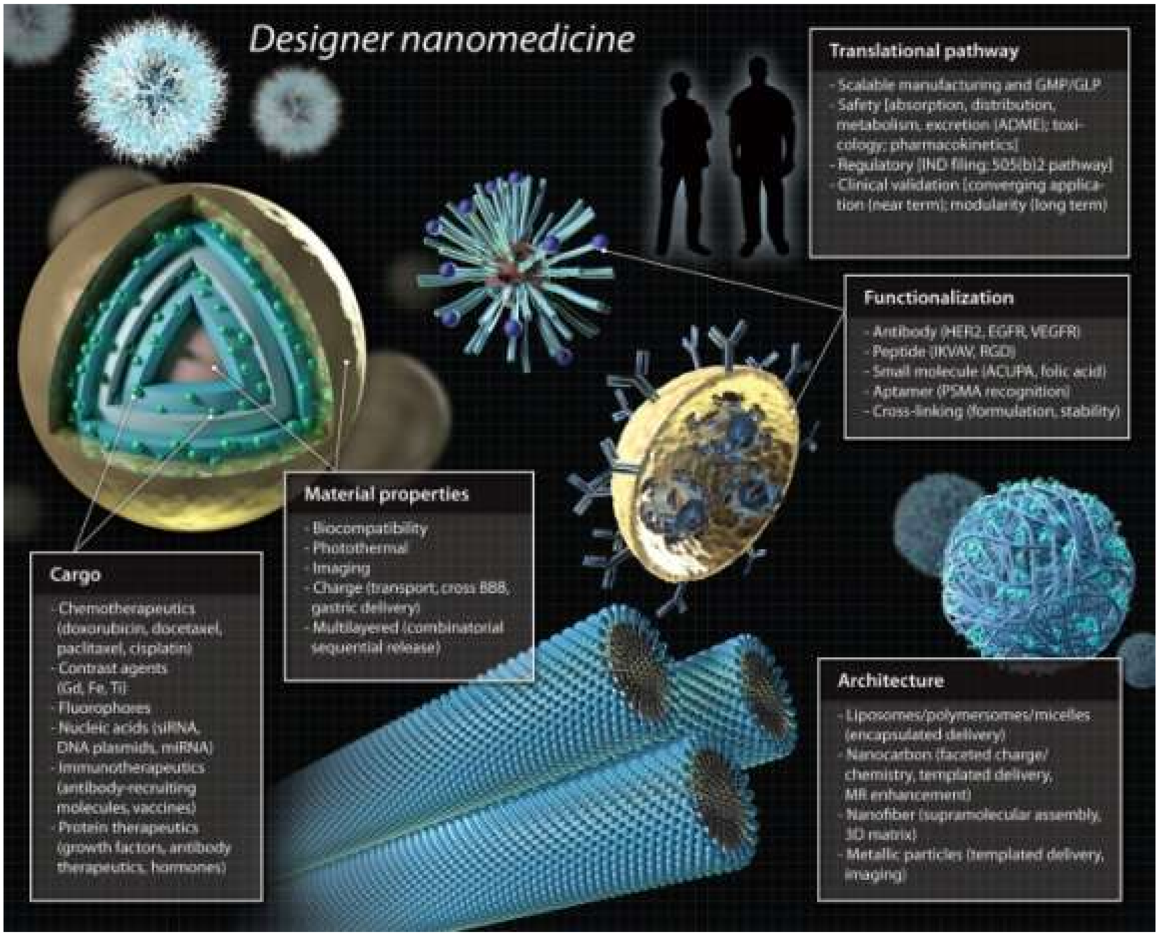

Figure 1-1. Nanomedicine platform offers a variety of properties that enable designers to customize therapies and imaging systems, ultimately improving the chances of clinical translational. Adapted with permission from Ref. 13 (Copyright © 2013 AAAS)

In addition to inorganic-based nanoparticles, various organic materials have been used to generate nanostructures for cancer diagnostic and drug delivery purposes. For instance, liposome composed of phospholipids has been utilized for gene, chemotherapeutic drugs, and contrast agents delivery.[14-17] Besides, a number of polymeric-based micelles systems have been developed as the carrier or vehicles for chemotherapeutic drugs and imaging modality. In general, hydrophilic and hydrophobic block copolymers were designed to encapsulate or conjugate molecules of interest to induce the micelle formation.[18,19] Another type of organic-based nanoparticle is the dendrimer, a spherical nanosized tree-architecture that can attach multiple drugs, contrast agents, and targeting ligands.[20,21]

1.1.2 Passive targeting

One of the advantages offered by nanomedicine is the passive targeting, an accumulation of particles at the tumor site owing to its nano size. Due to the elevated nutrient requirement from abnormal growth of cancerous tissues, the formation of new blood vessels around the tumor site, also known as angiogenesis, is often impaired and leaky. The defective angiogenesis was shown to increase permeability of nanostructures, where the gap between the blood vessel's endothelial cells could be as large as 300 nm – 800 nm while normal endothelial cells were well aligned with the gap size of ~2 nm. In addition, the tumor site was found to have a dysfunctional lymphatic drainage system, where extravasated nanoparticles could have a longer retention time and enabled drug release close to tumor cells. This phenomenon is termed as the enhanced permeability and retention (EPR) effect where nano-sized systems could achieve passive targeting to the tumor site for diagnostic or drug delivery purposes.[22,23] Although the gap of leaky blood vessels could be as large as 800 nm, other considerations should be taken into account when designing the size of nanoparticles to overcome numerous physical barriers such as mucosal entrapment, immunogenicity, and non-specific uptake. For instance, nanoparticles of larger than 200 nm in size encounter stronger opsonization, which surface deposition of blood opsonic factors would aid particle recognition by macrophages resulting in rapid clearance of nanoparticles in the blood stream.[24] On the contrary, nanoparticles with sizes smaller than 6 nm can be cleared efficiently from the body through renal filtration and urinary excretion.[25] Interestingly, mathematical modeling showed that hemodynamic forces and other interactions acting on spherical nanoparticles of about 100 nm in diameter tend to keep them in the center of blood vessels, which could potentially decrease the chance for nanoparticles to extravasate through the vessel walls.[26,27] In addition to the particle's size, other parameters such as shape and surface charges of nanoparticles also govern the circulation properties in the blood stream, which requires in-depth physicochemical understanding for optimization.

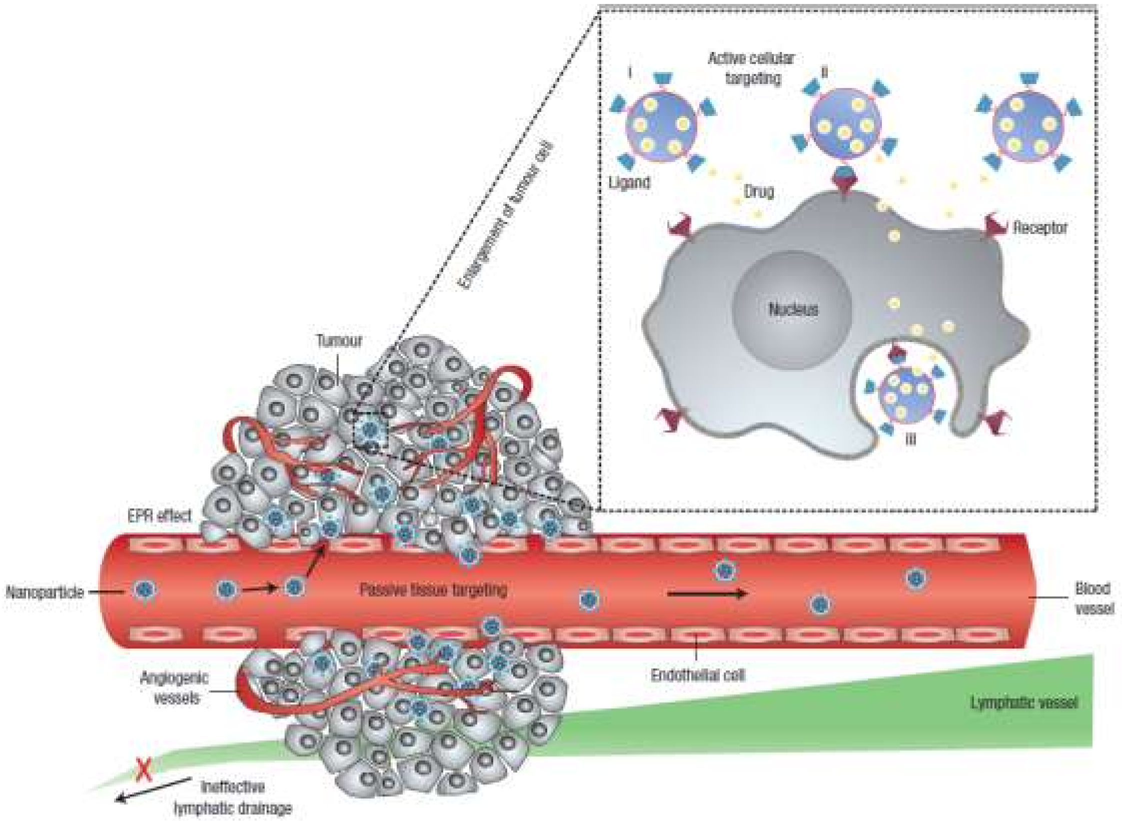

Figure 1-2. Schematic illustration of two different delivery mechanisms in which nanoparticles accumulate at tumor site. The increased permeability of tumor vasculature and ineffective lymphatic enable extravasation of nanoparticles through passive targeting (EPR). Active targeting (inset) is achieved by conjugating targeting ligands on the surface of nanoparticles which enhances cell-specific recognition and binding. Reprinted with permission from Ref. 28 (© 2007 Nature Publishing Group)

1.1.3 Active targeting

In order to increase the specificity of nanoparticles, active targeting, also known as ligand-mediated targeting, selectively presents bioactive ligands on the surface of nanoparticles to induce binding affinity towards targeted disease cells.[29] Upon selective binding of ligand to surface molecules or receptors overexpressed on diseased cells, nanoparticles are internalized into targeted cells and subsequently release their cargo for therapeutic or imaging purposes. For example, Anti-HER2 targeting ligands were conjugated on the surface of liposomes and were shown to increase the uptake of liposomes in HER2-expressing cancer cells, in contrast to the non-targeted liposomes which tend to accumulate in the perivascular or stromal space.[30] With the high tunability of nanoparticles, researchers have shown that a combination of ligands such as folic acid and EGFR antibodies could be utilized to improve cellular internalization through multiple surface receptor targeting.[31] Another category of ligand comes from the peptide family, such as the RGD (arginine-glycine-aspartic acid) peptide sequence. This peptide ligand can bind specifically to $\alpha_v\beta_3$ integrin receptors, and it has been used to target both cancer and angiogenic endothelial cells.[32] Although RGD is a very short peptide sequence, its molecular geometry such as linear or cyclic RGD conformation was found to affect its targeting efficiency dramatically. Studies showed that cyclic RGD has a higher binding affinity than its linear counterpart in anti-tumor targeting.[33] Although many of the actively-targeted nanoparticles have shown great promise, most of them are still in the stage of clinical development and have not been commercialized yet. Depending on the type of ligand-receptor pair, the ligand density displayed on the surface of nanoparticles, ligand charge status, ligand orientation, and binding affinity highly affect the end results of targeting *in vitro* and *in vivo*.[29]

1.3 Enzyme-activatable systems for diagnostic and drug release

1.3.1 Proteolytic enzymes in cancer

Proteolytic enzymes regulate various biological processes such as proliferation, migration, cell death, invasion, and protein turnover. Through proteolysis, enzymes degrade protein by hydrolysis, a process to break down peptide bonds of covalently-linked amino acids. There are at least 569 proteases in human system and they can be categorized into five major types of mammalian protease, namely, aspartic, cystein, serine, threonine, and metalloproteases.[34] Each of these protease classes can perform catalytic reactions through different mechanisms. Given that proteases are highly regulated in DNA replication and transcription, angiogenesis, tissue morphogenesis and remodeling, inflammation, necrosis, apoptosis, cell proliferation and differentiation, an alteration in proteolytic systems could elicit multiple pathological conditions.[35] For instance, the matrix metalloproteinases enzymes have been associated to promote tumor progression because of their role in extracellular matrix degradation.[36,37] There is also increasing evidence to show that the overexpression of lysosomal cysteine protease, cathepsin B, C, L and S in various cancer cells may play a key role in the development and progression of malignant tumors.[38,39] Tremendous efforts have been focused to target these pathological relevant proteases to discover new enzyme inhibitors for cancer therapy and develop protease-responsive drug delivery and diagnostic systems.

Several approaches have been taken to construct materials or systems that are responsive to stimuli such as temperature, ionic strength, magnetic field, light or small biomolecules.[40,41] The enzymatic-responsive system has gained much interest in the community given its biological relevance and high potential in biomedical applications in diagnostic and drug-delivery.[42] Enzyme catalysis was recognized for a few advantages over other stimuli. First, enzymes are highly selective towards their catalysis reactions, demonstrating high specificity in reporting a biological event. Second, enzymes work under mild and physiological conditions such as 37 °C, aqueous environment and pH 5-8. Third, several enzymes have been reported to serve as important modulators in healthy as well as diseased biological pathways. These features enable enzymes to serve as a target or biomarker for responsive cancer diagnostic and drug delivery systems.

1.3.2 Enzyme-activatable drug delivery systems

Similar to the concept of zymogen, which exists in an inactive form of enzyme where protease cleavage of a specific peptide sequence to convert it into its active form,[43] drugs or diagnostic probes can be designed to incorporate enzyme-targeting peptide substrate for controlled release and enzyme detection. For instance, cathepsin B protease was found to involve in various cancer progressions and metastasis.[38,44] Peptide substrate such as Gly-Phe-Leu-Gly can be used as an enzyme linker to probe the activity of cathepsin B and construct a system with an enzyme-triggered drug release feature.[45] Since the system can only be activated by a specific enzyme at the disease site, this strategy could reduce the toxic side effects and potentially increase the therapeutic effect of the drug. For example, Doxorubicin (Dox), a chemotherapeutic drug was conjugated onto the N-(2-hydroxypropyl)methacrylamide (HPMA) polymer through Gly-Phe-Leu-Gly linker.[46] After the polymer-drug was internalizated into the cell, cathepsin B, which comes from the family of lysosomal proteases, degrades GFLG peptide linker and releases Dox drug intracellularly.[47] Another notable example is the Adcetris, also known as brentuximab vedotin (Seattle Genetics, WA, USA), an FDA-approved antibody-drug conjugate that targets cathepsin B for Hodgkin's lymphoma (HL) and systematic anaplastic large cell lymphoma (ALCL).[48] Cathepsin B cleavable peptide linkers such as valine-citruline and phenyalanine-lysine were used to linked monomethylauristatin E (MMAE) drug and monoclonal-antibody that is specific to CD30 on hematological malignancies. Compared to the hydrozone-sensitive linker, the antibody drug conjugates with protease-responsive linker was found to be more stable in plasma and exhibited greater in vitro specificity and lower in vivo toxicity.[49] Remarkably, *in vivo* studies of this antibody-drug conjugate showed high efficiency in tumor induced regressions with therapeutic indices as high as 60-fold, which is significantly higher than other mAb-drug conjugates. The biomolecular specificity offered by antibody as well as enzymatic-responsive activation has been shown to enhance drug efficacy and reduce chemotherapeutic damage to non-target tissues.

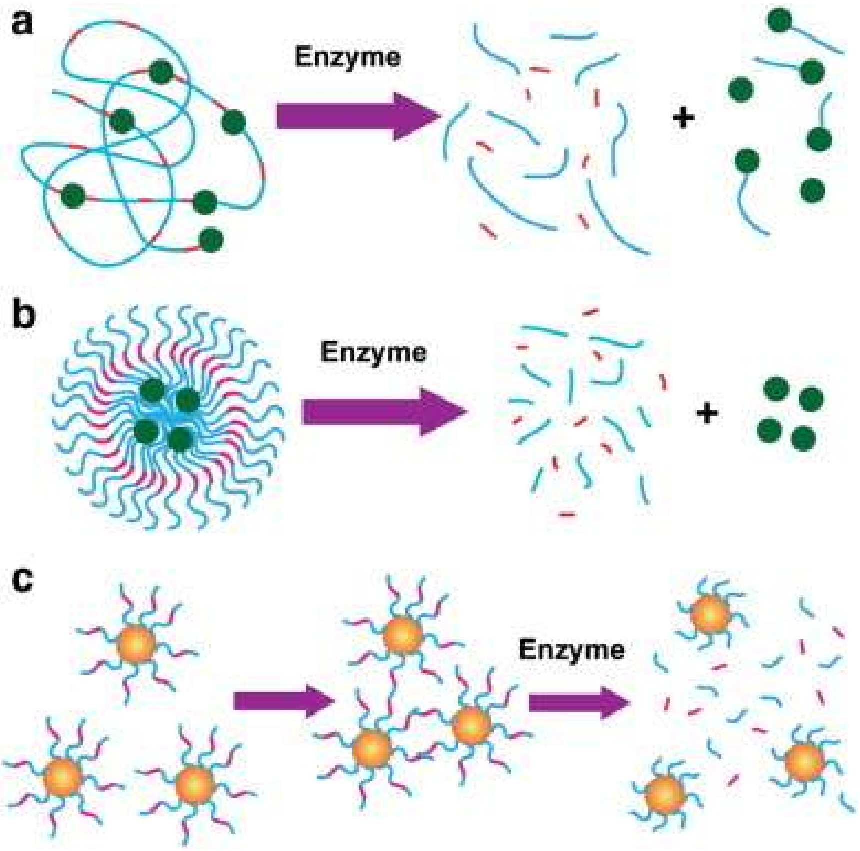

Figure 1-3. Nanomaterials with enzymatic-responsive feature for drug delivery and diagnostic. a) Enzyme activity triggers drug release by cleaving enzyme-specific linker conjugated to polymer-based nanoparticles. b) Drug-loaded polymer-stabilized liposomes,whose drug release can be programmed to be triggered by an enzyme. c) The assembly and disassembly of inorganic nanoparticles can be controlled by enzymatic activity, which changes the physical properties of the nanoparticle for diagnostic purposes. Adapted with permission from Ref. 42. (© 2012 Elsevier)

1.3.3 Enzyme-activatable diagnostic and imaging systems

In addition to drug delivery applications, enzyme-activatable probes are employed in various cancer diagnostic systems to image tumor *in vivo*. For example, Weissleder and coworkers have developed a near-infrared fluorescent (NIRF) probe that can be activated by lysosomal protease *in vivo*.[50] Multiple NIRF molecules were conjugated onto the poly-L-lysine side chain of a synthesis graft copolymer, which exhibit a self-quenching state (Off-state) due to close proximity of each NIRF molecules. However, upon internalization into cells, lysosomal cystein/serine protease such as cathepsin B, H and L activate the probe by degrading the poly-L-lysine backbone, therefore fluorescence resumed for detection and imaging (On-state). With this design, the fluorescence signal of NIRF probe after eznzyme activation (On-state) was 12-fold higher than the unactivated form (Off-state).[50]

Besides conjugating to polymer[51], cathepsin B-responsive features have been incorporated in other systems such as dendrimer[52,53], silica nanoparticles[54], gold nanoparticles[55], monoclonal antibody[49,56], and peptide-based systems.[57,58] The vast exploration of enzymatic-responsive biomaterials and systems demonstrated its interest and potential for future applications.

1.4 Self-assembly of peptide-based supramolecular nanostructures

1.4.1 The nature of self-assembly

Self-assembly is a process in which individual molecules or components spontaneously form ordered aggregates when the appropriate conditions are met. In general, there are two types of self-assembly: static and dynamic.[59] In static self-assembly, systems exist at a global or local equilibrium and do not involve any energy dissipation. However, some form of energy such as mixing and stirring may be required to form the stable ordered structure. For example, the self-assembly of molecular crystals and the folding of globular proteins are in the categories of static self-assembly.[60-63] In contrast, dynamic self-assembly refers to the organization of structures when the system is deliberately kept away from its energy minimum (non-equilibrium state) by continuous energy supply and dissipation.[64] As a result, it alters the interactions of molecules/components with each other and with their environment. Numerous biological systems such as the formation of living cells[65], schools of fish, and armies of ants[66] undergo dynamic self-assembly, which is in nature more challenging to understand than static self-assembly as it cannot be predicted through energy minimization.[67]

1.4.2 The driving forces of peptide self-assembly

In general, self-assembled peptide-based nanostructures are driven and stabilized by non-convalent bonds. These driving forces typically include hydrogen bonds, ionic bonds, π-π interactions, hydrophobic and van der Waals interactions. To sustain the stable and well-defined nanostructures, these molecules interact inter- and intramolecularly through a collective of interactions. These self-assembled nanostructures are generally thermodynamically favorable; therefore, they exist at a stable or meta-stable state.

To construct a one-dimensional or cylindrical shape nanostructure, such as nanofibers or nanotubes, hydrogen-bonding typically played a crucial role in directing the growth of nanostructure. A molecular simulation done by Velichko et. al. showed that strong hydrophobic interaction without hydrogen bonding leads to the formation micelles of finite sizes.[68] On the other hand, systems with exclusively hydrogen bonding favors 1-D β-sheet structure forming through step-by-step aggregation of molecules. In the presence of both hydrophobic interaction and hydrogen bonding, the final self-assemblies largely depend on the strength of intermolecular bonding and the self-assembly kinetics may take a longer time to reach equilibrium. With a stronger hydrophobic interaction, molecules may first self-assemble into spherical micelles with random β-sheet scattered around the corona. As the hydrogen bonding energy increases, the ordering of β-sheet disrupts the spherical interfacial curvature of micelle and further elongated forming a 1-D nanofiber. Experimentally, Hartgerink and coworkers also studied the effect of hydrogen bonding in directing the final self-assembled nanostructure.[69] They found that the disruption of hydrogen bonding through modifying the four amino acids closest to the core would lead to the formation of spherical micelle instead of nanofibers. This finding is in good agreement with Velichko's simulation which showed the importance of hydrogen bonding in the formation of 1-D nanostructure.

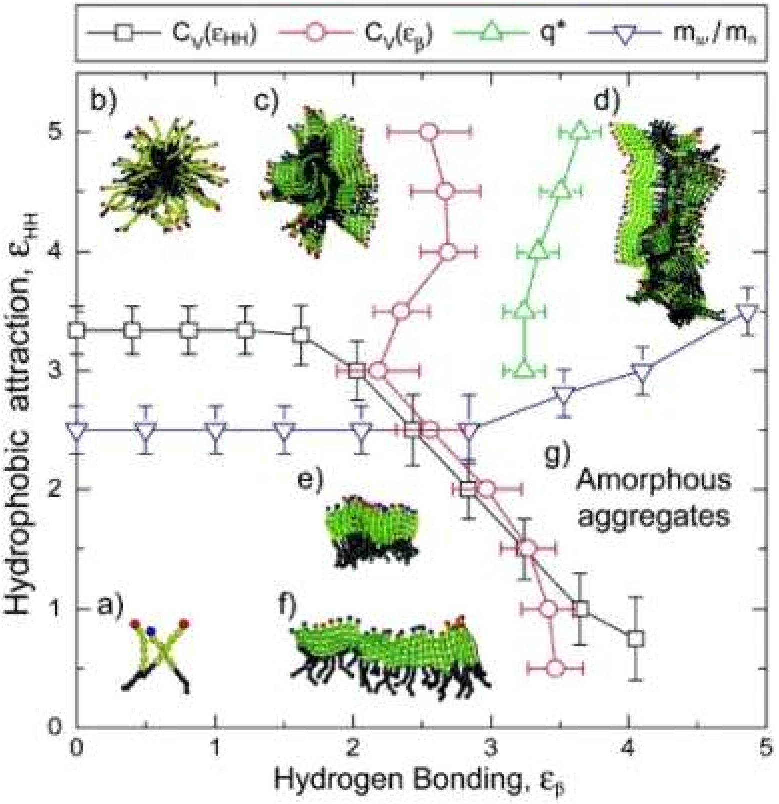

Figure 1-4. Schematic phase diagram illustrates the effects of hydrophobic attraction and hydrogen bonding implied by simulation results. The phase diagram shows regions with (a) free molecules, (b) spherical micelles, (c) micelles with β-sheets on the outside forming the corona, (d) long cylindrical fibers, (e) stacks of parallel β-sheets, (f) single β-sheets, and (g) the amorphous aggregate phase. Reprinted with permission from Ref. 68. (Copyright © 2008 American Chemical Society)

1.4.3 Rational design of self-assembling peptide molecule

The peptide-based system is highly versatile when given that each of the 20 common amino acids offers different properties such as hydrophobicity, hydrophilicity, functional group and charged or non-charged side chains. This allowed scientists and engineers to design and customize peptide molecules to self-assemble into different shapes of nanostructures such as spherical, cylindrical, vesicle and tubular, as well as demonstrating different functionalities for diagnostic, drug delivery, and tissue regenerative applications.[70-74] For instance, self-assembling peptide amphiphile typically composed of 4 regions, namely the hydrophobic domain to induce self-assembly, hydrophilic amino acids to aid molecule solubility in water, short peptide with high tendency of forming intramolecular hydrogen bonding, and bioactive epitope to enhance cells or protein interaction.[75] The basis of this design relies on the amphiphilic nature of the molecule, in which having a hydrophobic end of alkyl tail and grouping hydrophilic amino acids on the opposite site of the sequence to induce the self-assembly process.[72] To direct the self-assembly into one-dimensional cylindrical nanofibers, a hydrogen-bond forming sequence was incorporated into the design for stronger beta-sheet interaction. By presenting bioactive epitopes on the surface of nanofibers (similar to the concept of active targeting), self-assembling nanofibers were shown to foster cell adhesion using RGD peptide sequence and promote neurite outgrowth with IKVAV epitope.[76,77]

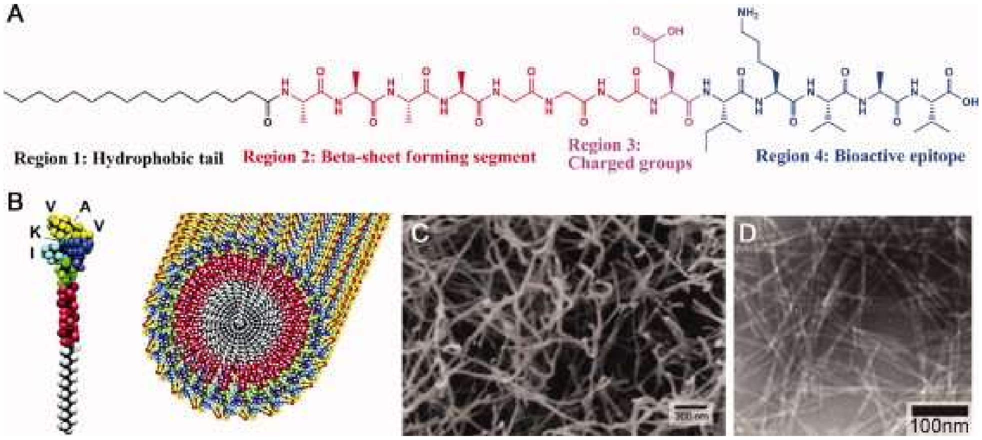

Figure 1-5. a) Molecular structure of a representative peptide amphiphile with four rationally designed chemical entities. (b) Molecular graphics illustration of an IKVAV-containing PA molecule and its self-assembly into nanofibers. (c) Scanning electron micrograph of the IKVAV nanofiber network formed by adding cell media (DMEM) to the PA aqueous solution. (d) Transmission electron micrograph of the IKVAV nanofibers. Adapted with permission from Ref. 76 (© 2004 AAAS) and Ref. 74 (© 2003 American Chemical Society).

Peptide can also be rationally designed to adopt a specific secondary conformation that would lead to the self-assembly of higher hierarchy structures such as nanofibers and hydrogel. Schneider and colleagues showed that peptide sequence with high β-sheet propensity amino acids and inducible β-hairpin structure would undergo self-assembly process to form nanofibers further associated into hydrogel scaffold.[78] This β-hairpin peptide model can be achieved by flanking (-V^{D}PPT-) tetrapeptide at the center of the 20-residue long peptide. By manipulating the charge status of lysine under basic conditions, the designed peptide would intramolecularly fold into β-hairpin structure to present one face lines with hydrophobic valine residues and another face lines with hydrophilic lysine residues, an amphiphilic arrangement of the peptide. This folding process or peptide conformation is reversible by lowering the pH to increase charge repulsion between neighboring lysine residues.

Another group of peptide self-assembly was termed as “molecular Lego” by Zhang and coworkers.[79] Similar to the Lego bricks that have pegs and holes, peptides were designed to present two separate faces with hydrophilic and hydrophobic nature, which would assemble at the molecular level. Focusing on the ionic charge arrangement, peptides were designed with regular repeats of alternating positively- and negatively-charged amino acids to systematically form complementary ionic bonds with the neighboring peptides. The pattern of cationic and anionic alteration can be classified into different moduli, such as modulus I with - + - + - + - +, modulus II with - - + + - - + + and modulus IV with - - - - + + + +.[80798058585858] The precise array of sequence enables these peptides to self-assemble in a well-ordered manner, mainly driven by its amphiphilicity as well as ionic interaction.

One of the common features in designing self-assembling peptide emphasizes the amphiphilic nature of the molecule. Distinctly grouping hydrophobic and hydrophilic into different faces facilitates the self-assembly process, and most importantly, enables the formation of discrete nanostructures.

1.5 Thesis Overview

This thesis aims to describe a platform that ultimately transforms anticancer drugs and imaging probes from molecular-level to nano-level constructs. The emphasis of nanostructure offers several advantages that could potentially address current limitations in cancer diagnostics and therapeutics. Through a rational design of the peptide-based system coupled with an in-depth understanding of molecular chemistry, this thesis covers several examples that illustrate the construction of diagnostic nanoprobes and therapeutic nanofiber hydrogel. Chapter 2 and Chapter 3 highlight the design and importance of nanobeacon diagnostic probe in spherical and cylindrical shapes. Chapter 4 illustrates the construct of drug beacon that comprises of both diagnostic and therapeutic functionalities. Next, Chapter 5 describes the formation therapeutic nanofiber hydrogel with magnetic resonance imaging properties. In the following Chapter 6, I investigate the self-assembly of natural and synthetic drug amphiphiles into discrete nanostructures. Lastly, Chapter 7 presents the conclusions as well as potential future work to improve and explore this peptide-based nanostructure system.

2 Design and Construction of Supramolecular Nanobeacons for Enzyme Detection*

2.1 Abstract

Molecular beacons are typically water-soluble molecules that can convert specific chemical reactions or binding events into measurable optical signals, providing a noninvasive means to help understand cellular and subcellular activities at the molecular level. However, the soluble form of the current molecular beacon design often leads to their poor stability and facile degradation by nonspecific enzymes, and as a result, this undesired activation could give rise to false signals and thus poses a limitation for accurate detection of enzymatic activities. Here we report a proof-of-concept design and synthesis of a new type of supramolecular nanobeacon that is resistant to nonspecific enzymatic degradation in the self-assembled state but can be effectively cleaved by the target enzyme in the monomeric form. Our results show that the nanobeacon with a GFLG peptide linker could serve as an indicator for the presence of a lysosomal enzyme, cathepsin B.

2.2 Introduction

Real time detection of the location and expression level of enzymes within living cells offers important information on many important cellular and subcellular events and

---

*Reprinted with permission from Lock, L.L.; Cheetham, A. G.; Zhang, P.; Cui, H., ***ACS Nano****,* 2013*,* 7 (6), 4924-4932. Copyright ©2013 American Chemical Society

L.L.L., C.A.G., Z.P., and C.H. designed the experiments. L.L.L. performed all experiments and analyzed the data. L.L.L. and C.H. prepared the manuscript.

thus provides unique opportunities for the development of new strategies for tumor diagnosis and cancer therapeutics.[2,50,81,82] The overexpression and relative abundance of certain proteases in cancers, such as cathepsins and matrix metalloproteases (MMPs), provide attractive targets for tumor screening.[50,82,83] In the design of polymer-drug conjugates with peptide linkers, enzymatic cleavage is an important step towards the release of bioactive anticancer drugs, with the release rate being a function of active enzyme concentration.[84-86] Recently, there is also a rapidly growing interest in the development of enzymatically responsive materials.[87-98] Therefore, it is important and necessary to precisely detect the activities or expression levels of enzymes of interest.

The advent and development of activatable molecular probes, such as molecular beacons that contain a fluorophore and quencher pair, have enabled possibilities for the highly sensitive detection of DNA/RNA through the conversion of specific binding events into detectable fluorescence signals.[99-101] Very recently, molecular beacons with proteolytically degradable peptide linkers have been devised for protease detection and other applications.[2,3,87,102-105] However, since the linkers that are designed to activate molecular beacons are typically exposed to the physiological environment, their poor stability and facile degradation by non-specific enzymes often give rise to an undesired false signal and thus pose a major limitation for accurate detection of enzymatic activities.

To develop molecular probes immune to undesired degradation, we report here a generic design platform of a new type of self-assembling supramolecular nano-beacon (NB) with a well-defined size and surface chemistry for protease detection. In contrast to *soluble* molecular beacons, the NB molecules are specifically designed to self-assemble into core-shell micelles, with the enzyme-sensitive design feature being deeply embedded within the micellar core and thus inaccessible to the enzyme (Fig. 2-1A). Only in the monomeric form can these NB molecules be cleaved by the target enzyme to generate fluorescence signals.

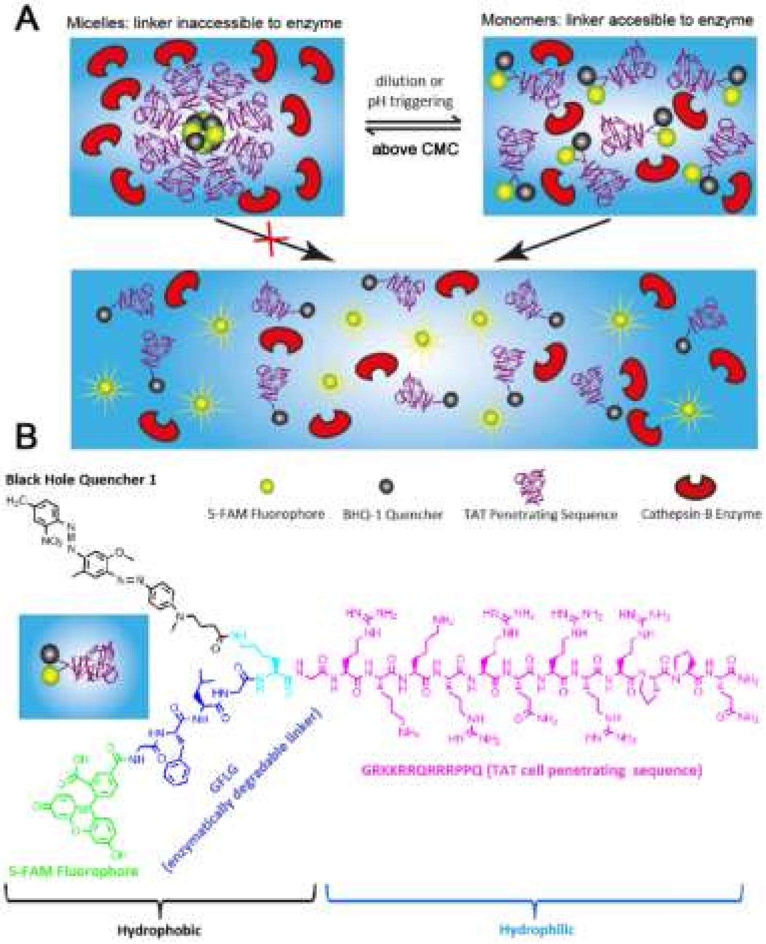

Figure 2-1. Schematic illustration of the expected cleavage and detection mechanism (**A**) and molecular structure of the designed nano-beacon molecule TFB (**B**). In the self-assembled state, the enzyme-sensitive linker is deeply buried in the micellar core, while in the monomeric form, the NB molecules become accessible for enzymatic cleavage. The designed molecule exists in the self-assembled NB form above its critical micellization concentration (CMC). The transition from NB micelles to monomeric form can be achieved either by dilution or by pH triggering.

2.3 Experimental Procedures

2.3.1 Molecular Synthesis

In brief, the Tat sequence and the peptide linker (Fmoc-GFLGK(Mtt)GRKKRRQRRRPPQ-Rink) of the TFB molecule was first synthesized on an automatic peptide synthesizer (details of synthesis can be found in the supporting information) using standard 9-fluorenylmethoxycarbonyl (Fmoc) solid phase synthesis protocols. After removal of the Fmoc protecting group, 5-FAM was manually coupled at the peptide N-terminus. Next, Black Hole Quencher-1 (BHQ-1) was incorporated onto the lysine ε-amine, following removal of the Mtt protecting group for lysine side chains. The completed peptide was cleaved from the Rink Amide resin using a mixture of TFA/TIS/H_2O. The two control molecules: TF and TB were synthesized by using acetic anhydride to replace the BHQ-1 and the 5-FAM segments with an acetyl group, following the same procedures for the synthesis of the TFB molecule. All the molecules were purified using preparative RP-HPLC and their purity was evaluated by analytical HPLC and MALDI-ToF mass spectrometry.

2.3.2 Cathepsin B Degradation Experiments

The reaction buffer containing 1 mM EDTA (enzyme stabilizer) and 25 mM L-cysteine (enzyme activator) in 1×PBS solution was prepared. The solution pH was adjusted to 5.0 through the addition of 3 M HCl. The desired amount of cathepsin-B was added to the buffer solution and pre-incubated at 37°C for 5 minutes to activate the enzyme. Stock solution was prepared by dissolving 0.6 mg of TFB molecule with 500 μL of pH 5.0 reaction buffer, yielding a TFB concentration of 0.4 mM. 0.25 μL of 0.4 mM stock solution was added to each reaction well and mixed thoroughly with the pre-incubated cathepsin-B solution. Cathepsin-B (Bovine Spleen) was purchased from EMD Chemicals (Gibbstown, NJ) and it was delivered in liquid form with stock concentration of 17 μM. Reaction kinetics was monitored using a Gemini XPS microplate reader (Molecular Devices, Sunnyvale, CA). Samples were excited at 492 nm and 5-FAM emission was measured at 520 nm with a 515 nm cutoff.

2.3.3 k_{cat}/K_M Calculation

The catalytic reaction of CatB has been reported to follow the kinetic behavior described by the Michaelis-Menten equation. According to Michaelis-Menten Equation, the reaction rate V can be expressed in the following form:

$$V = \frac{k_{cat}[E]_t[S]}{K_M + [S]}$$

in which k_{cat} is the first-order rate constant, $[E]_t$ is the total enzyme concentration, [S] is the substrate (TFB, in the case reported here) concentration, and K_M is the Michaelis-Menten constant. At the very low substrate concentrations reported herein ($[S] \ll K_M$), the equation can be rewritten as:

$$V \cong \frac{k_{cat}}{K_M}[E]_t[S]$$

The ratio of k_{cat}/K_M provides a direct measure of enzyme efficiency and specificity.

2.3.4 Cell Culture

Human breast adenocarcinoma cell line, MCF-7 was kindly provided by Wirtz Lab at Johns Hopkins University, and was grown in Dulbecco's Modified Eagle Medium (DMEM, Invitrogen) containing 10% of Fetal Bovine Serum (FBS, Invitrogen) and 1%

of penicillin and streptomycin (Invitrogen). This breast cancer cells were incubated at 37^{o}C in a humidified incubator with a 5% CO_2 atmosphere in all the cell experiments.

2.3.5 Cytotoxicity Assay

The cytotoxicity of the TFB was evaluated on MCF-7 cells to make sure that the cells were healthy in the following experiments. Briefly, MCF-7 cells were seeded onto a 96-well plate at a density of 5×10^3 cells/well, and allowed to attach overnight. The medium was replaced with fresh complete medium (as described in cell culture protocol) containing 0, 1, 5, or 10 μM TFB and incubated for 4 hours. Then, the medium was changed to fresh complete medium and incubated for another 48 hours, and the cell viability was evaluated using Sulforhodamine B (SRB) based method according to the manufacturer's protocol (TOX-6, Sigma).

2.3.6 Flow Cytometry Measurement

The time-dependent fluorescence increase on MCF-7 was quantified using flow cytometer (FACSCalibur, BD). MCF-7 cells were seeded onto a 24-well plate at density of 1×10^5 cells/well, and allowed to attach overnight. The medium was replaced with fresh complete medium containing 5 μM TFB and incubated for 0.5, 1, 1.5, 2, and 2.5 hours. Then, the cells were washed 1 time with DPBS, and further treated with Trypsin to harvest cells from each well. Finally, MCF-7 cells were washed 3 times with ice-cold DPBS, and immediately analyzed using flow cytometer at FL1 channel. The viable cells were gated according to forward scatter (FSC) vs. side scatter (SSC) profile, and the data was analyzed using Cell Quest Pro software.

2.3.7 Confocal Imaging

The time-dependent fluorescence increase in MCF-7 cells was imaged using a confocal laser scanning microscope (CLSM, LSM 510, Zeiss) leaving the pinhole wide open. Briefly, MCF-7 cells were seeded onto a collagen (Invitrogen) coated 8-chamber glass bottom plate (Lab-Tek) at a density of 3×10^4 cells/well, and allowed to attach overnight. The medium was replaced with fresh complete medium containing 5 μM TFB. After 0.5 and 1.5 hours incubation, the cells were washed 3 times with DPBS, and fixed with 100 μL of 4% paraformaldehyde for 10 min at 4 ^{o}C. Then, the paraformaldehyde was removed and the cells were washed 3 times with DPBS. In the colocalization experiment, the cells were seeded and treated in the same manner except 100 nM Lysotracker Red (Invitrogen) and 5 μg/mL Hoechst 33342 (Invitrogen) were added to stain the lysosome and nucleus, respectively. These two dyes were added 20 min before cell fixation. Finally, 100 μL of Fluomount-G (Southernbiotech) was added, and the samples were imaged immediately using CLSM (pinhole sizes were set to obtain optical slice at 0.9 μm).

2.4 Results and Discussions

2.4.1 Molecular Design

The core concept of the design is to construct an amphiphilic NB molecule having the potential to self-assemble into nano-objects under physiological conditions. This amphiphilicity is achieved by conjugating a hydrophobic quencher and a dye onto a hydrophilic peptide. The concept of attaining amphiphilicity by means of conjugating two or more small-molecular chemical moieties with distinct solvent selectivity has been used to successfully construct peptide amphiphiles,[69,106-109] peptide nucleic acid amphiphiles,[110] and amphiphilic molecules with π-conjugated segments.[111-113] Fig. 2-1B shows the chemical structure of the proof-of-concept NB molecule studied in this paper. First of all, the hydrophobic units are composed of a black hole quencher BHQ-1, and a green dye, 5-carboxyfluorescein (5-FAM). 5-FAM was chosen on the basis of its exceptionally high quantum yield in the visible light region. The BHQ-1 segment with broad absorption between 400-650 nm (major absorption between 480-580 nm) will, when placed in close proximity to 5-FAM, quench the 5-FAM fluorescence without generating fluorescence of its own, thereby offering a high signal-to-noise ratio. Second, a HIV-1 derived cell penetrating peptide $\text{Tat}_{48\text{-}60}$,[114] with positively charged arginine and lysine amino acids, was incorporated as the hydrophilic segment to allow effective penetration of the cell membrane. The weakly basic nature of the arginine and lysine residues allows for the design of pH-responsive supramolecular nanobeacons. Finally, the key and most critical component is the cleavable linker that bridges 5-FAM and the lysine N terminus. The peptide tetramer of -Gly-Phe-Leu-Gly- (GFLG), first identified by Kopecek, Duncan and coworkers,[84,85] can be effectively cleaved by cathepsin B (CatB), a lysosomal protease involved in cellular protein turnover and degradation. We choose CatB because it plays important roles in tumor growth and progression and serves as a potential marker for tumor screening.[50,83,115-117] CatB has also attracted considerable interest as the target enzyme in the design of many polymer-drug conjugates.[84-86]

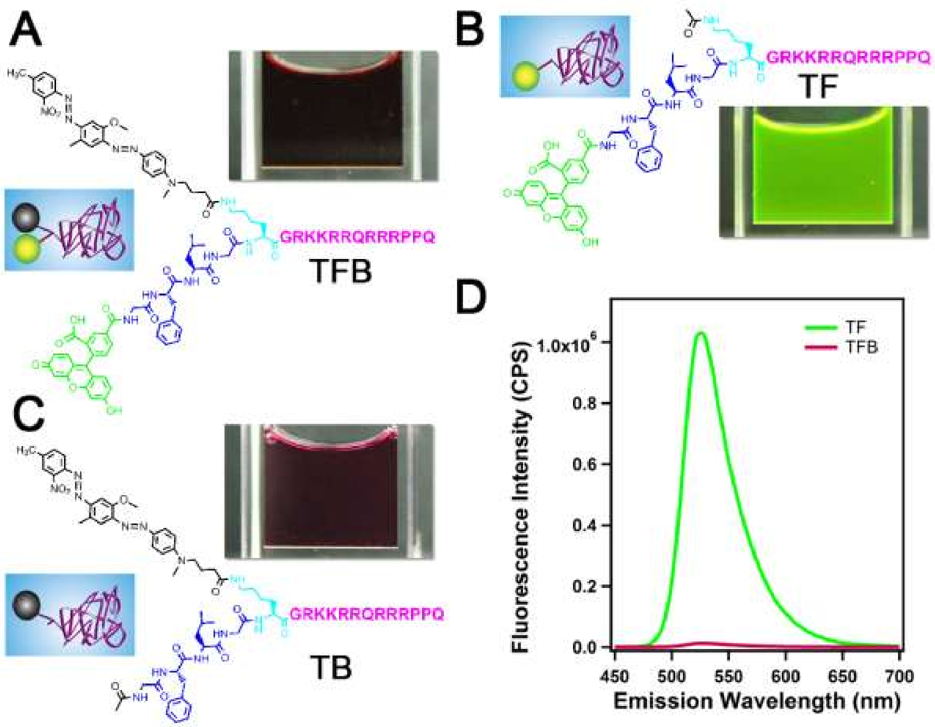

Figure 2-2. Photographs of 200 μM aqueous solutions of TFB (**A**), TF (**B**) and TB (**C**), and their respective molecular structures. The effective quenching of 5-FAM fluorophore by the BHQ-1 segment is reflected in the dramatic color change from bright green (**B**) to dark red (**A**). (**D**) 5-FAM fluorescence measurements of 1μM TF and 1μM TFB aqueous solutions.

2.4.2 Quenching Effect

We synthesized two control molecules: TF (Fig. 2-2B) and TB (Fig. 2-2C) to assist in better understanding of the quenching effect and self-assembly behaviors of the TFB NB molecule (S1-S2 in SI). The effective quenching of the 5-FAM fluorophore by BHQ-1 in the NB molecule can be inferred by a change in solution color between three molecules (Figs. 2-2A-2-2C). At a concentration of 200 μM, the aqueous solution of the TF conjugate appears bright green, owing to the 5-FAM fluorescence around 520 nm (Fig. 2-2B). In contrast, the aqueous solution of 200 μM TB displays a dark red color (Fig. 2-2C) due to the absorption in the visible light region between 400-650 nm. The dark red color of 200 μM TFB solution (Fig. 2-2A), similar to that of TB solution but distinct from that of TF solution, strongly suggests an effective quenching of 5-FAM fluorescence. This effective quenching was further supported by the measurements of the fluorescence of the 5-FAM chromophore. It was found that the 5-FAM fluorescence intensity of 1 μM TFB solution drops more than 80 times relative to that of a TF solution of the same molar concentration (Fig. 2-2D), implying a greater than 98% efficiency of 5-FAM fluorescence resonance energy transfer within the designed NB molecule.

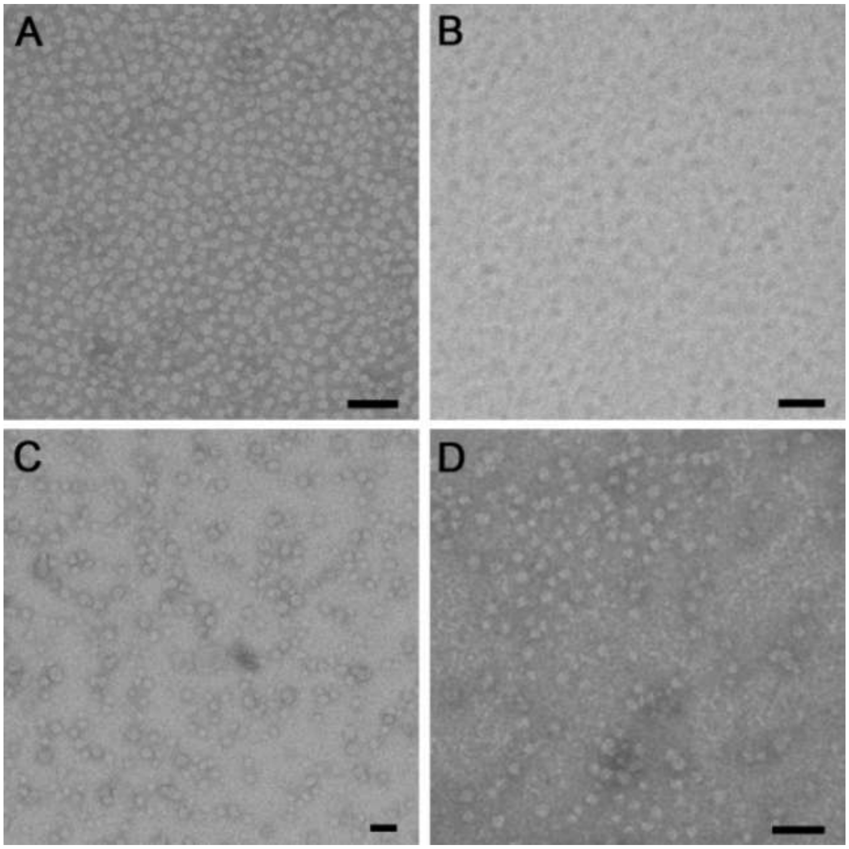

Figure 2-3. TEM (A) and cryo-TEM (B) images of 200 μM TFB in 1×PBS solutions reveal self-assembled nanoparticles of a uniform size (11.1±1.2 nm). TEM images of nanoparticles formed by self-assembly of 400 μM TF (C) and TB (D) in 1×PBS solutions with sizes of 18.4±3.7 nm, and 13.1±1.0 nm, respectively. TEM samples in (A), (C) and (D) were negatively stained using a 2 wt% uranyl acetate aqueous solution to enhance the image contrast. All scale bars: 50 nm.

2.4.3 Self-Assembly and Characterization

Self-assembly was initiated by dissolution of the molecule into either Milli-Q water or in phosphate buffered saline (PBS). Transmission electron microscopy (TEM) studies showed that all three molecules, TFB, TF and TB, self-assemble into spherical micelles under physiological conditions, with sizes of 11.1±1.2 nm, 18.4±3.7 nm, and 13.1±1.0 nm, respectively (Figs. 2-3A – 2-3D, and S3 in SI). A representative TEM image from a 1×PBS solution of 200 μM TFB is shown in Fig. 3A, revealing dominant nanoparticles with a uniform size of approximately 11 nm. In this image, the nanoparticles appear brighter than the background due to the use of uranyl acetate as a negative staining agent which deposits more on the background and thus reverses the image contrast. The size and shape of these nanobeacons was further confirmed using cryogenic TEM imaging techniques (Fig. 2-3B) which involve no staining but direct imaging of the liquid sample solution. Since the Tat peptide is rich in arginines and lysines, one would expect that the self-assembly behaviors of all the three studied molecules are pH-dependant. Indeed, we found that TB can self-assemble into supramolecular filaments in borate buffer (pH 9.5) (S4 in SI) in contrast to the spherical nanostructures in 1×PBS (pH 7.4). We believe the observed morphological transition is driven by the reduced electrostatic repulsions among the Tat peptides as a result of the deprotonation of the amines at higher pH

Circular dichroism measurements show that the hydrophilic Tat sequence assumes a random coil-like secondary structure under physiological conditions (S5 in SI). The diameter of 11 nm is reasonably close to twice that of the expected molecular length of TFB. The amphiphilic nature of the TFB leads us to conclude that nanoparticles observed in Fig. 2-3A are core-shell micelles with the 5-FAM and BHQ-1 segments comprising the core. Since enzyme-catalyzed reactions involve the formation of enzyme-substrate complexes, the fact that the –GFLG- linkers are deeply embedded within the micellar core suggests that in the assembled state the –GFLG- peptide linkers would be inaccessible to CatB for cleavage.

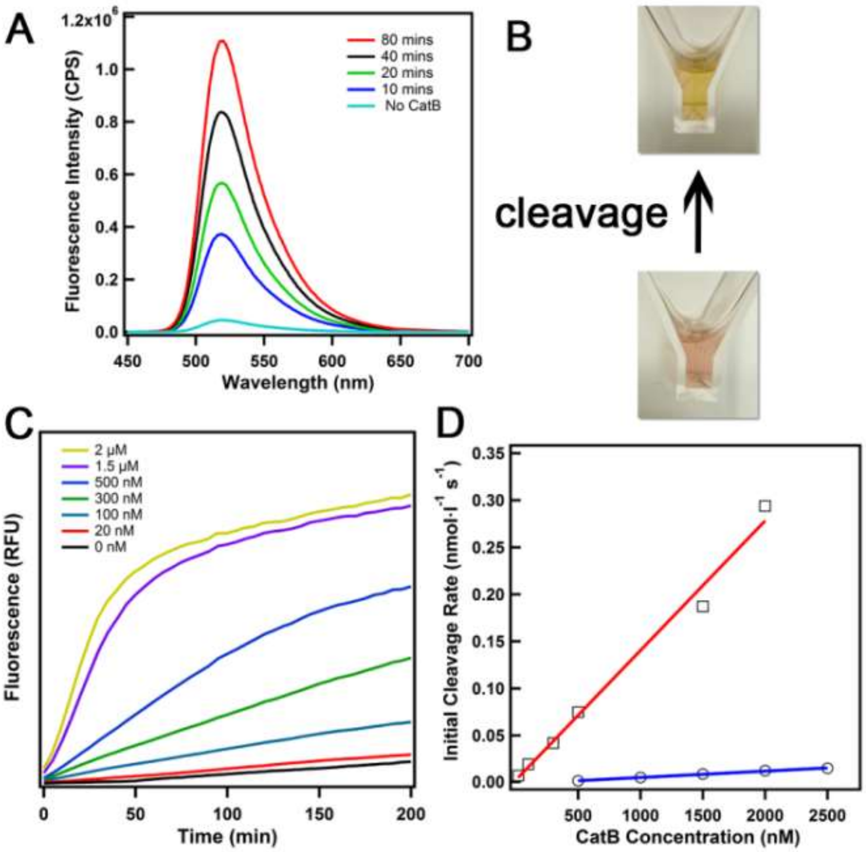

Figure 2-4. Fluorescence monitoring of the degradation process of NBs by CatB. (A) Time-course fluorescence measurements of a 3 μM TFB 1×PBS solution in the presence of 1 μM CatB; (B) photographs of NB solutions before and after CatB cleavage; (C) fluorescent measurement of 1 μM TFB PBS solutions in the presence of various concentrations of CatB; (D) plot of initial rate of 5-FAM cleavage versus CatB concentration (square, 1 μM TFB; circle, 50 μM TFB). The red and blue lines show a linear fit for the obtained data.

2.4.4 Enzymatic Degradation

Digestion experiments were carried out to evaluate the degradation kinetics of TFB NBs by CatB (S6 in SI). In these experiments, CatB was first activated for 5 mins at 37°C using a reaction buffer containing 1 mM EDTA and 25 mM L-cysteine. All solutions were adjusted to pH 5.0 to ensure proper CatB function. NB from a stock solution (1mM) was then introduced to solutions containing the desired amount of activated CatB, and the solution fluorescence was subsequently monitored.

Fig. 2-4A shows that in the presence of only 1 μM CatB the fluorescence intensity rapidly increases with time, with an approximate 25-fold increase in the peak intensity at 520 nm within 80 mins. After a sufficient time for cleavage, the solution color was observed to change from light red to light yellow (Fig. 2-4B). The small fluorescence peak in the absence of CatB arises from incomplete quenching of 5-FAM, and its intensity did not change over time, suggesting that the TFB molecules are rather stable under the experimental conditions. It is also important to note that when MMP-2 was added to the TFB NB solution, no noticeable cleavage reaction was observed throughout the course of 4 hour incubation (S7 in SI).

In order to correlate the fluorescence intensity to the enzyme activity and also to understand the enzyme cleavage efficiency on the studied NB molecule, we performed a series of experiments on 1 μM TFB solutions while varying the amount of CatB added. The 1 μM concentration is far below the critical micellization concentration (CMC) of TFB at pH 5, which was determined to be around 30 μM using a surface tension measurement method (S8 in SI). Fig. 2-4C clearly reveals that an increase in CatB concentration leads to faster cleavage of 5-FAM from TFB. It is also evident that concentrations of CatB as low as 20 nM can effectively cleave the peptide linker, although the reaction proceeds at a much slower rate.

We found that the initial rate of cleavage scales linearly with the concentration of CatB (Fig. 2-4D). The catalytic reaction of CatB has been reported to follow the kinetic behavior described by the Michaelis-Menten equation.[84,85] At the very low substrate concentrations, the equation can be simplified as: $V \cong \frac{k_{cat}}{K_M}[E]_t[S]$, in which k_{cat} is the first-order rate constant, $[E]_t$ is the total enzyme concentration, $[S]$ is the substrate (TFB, in the case reported here) concentration, and K_M is the Michaelis-Menten constant (S9 in SI). In the particular case reported herein (–GFLG- linker cleavage by CatB), the K_M has been reported to be on the scale of mM,[84,85] a value much higher than the 1 μM TFB concentration. The ratio of k_{cat}/K_M provides a direct measure of enzyme efficiency and specificity. The plot in Fig. 2-4D is in good agreement with this equation as the initial cleavage rate is indeed linear with respect to the CatB concentration. The initial reaction rates, V_0, were obtained from the linear region at the very beginning of the curves presented in Fig. 2-4C. k_{cat}/K_M was calculated using this simplified Michaelis-Menten equation, and was found to be approximately 137 $(\text{mol/L})^{-1}$ s^{-1} (S9 in SI). This value shows a reasonable degradation efficiency of the -GFLG- linker to CatB digestion. This finding also implies that quantitative detection of CatB in live cells is possible once accurate measurements of the initial reaction rate and the local concentration of the delivered NBs can be obtained.

We performed further experiments on a series of TFB solutions of different concentrations with a fixed CatB concentration (S10 in SI). We found that the initial cleavage rate first increased with the increase of TFB concentration from 50 nM to 1 μM as expected according to Michaelis-Menten equation but then started to drop after 3 μM. We attribute this drop in cleavage rate to the formation of dimers, trimers or other TFB molecular clusters that prevent the NB from being effectively cleaved by CatB. In order to gain a better understanding of the degradation kinetics of TFB micelles, we carried out experiments on a 50 μM TFB solution, a concentration above the CMC (~30 μM). As expected, the cleavage reaction was found to proceed much more slowly, and the k_{cat}/K_M was calculated to be around 0.135 $(\text{mol/L})^{-1}\ s^{-1}$ (Figs. 2-4D and S9 in SI), a value almost three orders of magnitude lower than that of CatB cleavage on the TFB monomers. Since TFB predominantly exists in aggregates above the CMC, these results clearly suggest that the -GFLG- peptide linker is inaccessible for effective CatB cleavage, and thus provide evidence for the expected cleavage mechanism presented in Fig. 2-1A.

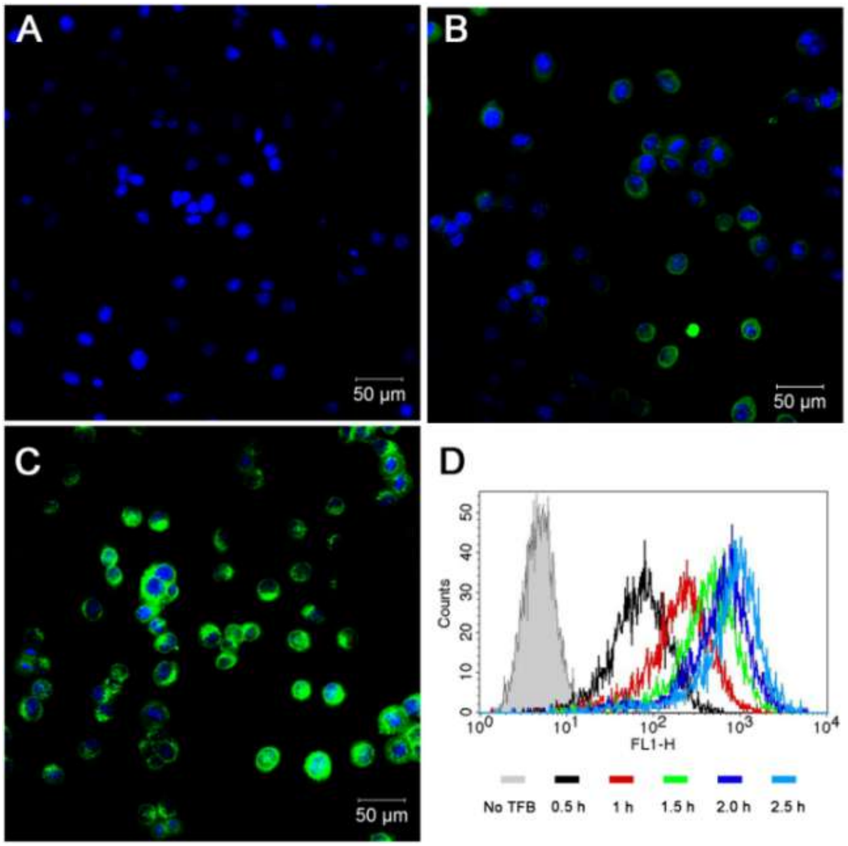

Figure 2-5. Time-dependent fluorescence of NB molecules inside MCF-7 human breast cancer cells. Fluorescence images of cells after 0 h (**A**), 0.5 h (**B**) and 1.5 h (**C**) exposure to TFB NB show increased 5-FAM fluorescence with time. The cell nuclei were stained with the blue dye Hoechst 33342. (**D**) Flow cytometry confirms the increased fluorescence intensity with time inside live MCF-7 cells.

2.4.5 Cancer Cell Imaging

To assess the possibility of using the designed NB for detection of CatB activities in cells, MCF-7 human breast cancer cells were incubated with 5 μM TFB at 37°C in cell media, and fluorescence images on the basis of 5-FAM emission were taken at different time points (0 h, 0.5 h, and 1.5 h) (S11 in SI). Figs. 2-5A-C reveals increased 5-FAM fluorescence intensity inside the MCF-7 cells with increased incubation time. Since intact TFB molecules remain dark and are not fluorescent, this result reveals that the NB molecule is not only capable of entering the cells but can also be effectively activated within cells to generate green fluorescence.

To confirm the observed 5-FAM fluorescence does not stem from potential artifacts associated with cell fixation, we used flow cytometry to investigate the time-dependant fluorescence in live cells (Fig. 2-5D). These results are consistent with the fluorescent imaging data. The continuous increase in fluorescence intensity with prolonged incubation time suggests effective cellular uptake of NB molecules. We speculate this effective internalization might be a combined effect of using the Tat cell penetrating peptide with the amphiphilic design of the NB molecule. A linear correlation of the geo-mean fluorescence intensity versus time was observed (Fig. S11 of S11 in SI), however, this correlation should be interpreted with caution and cannot be used to directly quantify CatB within cells because it is not clear whether the cellular uptake or the CatB cleavage reaction is the rate-limiting step, and whether other factors such as pH or ionic strength also contribute to the florescence intensity.

To evaluate if the internalized TFB NBs were indeed cleaved by the CatB enzyme, a CatB inhibitor (CA-074 Me) was used to suppress the CatB activity in cells. Both of our fluorescence and flow cytometery experiments reveal that the 5-FAM fluorescence intensity is significantly reduced in the presence of the inhibitor (Figs. S12-S13 of S11 in SI). We also performed experiments to show that the inhibitor does not interfere with the cellular uptake of the TFB and the viability of the studied cells (Figs. S14-S15 of S11 in SI). These experiments clearly suggest the specific cleavage of TFB NB by CatB. Colocalization experiments were also performed to verify the locations from where the 5-FAM fluorescence was generated. Lysosomes of MCF-7 cells were labeled with Lysotracker Red. As shown in Fig. 2-6, the merged fluorescence image (Fig. 2-6C) shows almost complete overlap of the 5-FAM green fluorescence with the Lysotracker Red fluorescence, indicating the 5-FAM fluorescence arises from lysosomes where CatB is expected to reside.

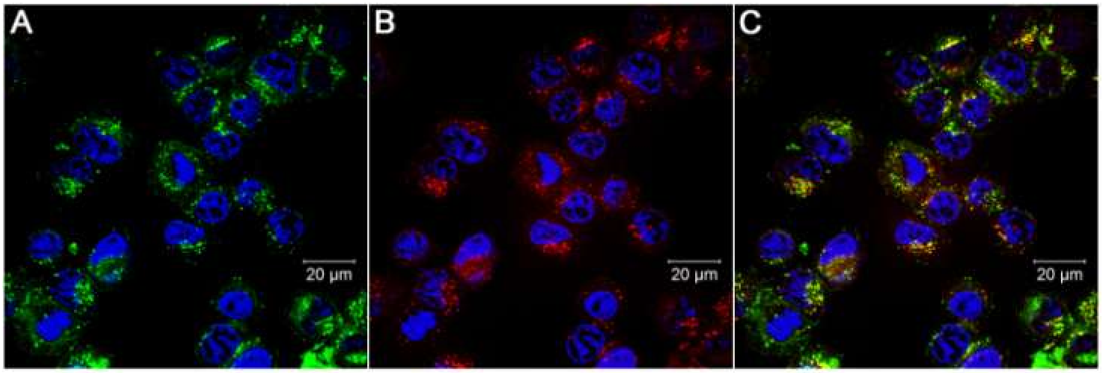

Figure 2-6. Confocal fluorescent images of MCF-7 cells after 2.5 h incubation with NB molecules show colocalization of the fluorescence signal of 5-FAM with that of the Lysotracker Red. (**A**) Image of 5-FAM fluorescence. (**B**) Image of Lysotracker Red fluorescence, and (**C**) merged image of (**A**) and (**B**). The cell nuclei were stained with the blue dye Hoechst 33342.

For the TFB concentrations used in all these studies, cell viability tests shows the TFB NB has little toxicity to MCF-7 cells during the incubation (Fig. S17 of S11 in SI). However, for concentrations higher than 30µM we found that our designed NB started to show great toxicity to cells, and we found that most cells died after incubating the beacon for only a few minutes, most likely due to the positive charge nature of the Tat peptide. Therefore, the future design must take into consideration the potential toxicity of positively charged cell penetrating peptides.

In a brief summary, these results reveal the possibility of using TFB NB for cancer cell imaging: under physiological conditions and above their CMCs, the designed NB molecules self-assemble into spherical micelles with the cleavable linker buried within the core. Upon accumulation in the tumor microenvironment or entering the lysosomes, which are known to have an acidic environment, the NBs can be expected to gradually dissociate to individual molecules due to dilution or/and pH triggering, thereby exposing the cleavable linker to the target enzyme. Eventually, in the presence of CatB, 5-FAM will be released and its fluorescence can be used as an indicator for the presence of CatB.

2.5 Conclusion and Future Prospects

In this work, we demonstrate a generic design of a new type of supramolecular nano-beacon by incorporating a fluorophore, a quencher and a hydrophilic cell penetrating peptide into one amphiphilic molecule. Our results clearly reveal the difference in CatB degradation kinetics between TFB molecules and supramolecular nanostructures, and demonstrate the potential for possible cancer cell imaging. However, there are still many challenges ahead for the development of supramolecular nanobeacons suitable for *in vivo* studies. First and foremost, the CMC value must be lowered to the nanomolar range for the construction of stable supramolecular beacons during the circulation. The CMC value of current design is around 30 μM, and our cytotoxicity studies have shown that it is not possible to maintain such a high concentration in plasma due to the toxicity of the Tat peptide. Second, a greater challenge is the controlled dissociation of supramolecular beacons into monomeric form. New features must be included in the future design such that once the supramolecular nano-beacons reach the targeted sites they could undergo a specific transition into monomeric form. The dilution and pH triggering mechanisms of the current system, although suitable for imaging purposes, could present a limitation or hurdle for quantification of enzymatic activities.

Third, other important parameters must also be considered, including the emission range of the used fluorescent dye (near infrared region is preferred for *in vivo* studies), the potential effects of pH and ionic strengths on the fluorescence intensity, cellular uptake mechanisms associated with different cell types, the rate-limiting steps in the cleavage reactions, and the inclusion of another type of molecular probes of different modalities (MRI, or PET) for deep tissue tracking. Despite these intimidating challenges, we believe that the facile tunability of supramolecular nanomaterials in size, shape and surface chemistry offers new opportunities for the development of enzyme sensors for the imaging and diagnosis of cancer cells.

2.6 Acknowledgements

I would like to thank the Integrated Imaging Center (IIC) at Johns Hopkins University for TEM and cryo-TEM imaging. Also, I would like to thank Dr. Ostermeier, Dr. Hristova, Dr. Konstantopoulos, Dr. Frechette for the use of fluorescence spectrometer, CD spectropolarimeter, flow cytometer and surface tension measurement instrument, respectively. The work reported here is supported by W.W. Smith Charitable Trust and the Johns Hopkins New Faculty Startup Grant.

3 Shape- and Charge-Dependent Cellular Internalization of Self-Assembling Supramolecular Nanobeacons by Cancer Cells†

3.1 Abstract

Intracellular sensing of pathologically relevant biomolecules could provide essential information for accurate evaluation of disease staging and progression, yet the poor cellular uptake of most water soluble molecular probes limits their use as effective protease sensors. Rational design of molecular probes capable of self-assembling into supramolecular nanoprobes presents a potential strategy to alter their interaction mechanisms with cells thus promoting their effective cellular entry and intracellular accumulation. Herein we report on the design and synthesis of both peptide-based molecular beacons that could spontaneously associate into either spherical or cylindrical supramolecular protease sensors, depending upon their growth kinetics and assembly conditions. Our confocal imaging and flow cytometry results suggest that cancer cells had difficulties internalizing negatively charged monomeric molecular beacon and also those with extremely high-aspect-ratio cylindrical nanobeacons regardless of their charge status, but could rapidly internalize positively charged spherical nanobeacons. These studies corroborate the shape-dependent cellular uptake of filamentous nanostructures and the charge-dependent internalization of spherical nanoparticles, and more importantly

---

† Lock, L.L., Zhang, P., and Cui, H. designed the experiments. L.L.L. and Reyes, C. performed the experiments and analyzed the data. L.L.L. and C.H. prepared the manuscript.

provide insight into the rational design of supramolecular nanoprobes with regulated cellular uptake characteristics by tuning their physicochemical properties.

3.2 Introduction

Molecular imaging has shown great potential in various applications such as drug-development, cancer early detection and cancer patient prognosis.[118-120] This emerging technology enables us to characterize and evaluate biological processes at subcellular and molecular level by visualizing or quantifying the signal that originates from interactions between biomolecules and molecular probes.[121,122]Molecular probe serves as the reporting agent that translates biological information regarding disease stages or tumor location into measurable signals, often possessing unique imaging modality such as positron emission tomography (PET), optical fluorescence, and magnetic resonance imaging (MRI).[121-123] To obtain explicit and reliable diagnostic information, desirable characteristics of an ideal molecular probe include high signal-to-noise ratio to discern cancer cells from normal tissue, high affinity to preferentially accumulate in target sites, high specificity and high sensitivity in detecting particular biomarkers, and high stability in *in vitro* and *in vivo* conditions to reduce chances of proteases degradation.[121-124] Due to their hydrophilic nature, one particular challenge in the use of water-soluble molecular probes for intracellular sensing is their effective cellular uptake into cells of interest, thus resulting in lower specificity and sensitivity to detect cancer cells. One effective approach to enhance cellular uptake is to covalently incorporate into the design a small auxiliary segment such as cell-penetrating peptide (CPPs)[125] and receptor targeting ligands.[126,127] However, the resulting conjugates are still water soluble which may suffer from premature degradation. To overcome this hurdle, we devised the molecular probe with hydrophobic segment to regulate cellular internalization as well as incorporating an amyloid-forming peptide sequence to induce the formation of supramolecular nanoprobes.

Our ultimate interest lies in the regulation of the cellular uptake of nanoprobes *via* modulating their physicochemical properties. Various studies have reported that nanoparticle size and shape can affect both their internalization efficiency and endocytosis pathway[128-130] due to the differences in size-dependent membrane wrapping time and the size limitation of certain endocytosis pathways.[131,132] For example, Discher and coworkers found that polymeric spheres and filomicelles in micrometer range were taken up by phagocytes more easily than longer filaments[133]; DeSimone's group used poly(ethylene glycol) hydrogel to make various nanoparticles and showed that HeLa cells internalized cylindrical particles faster than spherical ones[134]; using gold and silver nanoparticles coated with antibody, Chan and coworkers found that cellular binding and subsequent cellular response is strongly mediated by nanoparticle size[135]; while Mitragotri's group demonstrated higher cellular specificity for antibody-coated nanorods than their spherical polystyrene counterpart.[136] These vital studies revealed the importance of nanoparticle's size, shape and charge in cellular interactions; however, very few reports have investigated the interdependency of two or more parameters of nanoparticles in one single system. Therefore, a system with tunable properties that could closely mimic nanocarriers used in biomedical areas is needed to elucidate the interaction between nanocarriers and cells.

Our approach is to design self-assembling molecular probes by incorporating a hydrophobic fluorescence detection moiety into a self-assembling peptide domain with tunable hydrophilic terminus. This concept has been used to construct peptide amphiphiles[69,137-140] and other peptide-based self-assembling units,[141,142] which offers a feasible way to prepare nanostructures with different well-controllable properties by carefully tuning both the hydrophobic block and hydrophilic peptide sequence.[143-145] In this study, we synthesized two conjugates that differ only in their terminal residues: one is positively charged and the other one is negatively charged. These molecules of different charges can self-assemble into spherical or cylindrical micelles when prepared through different kinetic pathways. Noteworthy, we also included the beacon concept[99] into our design by introducing the 5-FAM and Black Hole Quencher-1 pair into the conjugates which will only fluoresces upon cathepsin B enzyme degradation after cellular entry, allowing us to exclude any false positive signals arising from the cell membrane absorption. Our results showed that positively-charged spherical nanoprobes were internalized ~3-fold higher than its soluble molecular probe counterpart which underlines the distinction between nano- and molecular system.

3.3 Experimental Procedures

3.3.1 Self-assembly of Spherical and Cylindrical Nanostructures/Nanobeacons

HFIP, known to break amyloid-beta interaction into homogenous monomeric form, was used in this sample preparation procedure. SFB-K and SFB-E molecules were first dissolved in HFIP and the concentration was calibrated to 200 μM in 200 μL HFIP (hexafluoroisopropanol). For SFB-KE, 100 μL of each SFB-K (200 μM) and SFB-E (200 μM) HFIP solutions were mixed to achieve molecular level mixing at 1:1 equimolar ratio. All sample SFB-K, SFB-E and SFB-KE in 200 μM and 200 μL HFIP were prepared in glass vials. HFIP was then removed using a rotary evaporator, in a 40 °C water bath for 10 minutes, leaving a thin film of dry nanobeacons on the wall of the glass vial.

For the monomers preparation, all samples were reconstituted in 200 µL of DMSO and kept at room temperature. For the spherical nanostructure formation, all samples were reconstituted in 50 µL 100 mM HEPES buffer and 150 µL of water was added to yield a final sample concentration of 200 µM in 25 mM of HEPES buffer and all samples were kept in 4 °C.

In the cylindrical nanostructure preparation, SFB-K and SFB-KE were dissolved in 50 µL 100 mM HEPES buffer and 150 µL of water was added to yield a final sample concentration of 200 µM in 25 mM of HEPES buffer. These samples were sonicated in a water bath for 20 minutes and kept at room temperature. The SFB-E nanobeacons were dissolved in 1xDPBS solution to yield a final concentration of 200 µM and were stored at room temperature.

All monomers, spherical and cylindrical samples were pre-treated with HFIP except the cylindrical SFB-E sample, which was dissolved directly in 1xDPBS from its lyophilized powder form.

3.3.2 Transmission Electron Microscopy (TEM) and Cryo-TEM

Spherical nanostructures (SFB-K, SFB-E and SFB-KE) were aged for 1 day in 4 °C and cylindrical samples were aged for >4 days at room temperature; 5 µL of sample was spotted on a carbon film copper grid with 400 square mesh (from EMS: Electron Microscopy Sciences) and the excess was removed with filter paper to leave a thin film of sample on the grid. After letting the sample dry for 10 minutes, 5 µL of 2% uranyl acetate was added to sample grid, and the excess was removed after 10 seconds. All samples were dried for at least 2 hours before TEM imaging.

Cryogenic TEM imaging was also performed on the FEI Tecnai 12 TWIN Transmission Electron Microscope, operating at 80 kV. 3-5 μL of sample solution were placed on a holey carbon film supported on a TEM copper grid (Electron Microscopy Services, Hatfield, PA). All the TEM grids used for cryo-TEM imaging were treated with plasma air to render the lacey carbon film hydrophilic. A thin film of the sample solution was produced using the Vitrobot with a controlled humidity chamber (FEI). After loading of the sample solution, the lacey carbon grid was blotted using preset parameters and plunged instantly into a liquid ethane reservoir precooled by liquid nitrogen. The vitrified samples were then transferred to a cryo-holder and cryo-transfer stage which was cooled by liquid nitrogen. To prevent sublimation of vitreous water, the cryo-holder temperature was maintained below -170 °C during the imaging process. All images were recorded by a SIS Megaview III wide-angle CCD camera.

3.3.3 Zeta Potential Measurement

Zeta-potential measurements were carried out using Malvern Zetasizer Nano instrument and its compatible disposable capillary cell (DTS 1070 from Malvern). Spherical and cylindrical SFB nanobeacons were instantly diluted from 200 μM to 5 μM in water with a final volume of 1 mL. Measurements were carried out in automated mode and repeated three times to obtain an average value and its standard deviation.

3.3.4 Activation of Nanobeacon with Cathepsin B Enzyme

CatB enzymatic reaction buffer was prepared in 50 mM sodium acetate buffer with 25 mM *L*-cystein as enzyme activator and 1 mM EDTA was added as enzyme stabilizer. 0.1 Unit of CatB was pre-incubated in reaction buffer for 5 minutes at 37 ^{o}C to activate the enzyme and SFB nanobeacons were added to reaction buffer to yield a final concentration of 5 μM and final volume of 100 μL. All samples were triplicated and the experiment was carried out in a 96-well standard opaque plate. 5-FAM molecule was excited at 492 nm and emission was collected at 520 nm with 515 nm cut off. Using a Gemini XPS microplate reader (Molecular Devices, Sunnyvale, CA), the kinetic mode was selected and fluorescence intensity was measured for 125 minutes with fluorescence readings at 5 minute intervals.

3.3.5 *In vitro* Cellular Uptake and Inhibition Protocol

PC3-Flu cells were seeded onto 24-well plate with cell density of $1x10^5$ cells/well and incubated in 37 ^{o}C, 5% CO_2 overnight. 5 μM of SFB nanobeacons (monomers, spherical and cylindrical, independently) was prepared by adding 12.5 μL of 200 μM SFB stock solution into 487.5 μL of 1640 cell medium for PC3-Flu. PC3-Flu cells were incubated with the cell medium containing 5 μM of SFB nanobeacons for 1 hour in 37 ^{o}C. On the other hand, the energy-dependent endocytosis was inhibited by pre-treatment with 10 mM sodium azide and 10 mM 2-deoxy-D-glucose for 15 minutes, followed by 5 μM SFB nanobeacons incubation for 1 hour in 37 ^{o}C. Cell medium was removed and 200 μL of Trypsin Gibco 0.25% Trypsin-EDTA (1x), phenol red (Life Technologies Corporation) was added to PC3-Flu cells and incubated for 2 minutes at room temperature. 500 μL of 1640 cell medium was added to each well and cell were re-suspended from the bottom of each well, then transferred into 1.5 mL Eppendoff tube and kept in ice. All cells were centrifuged at 1.7k RPM for 90 seconds and the supernatant was removed. 500 μL cold 1xDPBS was added to wash cells and re-centrifuged at 1.7k

RPM for 90 seconds. The supernatant was removed and 200 μL of cold 1xDPBS was added to re-suspend cells, and then transferred into flow-cytometry tube. 10,000 of live cells were gated and fluorescence intensity was detected using flow-cytometer (FACSCalibur, BD).

3.3.6 Confocal Laser Scanning Microscopy

PC3-Flu were seeded onto 8-well plate with cell density of 3×10^4 cells/well and incubated overnight in 37 ^{o}C incubator. 7.5 μL of 200 μM SFB nanobeacons were added to 292.5 μL of 1640 cell medium and transferred to each well containing PC3-Flu cells. The cells were kept in 37 ^{o}C for 1 hour and then the medium was removed, followed by a quick wash with 300 μL of cell medium without phenyl red. PC3-Flu cells were imaged directly without fixing the cells. The cell nuclei were stained in blue with Hoechst 33342 and lysosome compartments were stained with Lysotracker Red for 30 minutes before the cell imaging.

3.4 Results and Discussions

3.4.1 Molecular Design

Peptide-based system offers a versatile platform to rationally design a self-assembly nanoparticles with amphiphilic property, self-assembly-driven domain and tunable terminus charge. To achieve desired amphiphilicity in our design, a hydrophobic quencher and fluorophore were conjugated to a peptide domain with hydrophilic end. Apart from the contribution of amphiphilicity, another governing factor to attain controlled self-assembled nanoparticles relies on the peptide domain that consists of strong hydrogen-bond forming sequence, such as Sup35$_{7\text{-}13}$ heptapeptide GNNQQNY.[146] This feature allows one-dimensional cylindrical growth of molecular probes upon self-assembly in an explicit condition. In this study, we designed two self-assembling molecular beacon, namely SFB-K (Figure 3-1a) with three lysines as terminal residues and SFB-E (Figure 3-1a) with three glutamic acids serving as the charge source upon ionization of their side chains. Besides the differences in terminal residues, the two molecules are exactly the same and composed of four parts, consisting the amyloid-forming peptide $Sup35_{7\text{-}13}$,[147] a fluorophore with green fluorescence(5-FAM), it's compatible quencher (BHQ-1) and an enzyme degradable linker (-GFLG-tetrapeptide)[85,148] connecting 5-FAM to Sup35. The beacon concept utilized BHQ-1 to quench the 5-FAM fluorescence by their connection through an intracellular enzyme cleavable linker -GFLG-. In our previous work, we have proved that the breaking of this linker would release 5-FAM away from BHQ-1 quencher, therefore showing green fluorescence for detection.[149]

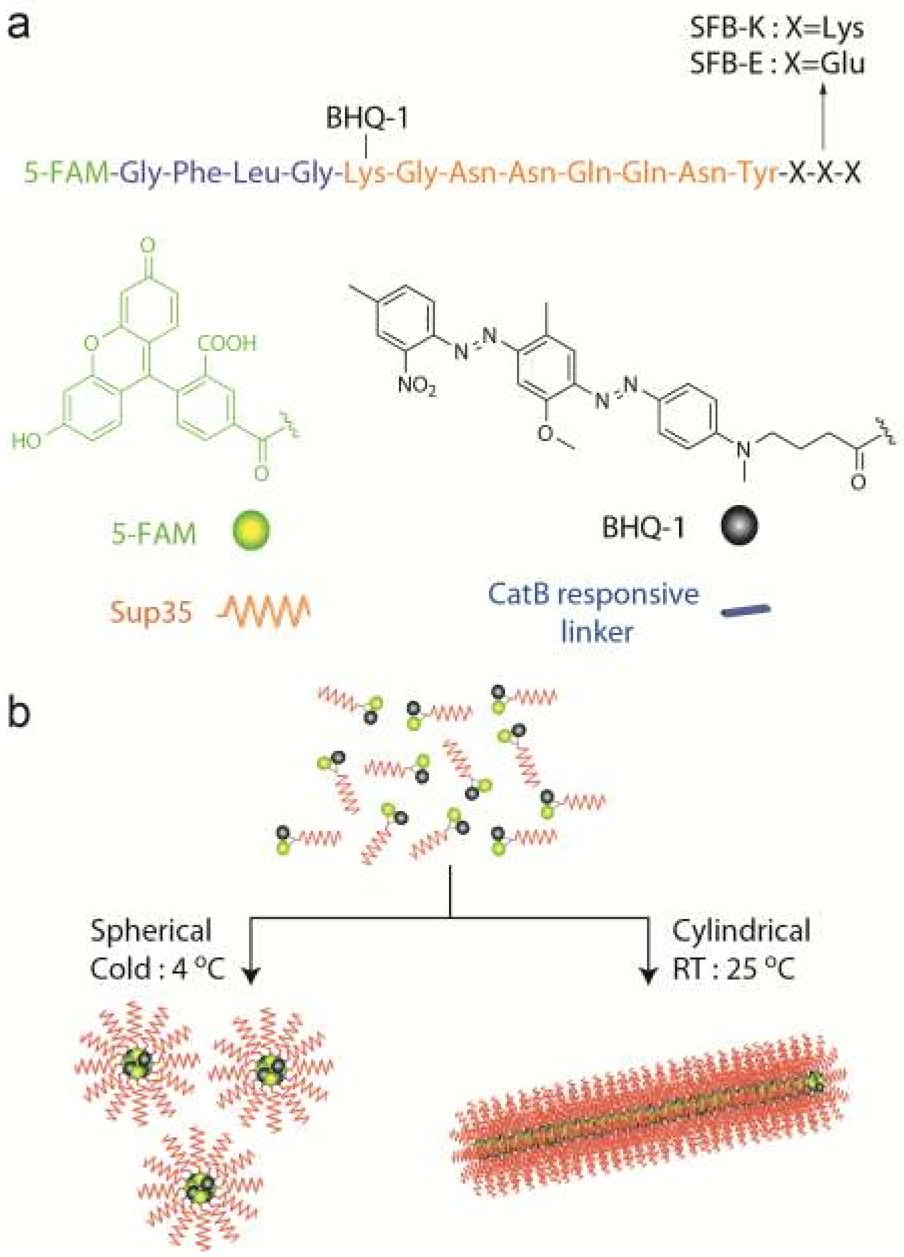

Figure 3-1. (a) Chemical structure of SFB-K and SFB-E nanobeacons; the terminal amino acids were designed to be lysine or glutamic acid, respectively. Sup35 (GNNQQNY) was used as self-assembling peptide domain and -GFLG- tetrapeptide was incorporated as CatB responsive linker. (b) The self-assembly of SFB molecules were conducted at different temperatures to obtain spherical (cold, 4 ^{o}C) and cylindrical (room temperature, 25 ^{o}C) nanostructures.

3.4.2 Molecular Self-Assembly

We found that spherical micelles can be formed from the same molecules through different kinetic pathways by controlling temperature, buffer and time of aging. In order to initiate self-assembly from molecular level, hexafluoroisopropanol (HFIP) was used to disrupt existing beta-sheet oligomers/fibrils[150,151] formed during peptide synthesis and purification. SFB-K and SFB-E nanobeacons were each dissolved in HFIP to obtain a 200 μM concentration. For SFB-KE sample preparation, SFB-K and SFB-E were mixed at molecular level in HFIP solution yielding 1:1 equimolar mixing ratio. All HFIP pre-treated samples were vacuum dried using a rotary evaporator, forming a thin peptide film on the glass vials. For spherical SFB nanobeacons (SFB-K, SFB-E and SFB-KE) preparation, the peptide film was reconstituted in 25 mM HEPES buffer and stored at 4 ^{o}C. For cylindrical nanobeacons preparation, HFIP-pretreated/dried SFB-K and SFB-KE thin films were reconstituted in 25 mM HEPES buffer and sonicated for 20 mins in a water bath. We observed that the HFIP-pretreated/dried SFB-E formed polydispersed nanostructures (spherical and cylindrical) after being reconstituted in 25 mM HEPES buffer. Therefore, we prepared the cylindrical SFB-E by dissolving its lyophilized peptide power directly in 1xDPBS buffer without HFIP pre-treatment. All cylindrical nanobeacons samples were stored at room temperature and aged for at least 3 days to ensure mature fibers formation (Detailed procedure in supporting information).

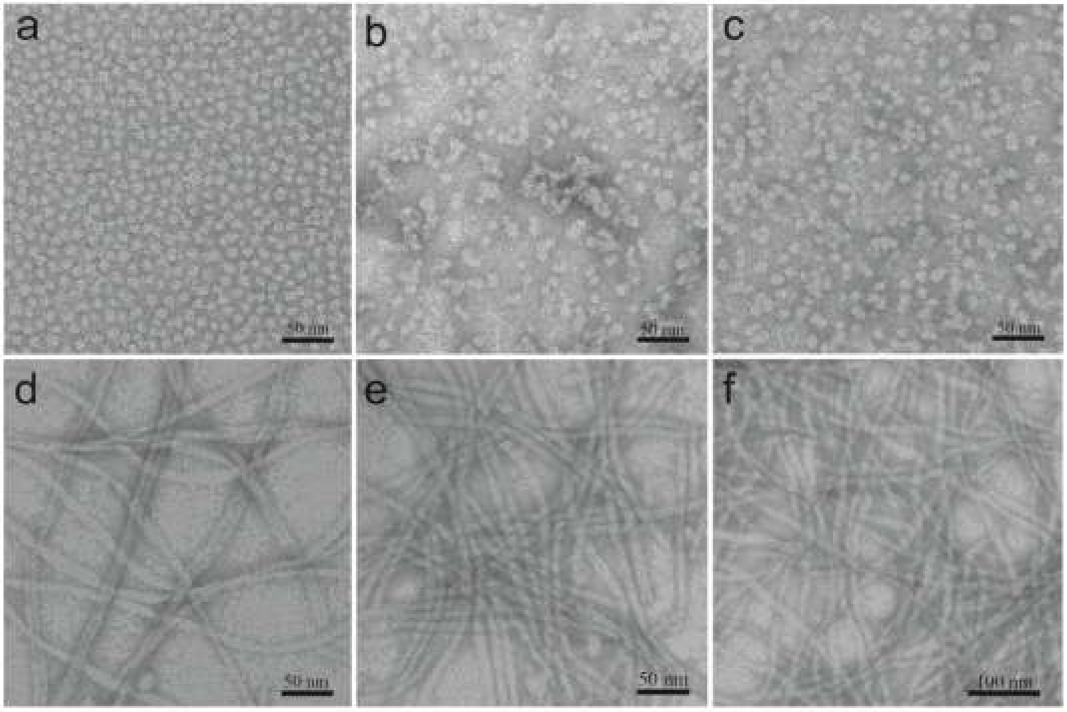

Figure 3-2. Regular TEM images of self-assembled spherical and cylindrical nanostructures formed by SFB-K (a,d), SFB-E (b,e) and SFB-KE (e,f) at 200 μM. All samples except cylindrical SFB-E were prepared from the HFIP pre-treated molecules and reconstituted in 25 mM HEPES buffer, Spherical nanostructures were kept at 4 ^{o}C while cylindrical nanostructures were aged for more than 4 days at room temperature, in the dark. Cylindrical SFB-E was prepared by directly dissolving the molecules in 1×DPBS.

3.4.3 Nanostructure Characterization

In order to validate the self-assembled structures formed by SFB-K, SFB-E and SFB-KE, TEM (Transmission Electron Microscopy) and cryo-TEM techniques were used to determine the nanostructure's morphology and diameter. TEM images in Fig 2(a-c) showed that 200 μM samples of SFB-K, SFB-E and SFB-KE formed spherical nanostructures of diameter 7.8 ± 0.9 nm, 7.6 ± 1.3 nm and 8.5 ± 1.0 nm, respectively. As shown in Figure 3-2(d-f), TEM images revealed cylindrical SFB-K, SFB-E and SFB-KE structures with 9.24 ± 1.9 nm, 8.86 ± 1.4 nm and 11.95 ± 1.6 nm diameters, respectively.

With the estimation of SFB molecule's extended length of 7 nm, these SFB molecules were most likely self-assembled into a core-shell structure with hydrophobic group embedded and overlapped in the center.[69] To avoid possible distortions resulting from negative staining in regular TEM, cryo-TEM was performed to capture images of cylindrical nanobeacons in their hydrated form as shown Figure S4. Both spherical and cylindrical nanobeacons were stable and were able to maintain their self-assembled nanostructures throughout the course of the studies (Figure S7).

To characterize the surface charge of these designed nanostructures, zeta-potential measurements were conducted for each of the samples. As expected, SFB-K with free amines on the lysine side chains resulted in a positive zeta potential of +40.7 ± 2.1 mV and +42.9 ± 0.7 mV for spherical and cylindrical nanostructures, respectively. On the other hand, the negative surface charge of SFB-E nanostructures was contributed by the free carboxylic group of glutamic acid's side chain and the C-terminus when they were deprotonated. The zeta potentials for spherical and cylindrical SFB-E were -50.2 ± 1.6 mV and -61.1 ± 6.2 mV, respectively. In a 1:1 mixing ratio of SFB-K and SFB-E, SFB-KE showed negative surface charge of -30.8 ± 1.1 mV and -40.4 ± 3.6 mV for spherical and cylindrical nanostructures, respectively. When dissolved in 50mM HEPES buffer that has pH 7.0, both the side chain of Lys (pK_a=10) and Glu (pK_a=4) as well as the C-terminus of Glu (pK_a=2) will be fully ionized. Therefore, the anionic characteristic of SFB-KE nanostructure was a result of an overall negative charge upon mixing of SFB-K with three free amine groups and SFB-E with three side chain carboxylic acids and one terminal carboxylic acid group. The nature of our designed molecule self-assembling into different shapes with different surface charges offers an interesting system that can be utilized to study the effect of shape and surface charge of nanostructures on cellular uptake. The successful preparation of spherical and cylindrical nanobeacons using the same molecules provides nanostructures that only differ in their shape or surface charge, which allows us to understand the role of the individual parameters or their interplay in the cellular entry process.

3.4.4 Cellular Uptake of Nanobeacons

The cellular internalization of the self-assembled nanostructures was investigated using PC3-Flu, a metastatic human prostate cancer cell line, which showed increased expression of CatB due to its aggressiveness.[152-157] The pre-seeded cells were treated with complete medium containing 5 μM of SFB nanobeacons of respective charge and shape for 1 hour. To exclude the possibility of self-assembled nanostructures dissociating into their monomeric form during experimental condition, SFB monomers were prepared in DMSO and were included in the *in vitro* cell study as a control set. The internalization rate of SFB nanobeacons was evaluated by quantifying the released 5-FAM fluorescence through the flow cytometry method, because the SFB can be cleaved to release 5-FAM after their encounter with CatB regardless of their morphology and surface charge (Figure S6). Noteworthy, the intracellular concentration of CatB is much higher[158] than the concentration used in our enzymatic degradation experiments (3000 mU versus 25 mU per 1 μM of SFB), therefore the difference in cleavage rate of conjugates in different nanostructure is negligible.

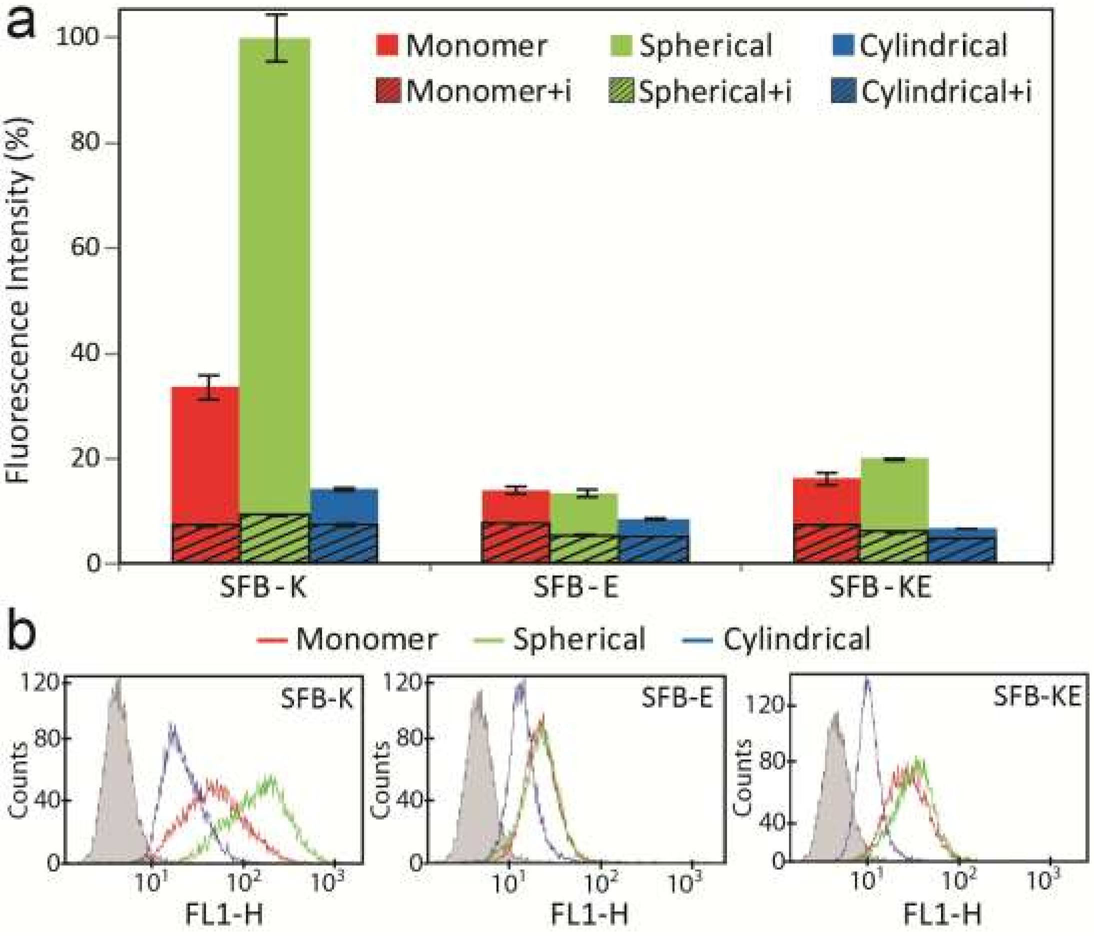

Figure 3-3. PC3-Flu cells were incubated with 5 μM of SFB nanobeacons for 1 hour and the cellular uptake rate of nanobeacons were compared by measuring each cell's fluorescence intensity. (a) Fluorescence intensity obtained from flow-cytometry showed spherical SFB-K internalized faster than SFB-K monomers and cylindrical state. Upon inhibition of energy-dependent endocytosis pathway, +i (dashed bar), PC3-Flu cells did not show appreciable uptake of SFB nanobeacons. (b) Flow cytometry spectra comparing fluorescence intensity of different shapes of SFB-K, SFB-E and SFB-KE. All the data was presented as mean ± s.d. (n = 3).

3.4.5 Shape Effect

From flow-cytometry results, we observed significant difference in the cellular uptake of spherical nanobeacons than its counterparts. PC3-Flu cells incubated with SFB-K spherical nanobeacons showed ~3 fold fluorescence increase than monomeric nanobeacons and ~ 7 fold increase than cylindrical nanobeacons, as shown in Figure 3-3a. When comparing monomeric and cylindrical nanobeacons, flow-cytometry showed approximately 2 fold increase in monomers cellular uptake than cylindrical nanobeacons, as shown by the red and blue bars of Figure 3-3a. These results support the stability of the self-assembled nanostructure we attested to earlier (Figure S7d-e), clearly indicating that the cylindrical micelles were stable throughout the experimental period of 1 hour in 37 ^{o}C. Through TEM characterization, however, it is more challenging to prove the stability of spherical micelles in complete medium due to the existing globular protein, such as human serum albumin, HSA (Figure S8). Using a biological relevant buffer (1xDPBS), we showed that spherical nanobeacons maintained their self-assembled state under experimental condition (Figure S7a-c). Moreover, the huge difference between cellular uptake of SFB-K in its monomer and spherical micelle form strongly suggests the stability of spherical micelles in cell culture medium. Therefore, we conclude that the observed differences in cellular uptake arise from their differences in self-assembled state. When comparing the intracellular accumulation of nanostructures with different shapes, we found that the spherical micelles outperformed cylindrical micelles regardless of their surface charge, which is in consistence with previous reports.[128]

3.4.6 Charge Effect

In terms of charge effect, cellular uptake of nanocarriers was known to be regulated by the surface chemistry, with the cationic nanoparticles showing higher intracellular accumulation.[159] We observed similar trend from our results where cationic SFB nanobeacons were internalized faster than SFB-E and SFB-KE which were negatively charged (Figure 3-3a). This phenomenon is most likely caused by the electrostatic interaction of cationic nanoparticles with a slightly anionic cell membrane.[159,160] More importantly, aside from these general observations, we found that only the cellular uptake of spherical nanoparticles is greatly affected by their surface charge: spherical cationic nanoparticles fluoresced in cells more than 6 times higher than anionic spheres did. Overall, cylindrical nanobeacons did not show significant uptake regardless of its surface charge. We speculated that the elongated cylindrical nanostructures in micro-meter length were too long for the cells to take in. Through this experiment, we observed an interdependent relationship between the shape and surface charge of nanostructure in order to achieve optimized cellular uptake.

3.4.7 Energy-dependent Endocytosis Inhibition

There have been several reports showing that nanoparticles with positive surface chemistry can directly penetrate across cell membranes without creating any toxicity to the cells.[161] To better comprehend the greater intracellular accumulation of cationic spherical nanobeacons, we assessed their endocytotic pathway and ability to penetrate cells directly. We compared the cellular uptake of nanocarriers and monomers by PC3-Flu cells with or without treatment with 10 mM sodium azide (NaN_3) and 10 mM 2-deoxy-D-glucose (DDG), the combination of which proved to inhibit the energy production efficiently.[162] PC3-Flu cells were pre-incubated with 10 mM NaN_3 and 10 mM DDG for 15 minutes, and then they were incubated with 5 μM SFB nanobeacons for 1 hour in 37 ^{o}C. The result in Figure 3-3a showed that the cellular uptake of all the formulations was inhibited to a basal level (shaded bars, <10%), clearly indicating that the cellular uptake of conjugates followed the energy-dependent endocytosis pathway regardless of shape and charge.

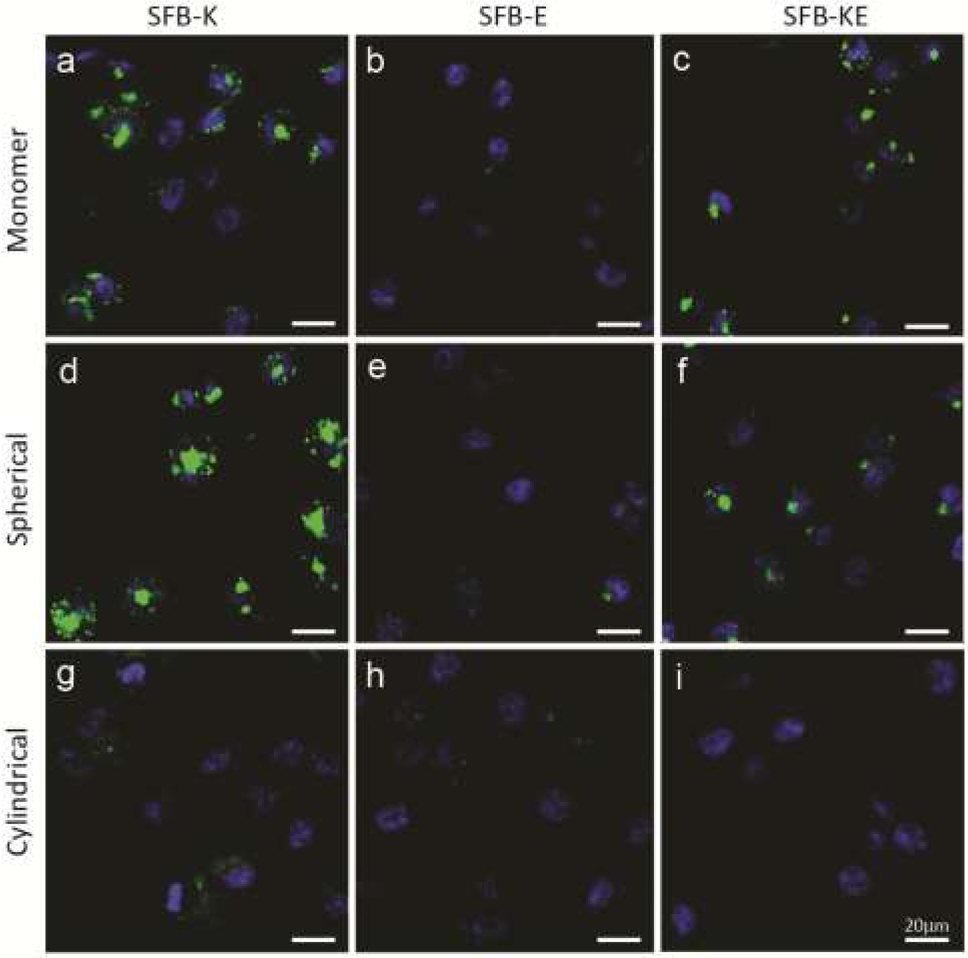

Figure 3-4. Confocal laser scanning microscopy of PC3-Flu cells after 1 hour of incubation with 5 μM of SFB nanobeacons in different shapes and charges. (a-c) Monomers of SFB-K, SFB-E and SFB-KE, respectively; (d-f) spherical nanobeacons of SFB-K, SFB-E and SFB-KE, respective ely; (g-i) cylindrical nanobeacons of SFB-K, SFB-E and SFB-KE, respectively. Scale bar: 20 μm.

3.4.7 Cancer Cell Imaging

Since the flow cytometer cannot differentiate whether the fluorescence originates from inside of the cells or on the cell membrane, the cellular uptake of different nanocarriers was further determined by confocal microscopy. This technique allowed us to visually observe the location of fluorescence in cell, thereby justifying our collected data was solely based on internalized nanobeacons and not false signals generated from premature degradation of beacon molecules outside of the cells. PC3-Flu cell nuclei were stained in blue using Hoechst 33342 and the released 5-FAM from the SFB nanobeacons fluoresced in green. The images in Figure 3-4 clearly showed that all the fluorescence was located inside the cells, and the strongest fluorescence was observed from the cells treated with positively charged spherical micelles (Figure 3-4d). It was reported that the positively charged particles can induce the formation of a temporary transmembrane pore, which is associated with its toxicity.[163-165] It is possible that higher intracellular accumulation of positively charged nanoparticles is a result of its toxicity to the cells. However, this possibility can be excluded since we did not observe any significant change in viability of cells treated by conjugates of different morphology and surface charge (Figure S9).

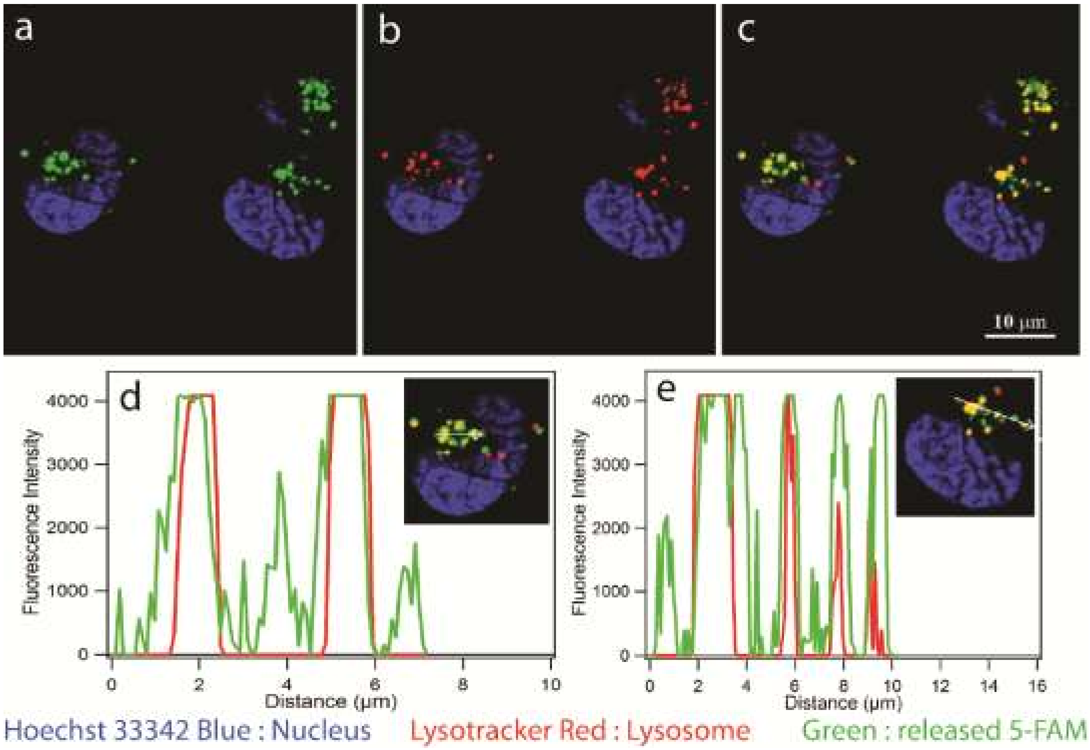

Figure 3-5. Confocal microscopy images of (a) released 5-FAM (green) and (b) Lysotracker Red staining lysosome (red) of PC3-Flu cells after incubation with 5 µM of spherical SFB-K for 1 hour. (c) Overlay of green and red channels showed co-localization of released 5-FAM in lysosome. (d-e) Colocalization of green and red channels was quantified and the weighted colocalization coefficient was determined to be 86.5 ± 8.4% (n = 20 cells).

Since the positively charged spherical nanoparticles showed the highest intracellular accumulation, nanocarriers with the same properties are of great interest to design intracellular sensing probe. Besides the intracellular accumulation, the subcellular distribution of nanoparticle has also proven to be critical for potential biomedical applications.[166,167] To better comprehend the internalization of the spherical SFB-K nanoparticles, PC3-Flu cells were pre-treated with Lysotracker Red to label the lysosomal compartments in the cells. The merged image of 5-FAM green fluorescence (Figure 3-5a) and lysotracker red (Figure 3-5b), showed in yellow (Figure 3-5c), indicated the colocalization of 5-FAM in the lysosome. The fluorescence intensity of 5-FAM and lysotracker red across PC3-Flu cell was quantified in Figure 3-5d-e and the colocalization coefficient coefficient was determined to be 86.5 ± 8.4%, which indicated high correlation of 5-FAM in the lysosomal compartment.[168] Therefore, if cytosolic or other organelle, deposition of enzyme-susceptible-molecule is required, a lysosome escape mechanism or organelle targeting moiety should be incorporated into the nanobeacon design for future applications.

3.5 Conclusion

In this study, we showed that the self-assembly of SFB nanobeacons were tunable into different shapes, such as spherical and cylindrical, as well as presenting different surface charges based on the peptide design sequence. The SFB nanobeacons were activatable by the degradation cathepsin B enzyme, releasing 5-FAM for fluorescence detection. *In vitro* studies showed a higher cellular uptake rate for spherical SFB than its counterparts - monomers and cylindrical nanobeacons. Also, the nanostructure's surface charges showed distinct effect in cellular uptake rate where cationic nanobeacons were internalized faster than catanionic mixture and anionic nanobeacons.

3.6 Acknowledgements

The work reported here is supported by W.W. Smith Charitable Trust and the Johns Hopkins New Faculty Startup Grant. We thank the Integrated Imaging Center (IIC) at The Johns Hopkins University for TEM, cryo-TEM imaging and confocal microscopy. We also thank Dr. Pomper (Dept. of Radiology - JHMI) for the PC3-Flu cell line.

4 Enzyme-specific doxorubicin drug beacon as drug-resistant theranostic molecular probes‡

4.1 Abstract

We report here on the use of anticancer drug doxorubicin (Dox) to construct a FRET-based theranostic molecular probe by covalently linking together through a lysine junction a fluorescent drug, a black hole quencher, and a cell penetrating peptide. We show that upon cleavage by the target lysosomal protease cathepsin B (CatB), the designed drug beacon could release the fluorescent drug serving as an indicator for CatB. Our cell studies suggest that the drug beacon design can help to circumvent the Dox drug resistance in NCI/ADR-Res ovarian cancer cells, showing significant improvement in cell cytotoxicity compared to the free drug. We believe our design opens up new opportunities to exploit the new functional and structural features of anticancer drugs in addition to their characteristic cytotoxicity.

4.2 Introduction

Proteases are known to play a critical role in the development and progression of many human diseases such as cancer.[35,169,170] Accordingly, a number of oncological treatments have targeted the over-expression and abnormal activities of cancer-relevant proteases for on-site release of drugs,[171-173] enzyme-responsive diagnostic agents,[50]

---

‡Reproduced with permission from Lock, L.L.; Tang, Z.; Keith, D., Reyes, C.; Cui, H., ***ACS Macro Letters***, 2015, 4, 552-555. Copyright © 2015 American Chemical Society.

L.L.L. designed the experiments and analyzed the data. L.L.L, T.Z., K.D., and R.C., performed the experiments. L.L.L. and C.H. prepared the manuscript.

enzyme-triggered therapy[102] and imaging,[174] as well as the development of protease inhibitor drugs.[175] One particular application has been the creation of polymer-drug and peptide-drug conjugates through an enzymatically activatable linker to improve the tumor targeting efficiency and to circumvent multidrug resistance mechanisms.[148,173,176-179] In such a prodrug design, the release rate and location of the conjugated drug is primarily determined by the enzymatic activities of the protease of interest. Therefore, in conjunction with the development of novel molecular imaging agents for cancer detection and prognosis, great effort has been devoted to the design of activatable molecular probes for sensing protease activities.[2,149,180-183] For example, Chen and co-workers reported the design of protease-activatable probes for matrix metalloproteinases detection.[184] The activation mechanism for these optical probes is primarily based upon a change in Förster resonance energy transfer (FRET) between a pair of fluorescing reporter and quencher moieties before and after the enzymatic degradation. In this communication, we report the design, synthesis and *in vitro* evaluation of a doxorubicin (Dox) drug-beacon system, which to the best of our knowledge, is the first enzyme-specific Dox prodrug conjugated with a dark chromophore quencher, possessing both therapeutic and diagnostic functions. The designed Dox drug-beacon was also found to circumvent the drug-resistant mechanism in NCI/ADR-Res ovarian cancer cells and induce higher cytotoxicity relative to the free Dox.

4.3 Results and Discussions

4.3.1 Molecule Design

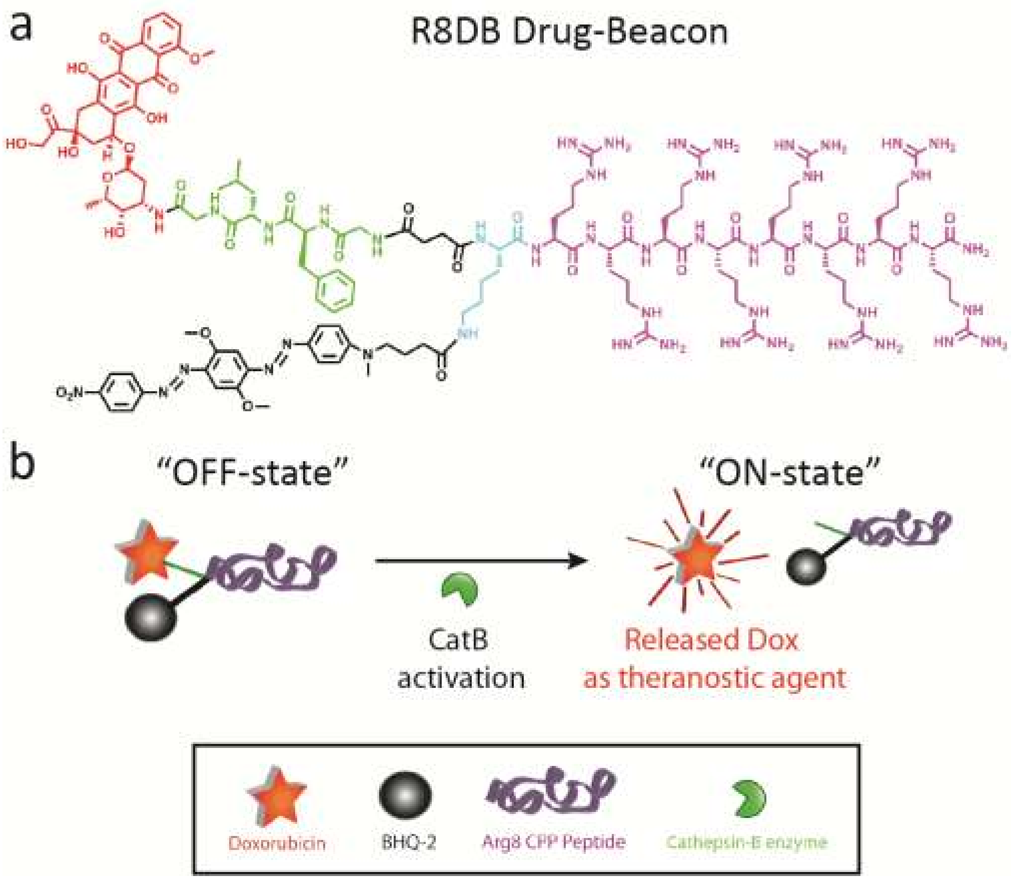

Figure 4-1. a) Chemical structure of the designed R8DB drug beacon with octa-arginine sequence (purple), -GFLG-linker (green), Dox (red) and BHQ-2 (black). b) Schematic illustration of R8DB activation from off-state to on-state after cathepsin B degradation. The designed Dox drug-beacon is expected to remain dark (OFF-state) prior to cellular entry. Following cellular uptake and CatB cleavage of the –GFLG-linker, Dox will be released thus emitting fluorescence while acting as a therapeutic agent (ON-state).

Figure 4-1 shows the chemical structure and the expected activation mechanism of the designed Dox drug-beacon (R8DB) containing four major components. First, the anticancer drug Dox, the reporter moiety, is an anthracycline antibiotic that has been widely used as a chemotherapeutic drug for various cancer treatments,[185] emitting a red fluorescence in the range of 560–590 nm when excited at 480 nm. Second, Black Hole Quencher-2 (BHQ-2) was chosen as the acceptor/quencher moiety due to its strong and broad absorbance from 500 nm to 650 nm. Its pairing with Dox is expected to effectively quench the Dox fluorescence through the FRET mechanism due to its absorption overlap with the Dox emission. Upon excitation, BHQ-2 preferentially relaxes to the ground state through non-radiative processes instead of generating new photons, thereby offering a high signal-to-noise ratio. This FRET-based concept has been extensively used to construct molecular beacons for sensing of DNA, RNA and other biomolecules.[186-189] Third, the tetrapeptide -GFLG-, a well-established cathepsin B (CatB) substrate[85,148] was used as the cleavable linker to bridge the drug to the BHQ-2 quencher through a lysine junction, modulating the release of Dox while serving as a CatB sensor. Cathepsin B is a lysosomal protease known to be overexpressed in many types of cancer.[155,190-194] Finally, octa-arginine (R8), a well-studied cell penetrating peptide (CPP) sequence,[195] was used to assist in the effective cellular internalization.[196] All the molecules studied here were synthesized using a combined automatic and manual solid phase peptide synthesis (SPPS) method as reported previously.[149] After HPLC purification, analytical HPLC and Mass Spectrometry were used to confirm the purity and expected molecular mass for the synthesized compounds. Their details can be found in Electronic supporting information (ESI, schemes S1–S3).

4.3.2 Quenching Effect and Enzymatic Activation

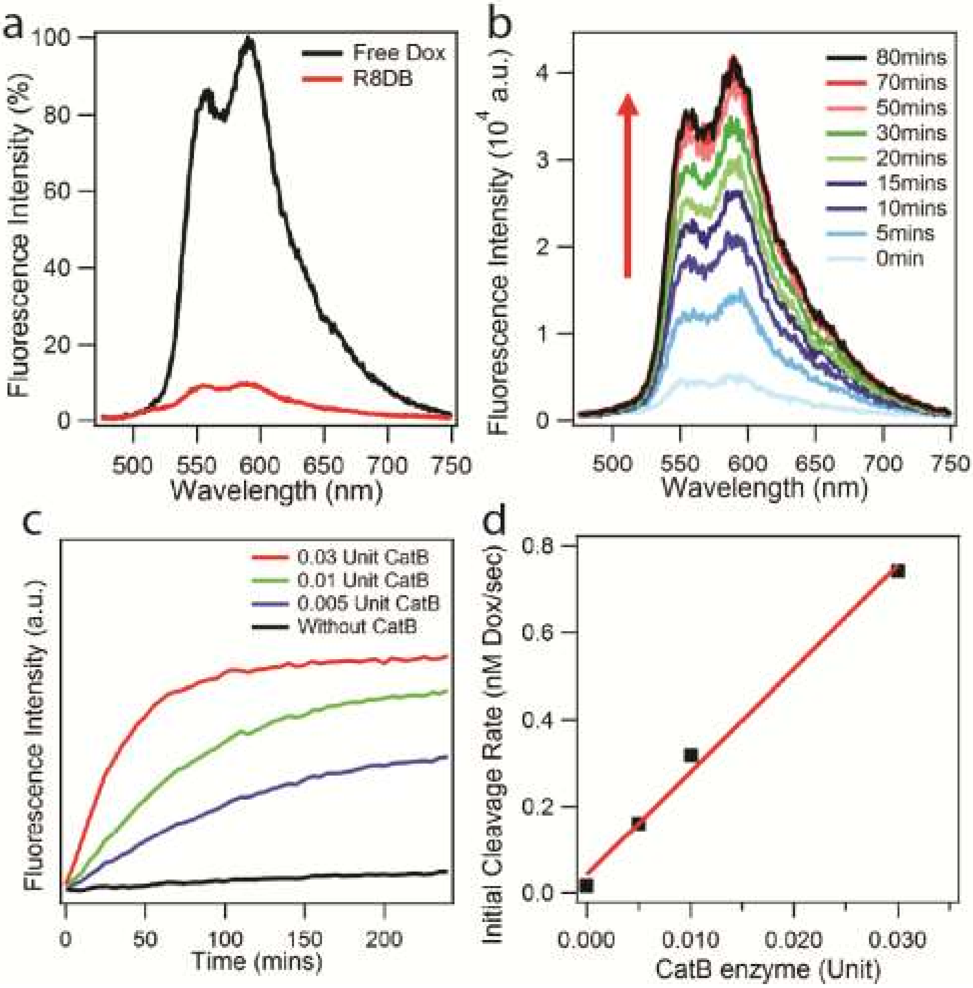

Figure 4-2. a) Fluorescence emission spectra of free Dox (black line) and R8DB (red line) at 3μM. b) Fluorescence emission spectra of a 3 μM R8DB solution at different time points after introducing 0.05 U of CatB. c) Changes in fluorescence intensity of a 3 μM R8DB solution in the presence of various amounts of CatB: 0.00 U (Black), 0.005 U (Blue), 0.01 U (Green) and 0.03 U (Red). d) Plot of initial cleavage rates (obtained from time 0-30 minutes of (c)) shows a linear correlation with the CatB concentration.

We first determined the quenching efficiency of BHQ-2 after its conjugation onto the Dox beacon. In this fluorescence experiment, we excited the R8DB solution (3μM in 1xPBS) at 465nm and collected the emission spectra as shown in Figure 4-2a, with the free Dox of the same molar concentration as control. The quenching efficiency was calculated to be 90.6±1.6%, equivalent to a 10 fold decrease in Dox fluorescence intensity after incorporating the BHQ-2 quencher. Next, in an effort to demonstrate the enzyme-responsive feature of the R8DB drug-beacon and its possible use for CatB sensing, we studied their activation in a CatB-containing solution and measured their emission spectra at different time points. The fluorescence intensity of a 3 μM R8DB drug-beacon aqueous solution was observed to increase gradually after exposure to 0.05 Units (U) of CatB enzyme for 80 minutes, exhibiting the typical emission spectrum of free Dox (Figure 4-2b). According to the work by Kopecek and coworkers,[85]CatB was reported to cleave GFLG linker at the amide bond of F and L, as well as at the C-terminal of GFLG. Therefore, two amino acid residues could be possibly attached to Dox (Dox-GL) upon initial cleavage which could undergo further degradation to release free Dox over time.[197] To evaluate the Dox release profiles, we monitored the change in Dox fluorescence intensity over time in the presence of varying concentrations of CatB (Figure 4-2c). We observed that the R8DB solution without CatB showed a minimum level of Dox fluorescence throughout the course of study (OFF-state), while solutions containing 0.005 U, 0.01 U and 0.03 U of Cat B exhibited a rapid increase in Dox fluorescence (ON-state), commensurate with the amount of CatB used. The initial cleavage rates were obtained from the slope between t = 0 and t = 30 min, and found to scale linearly with the CatB concentration (Figure 4-2d). The $k_{cat}/\mathrm{K_M}$ value was calculated to be 568.4 $(\mathrm{mol/L})^{-1}\cdot\mathrm{s}^{-1}$ using the simplified Michaelis-Menten equation (S2 in ESI). This number is four times as high as our previous finding in a different molecular beacon system[149], and is in the same order of magnitude with other systems using the same peptide substrate.[148] This implies that the drug beacon design does not compromise the cleavage specificity of the GFLG substrate by CatB. These results also clearly suggest that R8DB drug-beacon can be specifically activated by the CatB enzyme, recovering the drug's native fluorescence for intracellular tracking and/or CatB sensing.

4.3.3 *In vitro* Cell Study

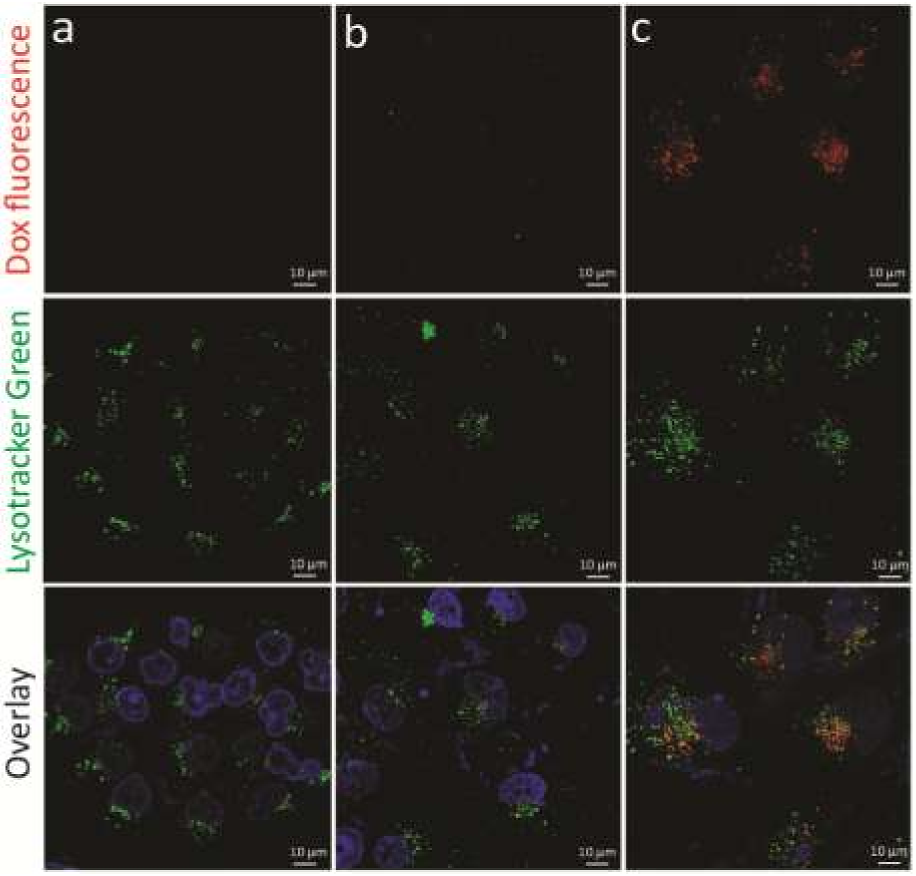

Figure 4-3. Live cell confocal images of NCI/ADR-Res drug-resistant ovarian cancer a) without any drug (blank), b) in the presence of 3 µM free Dox and c) in the presence of 3 µM R8DB incubated for 96 hours. Dox fluoresced in red, and lysosomal compartments were stained with Lysotracker Green and cell nuclei were stained in blue with Hoechst 33342.

We further evaluated the theranostic feature of the R8DB drug beacon in drug resistant ovarian cancer cell lines. It is well known that Dox is transported into cells through a passive diffusion mechanism, and subsequently accumulates in the cell nucleus whereupon intercalation with DNA occurs to induce cell apoptosis. However, drug-resistant cell lines could have evolved with a defensive system known as P-glycoprotein efflux pump to avoid accumulation of drug above its cytotoxic threshold.[198] For a better comparison of drug internalization and efficacy, we incubated 3 μM of Dox and R8DB drug-beacon, respectively, in the drug-resistant NCI/ADR-Res ovarian cancer cell line, followed by fluorescence imaging of live cells using confocal laser scanning microscopy (Figure 4-3). Cells after 72 hours of incubation were replaced with fresh media containing either the drug or R8DB drug beacon due to the depletion of nutrition. As shown in Figure 4-3, it is evident that R8DB drug-beacon (Figure 4-3c) exhibits much stronger red fluorescence in cells than the free Dox (Figure 4-3b), indicating both effective cellular internalization and CatB activation. This phenomenon has also been observed in other prodrug designs possessing CPP features that interact with drug-resistant cell lines.[199-201] A few studies have showed that the azo moiety in BHQs quencher is susceptible to reduction reaction which could possibly give rise to false fluorescence increase.[202,203] However, we have previously shown that under similar experimental condition BHQ was able to quench and maintained fluorescence of our designed molecular beacon in the presence of CatB inhibitor which is known to suppress CatB's activity in cleaving the GFLG substrate.[149] To validate the subcellular colocalization of the R8DB drug-beacon, we selectively stained the lysosomal compartments with LysoTracker Green. As shown in Figure 4-3c, the red fluorescence coming from the released Dox was mostly located within the lysosomal compartments as they co-localized with Lysotracker Green. This observation confirms our assumption that R8DB drug-beacons are internalized by cancer cells through endocytosis pathways.[204-207]

In addition, we have attempted to trace the intracellular Dox localization for longer periods of time, however, cell conditions were severely deteriorated (cells started to die), preventing more detailed analysis of the intracellular trafficking pathways of Dox beacon. In Fig. 2b, the negligible red fluorescence suggests that free Dox entering cells through diffusion is likely pumped out by the cell drug resistance mechanism.[208,209] Therefore, the enhanced accumulation of released Dox in drug resistant cancer cells means that R8DB drug beacon could possibly help circumvent the drug-resistance mechanism that many cancer cells could develop over the course of chemotherapy. It should be noted that although the R8DB drug beacon has amphiphilic character and thus the potential to assemble into micellar structures in aqueous solutions, the extremely low concentrations in all experimental conditions (3 μM) and the prolonged incubation (in days) suggest that R8DB would have most likely remained in its monomeric form in these studies.

4.3.4 Drug Beacon Efficacy

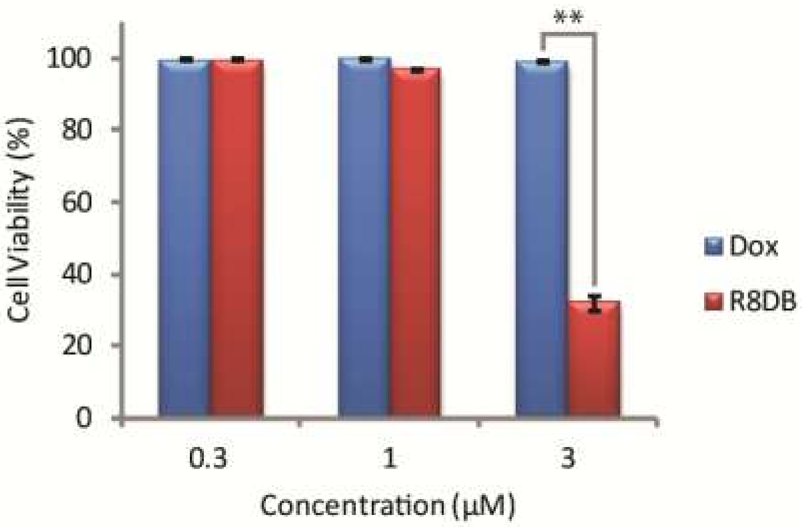

Figure 4-4. Cytotoxicity assay of NCI/ADR-Res cells incubated with various concentrations of free Dox and R8DB drug-beacon (0.3 μM to 3 μM). Data are given as

mean ± sd (n = 3). Fresh cell media with respective drugs were used to replace the cell media after 3 days and the cells were further incubated for another 3 days. **P<0.001.

To validate the *in vitro* efficacy of the Dox drug-beacon design, a dose–response study was conducted using an SRB assay (Figure 4-4), using free Dox as control. As expected, free Dox did not exhibit any toxicity after 6 days of incubation for any of the studied concentrations (0.3 μM to 3 μM, blue bars in Figure 4-4). At lower concentrations (0.3 and 1 μM), the R8DB drug-beacon also showed a negligible effect on cell viability (red bars in Figure 4-4). Although the octa-arginine peptide was known to facilitate the effective internalization of R8DB, the released Dox within cell could still be lower than the toxicity concentration threshold. At 3 μM, the R8DB drug-beacon exhibited remarkable improvement in drug-efficacy with only ~30% of cells remaining viable. This observation is consistent with our confocal imaging study, where R8DB showed higher Dox fluorescence intensity in cells compared to free Dox of the same concentration. Since octa-arginine is a highly positively charged peptide, it could potentially disrupt cell membranes thus causing cytotoxicity.[210] As a result, R8DB concentration was deliberately set below 5 μM, a condition where the R8 peptide sequence was known to show negligible cytotoxicity.[211] Therefore, our cytotoxicity result reflects the drug beacon's ability to overcome the drug-resistance mechanism in NCI/ADR-Res ovarian cancer cells.

4.4 Conclusion

In summary, we have reported a novel design of an enzyme-specific theranostic probe by taking advantage of the fluorescence capacity of the anticancer drug Dox. Incorporating a fluorescing drug into the beacon design opens up a new platform to explore the diagnostic functionality of therapeutic agents. This synergistic effect could potentially reduce the discrepancy between tumor diagnostic locations with actual drug-delivered sites, which is one of the important challenges in current treatment paradigm.

4.5 Acknowledgement

We thank National Science Foundation (DMR 1255281) and the W.W. Smith Charitable Trust for support of the project. We thank the JHU Integrated Imaging Center (IIC) for the use of confocal imaging facility, and the JHU Department of Chemistry Mass Spectrometry facility for mass spectrometry analysis

5 Self-assembling Drug-Peptide Nanofiber Hydrogel with Inherent MRI Signal[§]

5.1 Abstract

Small molecule anticancer drug remains one of the major components in chemotherapy regimes. However, each anticancer drug will have unique pharmacokinetics profile due to tumor variation in patients, resulting in unpredictable therapeutic outcome. More importantly, treatment failures could not be addressed appropriately because of limited resources and technologies to track anticancer drug in real time. Here we report a proof-of-concept design and utilization of anticancer drugs with exchanging protons, to generate chemical exchange saturation transfer (CEST) MRI signal under specific radio frequency, enabling real-time report of drug distribution. The incorporation of self-assembling peptide offers structural advantage by promoting nanofibers hydrogel formation. Our results showed that Pemetrexed (Alimta) anticancer drug has intrinsic CEST signal at 5.4 ppm and *in vivo* study revealed that this approach was able to detect drug distribution in brain after 4 days of local injection. This strategy can be extended to other anticancer drug with exchanging proton, therefore presents new opportunities for the development of image-guided drug delivery system.

---

§ Lock, L.L., Li., Y., Liu, G., and Cui. H. designed the experiments. Lock, L.L. and Mao, X. performed peptide-drug synthesis and analyzed nanofiber data. L.Y. and L.G. performed *in vitro* and *in vivo* CEST experiments and analyzed the data. Bai, R. and Staedtke, V. prepared and performed the *in vivo* experiments. Lock, L.L., Li., Y., Liu, G., and Cui. H. prepared the manuscript.

5.2 Introduction

The exploration of peptide-based nanofiber hydrogel has expanded the field of biomedical applications such as tissue regeneration,[212-215] cell-encapsulated transplant,[76,216] electro-conducting biomaterials[217-219] and drug delivery system[220-222] due to its biocompatibility, biodegradability and high tunability for different purposes. Similar to the notion of biomolecules assembly in Nature, the self-assembly of peptide-based hydrogel mainly driven by a collective of weak intra- and inter-molecular interaction such as hydrogen bond, electrostatic, van der Waals, pi-pi stacking and hydrophobic interaction,[69,70,223] forming well-defined nanofiber and further associated into three-dimensional hydrogel network. The ability to customize peptide sequence enabled to peptide hydrogel conforms to desired properties and functionality. For instance, charged amino acids can be incorporated into peptide design to obtain cationic or anionic system, various hydrophobic entities are to be modified to facilitate the self-assembly process[224] and most importantly, bioactive ligand can be presented on the nanofiber hydrogel to target a specific receptor or exhibit bio-responsive feature.[74,225 5] A promising feature offered by peptide-based hydrogel is the capacity to achieve controlled-release of payload,[226,227] in contrast to the burst-release profile of polymer-based material, which has long been recognized as one of the challenges in drug delivery system.[228,229] As the therapeutic efficacy of most anti-cancer drugs has been limited by carrier's encapsulation capacity and efficiency as well as causing undesired side effects,[230] a carrier-free self delivery system has attracted much attention. Through the conjugation of drug with a small molecule or short peptide that could induce the self-assembly of nanofibers, a prodrug carrier-free self-delivery system can be realized.[231,232]

Despite remarkable advancement in the development of drug delivery strategies, the efficacy of chemotherapeutic drugs in cancer treatment is still limited, largely due to the unspecific accumulation in other organs such as liver spleen, kidney;[233] with only small amount of drug arriving at tumor site. Another challenge is the chemotherapeutic drugs were generally distributed around the peripheral of tumor owing to the high interstitial fluid pressure within tumor, limiting the penetration depth of drug into the tumor.[234] Therefore, the ability to monitor and track therapeutic drug is highly desirable to identify premature clearance, locate drug accumulation site and distribution to have a better drug prognosis and comprehend for any treatment failures.[235] Image-guided drug delivery or theranostic systems have been explored to incorporate chemotherapeutic drugs with different imaging modalities such as PET,[236] SPECT,[237,238] MRI,[239,240] and ultrasonic[241] to render real time reporting of drug circulation and distribution upon *in vivo* administration.

A newly explored MRI imaging technique, Chemical Exchange Saturation Transfer (CEST), utilizes the unique chemical shift (frequency offset) of exchangeable protons on each probe, translating them into a frequency-specific agent for molecular imaging.[242,243] Unlike conventional MRI agents, these 'frequency-encoded' agents offer several advantages such as the possibility of turn the contrast 'on' or 'off' by manipulating the frequency offset and allowing multiple agents to be monitored at the same time.[244,245] Through CEST MRI approach, bio-organic molecules[246-249] which composed of exchangeable protons such as –O**H**, –N**H** and $–N\mathbf{H_2}$ groups can be saturated by a specific radiofrequency pulse and undergo rapid protons exchange with surrounding water molecules, resulting in a darker imaging site. For example, a series of X-ray contrast agents, Iopamidol,[250] Iopromide,[251,252] and Iobitridol[253] with –NH proton were shown to exhibit CEST MRI signal that enabled *in vivo* microenvironment pH mapping. To improve the accuracy of Iopromide and Iobitridol CEST pH evaluation, ratiometric analysis of multiple magnetically non-equivalent protons[251] and different radio frequency pulse power were developed,[253] respectively. Recently, salicylic acid, a metabolite of aspirin, was reported to produce CEST contrast at 9.3 ppm downfield from water,[249] a frequency that is far from endogenous tissue amine and amide signals.[247,254] These new discoveries explored additional imaging functionality to existing drugs or contrast agents.

Herein, we report an FDA-approved anticancer drug, Pemetrexed (Pem), trade name Alimta,[255] with inherent CEST MRI signal at 5.4 ppm frequency offset away from the water signal. To achieve longer retention time at target site after local administration, we covalently linked Pem to a short peptide that drives the self-assembly process of Pem-peptide conjugate forming nanofibers hydrogel. Through *in vivo* mouse model, we demonstrated that Pem can be used as a new class of CEST MRI agent and enabled real time monitoring of drug distribution.

5.3 Results and Discussions

5.3.1 Molecular Design

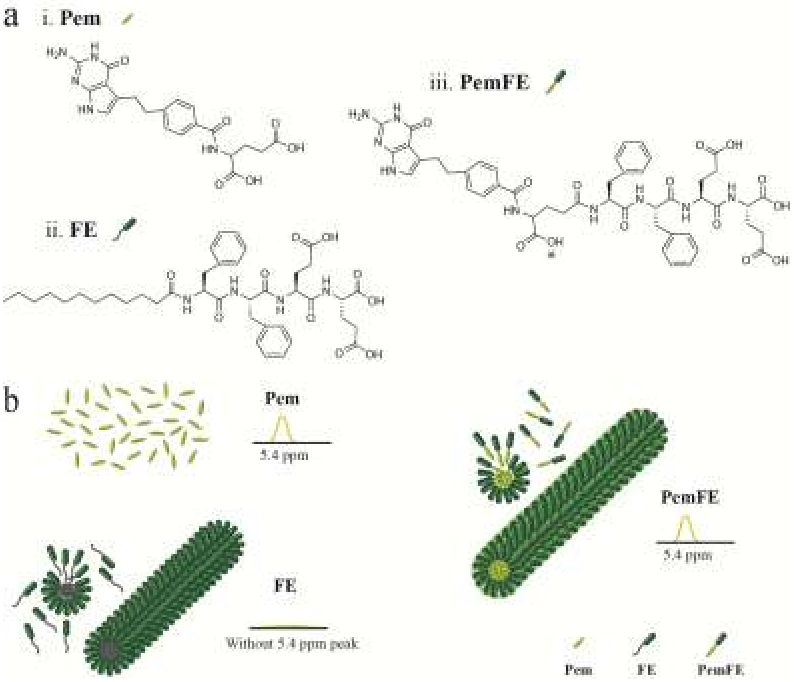

Figure 5-1. (a) Chemical structure of (i) Pemetrexed (Pem), (ii) FE, and (iii) PemFE molecules. (b) Illustration of soluble free Pem while FE and PemFE self-assembled into nanofibers. PemFE composed of MRI CEST signal at 5.4 ppm inherently from Pem molecule and 2.0 ppm from the side chain of glutamic acid as a result of closely packed self-assembled nanofibers state.

Pemetrexed (Pem) is a chemotherapeutic drug composed of aromatic amines and secondary amines in its nature structure (Fig. 5-1a-i). These slowly exchanging protons posses a chemical shift distinct from water, in which can be selectively saturated and transferred to bulk water through chemical exchange, resulting in a CEST signal at 5.4ppm shift (Fig. 5-1b). With this unique property, Pem can be used as a CEST contrast agent. The rationale of our design is to construct a Pem-based peptide conjugate, PemFE (Fig. 5-1a-iii) that has the potential to self-assemble into nanofibers under physiological condition. Utilizing the hydrophobic nature of most anticancer drug, we chemically conjugating Pem to a hydrophilic peptide (EE) to create an amphiphilic prodrug molecule that can self-assemble into nanostructure.[256,257] Glutamic acid residues which carry negative charge at its side chain are deliberately included in our design, as other studies have reported that positively charge nanoparticles are prone to induce cytotoxicity.[258] To promote the self-assembly of PemFE into nanofibers hydrogel, two phenylalanine (FF) was incorporated into the peptide sequence. The phenylalanine benzyl side chain composed of π-segment that was shown to direct the self-assembly of amphiphilic peptide into 1-dimensional nanostructures, such as nanotubes or nanofibers through π-π stacking.[259,260] With this drug-peptide conjugate design, the Pem drug loading can be precisely fixed at 42 wt% which is defined by the mass of Pem divided by the total molecular weight of PemFE conjugate (Supporting information). Our previous work[179,256,257] also demonstrated that this concept can be employed for other anticancer drugs to achieve higher drug loading compared to tradition drug encapsulation method which is typically below 5 wt% and drug-polymer conjugates with ~10 wt%.[55] As a control molecule, we have designed the FE molecule (Fig. 5-1a-ii) which replaced the Pem drug with a C12-hydrocarbon tail as a hydrophobic entity to facilitate the self-assembly process.

5.3.2 Self-assembly and Characterization

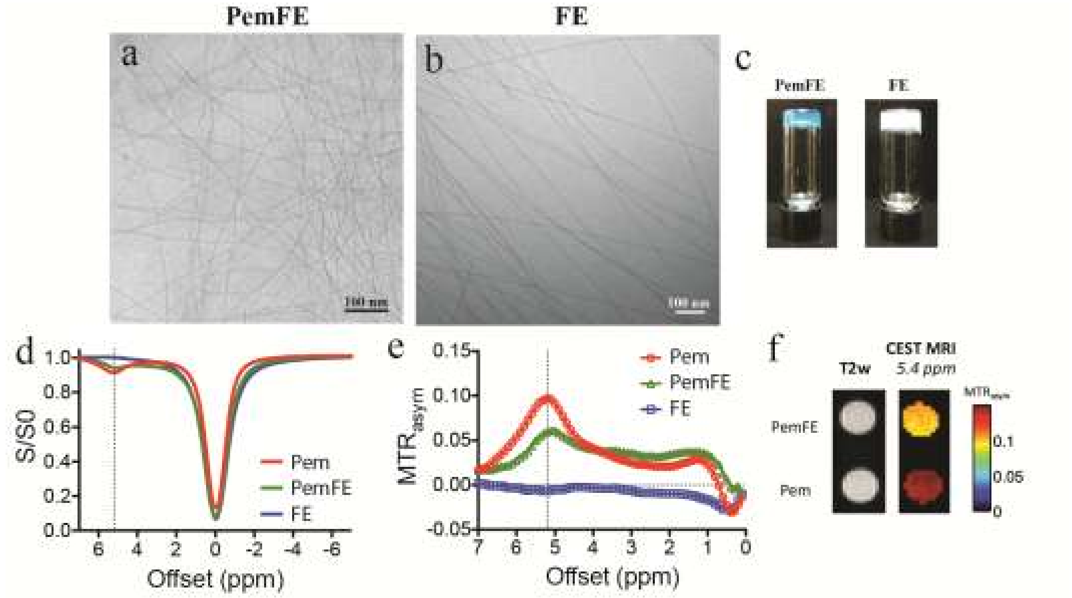

Figure 5-2. Cryo-TEM images of (a) PemFE, 4mM and (b) FE, 10mM showed self-assembled nanofibers with a diameter of 9.1±1.4 nm and 8.5±0.9 nm, respectively. (c) Photographs of PemFE and FE in 30mM dissolved in 1xDPBS: inversion demonstrates self-supporting hydrogel formed by PemFE and FE self-assembling nanofibers. MRI data determining the CEST contrast for all molecules, PemFE, Pem, and FE. (d) Z-spectra and (e) MTR_{asym} of PemFE nanofibers (green) and free Pem (red) showed CEST peak at 5.4 ppm. (f) CEST contrast (MTR_{asym}) map at 5.4 ppm for PemFE and free Pem.

The self-assembly of PemFE and FE were initiated by dissolving the lyophilized powder form of molecules into Dulbecco's phosphate-buffered saline (1xDPBS). The self-assembled nanostructures were observed under cryogenic transmission electron microscopy (cryo-TEM). As shown in Figure 5-2a,c, TEM images showed that both PemFE and FE molecules self-assemble into cylindrical-shaped nanofibers, under physiological condition. According to the diameter analysis of PemFE and FE nanofibers obtained from the TEM images, their respectively diameter are 9.1±1.4 nm and 8.5±0.9 nm. From the cryo-TEM images (Fig. 2b,d), the length of these nanofibers appeared to be in the range of micrometer, which prone to nanofibers entanglement at high concentration. Consequently, at macroscopic level, PemFE and FE formed a self-supporting hydrogel at 30mM as shown in Figure 5-2c. This hydrogel characteristic is highly desirable as it offers another important feature for drug-delivery system, a controlled-release of prodrug.

5.3.3 *In vivo* CEST MRI Time-point Study and Spatial Comparison

To assess the potential use of PemFE hydrogel in *in vivo* settings, we conducted CEST MRI experiments on mice bearing U87 brain tumor injected with PemFE hydrogel. U87 mouse brain tumor cells were implanted into right hemisphere of mouse brain and inoculated for 25 days. Brain tumor anatomy was obtained using T2 weighted image to verify tumor size and location. PemFE hydrogel was administrated through stereotactical injection into the middle of tumor. Anatomical images and CEST map with respect to 5.4 ppm were collected pre-injection, 2 hours and 4 days post-injection (Figure 5-3a). In 2 hours and 4 days PemFE hydrogel post-injection images, brain tumor resided at right hemisphere showed significantly higher CEST signal compared to the left hemisphere and pre-injection scan. After 4 days of injection, PemFE hydrogel was deemed to diffuse slowly to nearby tissue hence the dispersed distribution in CEST maps as opposed to the concentrated CEST signal at 2 hours post-injection. This study demonstrated that the CEST MRI feature of PemFE hydrogel is detectable in *in vivo* model and retained at injection for up to 4 days, which hold promises for extended real-time monitor of drug release.

In order to attain high resolution imaging system, the CEST signal has to be significantly higher than background noise. To further evaluate the performance of

PemFE hydrogel, we quantitatively analyze the CEST MRI signal at injection site compared to its surrounding/background. Figure 5-3b showed an overlay image of CEST/MTw (magnetization transfer-weighted) using a frequency offset of 5.4 ppm, in which ROI1 (region of interest - ROI) sets a boundary for 2 hours post-injection of PemFE hydrogel and ROI2 corresponded to the surrounding/background. The CEST contrast of ROI1 and ROI2 (red and blue lines) were plotted in Figure 5-3c and the difference (gray line) was obtained by subtracting the CEST signal of ROI2 from ROI1. Based on the MTw image, both ROI1 and ROI2 are located within the tumor. As shown in Figure 5-3d, the average MTR_{asym} values or CEST signal for the PemFE at 5.4ppm was higher than its surrounding. Given that the intrinsic CEST signal of Pem arises at 5.4 ppm, it is relatively far from the possible background signal of amine and amide CEST, which generally spans from 2.75 pm to 3.5 ppm that accounts for amine and amide bond CEST signal.[247] The larger chemical shift of Pem containing molecule (>3.5ppm) enables higher signal to background ratio and offers a unique identification of Pem drug in the CEST detection system.

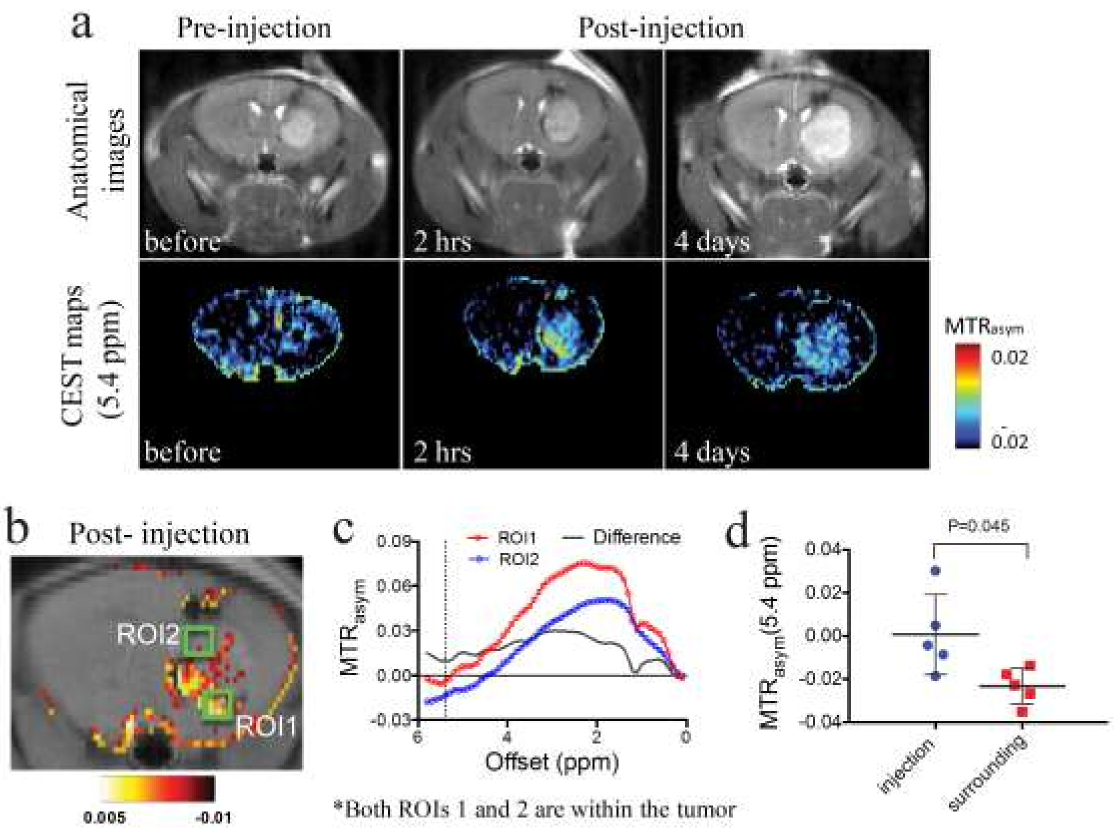

Figure 5-3. MRI detection of Pemetrexed (Alimta) conjugated nanofibers hydrogel that was stereotactically injected in brain tumors (day 25 after tumor implantation). (a) On the top, MRI images showing GL261 brain tumor at different time points (with respect to the time of injection of nanofiber hydrogel); On the bottom, CEST maps at 5.4 ppm of the mouse brain before, 2 hours and 4 days after the hydrogel injection. (b) After 2 hours of PemFE hydrogel injection, two ROIs were manually drawn to represent the region with increased CEST MRI contrast at 5.4 ppm and the region in the tumor without CEST MRI contrast increase. (c) The MTR_{asym} versus frequency offset plot of PemFE injected ROIs and their absolute difference. (d) The average of MTR_{asym} values at 5.4 ppm comparing the injection site and surrounding for PemFE hydrogel after 2 hours of injection.

5.4 Conclusion

In summary, we have demonstrated that chemotherapeutic drug, Pem can be utilized as a CEST agent in *in vivo* to monitor drug distribution over time. The CEST signal at 5.4 ppm which is uniquely attributed to Pem slow-exchanging protons serves as a marker to identify and quantify Pem in real time. In addition, the conjugation of self-assembling peptide to Pem drug entails the formation of nanofibers hydrogel, exhibits sustained-release characteristic of Pem over time. While further therapeutic evaluations are needed in *in vivo* model, our work realized the proof-of-concept in employing chemotherapeutic drug as a CEST contrast agent and opens up a new platform for MR guided drug-delivery system. The MRI capability to the drug-peptide system without additional burden of imaging tags conjugation could greatly facilitate the clinical translation.

5.5 Acknowledgement

We thank National Science Foundation (DMR 1255281), JHU Integrated Imaging Center (IIC) for the use of electron microscopy facility, and the JHU Department of Chemistry Mass Spectrometry facility for mass spectrometry analysis.

6 Self-Assembly of Natural and Synthetic Drug Amphiphiles into Discrete Supramolecular Nanostructures[**]

6.1 Abstract

Molecular assembly provides an effective approach to construct discrete supramolecular nanostructures of various sizes and shapes in a simple manner. One important technological application of the resulting nanostructures is their potential use as anticancer drug carriers to facilitate targeted delivery to tumour sites and consequently to improve clinical outcomes. In this carrier-assisted delivery strategy, anticancer drugs have been almost exclusively considered as the cargo to be carried and delivered, and their potential as molecular building blocks has been largely ignored. In this discussion, we report the use of anticancer drugs as molecular building units to create discrete supramolecular nanostructures that contain a high and quantitative drug loading and also have the potential for self-delivery. We first show the direct assembly of two amphiphilic drug molecules (methotrexate and folic acid) into discrete nanostructures. Our results reveal that folic acid exhibits rich self-assembly behaviours *via* Hoogsteen hydrogen bonding in various solvent conditions, whereas methotrexate was unable to assemble into any well-defined nanostructures under the same conditions, despite its similar chemical

---

[**] Reproduced with permission from Lock, L. L.; LaComb, M.; Schwarz, K.; Cheetham, A. G.; Lin, Y.-A.; Zhang, P.; Cui, H., ***Faraday Discussions***, 2013, 166, 285-301. Copyright © 2013 Royal Society of Chemistry.

L.L.L. and C.A.G designed the experiments and analyzed the data. L.L.L., L.M., S.K., performed the folic acid and methotrexed experiments. C.A.G., L.Y., and Z.P. performed the drug amphiphile experiments. Lock, L.L. and Cui. H. prepared the manuscript.

structures. Considering the low water solubility of most anticancer drugs, hydrophilic segments must be conjugated to the drug in order to bestow the necessary amphiphilicity. We have demonstrated this for camptothecin through the attachment of β-sheet-forming peptides with overall hydrophilicity. We found that the intermolecular interactions among camptothecin segments and those among β-sheet peptides act together to define the formation of stable one-dimensional nanostructures in dilute solutions, giving rise to nanotubes or nanofibers depending upon the processing conditions used. These results lead us to believe that self-assembly of drugs into discrete nanostructures not only offers an innovative way to craft self-delivering anticancer drugs, but also extends the paradigm of using molecular assembly as a toolbox to achieve functional nanostructures, to a new area which is specifically focused on the direct assembly of functional molecules (e.g. drugs, or imaging agents) into nanostructures of their own.

6.2 Introduction

Drugs are a special class of chemicals that produce a biological effect when administered to a living organism. In clinical practice, drugs are often co-administered with other substances, such as excipients, stabilizers, solvents, or even other drugs, to maximize the therapeutic effects while minimizing the possible side effects. Given the low therapeutic index of most anticancer drugs (the ratio of the lethal or toxic dose to the therapeutic dose) and their great toxicity toward healthy cells, it is important and desirable to maintain a high therapeutic level of drugs only in the tumour sites.[261] Over the past three decades, the use of nanoscale carriers to modify the drug's pharmacokinetic properties and biodistribution profiles has been the primary focus of research in the drug delivery community, with the goal of achieving targeted delivery to tumour sites.[5,28,262-267] Two main strategies have been actively pursued: the first involves covalently modifying hydrophobic drugs with hydrophilic polymers to form polymer-drug conjugates.[5,266,267] The purpose of this conjugation is to improve drug solubility, to increase drug targeting efficiency and to reduce drug toxicity. The great advantage of this strategy is that the pharmacokinetic properties of the drug are determined by the molecular weight and characteristics of the conjugated polymers. However, this strategy is limited by the polydispersity in polymer length and drug loading per polymer chain, and also by the limited choice of hydrophilic polymer due to concerns regarding potential cytotoxicity and biodegradability.[5,266,268]

The other strategy is the use of well-defined nanoscale architectures, with drugs being either encapsulated within, or conjugated onto, the carriers.[28,262-264] These nanocarriers often present well-defined size, shape and tuneable surface chemistries, allowing robust pharmacokinetic protocols independent of the drug encapsulated to be established. A great diversity of nanostructures have been evaluated for their potential applications as drug carriers, including liposomes,[17] vesicles,[269] dendrimers,[270,271] inorganic nanoparticles,[272,273] polymer nanoparticles,[274] and self-assembled nanostructures.[133,275,276] Among these nanocarriers, self-assembled nanostructures are of particular interest because they can be readily prepared to assume a variety of sizes and shapes with adjustable surface chemistry through solution-state assembly processes. A further attraction is that these supramolecular carriers can dissociate into individual molecules that could be removed through renal clearance once their desired function is accomplished. The limitations of using nanostructured material as drug carriers lie in three aspects. First, their drug carrying capacity is very low, typically below 5% (*w*/*w*). Second, there is an inherent difficulty to control and characterize the amount of drugs loaded in each particle. There will also be a loading variation from particle to particle, and as such the loading capacity only represents the averaged amount of drug loaded in the whole system. Finally, the long term toxicity of these synthetic nano-objects remains unclear.

Our strategy presented here is to devise approaches that enable anticancer drugs to directly assemble into discrete well-defined nanostructures. We first chose two amphiphilic drug molecules, methotrexate (MTX) and folic acid (FA), as proof-of-principle building blocks to illustrate this concept (Figure 6-1A). MTX is an antifolate drug used for the treatment of blood, lung, breast, and other kinds of cancer.[277] The mechanism by which MTX exerts its toxicity is through competitive inhibition of dihydrofolate reductase, possessing a one thousand-fold greater binding affinity than folate, which leads to eventual inhibition of DNA and RNA synthesis.[277-279] Folic acid is a biologically active molecule (also known as vitamin M or B_9) that has several important functions in cell sustainability and proliferation,[280] and has been recently reported to be an effective targeting ligand for various cancers.[281] It is known that the pterin (2-aminopteridin-4-ol) moiety could potentially induce a particular arrangement of H-bonding interactions among four FA molecules.[282] Several studies have shown that the resultant Hoogsteen-bonded tetramers of folic acid or its derivatives can stack into chiral columns which further pack into ordered mesophases.[62,282-288] Only in a few cases have discrete nanostructures formed by self-assembly of FA or FA derivatives been reported to template the formation of mesoporous silica[289] and to improve the mechanical properties of chitosan hydrogels.[290]

The majority of anticancer drugs are, however, hydrophobic and do not possess the key amphiphilic feature to produce self-assembled discrete nanostructures in aqueous solutions.[256,257] It is therefore necessary to incorporate a small hydrophilic segment onto the drugs of interest. Figure 6-1B illustrates the concept of design for a self-assembling drug amphiphile (DA). In this particular case, we conjugated a β-sheet forming peptide onto the hydrophobic drug CPT to impart the necessary amphiphilicity for assembly into discrete nanostructures. This conjugation strategy has been extensively used by a few other groups to create self-assembling peptide amphiphiles,[75,106-108,291-293] peptide nucleic acid amphiphiles,[110] and amphiphiles containing either therapeutic agents[96,294-296] or π-conjugated aromatic units.[276,297] The peptides sequences used here serve as a structural control unit that play an important role in defining the final morphologies, providing the impetus for one-dimensional elongation through β-sheet formation. CPT constitutes not only the bioactive component of the drug amphiphile,[298] but is also the driving force for hydrophobic collapse that helps to initiate self-assembly.[256] Its rigid nature and potential for π-π interactions provide further means of influencing the nanostructure morphology formed. Herein, we discuss how solution processing of the nanotube-forming, four CPT-containing drug amphiphile can affect the self-assembly mechanism and provide insight into the stability of such structures.

In both cases of using anticancer drugs as building units, the resulting self-assembled drug nanostructures will 1) have a high drug loading capacity (up to 100%

if the nanostructure is made of free drug), 2) allow for a quantitative control of the drug content in each drug carrier since the assembled nanostructures have the identical drug content as the individual molecule, and 3) can minimize the toxicity of using additional synthetic carriers.

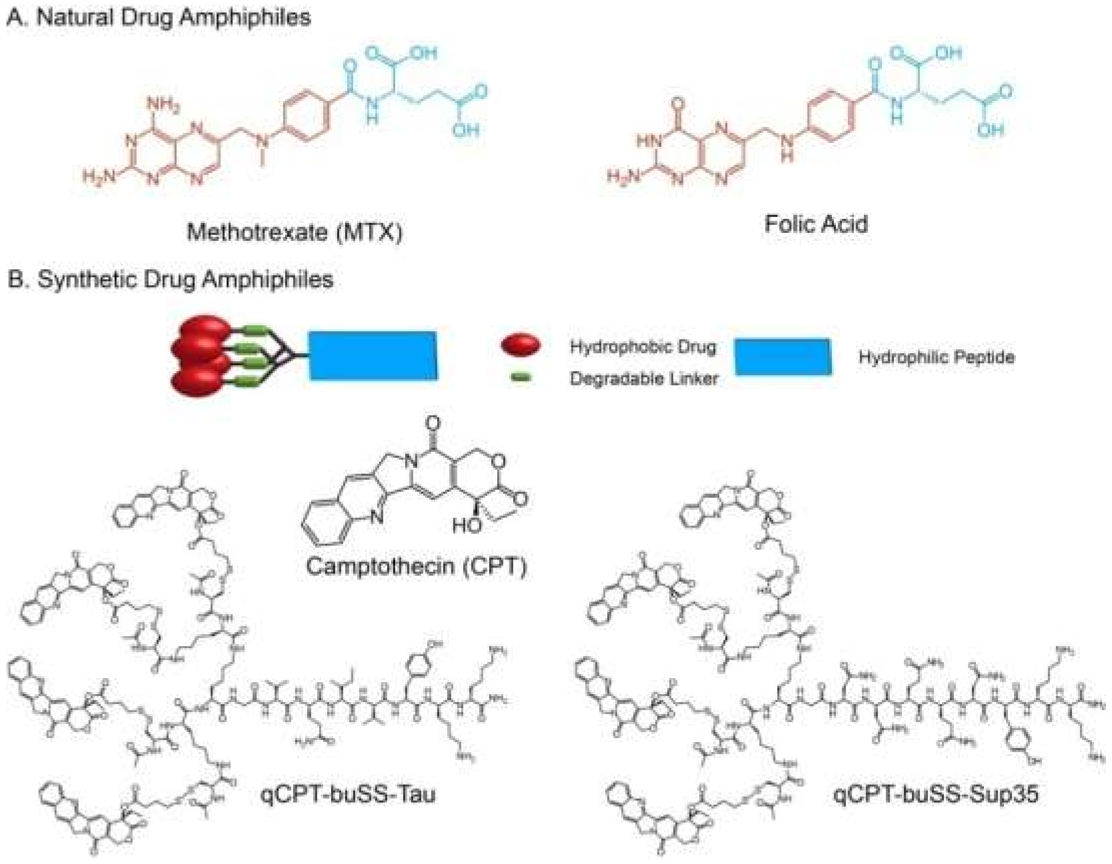

Figure 6-1. Chemical structures of natural and synthetic drug amphiphiles used in this study.(A) Both methotrexate and folic acid contain a glutamic acid residue (marked in blue) and can be regarded as amphiphilic molecules when deprotonated at a higher pH. (B) The creation of camptothecin (CPT) drug amphiphiles by conjugating four CPT molecules to one *β*-sheet forming peptide via a biodegradable linker. Two *β*-sheet forming sequences (VQIVYK and NNQQNY) were used to create two drug amphiphiles: qCPT-buSS-Tau and qCPT-buSS-Sup35. The linker used to bridge the drug and the peptide is responsive to glutathione, a reducing agent within cells.

6.3 Experimental Procedures

6.3.1 Materials

Folic acid and methotrexate were purchased from Sigma-Aldrich and used as received. Fmoc amino acids, Rink Amide resin and coupling agents (HBTU and HATU) were sourced from AAPPTEC (Louisville, KY) and camptothecin was obtained from Avachem (San Antonio, TX). Borate buffer, consisting of sodium borate decahydrate and sodium hydroxide, was purchased from RICCA Chemical Company. 10×DPBS (Dulbecco's Phosphate Buffered Saline without calcium or magnesium) was purchased from Lonza.

Buffer solutions used in the FA and MTX studies were prepared using the following protocols: Borate buffer (pH 9.5) was used as received; 1×DPBS solution (pH 7.4) was prepared by 10-fold dilution of 10×DPBS with water; 0.1M sodium acetate buffer (pH 5) was prepared by mixing 71.4mL of 0.1M acetic acid and 128.6mL of 0.1M sodium acetate solutions. The pH values of all buffered solutions were measured by a pH meter (Mettler Toledo) using an InLab Micro pH electrode. The solution containing 1 wt% FA was prepared by adding 5.1mg FA to 500μL of each buffer solution and vortexing until clear. The final pH of the solution was subsequently re-adjusted to the initial pH of the original buffer solution by the addition of 1M NaOH or 1M HCl.

6.3.2 Peptide Synthesis

The peptide, qCys-Sup35, was synthesized using a combination of automated (Focus XC, AAPPTEC) and manual solid-phase Fmoc peptide synthesis techniques. Branching lysines were introduced through the use of Fmoc-Lys(Fmoc)-OH

(Novabiochem, San Diego, CA). The peptide was cleaved from the resin using a mixture of trifluoroacetic acid, triisopropylsilane, water and ethanedithiol (90:5:2.5:2.5) for 2 h, isolating the crude peptide by trituration into cold diethylether. Purification to >95% homogeneity was performed using reversed-phase HPLC and identifying product fractions by MALDI-TOF mass spectrometry. The desired fractions were then lyophilized to give qCys-Sup35 as a white solid.

6.3.3 Drug Amphiphile Synthesis

The synthesis of the four CPT-containing drug amphiphile, qCPT-Sup35, was accomplished through the reaction of the peptide qCys-Sup35 with the activated disulphide, CPT-buSS-Pyr (prepared as described previously[256]). Briefly, qCys-Sup35 (15 mg, 6.8 μmol) and CPT-buSS-Pyr (22.8 mg, 40.8 μmol) were dissolved in N_2-purged DMSO (2 ml) and allowed to react for 2 days. The resulting pale yellow solution was then diluted to ~18 ml with 0.1% aq. TFA (adding MeCN as required to solubilise any unreacted CPT-buSS-Pyr). The solution was then purified by reversed-phase HPLC, collecting and lyophilizing the desired product fractions. The resulting powder was dissolved in H_2O and MeCN and aliquotted into cryo-vials, before re-lyophilization. The CPT content was calibrated using a disulphide reduction method and HPLC analysis, indicating that the final yield was 6.8 mg (33%).

6.3.4 Transmission Electron Microscopy

A drop containing 3-5 μL of liquid samples was loaded onto a carbon-copper TEM grid. Sample solutions were wicked away with a piece of filter paper to result in a thin liquid layer on the grid, and were left to dry for 10 minutes. Next, the dried samples were stained with 5 μL of 2% uranyl acetate aqueous solution. After approximately 10 seconds, excess staining solution was wicked away, and the TEM samples were left to dry for at least 3 h before TEM imaging with a Philips EM 420 TEM equipped with SIS Megaview III CCD digital camera.

6.3.5 Circular Dichroism Measurement

All circular dichroism (CD) spectra were measured at room temperature using a Jasco J-710 circular dichroism spectrophotometer. In order to obtain consistent CD measurements, samples were diluted 10-fold from 1% to 0.1% FA immediately before each measurement to avoid high tension (HT) values above 800V. A final volume of 200 μL samples were loaded into a 1 mm pathlength cuvette and measurements were obtained from 200 to 450 nm with 0.5 nm data pitch, 200 nm/min scan speed, 2 s response time, and 2 nm band width. The CD spectrum of each sample is the average of 3 measurements with background subtraction and was smoothed by an integrative package in IGOR software.

6.4 Results and Discussions

6.4.1 Self-assembly of Folic Acid in Methanol-Water Mixtures

We found that folic acid has a low solubility in pure Milli-Q water but will immediately form a yellowish self-supporting gel upon dissolution in methanol at a concentration of 1% or above (*w*/*v*). TEM imaging reveals dominant filamentous nanostructures (Fig. 6-2A) with a diameter of 4.2 ± 0.5 nm. Inspired by the work of using mixed solvents to control solution-state self-assembly of block copolymers,[299-301] we explored the effect of water-methanol mixtures on the FA assembly. Samples were prepared using two different mixing protocols: a step-wise method and a premixed solvent method.

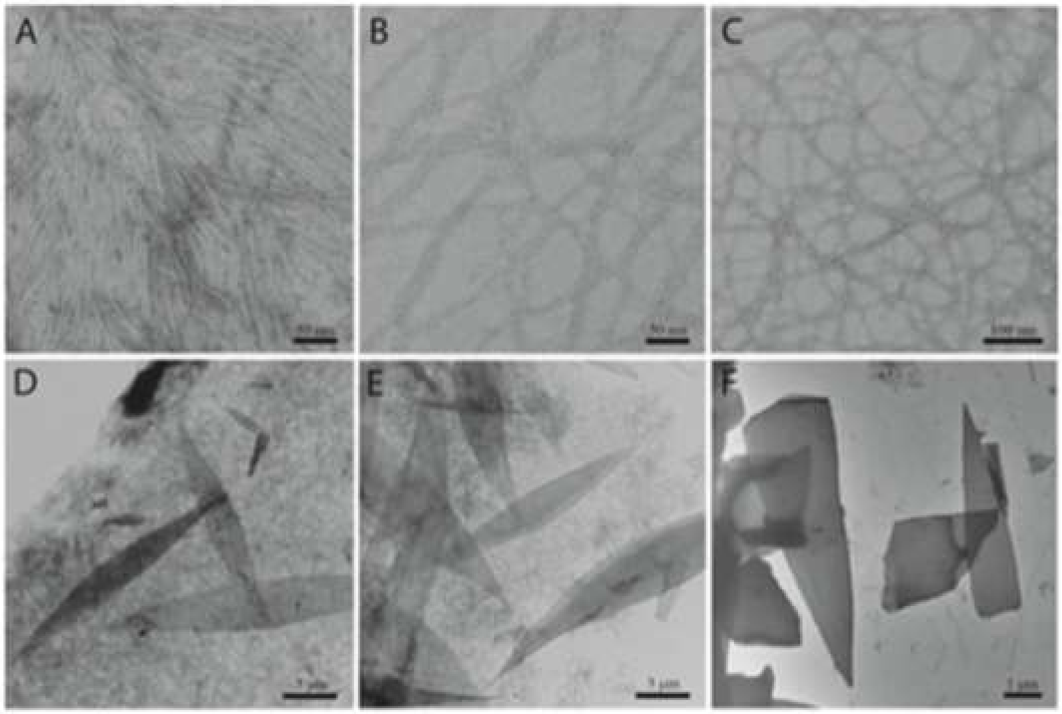

Figure 6-2. TEM images of self-assembled filamentous nanostructures and micron-sized platelets formed by 1 wt% folic acid in mixtures of methanol and water. The samples were prepared through a stepwise mixing method through which folic acid was first dissolved in methanol with subsequent addition of water to reach the desired mixing ratio. Filamentous nanostructures were observed as the dominant morphology in solution samples containing 100% (A), 80% (B), and 70% (C) methanol, with a diameter of 4.2±0.5 nm, 3.5±0.5 nm and 3.9±0.6 nm respectively. Lozenge-shaped platelets of micron size were dominant in solutions containing 50% (D), 25% (E) and 0% (F) methanol.

In the step-wise method, FA was first dissolved in an appropriate amount of pure methanol, followed by the addition of water in a step-wise manner to reach the desired mixing ratio of methanol to water (*v*/*v*). The concentration of FA in all the studied solutions was fixed to be 1% (*w*/*v*). TEM imaging was performed after aging the

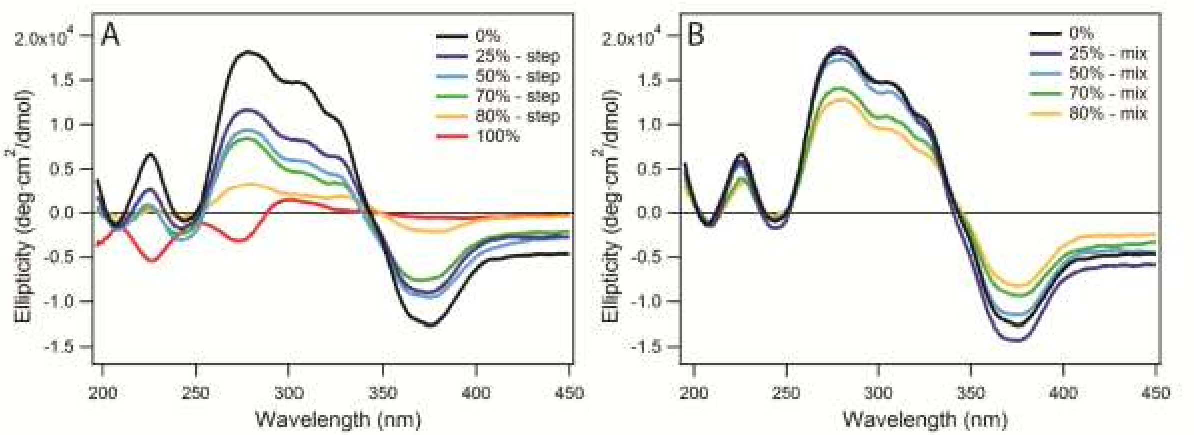

Figure 6-3. Circular dichroism spectra of 1wt% folic acid solutions in methanol-water mixtures of varying compositions, prepared by two different methods: step-wise addition of water to a methanolic solution of folic acid (A) and dissolution of folic acid in pre-mixed methanol-water mixtures (B).

solutions overnight. As shown in Fig. 6-2, similar filamentous nanostructures were observed as the dominant morphology in both 80% (Fig. 6-2B) and 70% (Fig. 6-2C) methanol solutions, with respective diameters of 3.5 ± 0.5nm and 3.9 ± 0.6 nm. The sample containing 80% methanol also formed a self-supporting gel, similar to the gel formed in pure methanol. Both could restore the gel state within seconds after vigorous vortexing. The 70% methanol solution on the other hand, while containing a significant amount of nanofibers, presented as a free flowing liquid only. Occasionally, a few lozenge-shaped platelets could be seen by TEM imaging.

These lozenge-shaped platelets became the dominant structures in solutions containing 50% or more water (Figs. 6-2D-F). On the basis of our TEM observations, most platelets appeared to be single layered, although some multi-layered platelets can also be seen. Frequently, these platelets broke into two halves or even smaller fragments, and thus lost their sharp edges and lozenge shape identity (Fig. 6-2F). The regular shape and dimension of the observed platelets are strongly reminiscent of those of polymer single crystals,[302] suggesting that the FA molecules are packed in a well-defined order within these platelets.

Circular dichroism (CD) spectroscopy reveals induced supramolecular chirality in both filamentous nanostructures and micron-sized platelets. The CD spectrum of FA in pure water (Fig. 6-3A, black curve) shows positive bands at 225, 279, and 308 nm, a coupled band centred at 345 nm with two extremes at 328 nm and 362 nm, and a negative peak at 375 nm. All the absorptions above 300 nm are ascribed to the pterin ring which has been shown to have UV–Vis absorptions both at 280nm and around 350 nm in chloroform.[285,286] We speculate that the positive band at 279 nm could be the superposed π-π^* transitions of the pterin ring and the aromatic group adjacent to the glutamic acid. The CD band at 225 nm most likely corresponds to the n–π^* transition of the benzamide group (between the glutamic acid and benzene moieties).

In pure methanol where FA assembles into filamentous nanostructures, the CD spectrum is dramatically different (Fig. 6-3A, red curve), displaying two negative signals at 225 nm and 273 nm and a weaker, broad positive band around 290 nm. Although FA possesses only one chiral carbon on the glutamic acid, it is not clear to us whether the observed supramolecular chirality is induced solely by glutamic acid packing, or is also affected by the packing of tetramerized pterin rings. It is clear, however, that the differences in CD spectra collected in water and in methanol are a direct reflection of internal chiral packing order. The negative absorption at 225 nm in pure methanol is similar to the characteristic CD absorption of β-sheets, though slightly red shifted. This shift may be due to a combination of the amide being connected to an aromatic moiety and the difference in solvent polarity between water and methanol. Nevertheless, the similarity indicates that glutamic acid may pack in a similar fashion to that found in β-sheet assemblies, helping to propagate the one-dimensional elongation. It is highly possible that the adjacent aromatic group, under the direct influence of this chiral packing, is induced to give rise to a similar negative absorption around 270 nm. With increasing water content in the step-wise method, both negative absorptions became positive in amplitude and gradually intensified, and at the same time the positive absorptions linked to the pterin rings became stronger. The observed change in sign of absorption suggests a different packing order between the filaments and the platelets. Also, the increasing intensity of the CD band around 280 nm as the methanol percentage decreases implies that more stable chiral aggregates are formed in low methanol content mixtures.

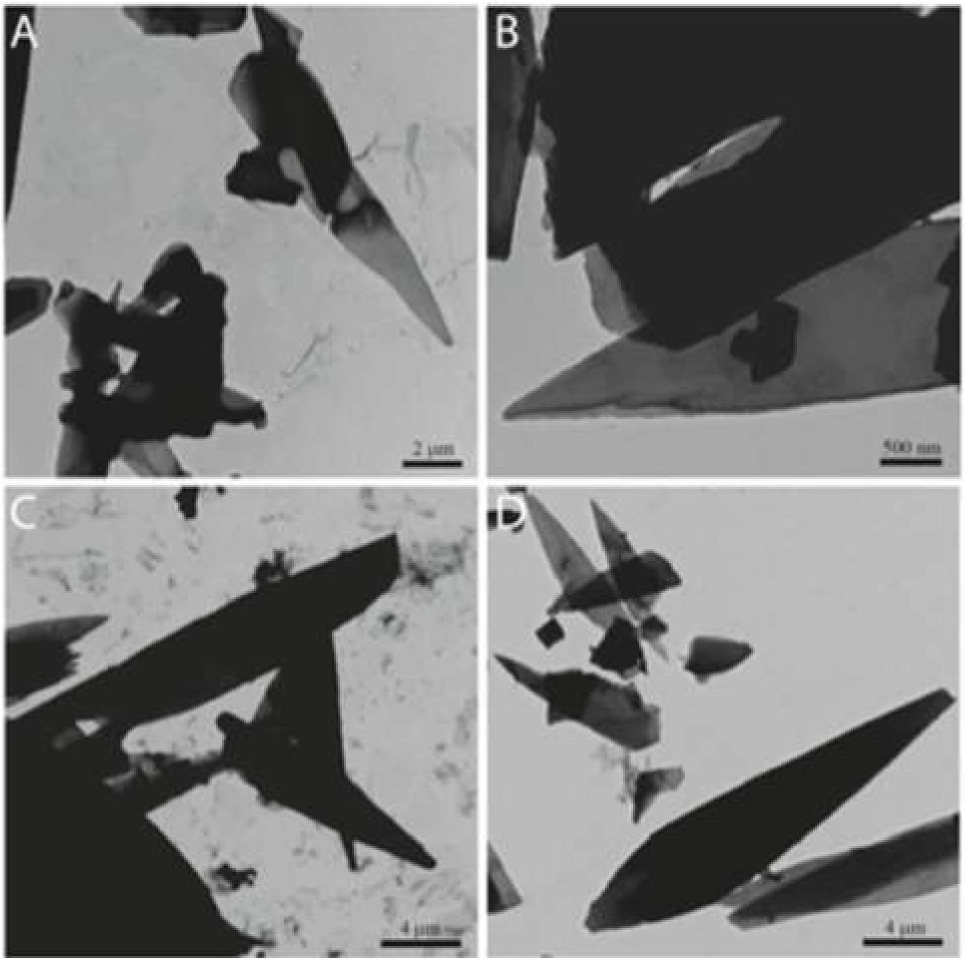

Figure 6-4. TEM images of micron-sized, lozenge-shaped platelets at mixed solvents containing 80% (A), 70% (B), 50% (C) and 25% (D) methanol. The samples were prepared by directly dissolving folic acid into the mixed solvents with predetermined ratio to reach a final concentration of 1%.

We found the self-assembly of FA, particularly the formation of FA nanofibers, in methanol-water mixtures to be pathway-dependant. In the pre-mixed method, FA was directly dissolved in previously prepared water-methanol mixtures (80%, 70%, 50% and 25% *v*/*v* methanol). All solutions that were studied exhibited micro-lozenge formation only, with no evidence of any filamentous nanostructures (Figs. 6-4,A–D). CD analysis of these solutions indicated these structures possessed the same secondary structure and packing modes as those formed by the step-wise addition method (Fig. 6-3B). These experiments suggest that water plays a significant role in the formation of the platelet structures, while methanol seems to favour the filamentous nanostructures.

The TEM studies and CD measurements collectively suggest that the observed nanofibers in pure methanol are one-dimensional stacks of FA tetramers. It has been shown by a number of laboratories that FA and its derivatives are capable of forming Hoogsteen-bonded tetrads through self-recognition of the pterin rings that contain both H-bond donors and acceptors.[283,286-288] The resulting disklike tetramers can form one-dimensional nanostructures that further stack into hexagonal mesophases.[283,286-288] In the case reported here, the diameters of the nanofibers are in the range of 3.5 to 4 nm, which are in good agreement with the expected width of the disklike tetramers. Other evidence comes from the studies on the self-assembly of MTX. Our results showed that MTX could not form any well-defined nanostructures in all the studied conditions. In the case of MTX, the H-bond donor C=O in the pterin ring is replaced with the $-NH_2$ group. This replacement appears to prevent it from forming the tetrameric disks that can aggregate into defined nanostructures. This is consistent with studies on the interaction of FA and MTX with the dihydrofolate reductase enzyme, which showed the two molecules binding with strikingly different orientations as a result of their differing H-bond donor/acceptor arrangements.[278,303] It can therefore be concluded that, the formation of the tetrameric structure represents the first step toward the formation of all the observed morphologies.

The driving forces for one-dimensional stacking of tetrads could possibly stem from combined contributions of both the associative interactions between the tetramerized pterin rings (π–π stacking) and the hydrogen bonding between the glutamic acid segments. In pure methanol, where only discrete nanofibers were observed, this stacking seems to be rather loose as the CD spectrum (Fig. 6-3A) reveals only the absorption bands linked to the glutamic acid and the adjacent aromatic ring, with the pterin moiety showing only weakly induced supramolecular chirality.

Addition of water into methanol solutions containing FA nanofibers leads to the transition from nanofibers to lozenge platelets. The stacking of the FA columns into lozenge platelets is likely driven by inter-fiber interactions of the *C*-terminal and side-chain carboxylic acid groups. At the same time, the significant increase in the intensity of the pterin-associated CD signals also suggests changes in internal packing between the FA tetrads. It is therefore reasonable to assume that the supramolecular chirality of the pterin rings is linked to the crystalline packing among the FA columns. It is also possible that the increasing water content may affect the packing between the tetramerized pterin rings, leading to more compacted and ordered packing among them.

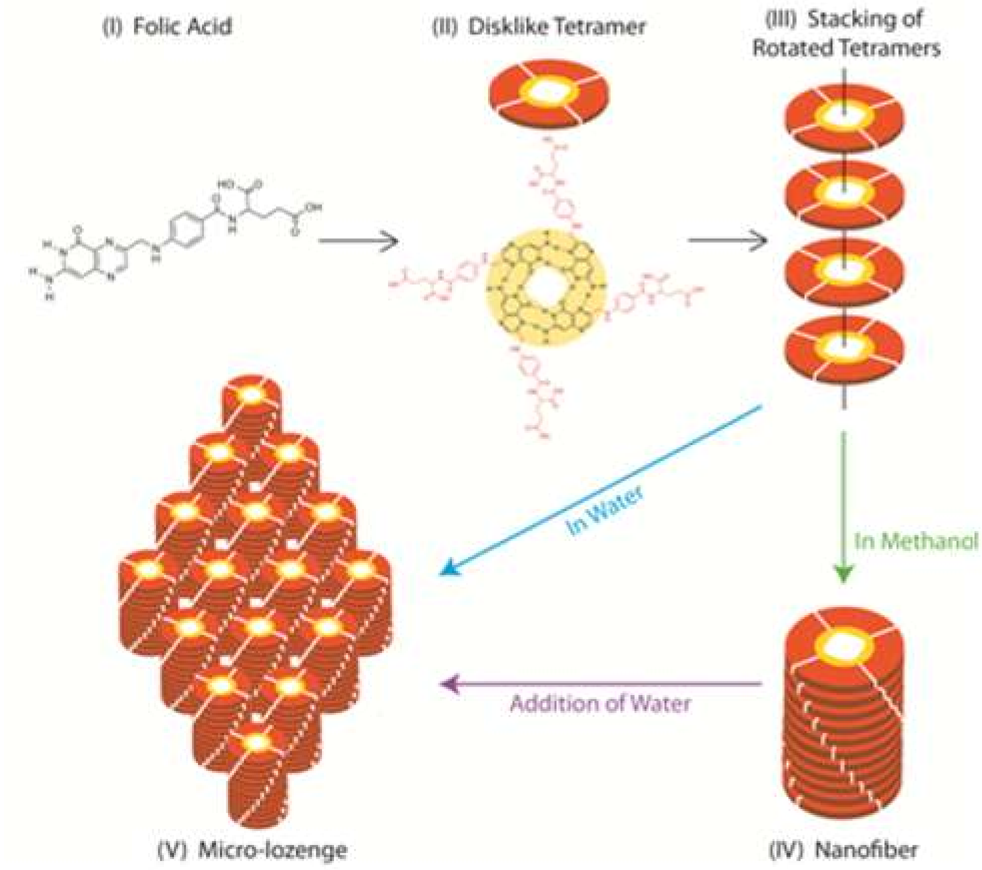

Figure 6-5. Proposed self-assembly pathways of folic acid into nanofibers and micro-lozenges. The pterin ring of folic acid (I) interacts with two adjacent folic acid molecules through Hoogsteen H-bond to form disklike tetramers (II). These tetramers stack up in a rotated manner (III) to form a nanofiber (IV) in methanol. These stacked columns can further associate to give lozenge-shaped platelets in water (V). Addition of water into nanofiber-containing methanol solution leads to a morphological transition into platelets.

6.4.2 Self-assembly of Folic Acid at Different pH

The proposed model in Figure 6-5 leads us to assume that at relatively higher pH values, at which carboxylic acid groups became highly deprotonated, the electrostatic repulsions will likely dissociate the lozenge platelets into individual nanostructures. We therefore carried out a series of experiments using three different buffers: sodium acetate buffer (buffer zone: ~5), phosphate buffered saline (buffer zone: ~7.5), and borate buffer (buffer zone: ~9.5). FA was directly dissolved in the buffered solutions and their pH was carefully monitored and readjusted to be within their respective buffer zones if necessary. FA was found to have a very low solubility in acetate buffer. Fig. 6-6A reveals that fragmented platelets were the dominant nanostructure formed under these conditions. It should be noted that a 1 wt% solution of FA in pure water is also around pH 5, and so it would be expected that a buffered solution at this pH would give similar structures. At pH 7.4 (1× DPBS buffer) FA was observed to self-assemble into 1D nanostructures with an average diameter of 4.1 ± 0.4 nm (Fig. 6-6B). These nanofibers are remarkably similar to those formed in pure methanol. At pH 9.5 (borate buffer), much shorter nanofibers were observed with an average diameter of 4.0 ± 0.4 nm. It is very likely that electrostatic repulsions among glutamic acid segments as a result of almost complete deprotonation at this pH are responsible for the short length of nanofibers.

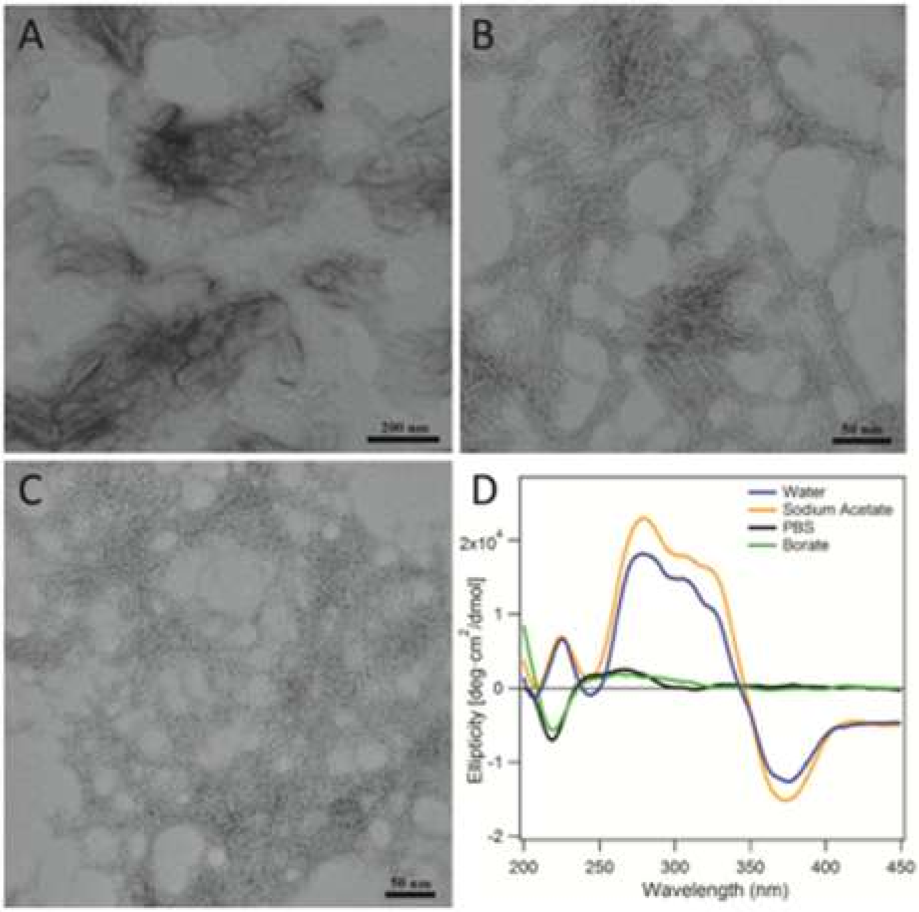

Figure 6-6. TEM images of folic acid formed at three different buffers (A-C) and their corresponding CD spectra (D). (A) Sodium acetate buffer (pH 5), (B) 1×DPBS (~pH 7.4), and (C) borate buffer (~pH 9.5).

CD measurements were then obtained to probe the internal structure of the FA assemblies formed at three buffered solutions (Fig. 6-6D). Nanofiber-dominated samples in both buffered solutions (1×DPBS and borate) consistently showed a characteristic negative peak around 220–225 nm, indicative of the n→π* transition of the amide group. However, compared to the CD spectra collected from pure methanol, the CD signals of FA in 1×DPBS and borate buffers did not exhibit the negative peak at 273 nm that was observed for the pure methanol samples, instead showing a very weak positive band. The reason for this may lie in the nature of the solvent system used. Since methanol is less polar than water, the spacing between the stacked tetrads may be increased as there is less need to shield the more hydrophobic pterin rings from the bulk solvent.[304] This would lessen interactions between adjacent layers, and as such the induced chirality would be determined to a great extent by the chiral packing between the glutamic acid segments, only giving rise to the negative signal observed at 273 nm. The aqueous buffers 1×DPBS and borate, on the other hand, are polar that may cause the layers to stack more tightly, thereby contributing greatly to the induced supramolecular chirality and shifting the signal toward a positive amplitude.

Similar to the CD spectra observed in water and aqueous methanol mixtures, 1 wt% solutions of FA in water and sodium acetate exhibited almost identical intense pterin ring absorptions over the 270–400 nm range. In addition, the 225 nm CD signal due to the amide group had a positive amplitude for the water and sodium acetate buffer solutions, as previously observed for the platelet structures. These observations show a clear correlation with the morphology that is adopted and can be used as a predictor for the structure formed. Filamentous structures correspond to a negative peak in the 220–225 nm region, whereas the platelet structure is indicated by a positive peak in the 220–225 nm region and multiple strong pterin ring absorptions.

Comparing the results from the buffered solutions, it is clear that the stacking of the filamentous structures to form the micro-lozenges is dependent upon shielding of the carboxylic acid groups of the glutamate residue. In pure water, methanolic water and sodium acetate buffer, there is partial shielding of the negative charges that allows the filaments to pack together and ultimately yield the platelet structure. It is likely that water will help to bridge the filaments through hydrogen bonding interactions. In 1×DPBS and borate, however, there is insufficient shielding and the negative charges introduce strong repulsive forces between the individual filaments that prevents association with one another. Accordingly, only one-dimensional structures are observed in these conditions. The case of methanol is likely different as this less polar solvent will favour the more protonated state of the carboxylic acids due to its lower ability to solvate charges. The lack of micro-lozenge structure is therefore a consequence of methanol being unable to act as a hydrogen bonding bridge between the carboxylic acids.

6.4.3 Nanotubes Formed by Self-assembly of CPT Amphiphiles

The conjugation of a peptide segment with overall hydrophilicity onto the hydrophobic drug camptothecin creates amphiphilic molecules that could potentially self-assemble into discrete nanostructures in an aqueous environment.[256,257] The resulting supramolecular nanostructures, regardless of the size, shape, or morphologies, would contain the same drug loading as the individual molecule. Here we discuss our efforts to probe the self-assembly pathway of drug amphiphiles (DAs) that were found to form a nanotube morphology. These DAs were synthesized by attaching four CPT molecules to a β-sheet-forming peptide. In this study, we used peptide sequences derived from the Tau protein[305] and the Sup35 yeast prion[146] that are both capable of forming parallel β-sheet assemblies. After conjugation with four CPT units, the drug loadings are 38% (*w*/*w*) for qCPT-Tau and 36% (*w*/*w*) for qCPT-sup35.

The self-assembly of the two synthesized drug amphiphiles was initially probed by dissolving the respective conjugates into water (100 μM) and using TEM to

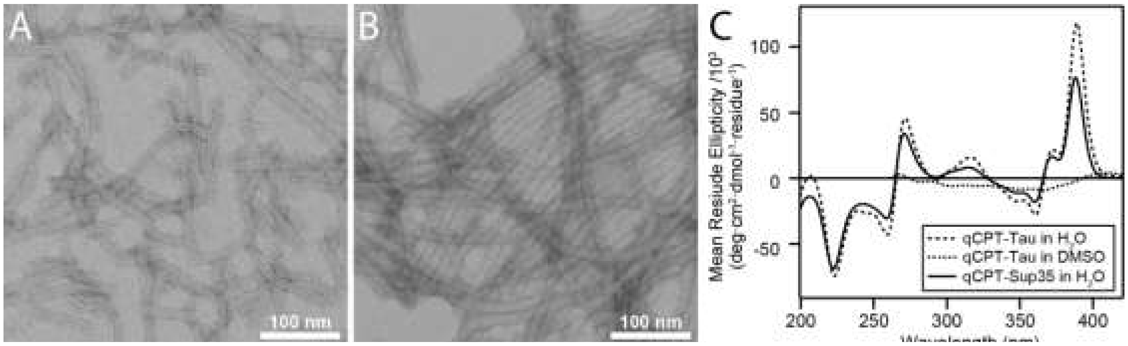

Figure 6-7. Representative TEM micrographs of nanotubes formed by qCPT-Tau (A) and qCPT-Sup35 (B) in water at 100 *μ*M. TEM samples were negatively stained with 2% uranyl acetate. (C) Circular dichroism spectra of qCPT-Tau in water (1 *μ*M) and DMSO (500 nM), and qCPT-Sup35 (50 *μ*M) in water.

determine the assembly morphology. It can be seen from Fig. 6-7 that both qCPT-Tau (Fig. 6-7A) and qCPT-Sup35 (Fig. 6-7B) formed nanotubes with outer diameters of 9.5 ± 1.0 nm and 9.9 ± 1.1 nm, respectively. The tubular morphology is inferred by the dark centre line throughout the observed filamentous morphologies due to the preferential deposition of the staining agent uranyl acetate onto the collapsed cores. These results also suggest that the replacement of the Tau *β*-sheet-forming peptide with the Sup35 *β*-sheet-forming peptide has little or no effect on the nanostructure morphology. The only notable difference was the longer contour length of the Sup35-based nanotubes, which may be due to the greater solubility of this conjugate compared with the Tau-based conjugate. CD spectroscopy further reveals that the two assembled conjugates possess similar packing arrangements (Fig. 6-7C), with both displaying excitonic coupling that arises from electronic interactions between neighbouring CPT units. Strong *β*-sheet signals can also be seen for both conjugates, albeit red-shifted to around 224 nm from the typical value of 216 nm. We noted that the organic solvent DMSO can disrupt the nanotube structures, as the CD spectrum of qCPT-Tau in DMSO only displays a weak negative signal, most likely due to the drug's own chirality.

We found that assembly into nanotubes is also a path-dependent process. In these experiments, we first used hexafluoroisopropanol (HFIP) to break any pre-existing aggregates formed by the conjugates during purification and lyophilisation. HFIP is a fluorous solvent commonly used for the solubilisation of amyloid-forming peptides. We chose HFIP over DMSO as its volatility allows for easy removal. After removal of HFIP, the qCPT-Sup35 residue was reconstituted in water to reach a final concentration of 100 μM, however a turbid solution was formed that contained visible aggregates. TEM imaging after overnight aging did not show any dominant well-defined structures except for the occasional observation of several short fibers or tubes (Fig. 6-8B). We speculate that the thin films formed upon drying of the HFIP solution were too insoluble in water, possibly due to strong interactions among the CPT segments that prevented any structural rearrangement on our experimental timescale. However, when a mixture of water and acetonitrile (50/50) was used to reconstitute the HFIP-treated sample, a clear solution was formed immediately. Interestingly, TEM imaging (Fig. 6-8C) shows nanofibers to be the dominant structure rather than the tubular morphology formed without HFIP-treatment (Fig. 6-8A). The diameter of these nanofibers is 5.8 ± 0.7 nm, a value much smaller than the outer diameter of the nanotubes (9.9 ± 1.1 nm), indicative of a possible core-shell micellar structure. CD spectroscopy of this solution (Fig. 6-8D) shows that the level of electronic interaction between CPT units is strongly diminished in comparison to that of the nanotube morphology, with no bisignate peaks observed in the CPT absorption regions. The continued presence of the peak around 389 nm does, however, suggest that there still exist some CPT–CPT interactions, perhaps due to interactions between CPT molecules of the same conjugate. It is also evident that the CD spectrum of the nanofiber solution exhibits a more typical β-sheet signal at 216 nm, rather than the red-shifted and more intense signal observed for the nanotube structure. These experiments reveal that even for small molecule amphiphiles, the resulting self-assembled structure could still be kinetically trapped due to the involvement of molecular interactions such as hydrogen bonds or π-π interactions that provide strong stabilization when present in a large number.

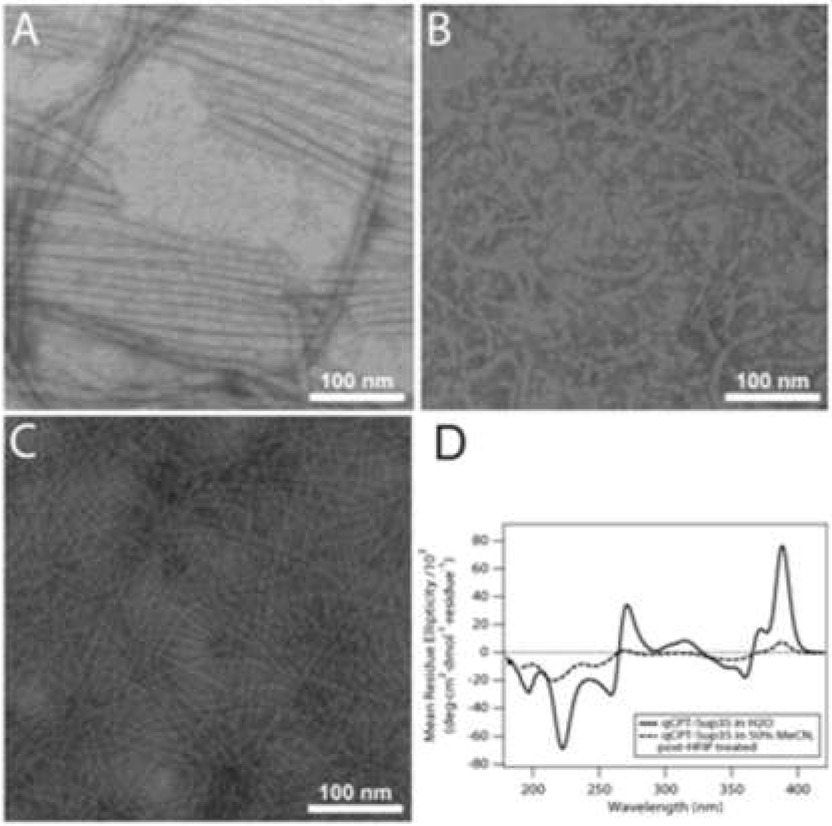

Figure 6-8. TEM micrographs of the assembled structures formed by qCPT-Sup35 via different preparative pathways. Nanotubes of qCPT-Sup35 were observed after dissolution in water at 100 μM after peptide purification (A). Only very few short nanofibers were observed upon reconstitution of qCPT-Sup35 in water at 100 μM after initial lyophilization from HFIP (B). Core-shell nanofibers were observed as the dominant structures when qCPT-Sup35 was reconstituted at 50 μM in 50% aqueous MeCN after initial lyophilization from HFIP (C). All TEM samples were negatively stained by 2% uranyl acetate. (D) CD spectra of qCPT-Sup35 in H_2O (solid line, 50 μM), where nanotubes are the dominant self-assembly morphology, and qCPT-Sup35 in 50% aqueous MeCN after lyophilization from HFIP (dashed line, 50 μM). The latter process of solution preparation favors the formation of single filaments rather than nanotubes.

6.5 Conclusion

In this discussion, we reported our work on the self-assembly of small molecule drugs in dilute solutions. First of all, we demonstrated the possibility of using drug molecules as molecular building blocks to create discrete supramolecular nanostructures. We showed that the free folic acid can assemble into both nanofibers and micro-sized lozenges depending on the solvent conditions and mixing procedures. In the case of hydrophobic anticancer drugs, conjugation to a peptide segment with overall hydrophilicity presents an effective strategy to create self-assembling drug amphiphiles that have the ability to assemble into discrete nanostructures. Second, we demonstrated the tunability of the resulting supramolecular nanostructures, for example, the morphological transition from nanofibers to lozenges for folic acid, and also the transition from nanotubes to nanofibers in the case of CPT drug amphiphiles. Third, we demonstrated the complexity of assembling small molecule drugs. Unlike traditional low-molecular-weight surfactants which are known to assemble into dynamic, thermodynamically stable micellar structures, small molecule drugs often posses the ability to form strong intermolecular interactions such as hydrogen bonding, or π-π interactions. These strong interactions are critical for the drug's biological functions. The presence of these interactions is twofold: on one hand, it allows for the formation of stable, far-from-equilibrium nanostructures in dilute solutions. Stability is often a very important consideration in the design of supramolecular drug carriers. On the other hand, it results in difficulties in understanding the path-dependent assembly behaviours.

6.6 Acknowledgement

We thank National Science Foundation (DMR 1255281) for support of the project, and NIH for funding A.C. (T-32CA130840) and Y.L. (R25CA153952). We thank the JHU Integrated Imaging Center (IIC) for the use of the TEM facility, and the JHU Department of Chemistry Mass Spectrometry facility for MALDI-ToF (NSF CHE-0840463) and ESI analysis. We also thank Prof. Kalina Hristova (MSE, JHU) for the use of CD spectrometer.

7 Conclusions and Future Work

7.1 Conclusions

The main objective and motivation for this dissertation is to explore the incorporation of peptide-based material with various anticancer drugs and imaging agents, ultimately transforming them into supramolecular nanostructures. Based on their applications, nanostructures of different shapes (spherical and cylindrical) and surface charges (cationic and anionic) have been generated. In addition, enzymatic-responsive feature has been integrated in a few examples to confer a triggered-release mechanism within the nanostructure. Coupled with a rational design of peptide design, the hydrophobic nature of anticancer drug and imaging agents demonstrated a self-sufficient building unit for nanostructure self-assembly.

Chapter 2 and 3 present the beacon probe concept with a degradable peptide linker, primarily focused at the diagnostic aspect for enzyme detection, which is often overexpressed in cancer cells. As a proof of concept, the supramolecular nanobeacon is resistant to nonspecific enzymatic degradation in the self-assembled state but can be effectively activated by target enzyme in the monomeric form. The manipulation of peptide design enables morphological transition and customizable charge property on the surface of nanostructures. Our studies showed that cationic spherical nanostructure has higher cellular uptake than its anionic and cylindrical counterparts. In Chapter 4, a fluorescing anticancer drug is utilized to construct the drug beacon with a degradable linker. This design possesses both therapeutic and diagnostic attributes, and it is activatable by a specific enzyme.

In Chapter 5, an anticancer drug with inherent MRI signal was implemented with a self-assembling peptide sequence, generating one-dimensional nanofibers hydrogel. This work has demonstrated the feasibility of monitoring CEST MRI agent *in vivo*, and more importantly, anticancer drug with this intrinsic property can be engineered to bestow a new mechanistic aspect, such as biodegrable hydrogel. Chapter 6 mainly studied and discussed the self-assembly of natural and synthetic amphiphilic drug into discrete nanostructures. The findings revealed the importance of native chemical structure and their intermolecular interaction in directing the self-assembly of nanostructures. Besides, the solvent mixture and processing conditions could fundamentally affect the final state of self-assembled structures.

7.2 Future Work

While great advances has been made in this dissertation to devise peptide-based materials for cancer diagnostic and drug delivery systems, further efforts are needed to improve current constructs and have a better understanding in the design principle. The following sections discussed several interesting directions that can be pursued to achieve these goals.

7.2.1 Targeted Delivery

There are several targeted delivery approaches that can be incorporated to increase specificity towards cancer cells, including monoclonal antibodies[306], aptamers[307,308], peptides[295,309] and non-peptidic ligands[310,311]. While two antibody-drug conjugates[312,313] have shown great success in the market, other targeting ligands could potentially undergo clinical translation in the near future. Considering the peptide-based self-assembly platform, peptide targeting ligands present the highest compatibility and ease of modification (in terms of conjugation chemistry). Several targeting ligands such as RGD peptide[314,315], NGR peptide[316,317], SP5-52 (sequence: SVSVGMKPSPRP)[318], PIVO-8 (sequence: SNPFSKPYGLTV) and PIVO-24 (sequence: YPHYSLPGSSTL)[319] have been explored intensively and showed promising results with increasing therapeutic efficacy. Interestingly, a nine-amino cyclic peptide, LyP-1 (sequence: CGNKRTRGC)[320] demonstrated both tumor-targeting capability and cytotoxic activity on its own. Such peptide with multiple functionalities, are of great interest and can be rationally improvised to transform it into a self-assembling nanostructure. In addition, folate-targeting and prostate-specific membrane antigen (PSMA) ligands are two ideal candidates for future modifications. The conjugation of targeting ligands to nanobeacon or drug beacon systems could potentially increase the specificity of tumor site accumulation; however, the choice of ligands should be thoroughly considered to retain the overall amphiphilicity requirement for self-assembly process.

7.2.2 Self-assembling CEST MRI Nano-Systems

Numerous research groups have progressively discovering and exploring new small molecule CEST MRI contrast agents for *in vivo* imaging applications. McMahon and co-workers reported a series of salicylic acid and analogues[249] as well as anthranilic acid analogs[321] possess diamagnetic CEST MRI property with desirable signals far from water peak. The incorporation of these small molecule CEST contrast agents to self-assembling peptide is worth exploring to generate novel nanostructure imaging systems or theranostic systems with the addition of therapeutic agents. From a fundamental stand-point, the CEST MRI property under highly-dense molecular arrangement of self-assembled state could be further explored and investigated. Furthermore, CEST contrast agents encapsulated within liposome structure have shown enhancement in CEST signal.[322,323] The combination of CEST constrast agent with self-assembling peptide directed to nanovesicle formation[324,325] would create similar intra-liposomal aqueous environment that could potentially enhance CEST signal. These explorations can greatly expand the field of CEST MRI imaging as well as crafting innovative functionality to self-assembling peptide systems.

Appendices

Supporting Information for Chapter 2

Design and Construction of Supramolecular Nano-Beacons for Enzyme Detection

S1 Synthesis and Characterization of Peptide Molecules

S1.1 Materials

All Fmoc amino acids were purchased from Advanced Automated Peptide Protein Technologies (AAPPTEC, Louisville, KY) and Rink Amide MBHA resin was purchased from Novabiochem (San Diego, CA). 5-Carboxyfluorescein (5-FAM) was purchased from AnaSpec, Inc. (Fremont, CA) and Black Hole Quencher1 carboxylic acid (BHQ-1-CO_2H) was purchased from Biosearch Technologies, Inc. (Novata, CA). Cathepsin-B (bovine spleen) was purchased from EMD Chemicals (San Diego, CA).

S1.2 Synthesis

Standard 9-fluorenylmethoxycarbonyl (Fmoc) solid phase peptide synthesis was used to synthesize the TAT sequence and the enzyme degradable linker (Fmoc-GFLGK(Mtt)GRKKRRQRRRPPQ-Rink) on a 0.25 mmole scale. This procedure was carried out using the Focus XC automated peptide synthesizer (AAPPTEC, Louisville, KY). For TFB and TF molecules, 5-carboxyfluorescein (5-FAM) was manually coupled at the peptide *N*-terminus (after Fmoc removal) with 5-FAM/HBTU/DIEA at a ratio of 4:4:6 relative to the peptide, shaking overnight at room temperature. For TFB and TB molecules, Black Hole Quencher-1 (BHQ-1) was coupled to the Lys ε-amine (after Mtt removal) with BHQ-1/HBTU/DIEA at a ratio of 1:0.96:1.7 relative to the peptide, shaking overnight at room temperature. Fmoc deprotections were performed using a 20% 4-methylpiperidine in DMF solution for 10 minutes, repeating once. Mtt deprotections were carried out using a mixture of TFA/TIS/DCM with a ratio of 3:5:92 for 5 minutes, and the procedure was repeated twice. Acetylation was performed on TF and TB molecules at the Lys(Mtt) side chain amine and the *N*-terminal amine, respectively, using a 20% acetic anhydride in DMF solution with 100 µL of DIEA, shaking for 15 mins, and repeating once. In all cases, reactions were monitored by the ninhydrin test (Anaspec Inc., Fremont, CA) for free amines. Completed peptides were cleaved from the solid support using a mixture of TFA/TIS/H2O in a ratio of 95:2.5:2.5 for 3 hours. Excess TFA was removed by rotary evaporation and cold diethyl ether was added to precipitate the crude peptide, which was collected and dried under vacuum overnight.

Schemes 1-3 offer details of the synthesis procedures.

Abbreviations:
HBTU :*O*-benzotriazole-*N*,*N*,*N*',*N*'-tetramethyluroniumhexafluorophosphate
DIEA: diisopropylethylamine
Mtt: 4-methyltrityl
TFA: trifluoroacetic acid
TIS: triisopropylsilane
DCM: dichloromethane
DMF: *N*,*N*-dimethylformamide

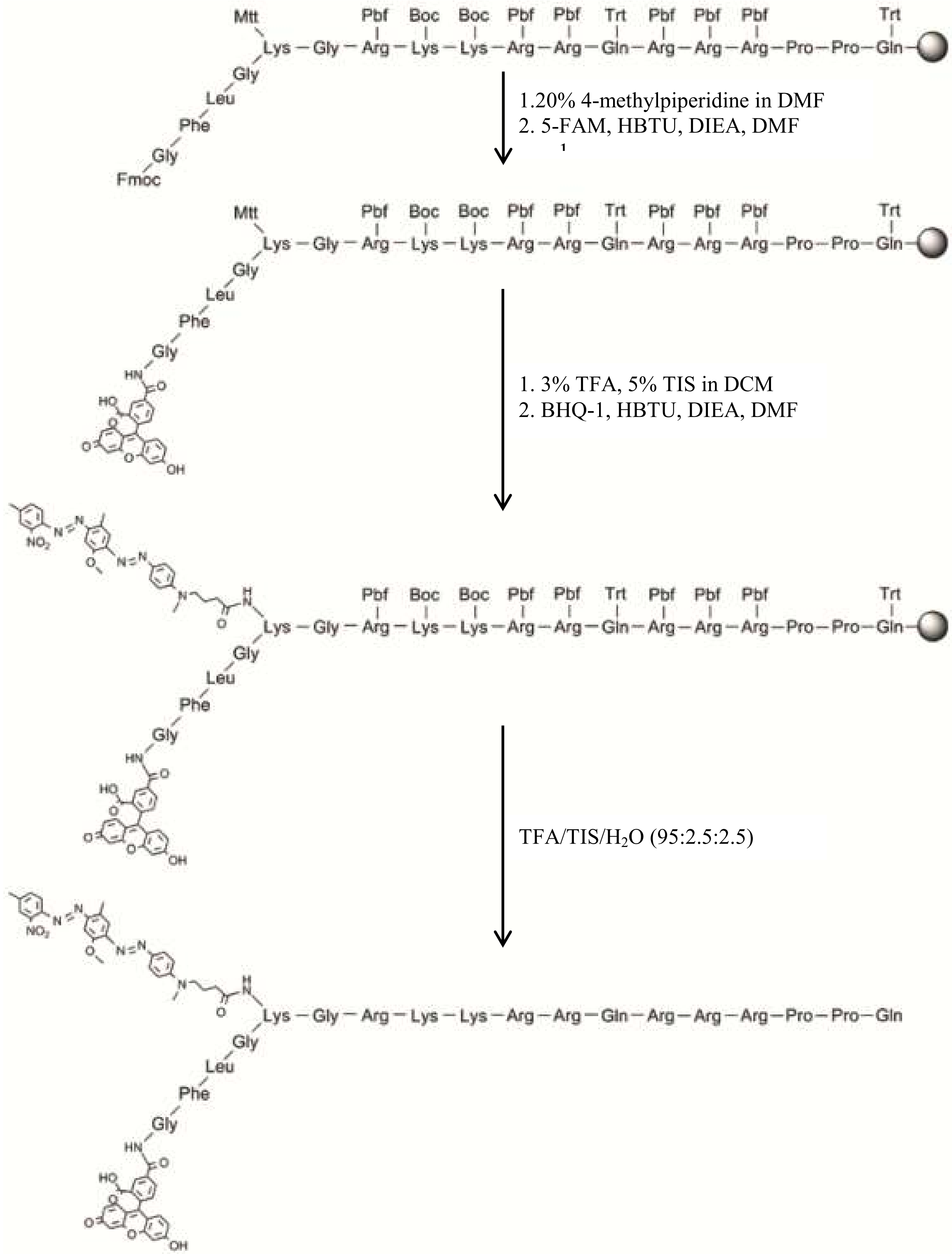

Scheme S1: Synthesis steps of TFB

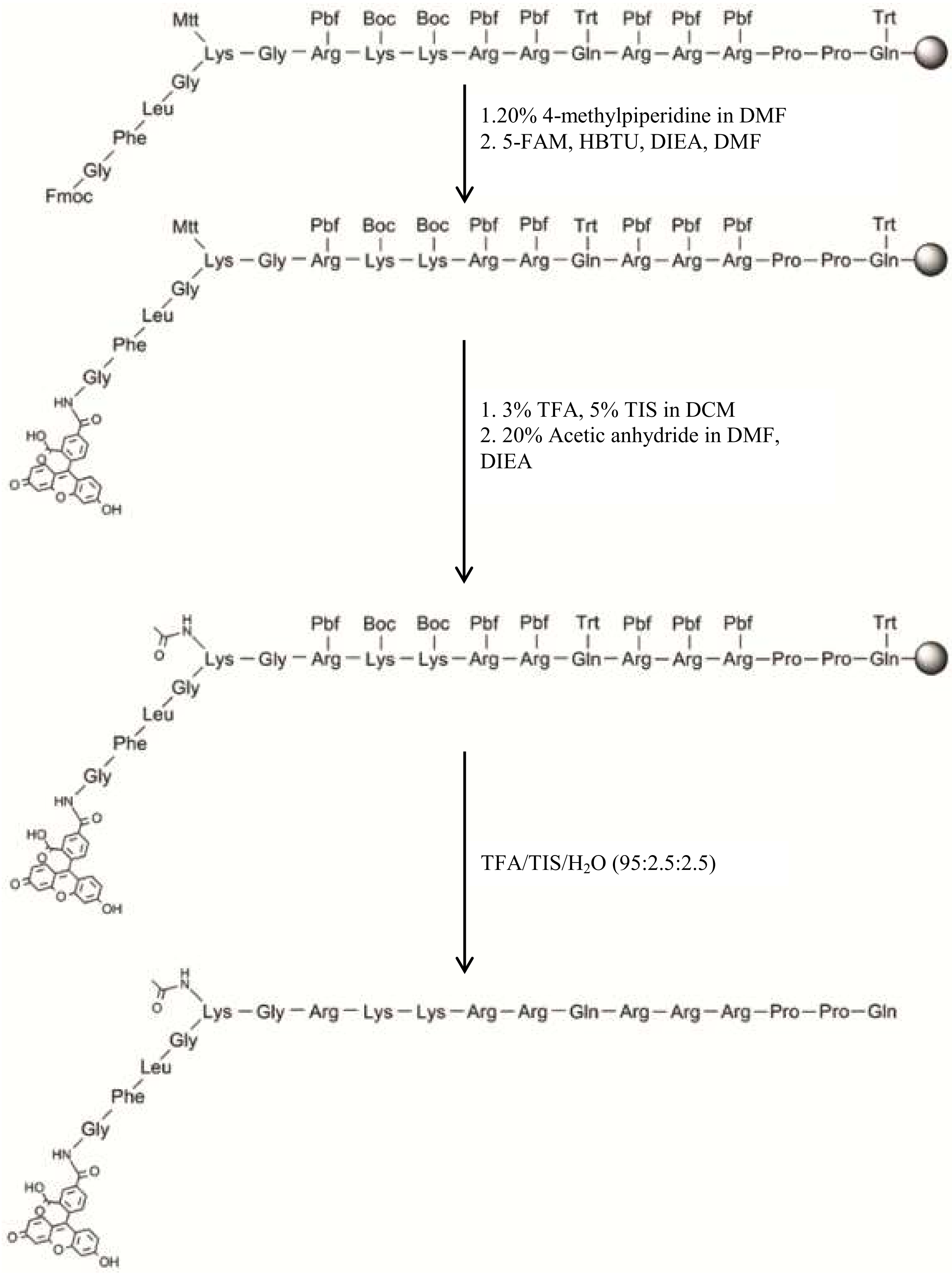

1.20% 4-methylpiperidine in DMF
2. 5-FAM, HBTU, DIEA, DMF

1. 3% TFA, 5% TIS in DCM
2. 20% Acetic anhydride in DMF, DIEA

TFA/TIS/H_2O (95:2.5:2.5)

Scheme S2: Synthesis steps of TF

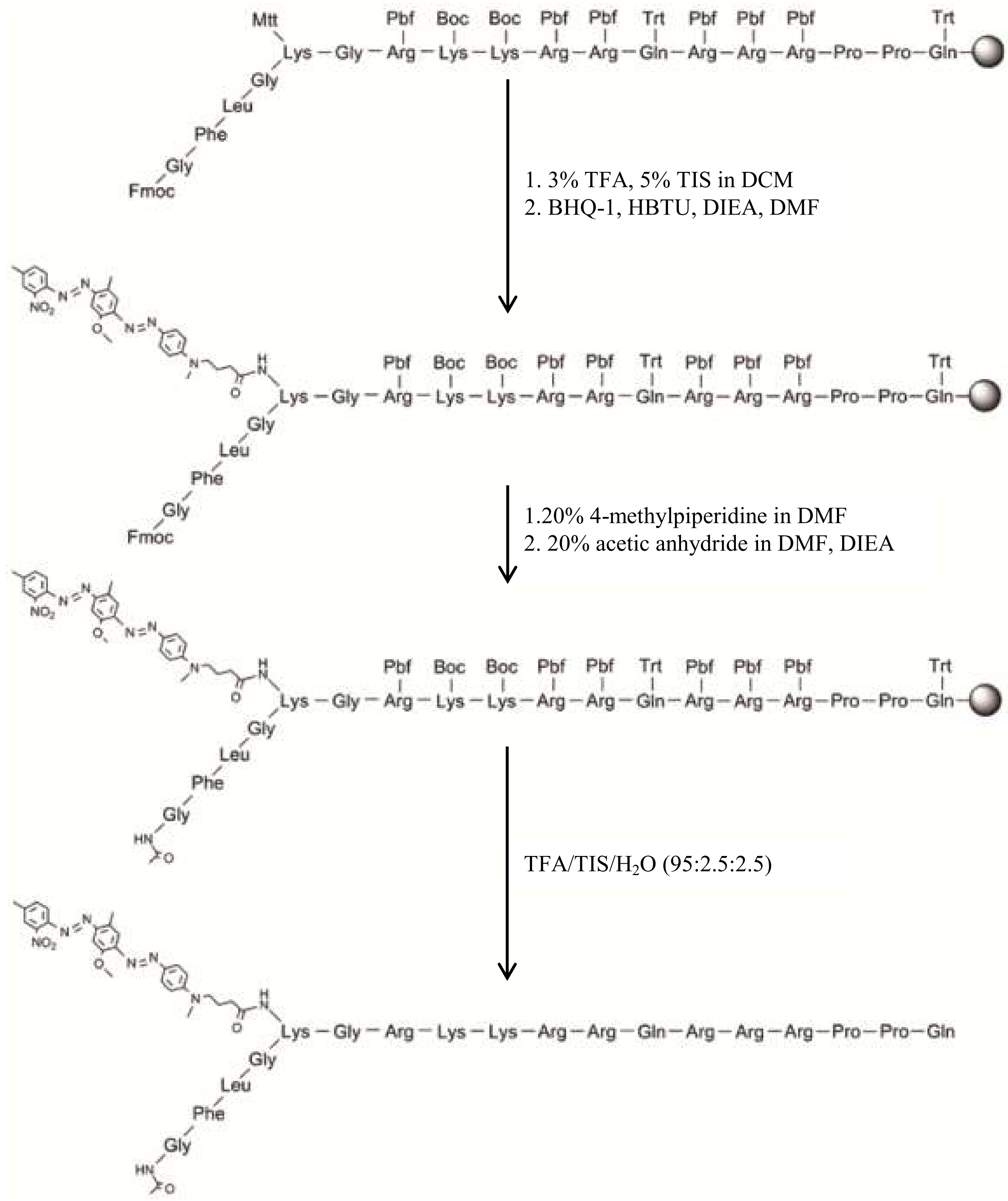

Scheme S3: Synthesis steps of TB

S1.3 Purification

The peptides were purified by preparative RP-HPLC using a Varian Polymeric Column (PLRP-S, 100 Å, 10 μm, 150 × 25 mm) at 25°C on a Varian ProStar Model 325 preparative HPLC (Agilent Technologies, Santa Clara, CA) equipped with a fraction collector. A water/acetonitrile gradient containing 0.1 % *v*/*v* TFA was used as eluent at a flow rate of 25 mL/min, monitoring the absorbance at 480nm and 534nm for TF and TB/TFB molecules respectively. The crude materials were dissolved in 30 ml of 0.1% aqueous TFA, and each purification run was carried out with a 10 ml injection. Collected fractions were analyzed by ESI-MS (LDQ Deca ion-trap mass spectrometer, Thermo Finnigan, San Jose, CA) and those containing the desired product were further concentrated by rotary evaporation to remove acetonitrile. The remaining solution was lyophilized (FreeZone -105°C 4.5 L freeze dryer, Labconco, Kansas City, MO) and stored at -30°C.

S1.4 MALDI-ToF Characterization

High resolution peptide masses were determined by MALDI-ToF mass spectrometry, using a BrukerAutoflex III MALDI-ToF instrument (Billerica, MA). Samples were prepared by depositing 1 μL of sinapinic acid matrix (10 mg/ml in 0.05% TFA in H_2O/MeCN (1:1), Sigma-Aldrich, PA) onto the target spot, and allowed to dry for 5 minutes. 1 μL of peptide aqueous solution (0.1% TFA) were deposited on the corresponding spot and quickly mixed with 1 μL of sinapinic acid matrix solution. Samples were irradiated with a 355 nm UV laser and analyzed in the reflectron mode.

Table S1: Expected and observed masses of the synthesized molecules

MALDI-ToF	Exact Mass	Observed Mass [M+H$^+$]
TFB	3063.607	3064.139
TF	2619.416	2621.686
TB	2747.570	2748.901

a)

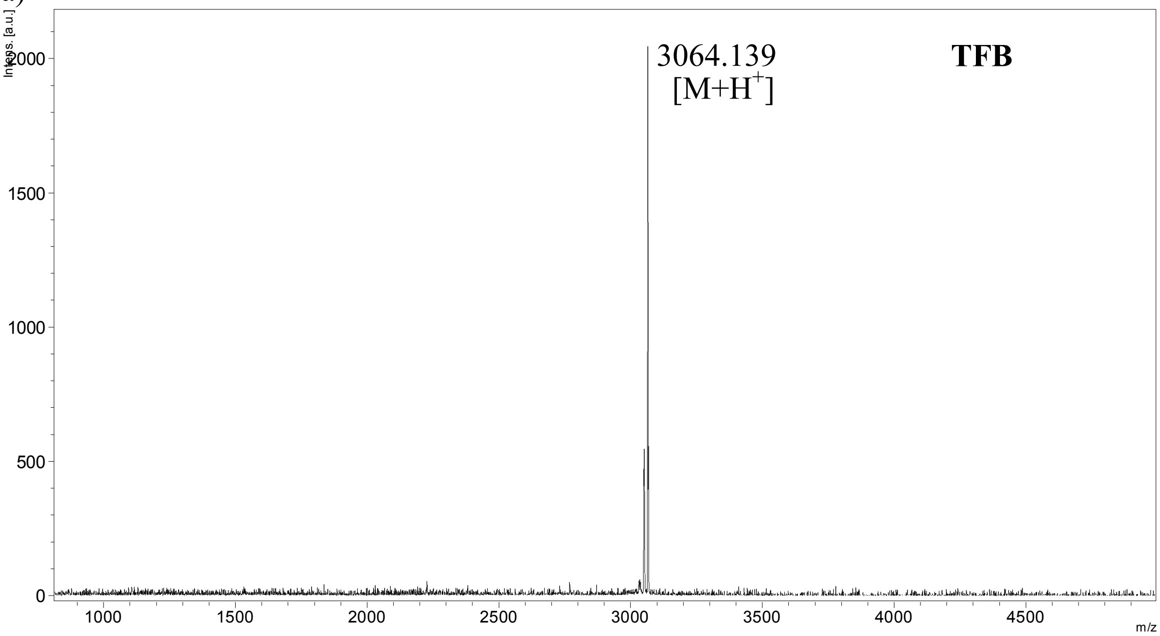

b)

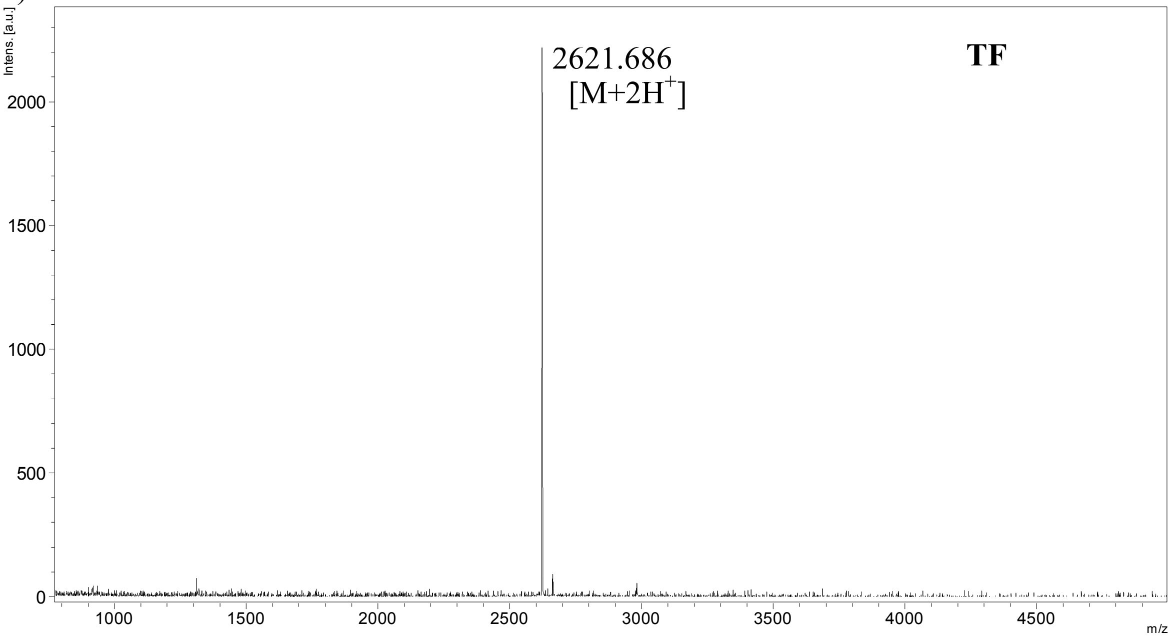

c)

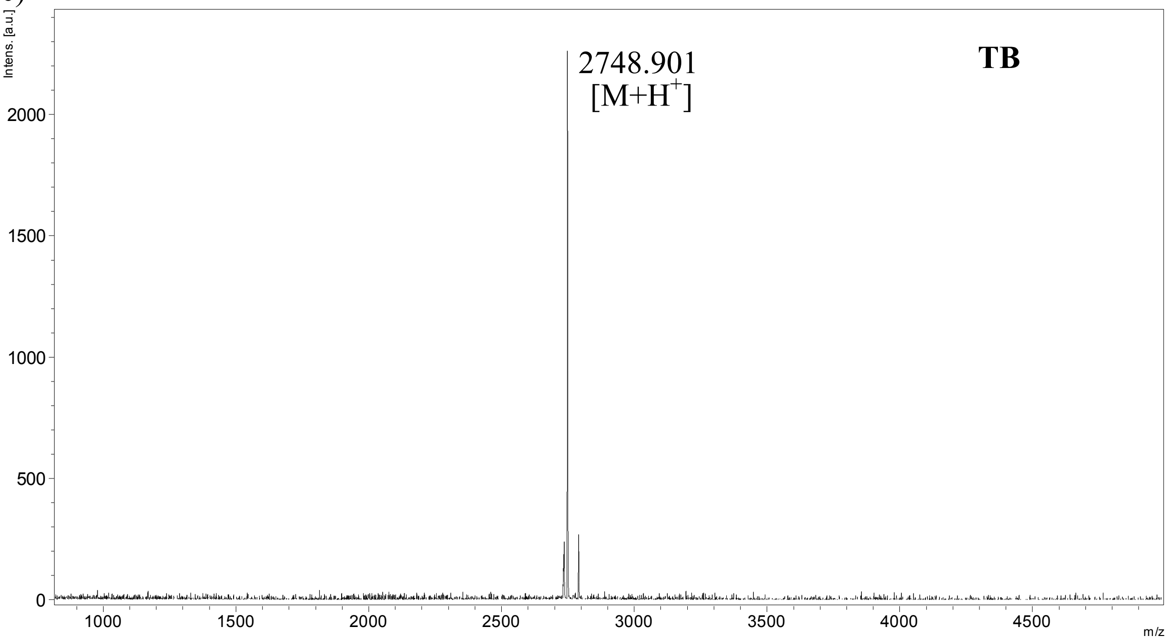

Figure S1. MALDI-ToF spectra of (a) TFB, (b) TF and (c) TB molecules.

S1.5 Analytical HPLC Characterization

Analytical reverse-phase HPLC was performed using a Varian polymeric column (PLRP-S, 100 Å, 10 μm, 150 × 4.6 mm) with 20 μL injection volumes. A water/acetonitrile gradient containing 0.1% *v*/*v* TFA at a flow rate of 1 mL/min was used and samples were dissolved at 1 mg/ml concentrations in 0.1% aqueous TFA.

(a)

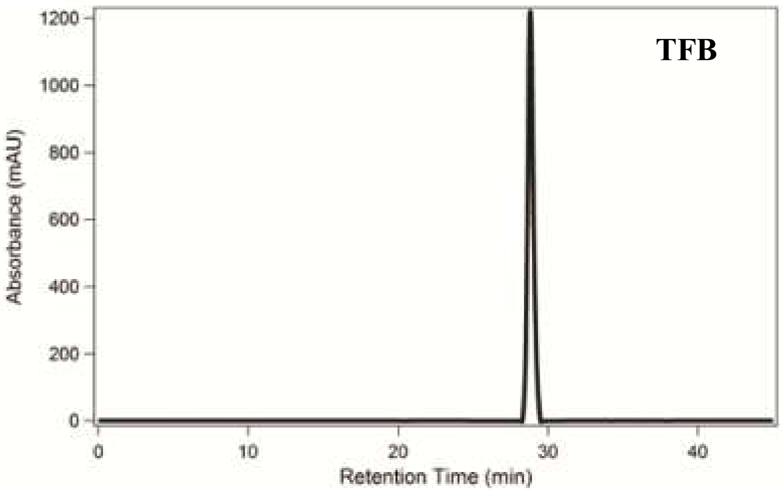

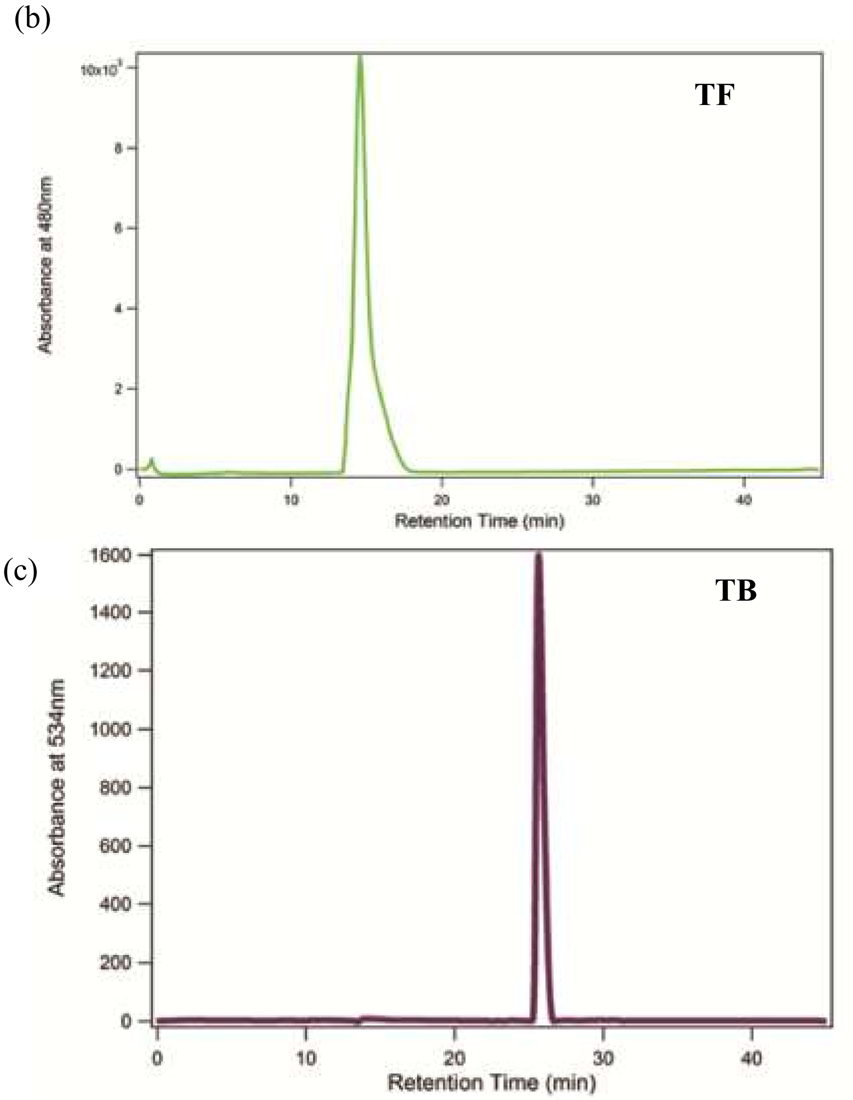

Figure S2. Reverse-Phase HPLC chromatograms of (a) TFB, (b) TF and (c) TB molecules.

S2 TEM and Cryogenic TEM Sample Preparation

S2.1 Transmission Electron Microscopy (TEM)

5µL of sample solution was deposited onto a carbon-coated copper grid (Electron Microscopy Services, Hatfield, PA), and excess solution was wicked away using a small piece of filter paper. The sample was then left to dry for 10-15 minutes. Next, 5 µL of 2 wt% uranyl acetate aqueous solution was placed on the grid. The excess solution was carefully removed using a piece of filter paper to leave a very thin layer of uranyl acetate aqueous solution on top of the pre-dried samples. This solution was allowed to dry at room temperature. Bright-field TEM imaging was performed on a FEI Tecnai 12 TWIN Transmission Electron Microscope operated at an acceleration voltage of 100 kV. All TEM images were recorded by a SIS Megaview III wide-angle CCD camera.

S2.2 Cryogenic Transmission Electron Microscopy (Cryo-TEM)

Cryogenic TEM imaging was also performed on the FEI Tecnai 12 TWIN Transmission Electron Microscope, operating at 80 kV. 3-5 μL of sample solution was placed on a holey carbon film supported on a TEM copper grid (Electron Microscopy Services, Hatfield, PA). All the TEM grids used for cryo-TEM imaging were treated with plasma air to render the lacey carbon film hydrophilic. A thin film of the sample solution was produced using the Vitrobot with a controlled humidity chamber (FEI). After loading of the sample solution, the lacey carbon grid was blotted using preset parameters and plunged instantly into a liquid ethane reservoir precooled by liquid nitrogen. The vitrified samples were then transferred to a cryo-holder and cryo-transfer stage which was cooled by liquid nitrogen. To prevent sublimation of vitreous water, the cryo-holder temperature was maintained below -170°C during the imaging process. All images were recorded by a SIS Megaview III wide-angle CCD camera.

S3 TEM image of TFB nanobeacons in DMEM

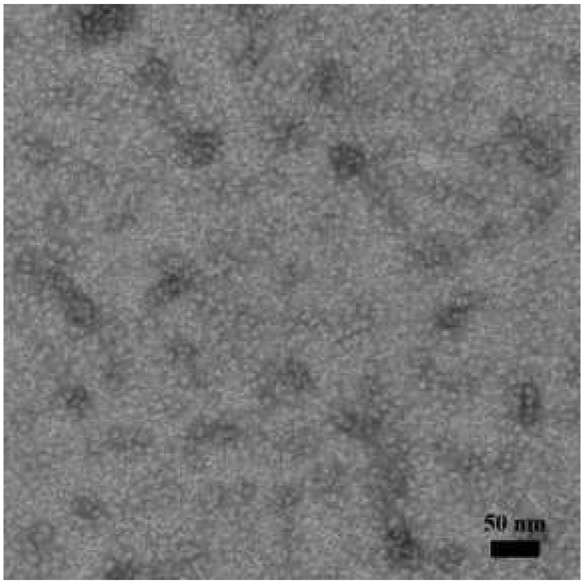

Figure S3. TEM image of TFB NB in DMEM cell medium reveals dominant spherical nanoparticles of approximately 10 nm. The NB concentration was 250 µM in DMEM. The TEM sample was negatively stained with 2% uranyl acetate aqueous solution.

S4 Supramolecular filaments of TB in borate buffer

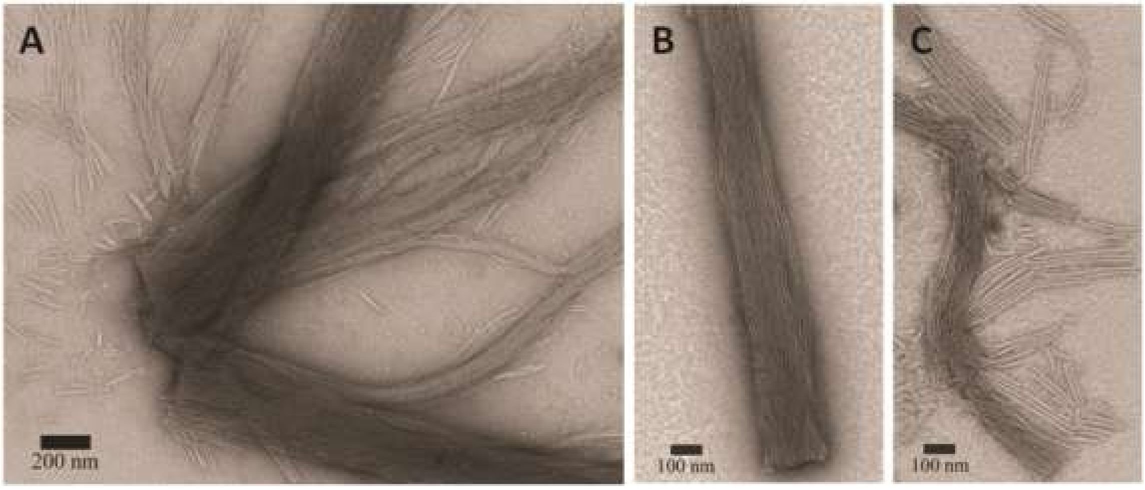

Figure S4. Supramolecular filaments formed by self-assembly of TB in borate buffer (pH 9.5) at a concentration of 200 µM. The diameter of these filaments is 12.5±0.9 nm, a value close to twice that of the fully extended length of the studied molecule, suggesting a cylindrical shape of the cross-sectional area.

S5 Circular Dichroism Measurement

CD spectra were recorded on a JASCO J-710 spectropolarimeter (JASCO, Easton, MD) and all three molecules of TFB, TF and TB were found to have a random coil secondary structure in 100 µM, 1xPBS solutions. All CD spectra were normalized using the equations below, where θ_{mr} is the mean molar ellipticity per residue[326].

$$\theta_{mr} = \theta_d \cdot \frac{M}{c \cdot l \cdot n_r}$$

$$\theta_{mr} = [deg \cdot \frac{g}{dmol} \cdot \frac{cm^3}{g} \cdot \frac{1}{cm} \cdot \frac{1}{residue}]$$

M : molecular weight (g/dmol)
c : concentration (g/cm^3)
l : path length (cm)
n_r : number of residue

(a)

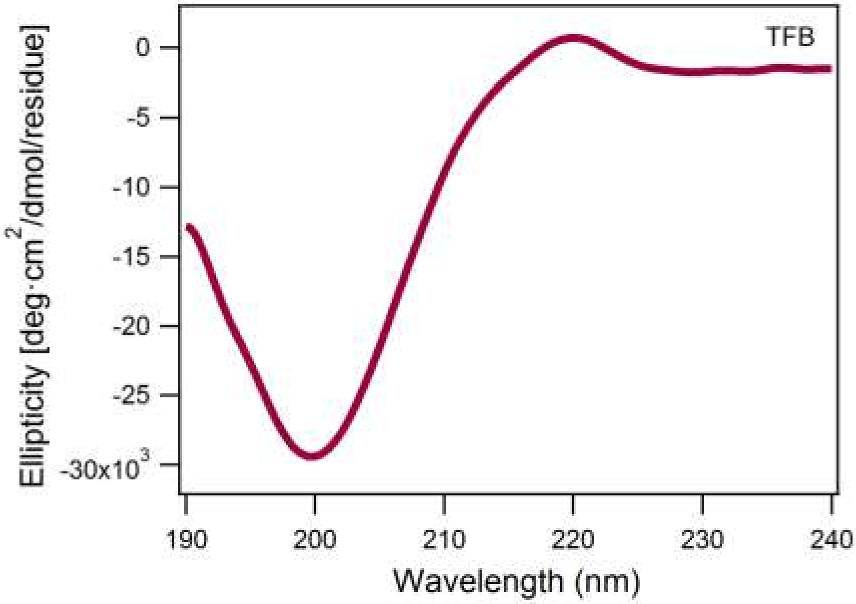
TFB
Ellipticity [deg·cm^2/dmol/residue]
0
-5
-10
-15
-20
-25
-30x10^3
190
200
210
220
230
240
Wavelength (nm)

(b)

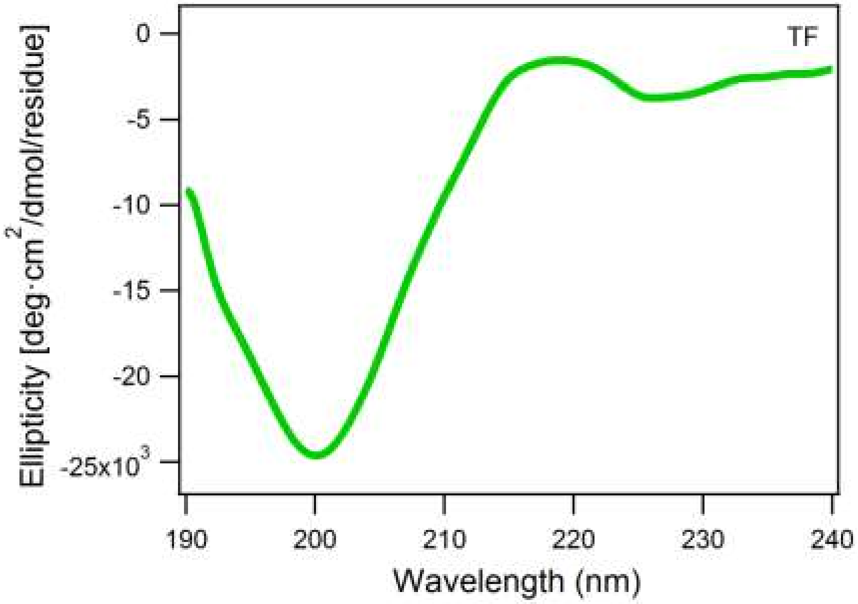
TF
Ellipticity [deg·cm^2/dmol/residue]
0
-5
-10
-15
-20
-25x10^3
190
200
210
220
230
240
Wavelength (nm)

(c)

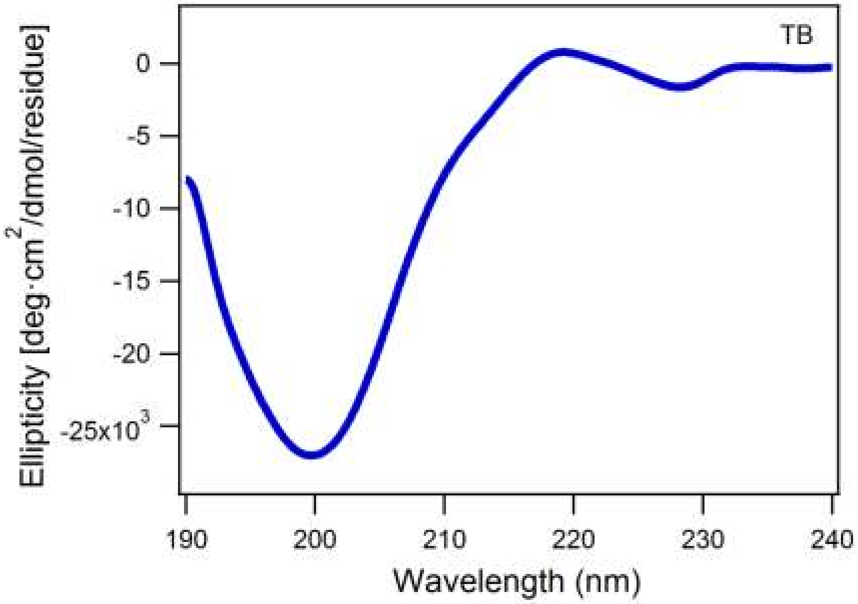

Figure S5. Circular dichroism spectra of (a) TFB, (b) TF and (c) TB molecules at 100 μM. These measurements were performed at room temperature. Spectra showed a negative peak at 199 nm and a positive peak at 219 nm, correlating well with literature values of random-coil secondary structure.[326]

S6 Enzymatic Degradation Experiment in Buffered Solutions

S6.1 Cathepsin-B (CatB) Enzyme

The reaction buffer containing 1 mM EDTA (enzyme stabilizer) and 25 mM L-cysteine (enzyme activator) in 1×PBS solution was prepared. The solution pH was adjusted to 5.0 through the addition of 3 M HCl. The desired amount of cathepsin-B was added to the buffer solution and pre-incubated at 37°C for 5 minutes to activate the enzyme. Stock solution was prepared by dissolving 0.6 mg of TFB molecule with 500 μL of pH 5.0 reaction buffer, yielding a TFB concentration of 0.4 mM. 0.25 μL of 0.4 mM stock solution was added to each reaction well and mixed thoroughly with the pre-incubated cathepsin-B solution. Cathepsin-B (Bovine Spleen) was purchased from EMD Chemicals (Gibbstown, NJ) and it was delivered in liquid form with stock concentration of 17 μM. Reaction kinetics was monitored using a Gemini XPS microplate reader

(Molecular Devices, Sunnyvale, CA). Samples were excited at 492 nm and 5-FAM emission was measured at 520 nm with a 515 nm cutoff.

S6.2 Matrix Metalloproteinase 2 (MMP-2) Enzyme

The reaction buffer containing 50mM Tris-HCl, 50mM NaCl, 10mM CaCl and 0.05% Brij-35 was freshly prepared and the solution pH was verified to be around 7.4. TFB molecule of 1µM in 100µL of reaction buffer solution was pre-incubated at 37°C for 5 minutes. Appropriate amount of MMP-2 (10nM – 40nM) from a stock solution of 200nM was added to the pre-heated solutions. Active human recombinant MMP-2 enzyme was purchased from EMD Millipore, Billerica, MA and was used as it is in all the relevant experiments. Reaction kinetics was monitored as described in S6.1.

S7 Degradation Kinetics Comparison of CatB and MMP-2 Enzymes

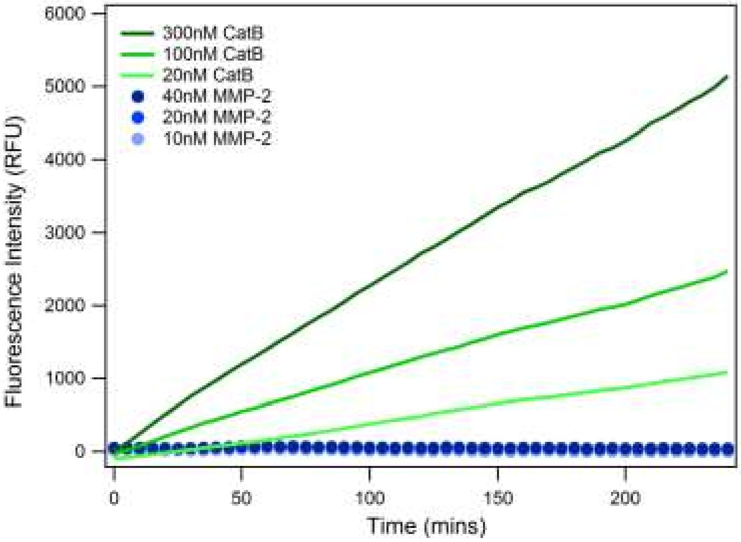

Figure S6. Reaction kinetics of 1000nM TFB molecules incubated with CatB and MMP-2 enzymes at different concentrations.

Enzymatic degradation was carried in buffered solutions and 1000nM TFB molecules were incubated with different concentrations of CatB and MMP-2 enzyme. MMP-2 enzyme used in these experiments was relatively lower as the plasma concentration of MMP-2 ranged from 10nM to 20nM (749µg/L - 1114µg/L).[327] The fluorescence intensity of TFB that was incubated with MMP-2 enzyme remained flat at baseline while CatB enzyme showed an increasing trend suggested a selective degradation by CatB.

S8 TFB Critical Micelle Concentration Determination

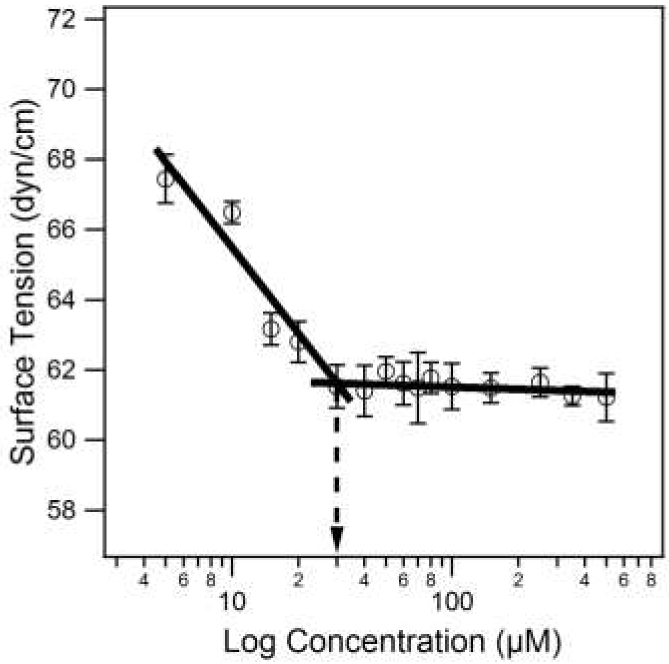

Figure S7. Plot of TFB surface tension versus log of concentrations. The intersection of two different slopes of lines indicates TFB critical micelle concentration around 30µM.

A 500µM of TFB stock solution were prepared in sodium acetate buffer (pH 5) and serial dilution method was used to prepare various concentrations of TFB samples to a final volume of 100µL. All samples were protected from light and left overnight at room temperature. Surface tension measurements were carried out using the pendant drop method[328]. Measurement apparatus includes micrometer syringe GE 2.0mL from Gilmont Instrument, dispensing needle 22 gauge x 0.5” blunt tip, and series of pendant drop images were taken by First Ten Ångstroms (FTA) 125. Surface tension measurements were further analyzed using FTA32 software. From the plot above, TFB critical micelle concentration was determined to be 30µM at pH 5.

S9 k_{cat}/K_m Calculation

The catalytic reaction of CatB has been reported to follow the kinetic behavior described by the Michaelis-Menten equation. According to Michaelis-Menten Equation, the reaction rate V can be expressed in the following form:

$$V = \frac{k_{cat}[E]_t[S]}{K_M + [S]}$$

in which k_{cat} is the first-order rate constant, $[E]_t$ is the total enzyme concentration, $[S]$ is the substrate (TFB, in the case reported here) concentration, and K_M is the Michaelis-Menten constant. At the very low substrate concentrations reported herein ($[S] << K_M$), the equation can be rewritten as:

$$V \cong \frac{k_{cat}}{K_M}[E]_t[S]$$

The ratio of k_{cat}/K_M provides a direct measure of enzyme efficiency and specificity. The plot in Fig. 4D is in good agreement with this equation as the initial cleavage rate is indeed linear with respect to the CatB concentration.

S9.1 Enzymatic Cleavage Experiments at a Concentration of 1 μM NB Molecule

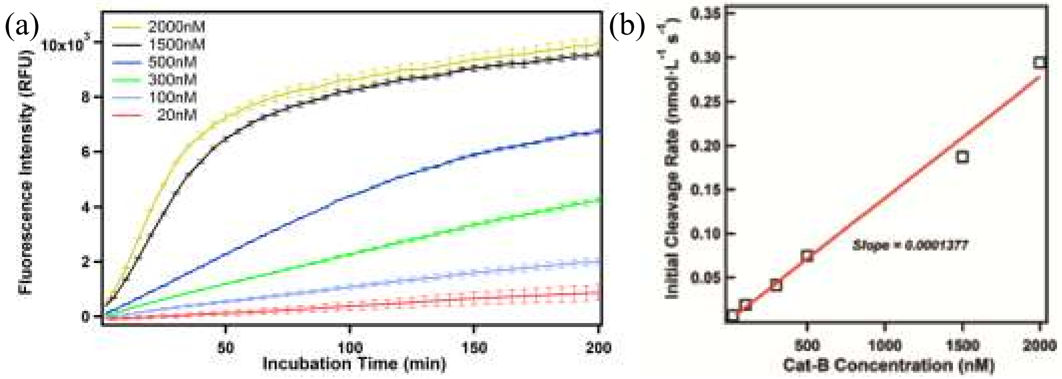

Figure S8. (a) Reaction kinetics for 1000 nM TFB with different concentration of Cathepsin-B enzyme. (b) Plot of initial cleavage rate over Cathepsin-B concentration after unit conversion from RFU to nmol·L^{-1} s^{-1}.

This series of experiments were carried out with constant substrate concentration, 1000 nM TFB and various Cathepsin-B concentrations. The maximum fluorescence intensity at 200 minutes was assumed to correspond to 100% cleavage of 1000nM TFB, releasing 1000 nM 5-FAM molecule and therefore yielding 1×10^4 RFU.

$$Conversion\ unit = \frac{1 \times 10^4\ RFU}{1000nM\ 5FAM}$$

For example: Initial Cleavage Rate for 1000nM TFB with 2000nM CatB is 176.28 RFU/min.

$$Conversion = 176.28\ \frac{RFU}{min} \cdot \frac{1000nM\ 5FAM}{1 \times 10^4\ RFU} \cdot \frac{1min}{60\ sec} = 0.2938 \frac{nM\ 5FAM}{sec}$$

By using the same method, each initial cleavage rate (V) was calculated and plotted in Figure 8(b).

$$Slope = \frac{V}{[E]_t} \cong 1.377 \times 10^{-4} \frac{nM\ 5FAM}{nM\ CatB \cdot sec}$$

From Michaelis-Menton equation,

$$V \cong \frac{k_{cat}}{K_M}[E]_t[S]$$

$$\frac{V}{[E]_t} \cong \frac{k_{cat}}{K_M}[S]$$

$$\frac{k_{cat}}{K_M} \cong \frac{V}{[E]_t}\frac{1}{[S]}$$

$$Substitute: \ \frac{V}{[E]_t} = 1.377 \times 10^{-4}\frac{nM\ 5FAM}{nM\ CatB \cdot sec}$$

$$\frac{k_{cat}}{K_M} \cong 1.377 \times 10^{-4}\frac{nM\ 5FAM}{nM\ CatB \cdot sec} \cdot \frac{1}{1000nM\ 5FAM}$$

$$\frac{k_{cat}}{K_M} \cong \frac{1.377 \times 10^{-7}}{1 \times 10^{-9}}\frac{1}{M\ CatB \cdot sec}$$

$$\frac{k_{cat}}{K_M} \cong 137.7\left(\frac{mol}{L}\right)^{-1} \cdot s^{-1}$$

S9.2 Enzymatic Cleavage Experiments at a Concentration of 50 µM NB Molecule

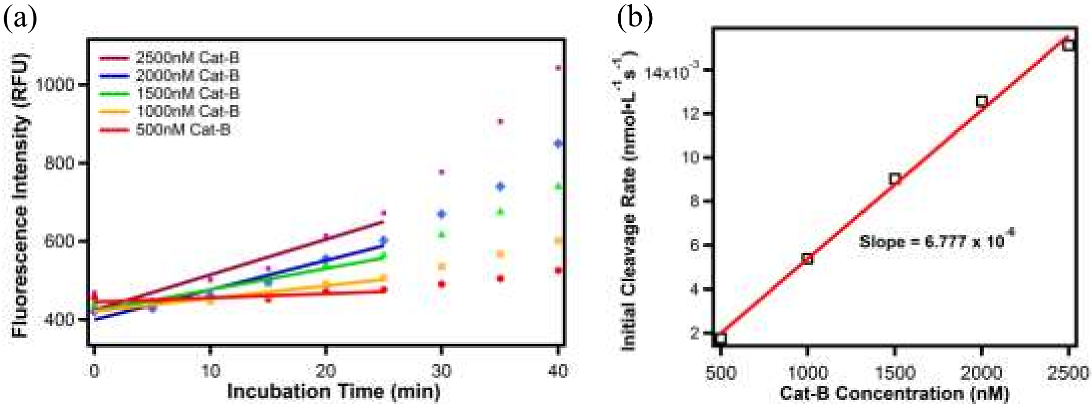

Figure S9. (a) Reaction kinetics for 50 µM TFB with different concentrations of Cathepsin-B enzyme. (b) Plot of initial cleavage rate over Cathepsin-B concentration after unit conversion from RFU to nmol·L^{-1} s^{-1}.

This series of experiments were carried out with 50,000 nM TFB and various concentrations of Cathepsin-B enzyme. Due to the high concentration of TFB, enzymatic reaction would take much longer time to reach completion. Therefore, the unit conversion in this experiment was assumed to be the same as the previous experiment, and the k_{cat}/K_m was calculated as below.

$$Conversion\ unit = \frac{5 \times 10^5\ RFU}{50{,}000nM\ 5FAM}$$

For example: Initial Cleavage Rate for 50,000nM TFB with 2500nM CatB is 9.06 RFU/min.

$$Conversion = 9.06\frac{RFU}{min} \cdot \frac{50{,}000nM\ 5FAM}{5 \times 10^5\ RFU} \cdot \frac{1min}{60\ sec} = 0.0151\frac{nM\ 5FAM}{sec}$$

By using the same method, each initial cleavage rate (V) was calculated and plotted in Figure 9(b).

$$Slope = \frac{V}{[E]_t} \cong 6.777 \times 10^{-6}\frac{nM\ 5FAM}{nM\ CatB \cdot sec}$$

$$Substitute: \ \frac{V}{[E]_t} = 6.777 \times 10^{-6}\frac{nM\ 5FAM}{nM\ CatB \cdot sec}$$

$$\frac{k_{cat}}{K_M} \cong 6.777 \times 10^{-6}\frac{nM\ 5FAM}{nM\ CatB \cdot sec} \cdot \frac{1}{50{,}000nM\ 5FAM}$$

$$\frac{k_{cat}}{K_M} \cong \frac{1.355 \times 10^{-10}}{1 \times 10^{-9}}\frac{1}{M\ CatB \cdot sec}$$

$$\frac{k_{cat}}{K_M} \cong 0.1355\left(\frac{mol}{L}\right)^{-1} \cdot s^{-1}$$

S10 Effect of Varying TFB Concentrations

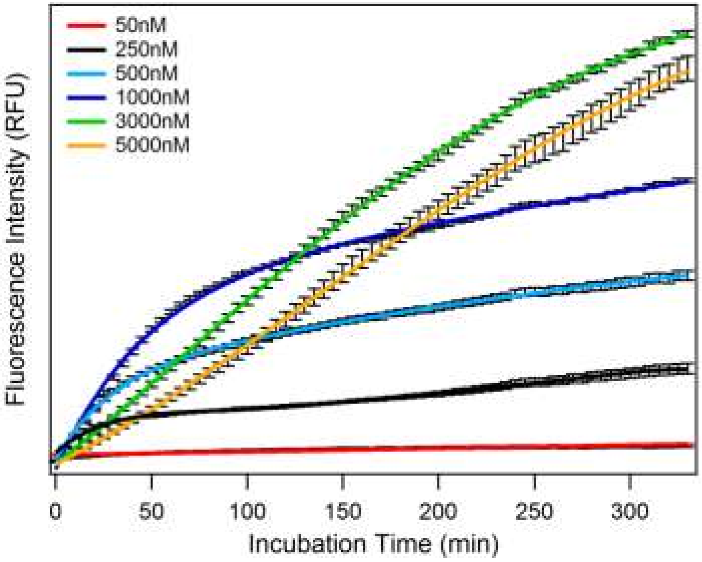

Figure S10. Reaction kinetics of Cathepsin-B (1000nM) incubated with various concentrations of TFB (50nM to 5000nM).

Cathepsin-B enzymatic degradation kinetics was performed with different TFB concentrations, 50nM to 5000nM and enzyme concentration was fixed to 1000nM. At lower concentration The cleavage rate increases as TFB concentrations increases from 50nM to 1000nM, however, a decreasing trend of reaction rate was observed for higher TFB concentration, 3000nM and 5000nM. We speculated that the formation of dimers, trimers or other non-micellar molecular clusters at these concentrations (3000nM and 5000nM) could have partially inhibited enzyme degradation which resulted in a decreasing trend of reaction rate.

S11. Cell Culture and *In-vitro* Studies

S11.1 Cell culture

Human breast adenocarcinoma cell line, MCF-7 was kindly provided by Wirtz Lab at Johns Hopkins University, and was grown in Dulbecco's Modified Eagle Medium (DMEM, Invitrogen) containing 10% of Fetal Bovine Serum (FBS, Invitrogen) and 1% of penicillin and streptomycin (Invitrogen). This breast cancer cells were incubated at 37^{o}C in a humidified incubator with a 5% CO_2 atmosphere in all the experiments.

S11.2 Flow Cytometry

The time-dependent fluorescence increase on MCF-7 was quantified using flow cytometer (FACSCalibur, BD). In brief, MCF-7 cells were seeded onto a 24-well plate at density of 1×10^5 cells/well, and allowed to attach overnight. The medium was replaced with fresh complete medium containing 5 μM TFB and incubated for 0.5, 1, 1.5, 2, and 2.5 hours. Then, the cells were washed 1 time with DPBS, and further treated with Trypsin to harvest cells from each well. Finally, MCF-7 cells were washed 3 times with ice-cold DPBS, and immediately analyzed using flow cytometer at FL1 channel. The viable cells were gated according to forward scatter (FSC) vs. side scatter (SSC) profile, and the data was analyzed using Cell Quest Pro software.

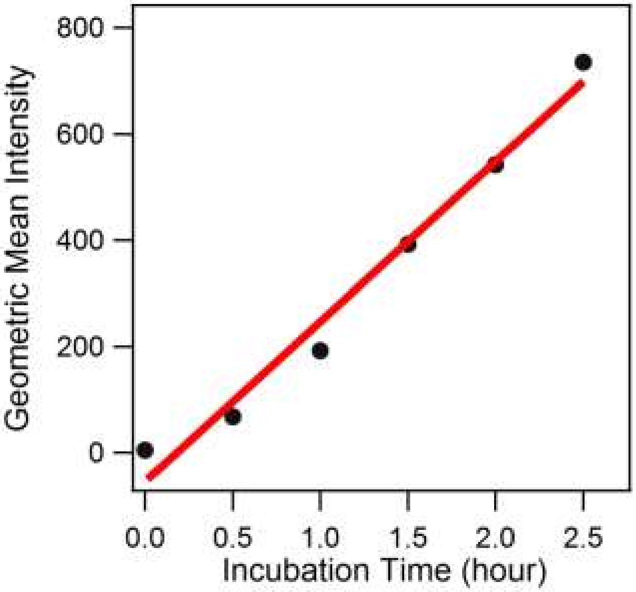

Figure S11. A plot of Geometric Mean Intensity versus incubation time shows a linear correlation.

S11.3 Confocal Imaging

The time-dependent fluorescence increase in MCF-7 cells was imaged using a confocal laser scanning microscope (CLSM, LSM 510, Zeiss) leaving the pinhole wide open. Briefly, MCF-7 cells were seeded onto a collagen (Invitrogen) coated 8-chamber glass bottom plate (Lab-Tek) at a density of 3 × 10^4 cells/well, and allowed to attach overnight. The medium was replaced with fresh complete medium containing 5 μM TFB. After 0.5 and 1.5 hours incubation, the cells were washed 3 times with DPBS, and fixed with 100 μL of 4% paraformaldehyde for 10 min at 4 °C. Then, the paraformaldehyde was removed and the cells were washed 3 times with DPBS. In the colocalization experiment, the cells were seeded and treated in the same manner except 100 nM Lysotracker Red (Invitrogen) and 5 μg/mL Hoechst 33342 (Invitrogen) were added to stain the lysosome and nucleus, respectively. These two dyes were added 20 min before cell fixation. Finally, 100 μL of Fluomount-G (Southernbiotech) was added, and the samples were imaged immediately using CLSM (pinhole sizes were set to obtain optical slice at 0.9 μm). The excitation lasers and filter used are listed in Table S2.

Table S2. Fluorescence parameters used in confocal imaging setting.

Fluorophore	Excitation Wavelength	Emission Filter	Color Observed
Hoechst 33342	405nm	420nm-480nm	Blue
5-FAM	488nm	505nm-550nm	Green
Lysotracker Red	543nm	561nm-754nm	Red

S11.4 Cathepsin-B inhibition by CA-074 Methyl ester (CA-074 Me)

In order to verify that Cathepsin-B is responsible to the cleavage of –GFLG- linker in MCF-7 cells, we carried out a series of experiments with and without the addition of CA-074 Me[330] , a highly selective, irreversible and membrane-permeable Cathepsin-B inhibitor that was purchased from Sigma-Aldrich (Saint Louis, MO). MCF-7 cells were seeded onto a 24-well plate at density of 1 × 10^5 cells/well, and allowed to attach overnight. Before adding TFB molecule, the cells were pre-incubated with different concentrations (0μM - 50 μM) of CA-074 Me for 1 hour[331] in 500μL of DMEM medium. 2.08μL of 1.2mM TFB stock solution was added into cell medium to yield a final TFB concentration of 5μM. After incubated for 1.5 hours, the cells were treated according to protocol in S10.3 for flow-cytometry evaluation. In fluorescence imaging study, MCF-7 cells were washed once with HBSS solution and were imaged using JENCO BC-366 Inverted Epifluorescent Microscope in 20x magnification. Both fluorescence imaging (Fig. S12) and flow-cytometry (Fig. S13) showed significant decrease in 5-FAM fluorescence intensity when CA-074 Me was added to inhibit the activity of Cathepsin-B in cells, which suggested that the main enzyme that corresponded to the cleavage of –GFLG- linker in TFB is Cathepsin-B.

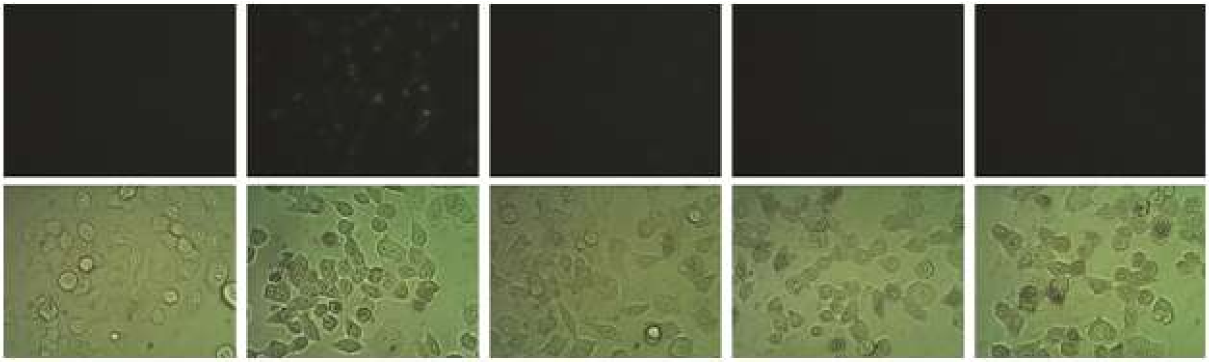
(a) MCF-7 Control (b) 0μM CA-074 Me (c) 10μM CA-074 Me (d) 20μM CA-074 Me (e) 50μM CA-074 Me

Figure S12. Fluorescence and transmit light images of (a) MCF-7 control that was not treated with any TFB and CA-074 Me molecule. (b)–(e) MCF-7 cells incubated with 5μM TFB and different concentrations (0μM, 10μM. 20μM and 50μM) of CA-074 Me (Cathepsin-B inhibitor).

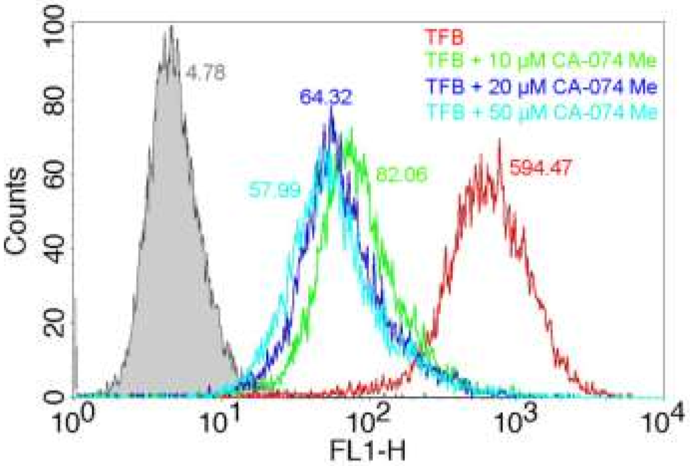

Figure S13. Flow-cytometry of MCF-7 cells treated with 5μM of TFB for 1.5 hours showed significant decreased in 5-FAM fluorescence intensity when CA-074 Me (CatB inhibitor) was added into medium.

S11.5 Effect of CA-074 Me on Cellular Uptake and Cytotoxicity

In order to justify that CA-074 Me was solely inhibiting CatB activity instead of interrupting cellular uptake pathway. We have synthesized a new molecule C_{16}TF where C_{16} hydrophobic alkyl chain was used to replace BHQ-1 segment in TFB molecule. We use $C_{16}TF$ where its fluorescence is independent of CatB activity to study the effect of CA-074 Me (CatB inhibitor) on cellular uptake. From the flow-cytometry data (Fig. S14), we observed similar fluorescence intensity after incubating MCF-7 with 5μM of $C_{16}TF$ in the presence or absence of CA-074 Me. This data further support our previous observation (Fig. S13) where CA-074 Me inhibited the activity of CatB in MCF-7 cells, resulting in lower fluorescence intensity even after internalization of TFB molecules.

Cytotoxicity of CA-074 Me was evaluated (Fig. S15) by incubating MCF-7 cells with different CA-074 Me concentrations (5μM to 50μM) for 4 hours and similar protocol in S10.2 was applied. Fig. S15 showed that MCF-7 remained its high viability after treated with CA-074 Me which validated the non-toxicity of the CatB inhibitor.

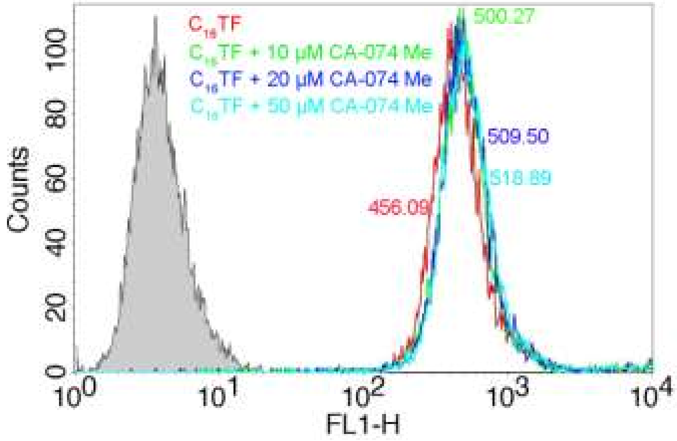

Figure S14. Flow-cytometry of MCF-7 cells treated with 5μM of $C_{16}TF$ for 1.5 hours showed that CA-074 Me (CatB inhibitor) is not affecting cellular uptake as MCF-7 cells fluoresced at the same magnitude with or without CA-074 Me incubation.

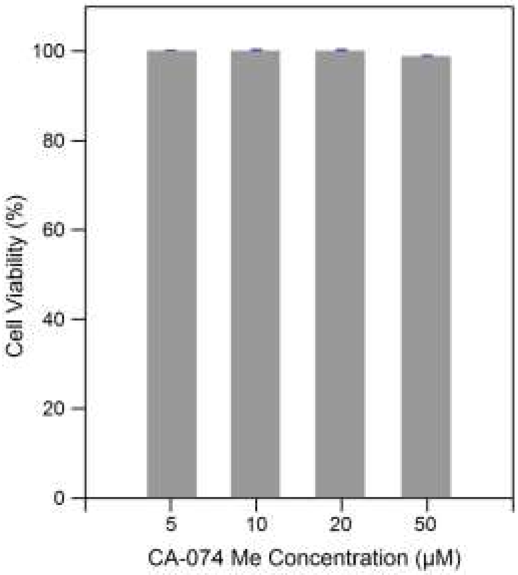

Figure S15. MCF-7 cells were incubated with various concentrations of CA-074 Me (CatB inhibitor) to monitor its toxicity to cells. SRB assay results showed almost 100% of cells remained viable after treated with 5μM, 10μM, 20μM, and 50μM of CA-074 Me for 4 hours.

S11.6 Cytotoxicity

The cytotoxicity of the TFB was evaluated on MCF-7 cells to make sure that the cells were healthy in the following experiments. Briefly, MCF-7 cells were seeded onto a 96-well plate at a density of 5×10^3 cells/well, and allowed to attach overnight. The medium was replaced with fresh complete medium (as described in cell culture protocol) containing 0, 1, 5, or 10 μM TFB and incubated for 4 hours. Then, the medium was changed to fresh complete medium and incubated for another 48 hours, and the cell viability was evaluated using Sulforhodamine B (SRB) based method according to the manufacturer's protocol (TOX-6, Sigma).

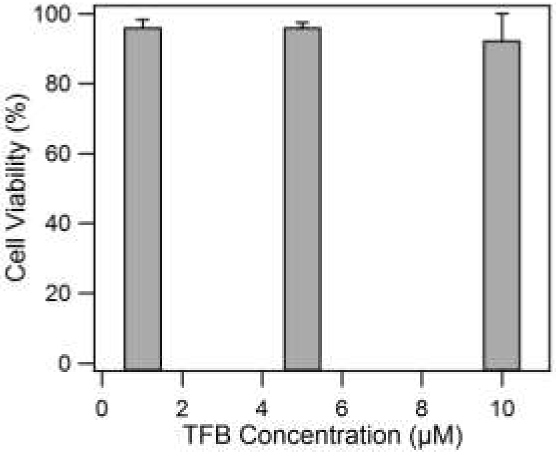

Figure S16. Cell viability test reveals that TFB NB at a concentration of 10 μM shows little toxicity to cells.

Supporting Information for Chapter 3

Shape- and Charge-Dependent Cellular Internalization of Self-Assembling Supramolecular Nanobeacons by Cancer Cells

S1 Synthesis and Characterization of Peptide Molecules

S1.1 Materials

All Fmoc amino acids were purchased from Advanced Automated Peptide Protein Technologies (AAPPTEC, Louisville, KY) and Rink Amide MBHA resin was purchased from Novabiochem (San Diego, CA). 5-Carboxyfluorescein (5-FAM) was purchased from AnaSpec, Inc. (Fremont, CA) and Black Hole Quencher1 carboxylic acid (BHQ-1-CO_2H) was purchased from Biosearch Technologies, Inc. (Novata, CA). Cathepsin-B (bovine spleen) was purchased from EMD Chemicals (San Diego, CA).

S1.2 Synthesis

Standard 9-fluorenylmethoxycarbonyl (Fmoc) solid phase peptide synthesis was used to synthesize the Sup35 sequence and the enzyme degradable linker on a 0.25 mmole scale. This procedure was carried out using the Focus XC automated peptide synthesizer (AAPPTEC, Louisville, KY). For both SFB-K and SFB-E molecules, 5-carboxyfluorescein (5-FAM) was manually coupled at the peptide N-terminus (after Fmoc removal) with 5-FAM/HBTU/DIEA at a ratio of 4:4:6 relative to the peptide, shaking overnight at room temperature. Subsequently, Black Hole Quencher-1 (BHQ-1) was coupled to the Lys ε-amine (after Mtt removal) with BHQ-1/HBTU/DIEA at a ratio of 1:0.96:1.7 relative to the peptide, shaking overnight at room temperature. Fmoc deprotections were performed using a 20% 4-methylpiperidine in DMF solution for 10 minutes, repeating once. Mtt deprotections were carried out using a mixture of TFA/TIS/DCM with a ratio of 3:5:92 for 5 minutes, and the procedure was repeated twice.

SFB-K: Fmoc-GFLGK(Mtt)GNNQQNYKKK-Rink

SFB-E: Fmoc-GFLGK(Mtt)GNNQQNYEEE-Wang

In all cases, reactions were monitored by the ninhydrin test (Anaspec Inc., Fremont, CA) for free amines. Completed peptides were cleaved from the solid support using a mixture of TFA/TIS/H2O in a ratio of 95:2.5:2.5 for 3 hours. Excess TFA was removed by rotary evaporation and cold diethyl ether was added to precipitate the crude peptide. Diethyl ether was slowly removed using low vacuum (~700 mbar) and 30 ^{o}C for 20 minutes, followed by high vacuum (~100 mbar) and 40 ^{o}C of rotary evaporation to form a thin film of peptide conjugate on the round bottom flask.

Schemes 1-2 offer details of the synthesis procedures of SFB-K and SFB-E.

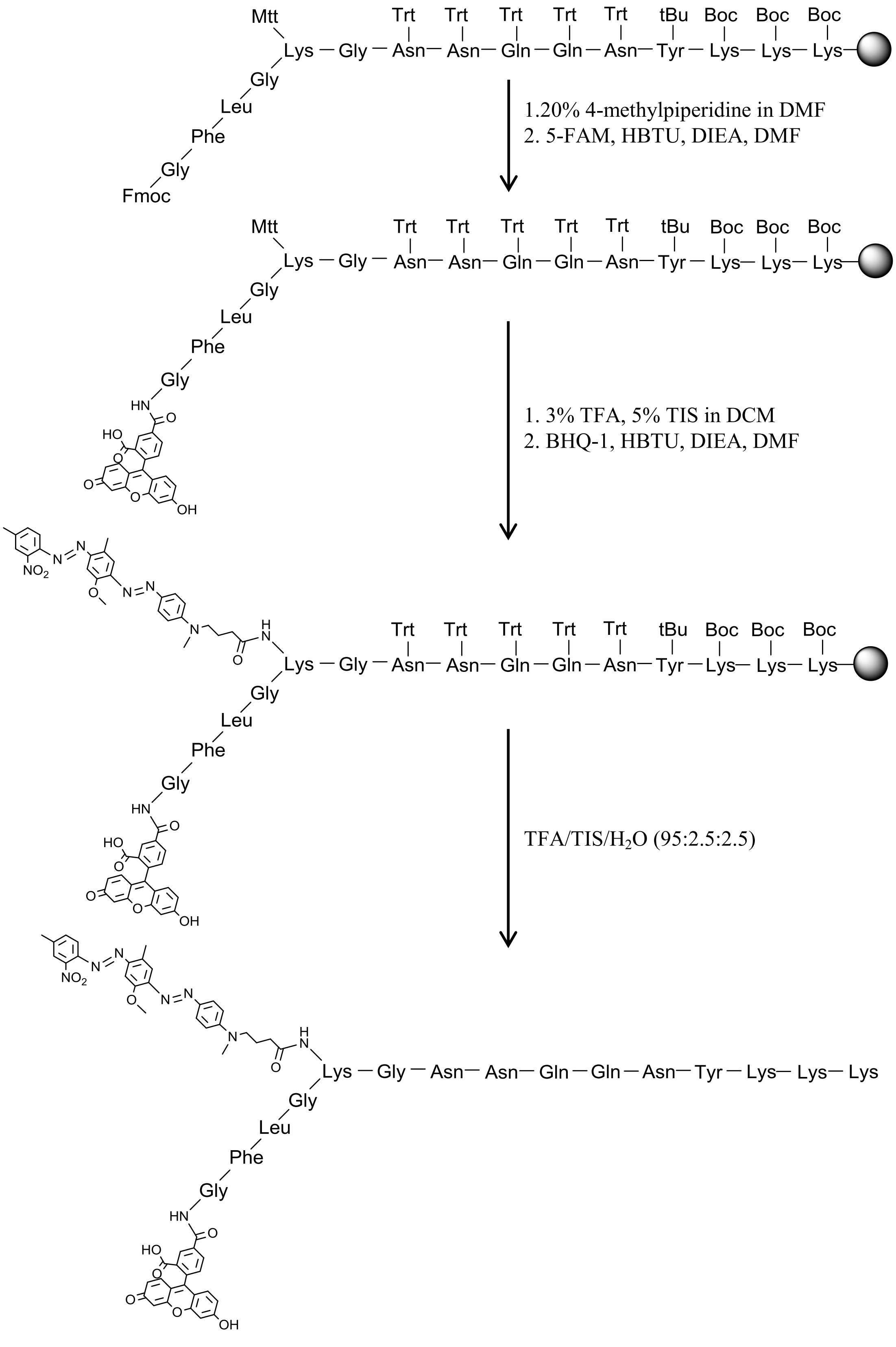

Scheme S4: Synthesis steps of SFB-K

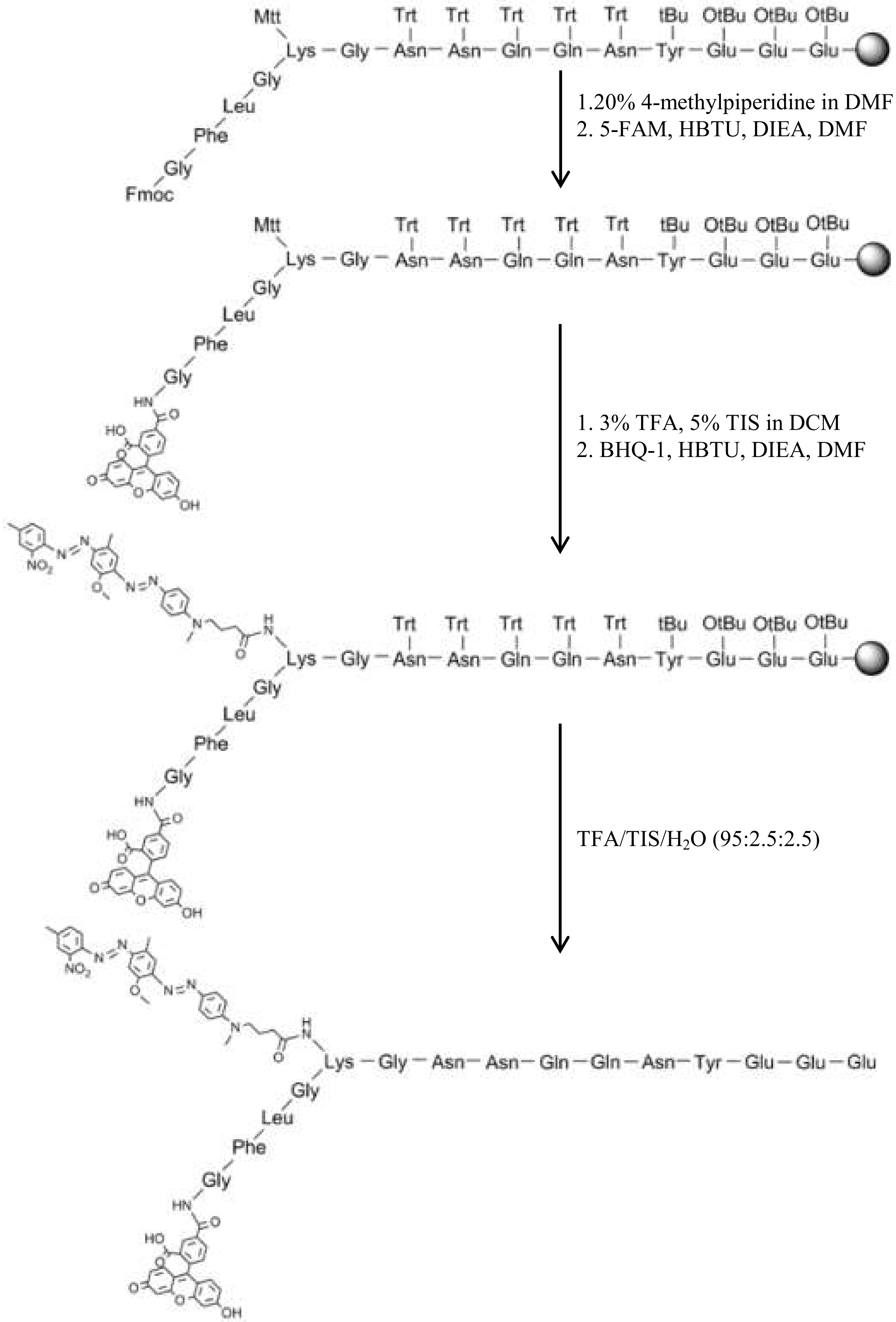

Scheme S5: Synthesis steps of SFB-E

Abbreviations:

HBTU :O-benzotriazole-N,N,N',N'-tetramethyluroniumhexafluorophosphate	
DIEA: diisopropylethylamine	Mtt: 4-methyltrityl
TFA: trifluoroacetic acid	TIS: triisopropylsilane
DCM: dichloromethane	DMF: N,N-dimethylformamide

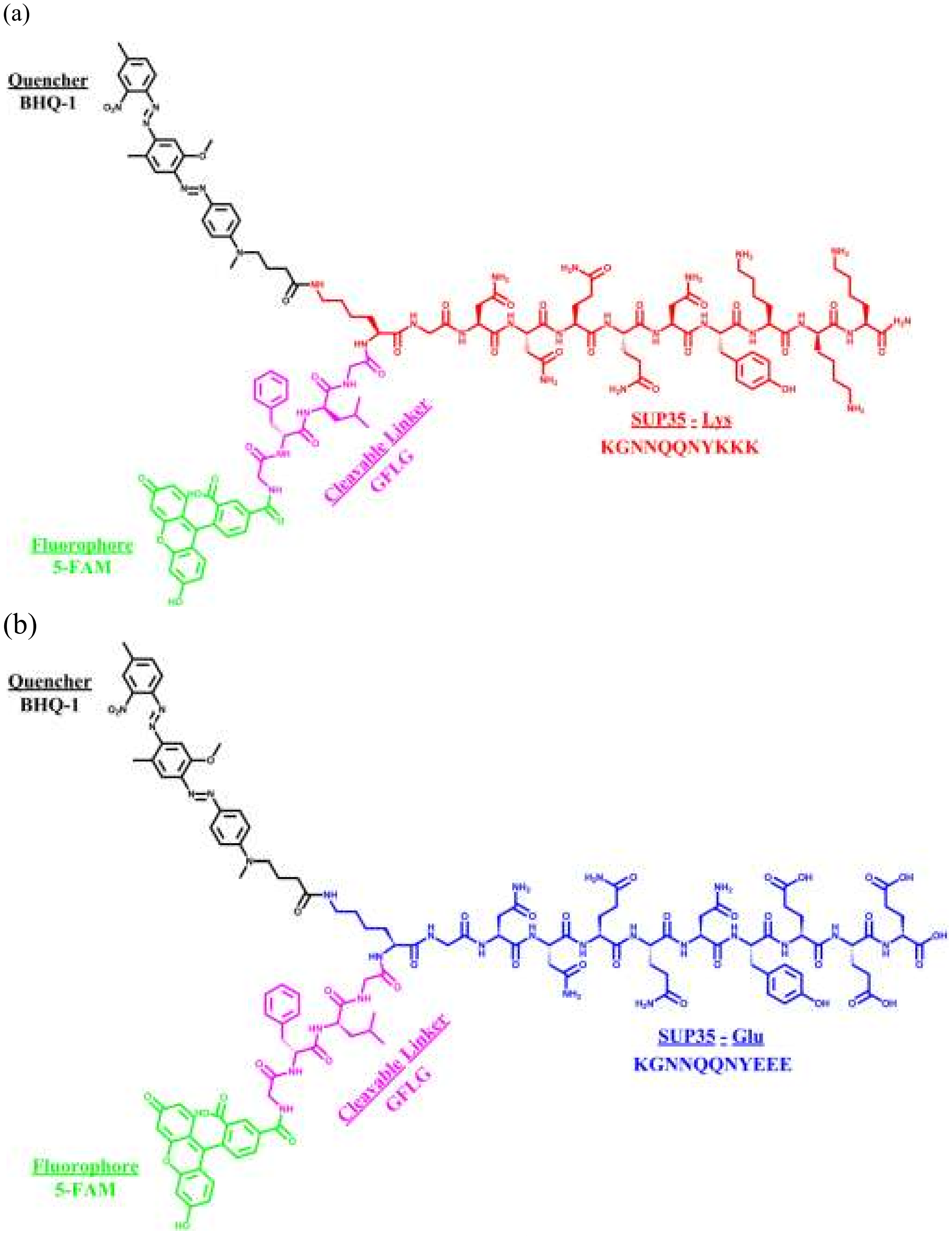

Figure S1 Chemical structure of (a) SFB-K and (b) SFB-E nanobeacons.

S1.3 Purification

The peptides were purified by preparative RP-HPLC using a Varian Polymeric Column (PLRP-S, 100 Å, 10 μm, 150 × 25 mm) at 25 °C on a Varian ProStar Model 325 preparative HPLC (Agilent Technologies, Santa Clara, CA) equipped with a fraction collector. A water/acetonitrile gradient containing 0.1% *v*/*v* TFA or NH_4OH was used as eluent at a flow rate of 25 mL/min for SFB-K and SFB-E, respectively. The absorbance peak was monitored at 534 nm for both SFB-K and SFB-E molecules. The crude materials of SFB-K and SFB-E were dissolved in 20 ml of 0.1% aqueous TFA or NH_4OH, respectively, and each purification run was carried out with a 10 ml injection. Collected fractions were analyzed by ESI-MS (LDQ Deca ion-trap mass spectrometer, Thermo Finnigan, San Jose, CA) and those containing the desired product were lyophilized (FreeZone -105 °C 4.5 L freeze dryer, Labconco, Kansas City, MO) and stored at -30 °C.

S1.4 MALDI-ToF Characterization

High resolution peptide masses were determined by MALDI-ToF mass spectrometry, using a BrukerAutoflex III MALDI-ToF instrument (Billerica, MA). Samples were prepared by depositing 1 μL of sinapinic acid matrix (10 mg/ml in 0.05% TFA in H_2O/MeCN (1:1), Sigma-Aldrich, PA) onto the target spot, and allowed to dry for 5 minutes. 1 μL of peptide aqueous solution, SFB-K in 0.1% TFA and SFB-E in 0.1% NH_4OH were deposited on the corresponding spot and quickly mixed with 1 μL of sinapinic acid matrix solution. Samples were irradiated with a 355 nm UV laser and analyzed in the reflectron mode.

Table S3: Expected and observed masses of the synthesized molecules

MALDI-ToF	Exact Mass	Observed Mass
SFB-K	2566.182	2567.747 $[M+H]^+$
SFB-E	2570.009	2593.878 $[M+Na]^+$

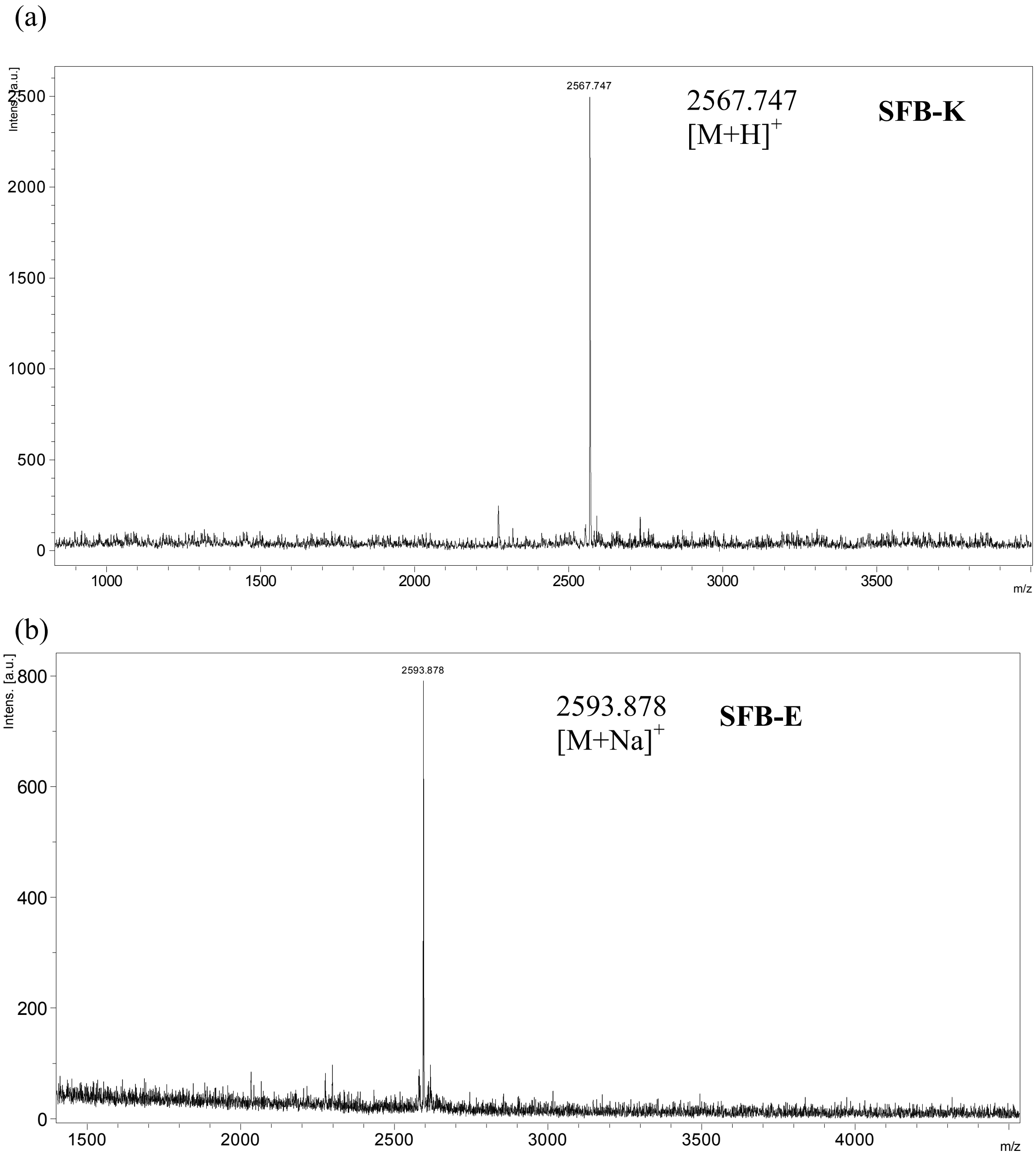

Figure S2. MALDI-ToF spectra of (a) SFB-K and (b) SFB-E molecules.

S1.5 Analytical HPLC Characterization

Analytical reverse-phase HPLC was performed using a Varian polymeric column (PLRP-S, 100 Å, 10 μm, 150 × 4.6 mm) with 20 μL injection volumes. A water/acetonitrile gradient containing 0.1% *v*/*v* NH_4OH at a flow rate of 1 mL/min was used and samples were dissolved at 1 mg/ml concentration in 0.1% aqueous NH_4OH.

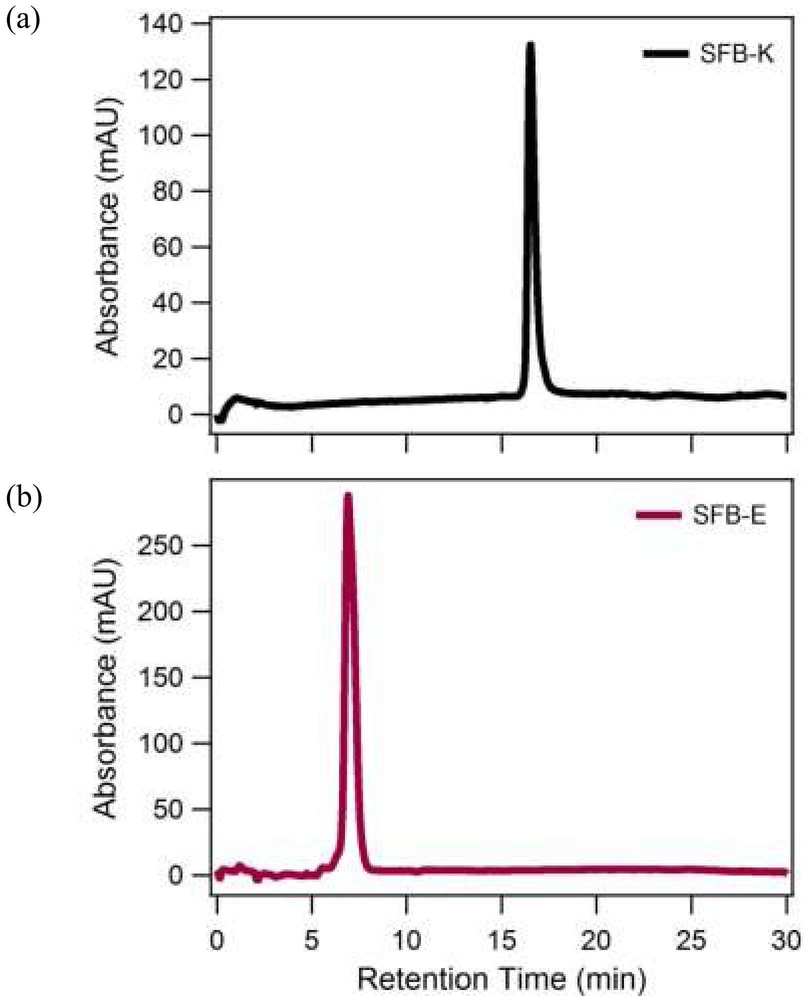

Figure S3. Reverse-Phase HPLC chromatograms of (a) SFB-K and (b) SFB-E molecules.

S2. Controlling Shape of Self-assembled Nanobeacons

S2.1 SFB-KE nanobeacon and sample pre-treatment

Purified and lyophilized SFB-K and SFB-E powders were pre-treated individually in HFIP to disrupt existing hydrogen-bonds and oligomers at concentration of 200 μM. SFB-KE was prepared by mixing SFB-K and SFB-E in HFIP at 1:1 ratio (i.e. SFB-K 200 μM 100 μL + SFB-E 200 μM 100 μL). Samples were aliquoted to glass vials with 200 μL in each vials and HFIP was removed using rotary evaporation method. The water bath temperature was set to 40 ^{o}C and samples were dried for 10 minutes with 190 rpm rotation.

S2.2 Spherical SFB-K, SFB-E and SFB-KE nanobeacons

SFB-K, SFB-E and SFB-KE HFIP pre-treated and rotavap dried samples were reconstituted in 25 mM of HEPES buffer and stored at 4 ^{o}C overnight.

S2.3 Cylindrical SFB-K and SFB-KE nanobeacons

SFB-K and SFB-KE HFIP pre-treated and rotavap dried samples were reconstituted in 25 mM of HEPES buffer and stored at room temperature for more than 3 days.

S2.4 Cylindrical SFB-E nanobeacons

After HFIP treatment, SFB-E formed polydisperse nanostructures such as spherical micelles and cylindrical fibers. To obtain monodisperse cylindrical fibers, purified and lyophilized SFB-E poweder was directly dissolved in 1xDPBS at 200 μM concentration and stored at room temperature for more than 3 days.

S2.5 Cryo-TEM images

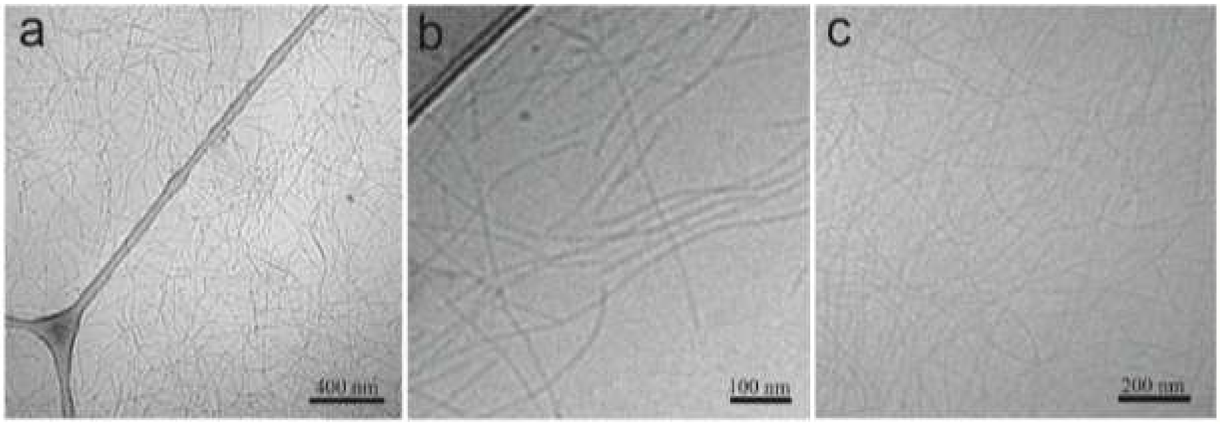

Figure S4. Cryo-TEM images of cylindrical nanobeacons (a) SFB-K, (b) SFB-E and (c) SFB-KE.

S3 Circular Dichroism of Spherical and Cylindrical SFB Nanobeacons

CD spectra were recorded on a JASCO J-710 spectropolarimeter (JASCO, Easton, MD) and all three spherical SFB nanobeacons (Figure S4 a,c,e) were found to adopt a random coil secondary structure while cylindrical SFB nanobeacons assumed β-sheet secondary structure (Figure S4 b,d,f). All samples were prepared as described in section S2 and measurements were conducted at room temperature, using 0.1 mm pathlength detachable cell. All CD spectra were normalized using the equations below, where θ_{mr} is the mean molar ellipticity per residue.

$$\theta_{mr} = \theta_d \cdot \frac{M}{c \cdot l \cdot n_r}$$

$$\theta_{mr} = \left[deg \cdot \frac{g}{dmol} \cdot \frac{cm^3}{dmol} \cdot \frac{1}{cm} \cdot \frac{1}{residue}\right]$$

M : molecular weight (g/dmol)
c : concentration (g/cm^3)
l : path length (cm)
n_r : number of residue

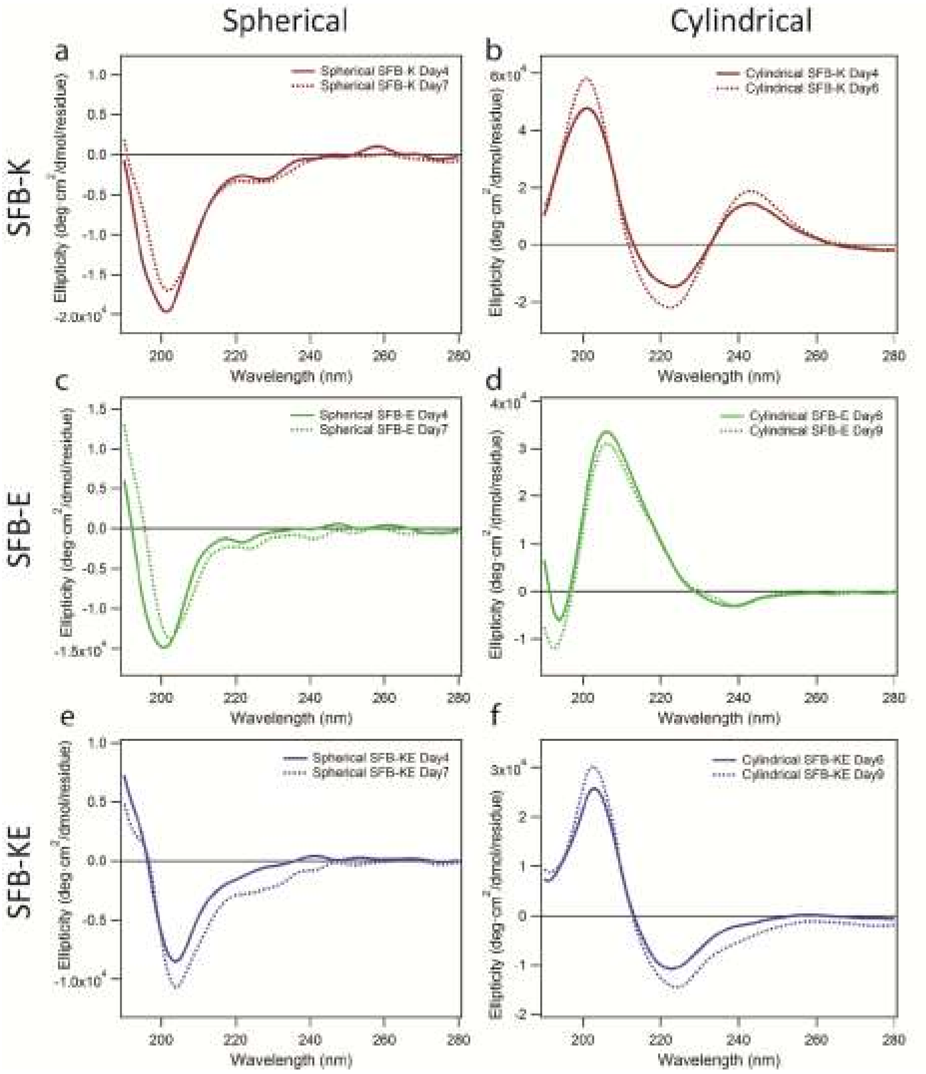

Figure S5. Circular dichroism of 200 μM spherical and cylindrical SFB-K (a,b), SFB-E (c,d) and SFB-KE (e,f), respectively.

S4 Cathepsin-B Enzymatic Activation

CatB enzymatic reaction buffer was prepared in 50 mM sodium acetate buffer with 25 mM L-cystein as enzyme activator and 1 mM EDTA was added as enzyme stabilizer. The pH of reaction buffer was validated to 5, the optimum pH for enzymatic activity. 0.025 Unit of CatB was pre-incubated in reaction buffer for 5 minutes at 37 °C to activate the enzyme and SFB nanobeacons were added to reaction buffer to yield a final concentration of 1 μM and final volume of 100 μL. All samples were triplicated and the experiment was carried out in a 96-well standard opaque plate. 5-FAM molecule was excited at 492 nm and emission was collected at 520 nm with 515 nm cut off. Experiment data was collected using a Gemini XPS microplate reader (Molecular Devices, Sunnyvale, CA) different time points. After 4 hours of cathepsin B incubation, fluorescence intensity increased significantly indicating the activation of SFB nanobeacons (release of 5-FAM) resulting from cathepsin B degradation on –GFLG- linker.

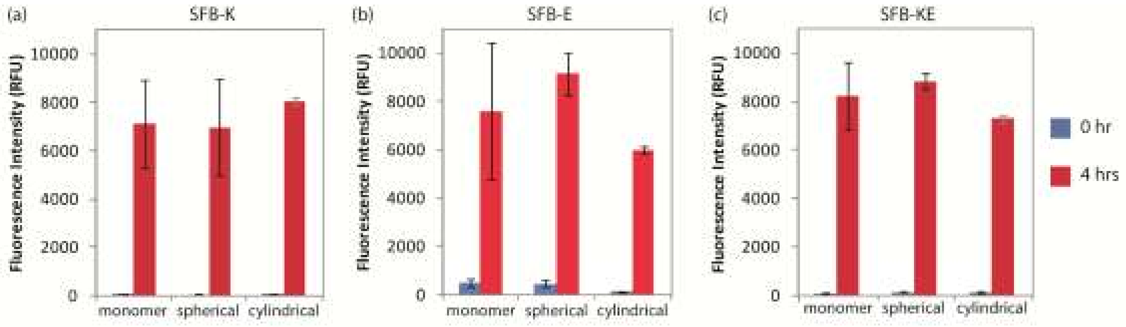

Figure S6. Fluorescence measurement of 1 μM (a) SFB-K, (b) SFB-E and (c) SFB-KE nanobeacons at time 0 hr and 4 hrs after the addition of cathepsin B enzyme (0.025 Unit), showed significant increase in 5-FAM fluorescence intensity, indicating the activation of SFB nanobeacons through cathepsin B degradation.

S5. Stability of nanostructures at 5µM concentration

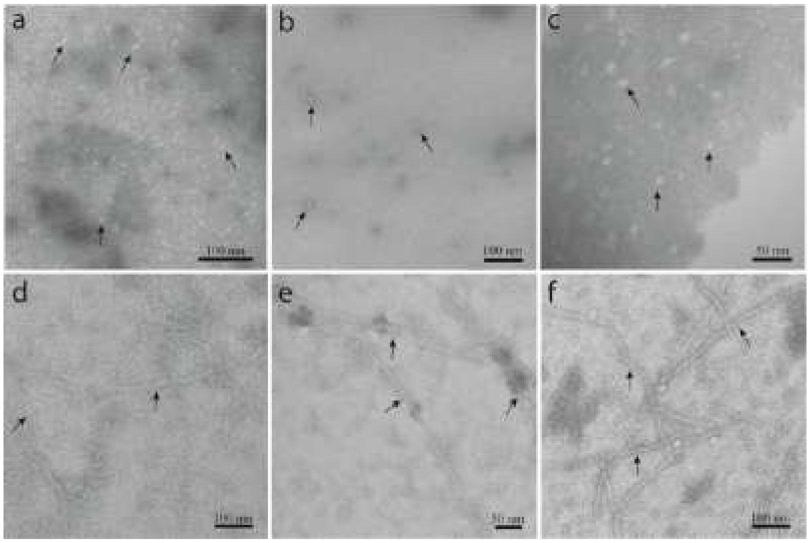

Figure S7. TEM images showed self-assembled nanobeacons (black arrows) maintained its structures at 5 µM concentration and 1 hour incubation in 37 °C. Spherical (a) SFB-K, (b) SFB-E and (c) SFB-KE in 1xDPBS buffer and cylindrical (d) SFB-K, (e) SFB-E and (f) SFB-KE in RPMI 1640 cell medium.

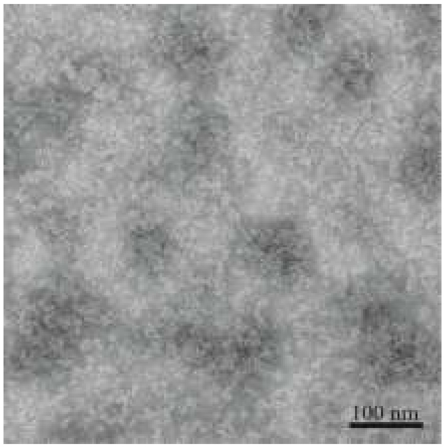

Figure S8. TEM image of RPMI 1640 cell medium (without SFB nanobeacons) showed globular protein structure such as human serum albumin (HSA).

S6 Cytotoxicity Evaluation

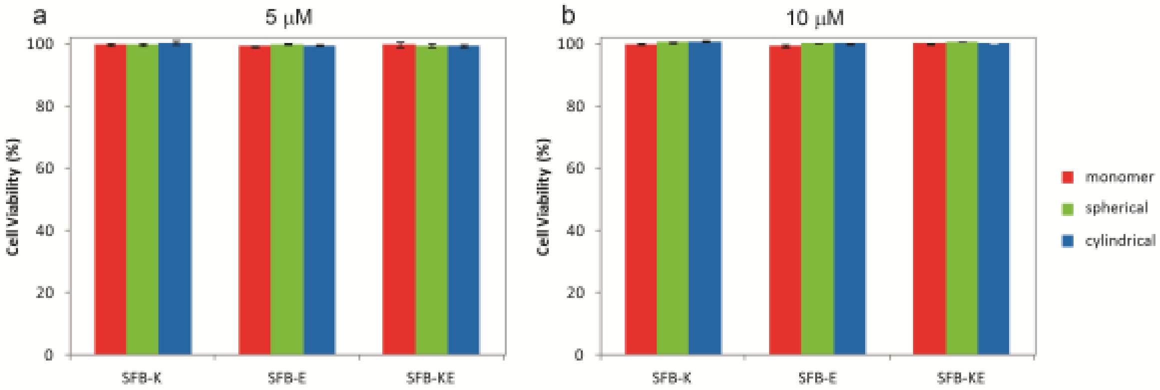

Figure S9. SFB nanobeacons were nontoxic to PC3-Flu cells under experimental condition, 1 hour incubation at 37 °C. Cell viability remained high (>95%) after treated with SFB nanobeacons at (a) 5 μM and (b) 10 μM.

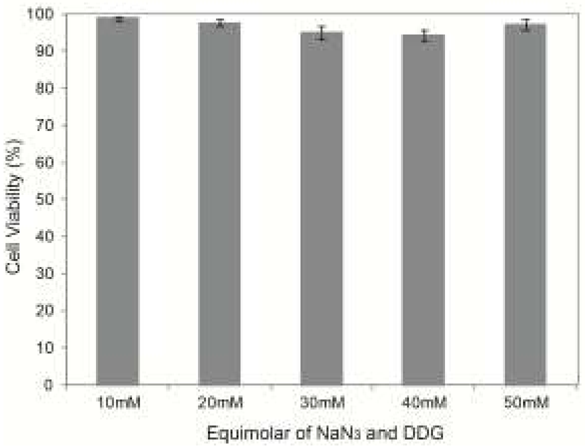

Figure S10. Equimolar of sodium azide (NaN_3) and 2-deoxy-*D*-glucose (DDG), energy-dependent endocytotic inhibitors are nontoxic to PC3-Flu cells under experimental condition. Cell viability remained high after treated with equimolar of NaN_3/DDG 10 mM (experimental concentration) and higher concentrations.

Supporting Information for Chapter 4

Enzyme-Specific Doxorubicin Drug Beacon as Drug-Resistant Theranostic Molecular Probes

S1. Synthesis, Purification and Characterization of R8DB Drug beacon

S1.1 Materials

All Fmoc amino acids were purchased from Advanced Automated Peptide Protein Technologies (AAPPTEC, Louisville, KY) and Rink Amide MBHA resin was purchased from Novabiochem (San Diego, CA). Doxorubicin·HCl was purchased from AvaChem Scientific. (San Antonio, TX) and Black Hole Quencher2 carboxylic acid (BHQ-2-CO_2H) was purchased from Biosearch Technologies, Inc. (Novata, CA). Cathepsin-B (bovine spleen) was purchased from EMD Chemicals (San Diego, CA).

S1.2 Synthesis of BHQ2-R8 and Dox-GLFG

Standard 9-fluorenylmethoxycarbonyl (Fmoc) solid phase peptide synthesis was used to synthesize the octa-arginine sequence (Fmoc-K(Mtt)RRRRRRRR-Rink) and the enzyme degradable linker (Fmoc-GFLG-Wang) on a 0.25 mmole scale. These procedures were carried out using the Focus XC automated peptide synthesizer (AAPPTEC, Louisville, KY). Doxorubicin (Dox) was manually coupled at the peptide C-terminus (after peptide cleavage from Wang resins) of Fmoc-GFLG-CO_2H and followed by Fmoc deprotection, yielding NH_2-GFLG-Dox prodrug. After Mtt removal from octa-arginine sequence (Fmoc-K(Mtt)RRRRRRRR-Rink), BHQ-2 was manually coupled to the Lys ε-amine BHQ-2/HBTU/DIEA at a ratio of 1:0.96:1.7 relative to the peptide, shaking overnight at room temperature. Subsequently, Fmoc was removed and synthesized NH_2-K(BHQ-2)RRRRRRRR was cleaved from Rink resins. To convert the N-terminus free amine into carboxylic acid form, 10 fold succinic anhydride was reacted with peptide in 5xPBS solution, shaked overnight at room temperature. In general, all Fmoc deprotections were performed using a 20% 4-methylpiperidine in DMF solution for 10 minutes, repeating once. Mtt deprotections were carried out using a mixture of TFA/TIS/DCM with a ratio of 3:5:92 for 5 minutes, and the procedure was repeated twice. In all cases, reactions were monitored by the ninhydrin test (Anaspec Inc., Fremont, CA) for free amines. All peptides were cleaved from the solid support using a mixture of TFA/TIS/H2O in a ratio of 95:2.5:2.5 for 3 hours. Excess TFA was removed by rotary evaporation and cold diethyl ether was added to precipitate the crude peptide. The precipitated crude peptide and diethyl ether were phase-separated using centrifugation technique (6000 rpm for 1 minute) and diethyl ether solution was discarded. To remove as much TFA as possible, the washing step was carried out by adding 20 mL of diethyl ether was added to crude peptide, shaked well and centrifuged. This procedure was repeated 3 times. All centrifuge tubes were tightly sealed with parafilm to minimize evaporation of diethyl ether during high-speed centrifugation.

S1.3 Synthesis of R8DB

BHQ2-R8 was first dissolved in 500μL of anhydrous DMF (6.8 μmole, 13.6mM). Dox-GLFG was also dissolved in 500μL of anhydrous DMF (8.0 μmole, 16mM). Both BHQ2-R8 and Dox-GLFG solutions were added to a 10 mL round bottom flask and DIEA (26.0 μmole, 4.14 μL) was added in afterward. The mixture was stirred for 10 minutes using a magnetic stirrer bar. 5.0 mg of PyAOP coupling reagent (9.6 µmole) was added into the solution and left to react for 2 days at room temperature, protected from light. Synthesized product was purified using RP-HPLC and characterized by ESI-MS and analytical HPLC. The R8DB expected mass is 2881.486 g/mol. Product yield = 1.4 mg, 0.49 µmole, 7%.

Schemes S1-3 offer details of the synthesis procedures of BHQ2-R8, Dox-GLFG and R8DB drug beacon.

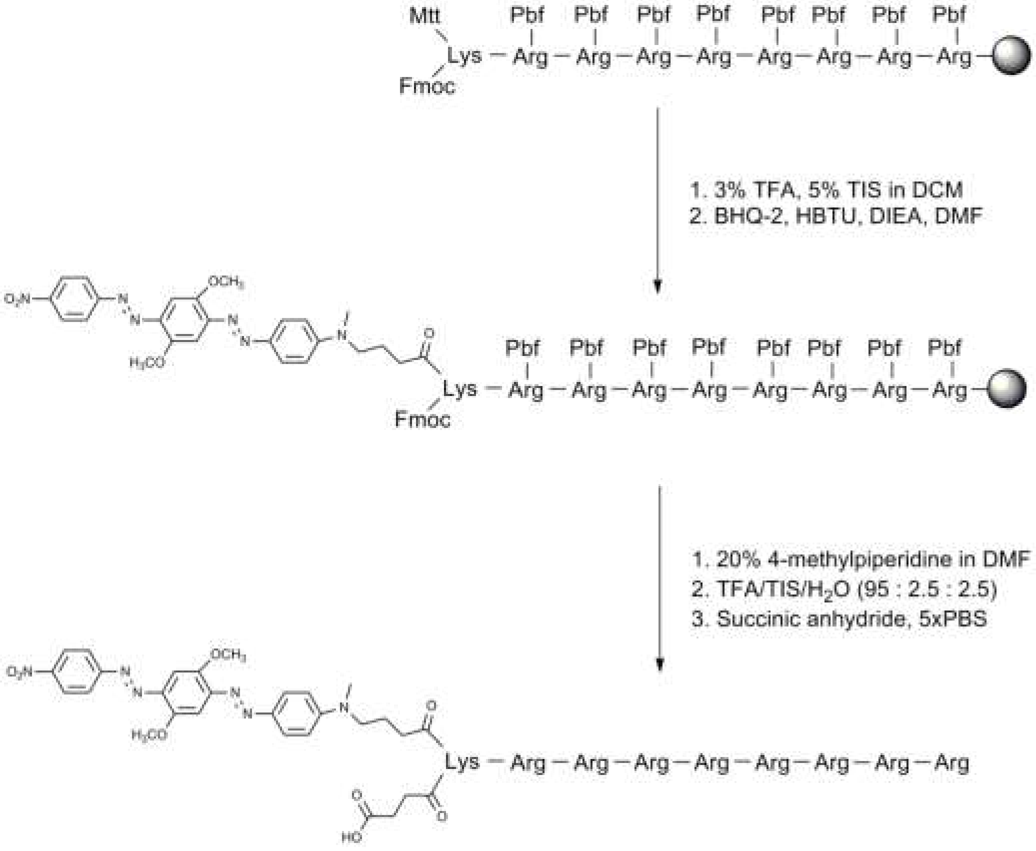

Scheme S1: Synthesis of BHQ2-R8 peptide.

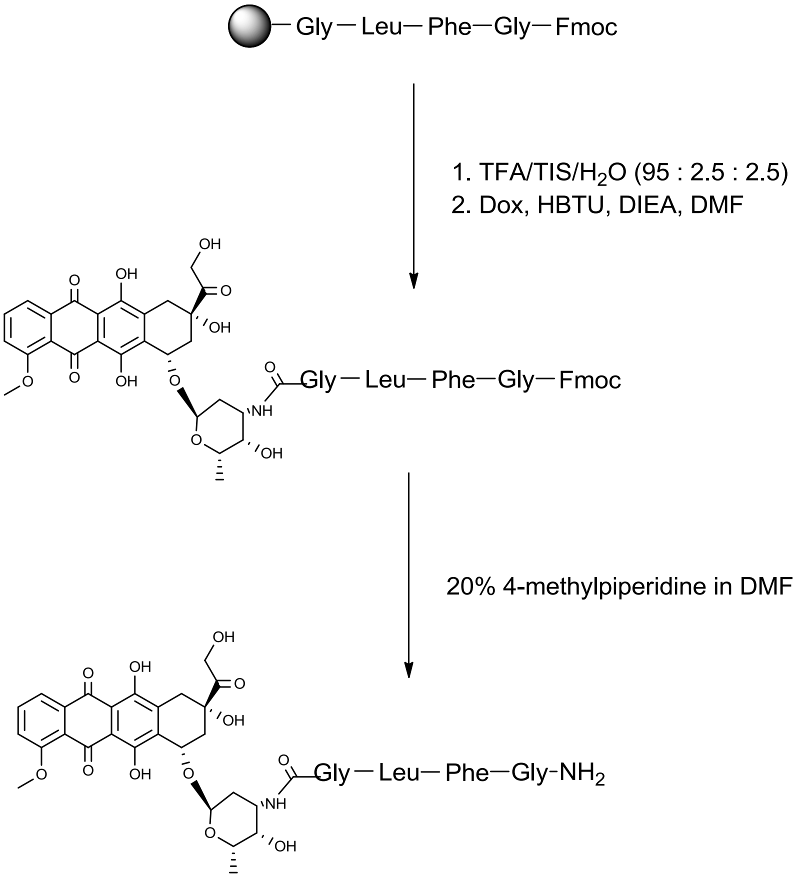

Scheme S2: Synthesis of Dox-GLFG peptide.

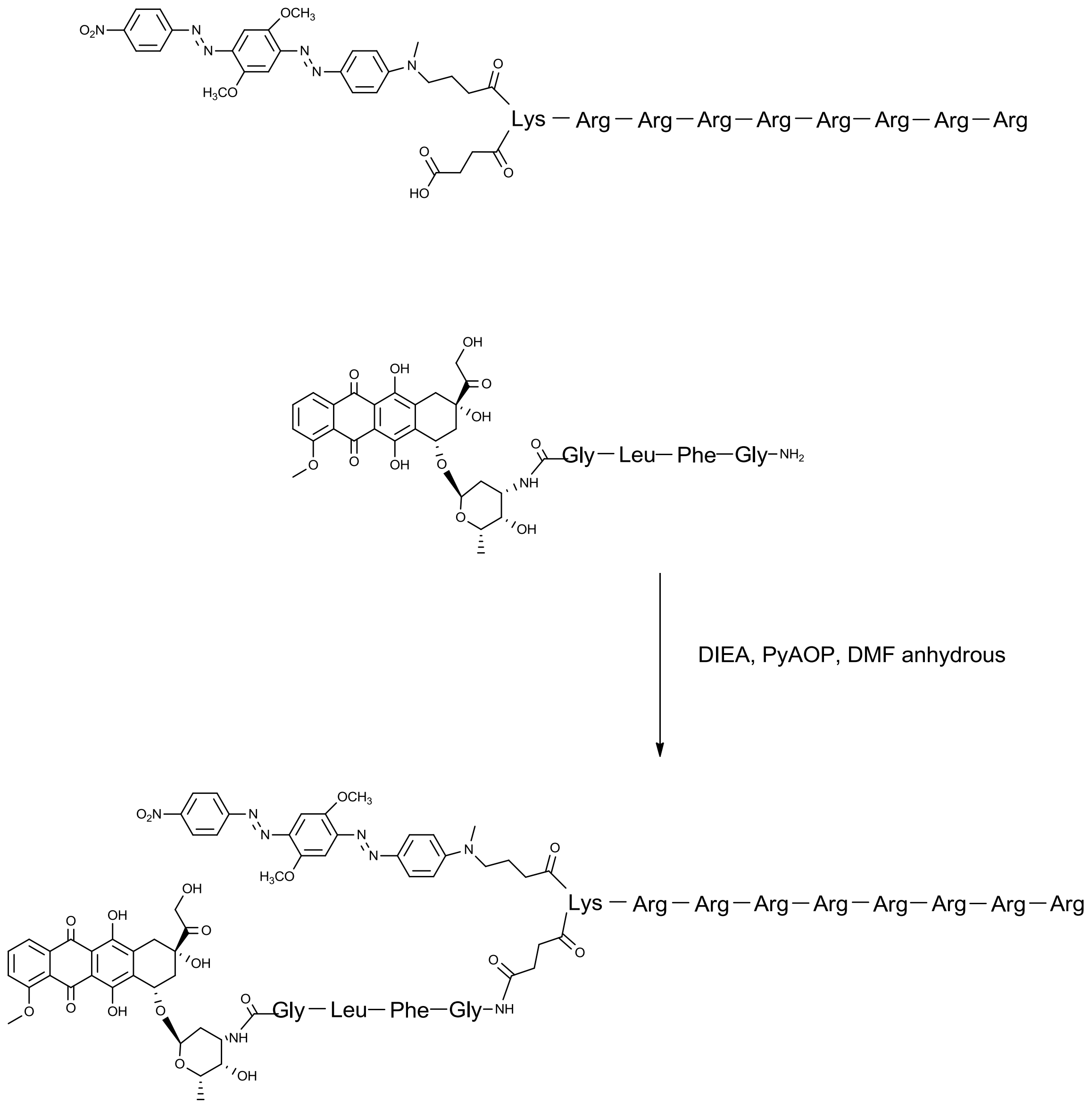

Scheme S3: Synthesis of R8DB drug beacon by reacting BHQ2-R8 and Dox-GLFG molecules.

S1.4 Purification

The peptides and the drug beacon were purified using preparative RP-HPLC with a Varian Polymeric Column (PLRP-S, 100 Å, 10 µm, 150 × 25 mm) at 25 ^{o}C on a Varian ProStar Model 325 preparative HPLC (Agilent Technologies, Santa Clara, CA) equipped with a fraction collector. A water/acetonitrile gradient 30%-70% was ran for 90 minutes containing 0.1% *v*/*v* TFA was used as eluent at a flow rate of 20 mL/min for R8DB drug-beacon. The absorbance peak was monitored at 580 nm for R8DB drug-beacon. The crude materials of R8DB was dissolved in 20 ml of 0.1% aqueous TFA and purification run was carried out with a 10 ml injection. Collected fractions were analyzed by ESI-MS (LDQ Deca ion-trap mass spectrometer, Thermo Finnigan, San Jose, CA) and those containing the desired product were lyophilized (FreeZone -105 °C 4.5 L freeze dryer, Labconco, Kansas City, MO) and stored at -30 ^{o}C.

S1.5 Electrospray Ionization-Mass Spectra (ESI-MS)

ESI mass spectra were acquired using a Finnigan LCQ Deca ion-trap mass spectrometer equipped with an electrospray ionization source (Thermo Finnigan, San Jose, CA). Samples were dissolved in water with 5% of acetonitrle containing 0.1% *v*/*v* TFA and introduced into the instrument at a rate of 10uL/min using a syringe pump via a silica capillary line. The heated capillary temperature was 250 degC and the spray voltage was 5kV.

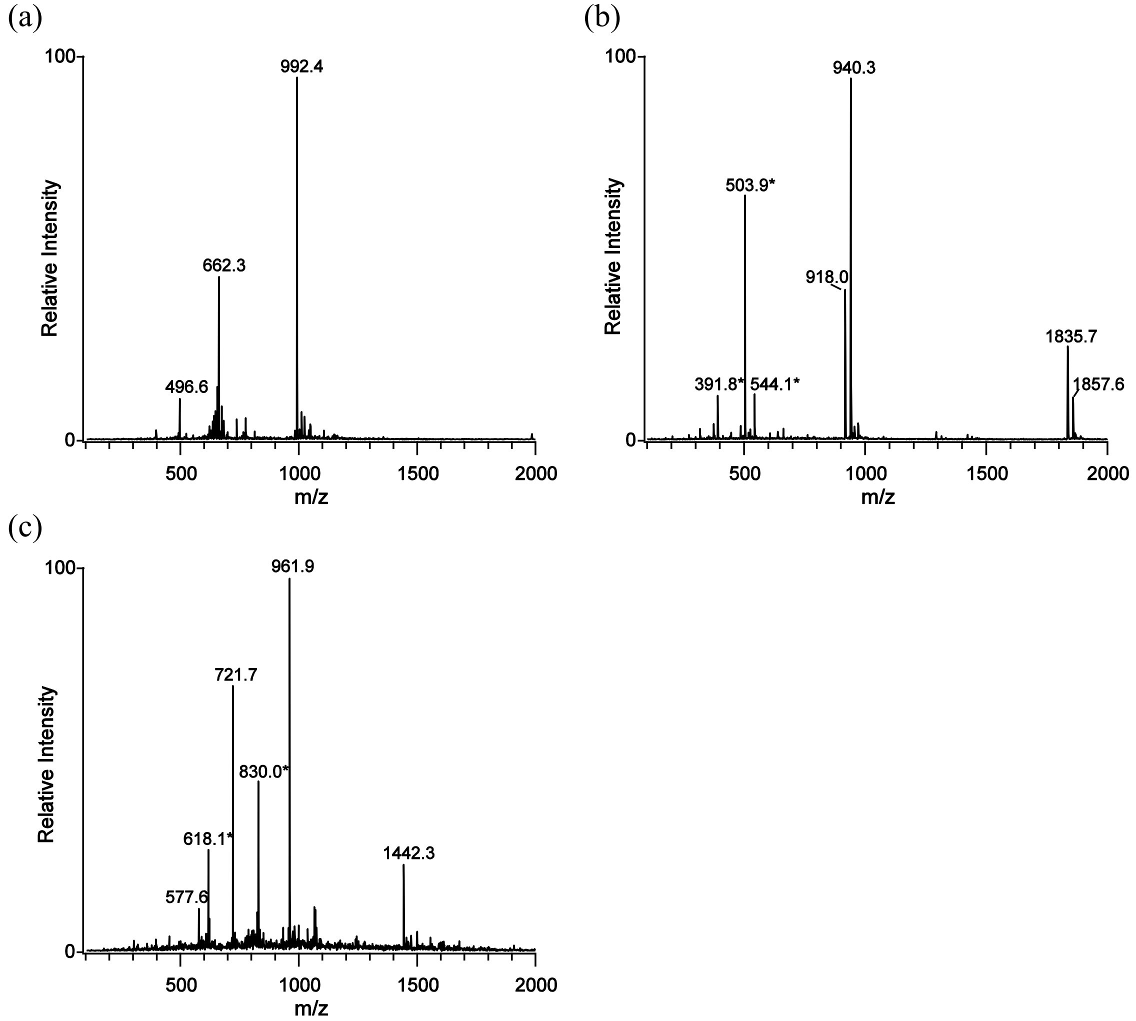

Figure S1: ESI-MS spectrum of (a) BHQ2-R8, (b) Dox-GLFG, and (c) R8DB drug-beacon. In Dox consisting molecule, in-source fragmentation was observed corresponding to the partial loss of Dox moiety (indicated by *). Higher laser power resulted in the loss of Dox fragments. This phenomenon was also observed in previous study.[173] BHQ2-R8 exact mass is 1982.127, MS (ESI): 992.4 $[M+2H]^{2+}$, 662.3 $[M+3H]^{3+}$, 496.6 $[M+4H]^{4+}$. Dox-GLFG exact mass is 917.369, MS (ESI): 1835.7 $[2M+H]^{+}$, 1857.6 $[2M+Na]^{+}$, 940.3$[M+Na]^{+}$, 918.0 $[M+H]^{+}$. R8DB exact mass is 2881.486, MS (ESI) : 1442.3$[M+2H]^{2+}$, 961.9 $[M+3H]^{3+}$, 721.7 $[M+4H]^{4+}$, 577.6 $[M+5H]^{5+}$

S1.6 Analytical HPLC Characterization

Analytical reverse-phase HPLC was performed using a Varian polymeric column (PLRP-S, 100 Å, 10 µm, 150 × 4.6 mm) with 20 µL injection volumes. A water/acetonitrile gradient 30%-80% was ran for 30 minutes containing 0.1% *v*/*v* TFA at a flow rate of 1 mL/min was used and samples were dissolved at 1 mg/ml concentration in 0.1% aqueous TFA.

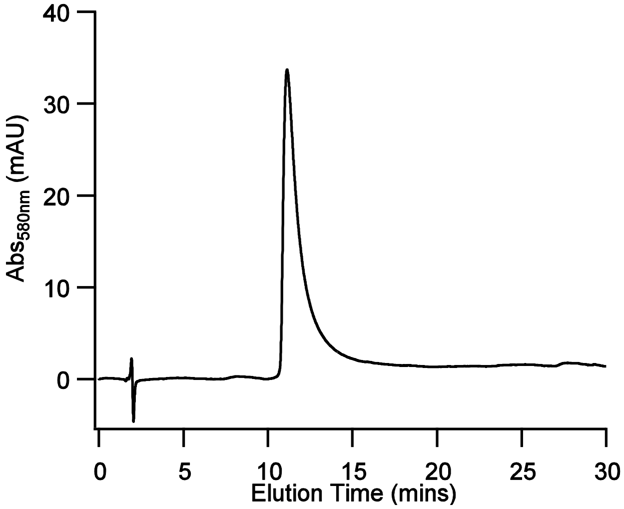

Figure S2: Analytical HPLC spectrum of R8DB drug-beacon showed a high purity of final product that has an elution time at 12 minutes.

S2 Cathepsin-B Enzymatic Activation

S2.1 Fluorescence Kinetics Measurement

CatB enzymatic reaction buffer was prepared in 50 mM sodium acetate buffer with 25 mM *L*-cystein as enzyme activator and 1 mM EDTA was added as enzyme stabilizer. The pH of reaction buffer was validated to 5, the optimum pH for enzymatic activity. CatB was pre-incubated in reaction buffer for 5 minutes at 37 °C to activate the enzyme and R8DB drug-beacon was added to reaction buffer to yield a final concentration of 3 µM and final CatB enzyme of 0.005, 0.01 and 0.03 Unit in 100 µL reaction volume. All samples were triplicated and the experiment was carried out in a

96-well standard opaque plate. Dox molecule was excited at 490 nm and emission was collected at 580 nm with 570 nm cut off. Experiment data was collected using a Gemini XPS microplate reader (Molecular Devices, Sunnyvale, CA) different time points. After 2 hours of CatB incubation, fluorescence intensity increased significantly indicating the activation of R8DB drug-beacon (release of Dox) resulting from cathepsin B degradation on –GFLG- linker.

S2.2 Fluorescence Emission Spectra

Similar to procedure described above, reaction sample consists of 3 μM R8DB and 0.05 Unit/100 μL of CatB was prepared in a final volume of 600 μL. Sample was loaded into a Quartz Fluorometer Cell Micro with stopper, 10mm (Starna Cells, Inc.) and fluorescence emimssion spectrum was acquired using Fluorolog spectrophotometer from Horiba Jobin Yvon (Edison, NJ). Sample was excited with 465 nm and emission spectrum was collected from 475 nm-750 nm, with 1 nm wavelength interval.

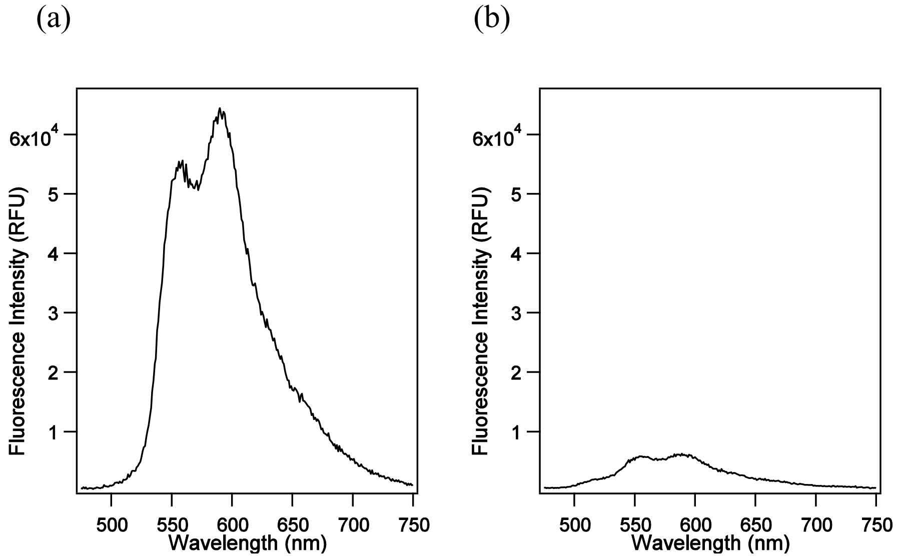

Figure S3: Emission spectrum of (a) Dox and (b) R8DB at 3 μM concentration without addition of CatB enzyme. Samples were excited with 465nm wavelength and emission was collected from 475nm – 750nm. Abbreviated RFU: relative fluorescence unit.

S2.3 k_{cat}/K$_M$ Calculation

$$Conversion\ unit = \frac{93.86\ RFU}{3000nM\ Dox}$$

For Example: Initial Cleavage Rate for 3000nM R8DB with 0.03 U/100 μL CatB is 1.3936 RFU/min.

$$Conversion = 1.3936\ \frac{RFU}{min} \cdot \frac{3000nM\ Dox}{93.86\ RFU} \cdot \frac{1min}{60\ sec} = 0.742\frac{nM\ Dox}{sec}$$

By using the same method, each initial cleavage rate (V) was calculated and plotted in Figure 1c (main text).

$$Slope = \frac{V}{[E]_t} \cong 23.788\frac{nM\ Dox}{(Unit\ CatB/100\mu L) \cdot sec}$$

CatB Unit information provided by manufacturer:

$$CatB\ Unit\ Conversion\ = \frac{25.6\ U}{mg} \cdot \frac{28000\ g}{mol} \cdot \frac{1000\ mg}{g} = 7.168\ \times 10^8\frac{U}{mol\ CatB}$$

From Michaelis-Menton equation,

$$V \cong \frac{k_{cat}}{K_M}[E]_t[S]$$

$$\frac{V}{[E]_t} \cong \frac{k_{cat}}{K_M}[S]$$

$$\frac{k_{cat}}{K_M} \cong \frac{V}{[E]_t}\frac{1}{[S]}$$

$$Substitute: \ \frac{V}{[E]_t} = 23.788\frac{nM\ Dox}{(U/100\mu L) \cdot sec} \cdot 7.168\ \times 10^8\frac{U}{mol\ CatB} \cdot \frac{1\ mol}{1 \times 10^9\ nmol}$$

$$\frac{k_{cat}}{K_M} \cong 1.705 \times 10^{-3}\frac{nM\ Dox}{nM\ CatB \cdot sec}\ \cdot\ \frac{1}{3000nM\ Dox}$$

$$\frac{k_{cat}}{K_M} \cong \frac{5.684 \times 10^{-7}}{1 \times 10^{-9}}\frac{1}{M\ CatB \cdot sec}$$

$$\frac{k_{cat}}{K_M} \cong 568.4\left(\frac{mol}{L}\right)^{-1} \cdot s^{-1}$$

S3 Confocal Laser Scanning Microscopy

NCI/ADR-Res were seeded onto 8-well plate with cell density of $3x10^4$ cells/well and incubated overnight in 37 ^oC incubator. 9 μL of 100 μM R8DB drug-beacon were added to 291 μL of RPMI 1640 cell medium and transferred to each well containing NCI/ADR-Res cells. The cells were kept in 37 ^oC for 3 days and then the medium was replaced with fresh medium containing drug (R8DB or Dox in corresponding well). The cells were incubated for 1 more day. NCI/ADR-Res cells were imaged directly without fixing the cells after 4 days of total incubation. The cell nuclei were stained in blue with Hoechst 33342 and lysosome compartments were stained with Lysotracker Green for 30 minutes before the cell imaging.

S4 Cell Cytotoxicity Assay

NCI/ADR-Res cells were seeded onto 96-well plate with cell density of 3000 cells/well and incubated overnight in 37 ^oC incubator. Free Dox and R8DB drug-beacon with different concentrations, 0.3 μM, 1 μM and 3 μM were added to corresponding well with final volume of 200 μL. All samples were triplicated. After 3 days of incubation in 37 ^oC, cells were replaced with fresh medium consisting respective drug and incubated for another 3 days (total of 6 days) Cell cytotoxicity was evaluated using *In Vitro* Toxicology Assay Kit, SRB based (Sigma-Aldrich, MO) and procedures were carried as described in manufacturer’s protocol.

Supporting Information for Chapter 5

Self-Assembling Drug-Peptide Nanofiber Hydrogel with Inherent MRI Signal

S1 Synthesis and molecular characterization

S1.1 Materials

Fmoc amino acids and Fmoc-Glu(OtBu)-Wang resin were purchased from Advanced Automated Peptide Protein Technologies (AAPPTEC, Louisville, KY). Pemetrexed (Pem) was purchased from AvaChem Scientific (San Antonio, TX). Lauric acid was purchased from Fisher Scientific (Pittsburgh, PA). Hydrochloric acid was purchased from EMD Millipore (Billerica, MA), and sodium hydroxide was purchased from Fisher Scientific (Fair Lawn, NJ).

S1.2 Synthesis of FE (C12-FFEE) and PemFE (Pem-FFEE)

The peptide Fmoc-FFEE was synthesized on a Focus XC automated peptide synthesizer (AAPPTEC, Louisville, KY) with the scale of 0.25 mmole by using standard Fmoc-solid phase synthesis techniques. Fmoc deprotection was followed using 20% 4-methylpiperidine in DMF solution for 15 minutes, repeating once. After Fmoc deprotection, lauric acid was manually coupled to N-terminus of NH_2-FFEE at the ratio of Lauric acid/HBTU/DIEA 4:4:6 relative to the peptide, shaking overnight at room temperature. The coupling of Pem was performed manually at N-terminus of NH_2-FFEE Pem/HBTU/DIEA at a ratio of 1.2:1.2:1.8 relative to the peptide, shaking overnight at room temperature. In all cases, reactions were monitored by the ninhydrin test (Anaspec Inc., Fremont, CA) for free amines. Both FE and PemFE were cleaved from the Wang resins using the standard cleavage solution of TFA/TIS/H_2O (95:2.5:2.5) for 3 hours. Excess TFA was removed by air blow, and the remaining peptide solution was titrated with cold diethyl ether to precipitate crude peptide. The precipitated crude peptide and diethyl ether were phase-separated using centrifugation technique (5900 rpm for 3 minute) and diethyl ether solution was discarded. To remove as much TFA as possible, the washing step was carried out by adding 25 mL of diethyl ether to crude peptide, vortexed and centrifuged. This procedure was repeated 3 times. All centrifuge tubes were tightly sealed with parafilm to minimize evaporation of diethyl ether during high-speed centrifugation. After centrifugation, the precipitate was dried under vacuum overnight.

S1.3 Purification

The peptides were purified by preparative RP-HPLC with a Varian Polymeric Column (PLRP-S, 100 Å, 10 µm, 150 × 25 mm) at 25 ^{o}C on a Varian ProStar Model 325 preparative HPLC (Agilent Technologies, Santa Clara, CA) equipped with a fraction collector.

FE peptide was dissolved in 20 ml of 0.1% v/v NH_4OH. A water/acetonitrile gradient 5%-100% was ran for 30 minutes containing 0.1% v/v NH_4OH was used as eluent at a flow rate of 20 mL/min.

The crude PemFE peptide was initially dissolved in 20 ml of 0.1% v/v NH_4OH, then diluting with 20 ml of 0.1% v/v TFA. A water/acetonitrile gradient 5%-50% was ran for 30 minutes containing 0.1% v/v TFA was used as eluent at a flow rate of 20 mL/min.

The absorbance peak was monitored at 220 nm. Peptide identity was confirmed by ESI-MS (LDQ Deca ion-trap mass spectrometer, Thermo Finnigan, San Jose, CA). Collected fractions containing desired products were lyophilized (FreeZone -105 °C 4.5 L freeze dryer, Labconco, Kansas City, MO) and stored at -30 ^{o}C.

S1.4 Electrospray Ionization-Mass Spectra (ESI-MS)

ESI mass spectra were acquired using a Finnigan LCQ Deca ion-trap mass spectrometer equipped with an electrospray ionization source (Thermo Finnigan, San Jose, CA). Samples were dissolved in water with 5% of acetonitrle containing 0.1% v/v NH_4OH and introduced into the instrument at a rate of 10 uL/min using a syringe pump via a silica capillary line. The heated capillary temperature was 250 ^{o}C and the spray voltage was 5kV.

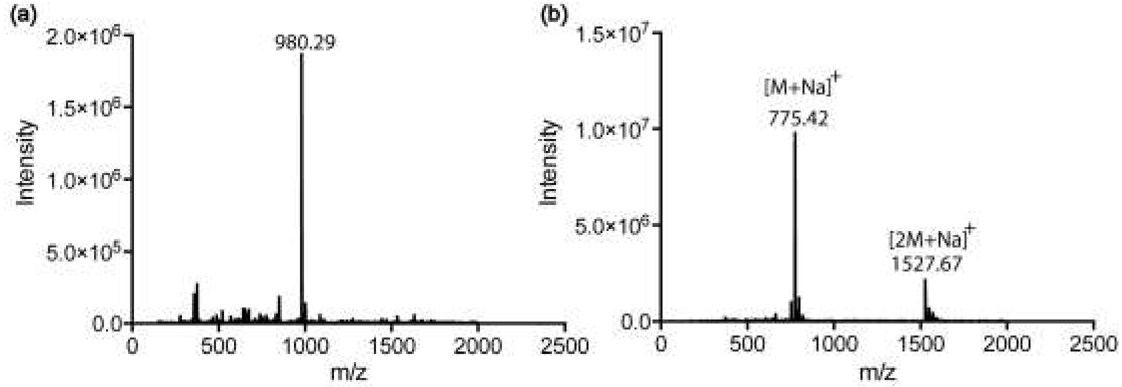

Figure S1. ESI-MS of (a) **PemFE** and (b) **FE** molecules.

S1.5 Analytical HPLC Characterization

Analytical RP-HPLC was performed using a Varian polymeric column (PLRP-S, 100 Å, 10 μm, 150 × 4.6 mm) with 20 μL injection volume. A water/acetonitrile gradient 5%-100% was ran for 30 minutes containing 0.1% v/v NH_4OH at a flow rate of 1 mL/min.

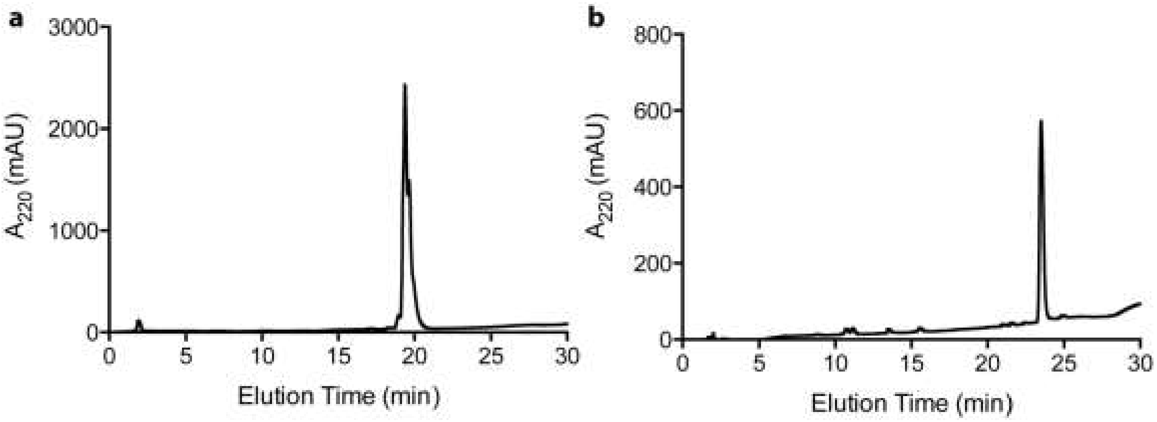

Figure S2. Analytical RP-HPLC of (a) **PemFE** and (b) **FE.** PemFE isomer resulting in the shoulder peak in plot (a).

S2. Self-Assembly Characterization Protocols

S2.1 Transmission electron microscopy (TEM) imaging protocol

4 mM solutions of **FE and PemFE** in PBS were prepared by directly dissolving lyophilized powders, and allowed to age overnight. A sample for imaging was prepared by depositing 5 μL of the solution onto a carbon-coated copper grid (Electron

Microscopy Services, Hatfield, PA, USA), wicking away the excess solution with a small piece of filter paper. Next, 5 µL of a 2 wt % aqueous uranyl acetate solution was deposited and the excess solution was carefully removed as above to leave a very thin layer. The sample grid was then allowed to dry at room temperature prior to imaging. Bright-field TEM imaging was performed on a FEI Tecnai 12 TWIN Transmission Electron Microscope operated at an acceleration voltage of 100 kV. TEM images were recorded by a 16 bit 2K × 2K FEI Eagle bottom mount camera.

S2.2 Cryogenic TEM protocol

To visualize structures without possible artificial effects caused by drying and staining, cryo-TEM imaging was performed on the FEI Tecnai 12 TWIN Transmission Electron Microscope, operating at 80 kV. FE and PemFE samples were prepared at 4mM in PBS, the same concentration as conventional TEM. Prior to sample preparation, all TEM grids were treated with plasma air to make the lacey carbon film hydrophilic. The Vitrobot with a controlled humidity chamber (FEI) was used to generate a thin film of sample on grid. The lacey carbon grid (Electron Microscopy Services, Hatfield, PA) was blotted and plunged into liquid ethane pre-cooled by liquid nitrogen. All vitrified samples were transferred to a cryo-holder filled with liquid nitrogen to prevent sublimation of vitrenous water. The images were recorded by a 16 bit 2K × 2K FEI Eagle bottom mount camera.

S3. *In vitro* MRI CEST measurement

FE, PemFE and free pemetrexed samples were prepared at 10mM in 1xDPBS solution. A pH series ranging from 6.0 to 8.5 with an increment of 0.5 was studied, and sodium hydroxide or hydrochloric acid solution was used to achieve expected pH. 1M solution of sodium hydroxide was prepared by dissolving solid sodium hydroxide in deionized water, while 11M hydrochloric acid was diluted with water to 1M hydrochloric acid. Samples were triplicated at each pH. After pH adjustment, samples were transferred to capillary tubes and then arranged on a sample holder.

S4. PemFE and FE Hydrogel

PemFE and FE hydrogel were prepared in the final concentration of 30 mM, dissolved in 1xDPBS solution and sonicated for 2 minutes to aid in dissolving lyphophilized powder form of respective molecules. Samples were left overnight and hydrogel photos were taken by inverting both sample vials.

S5. Cell Cytotoxicity Assay

The cytotoxicity of **PemFE**, **FE** and free pemetrexed was evaluated on a mouse glioma cell line (GL-261). Cells were seeded into 96-well plates at 1500 cells/well in the medium DMEM containing 10% FBS and 1% antibiotics solution (penicillin and streptomycin), and incubated overnight in 37 °C incubator with 5% CO_2 (Oasis CO_2 incubator, Caron, Marietta, OH).The three molecules with different concentrations, 0.01 µM, 0.1 µM, 0.5 µM, 1 µM, 2 µM, 4 µM, 10 µM and 50 µM were added to corresponding well with final volume of 200 µL. All samples were triplicated. After 4 days of incubation in 37 °C, cell cytotoxicity was evaluated using SRB based (Sigma- Aldrich, MO) in vitro Toxicology Assay Kit, and procedures were carried as described in manufacturer's protocol. The IC_{50} (the half maximal inhibitory concentration) values for each molecule were obtained by fitting the data using the non-linear regression (curve fit) analysis functions with Prism software.

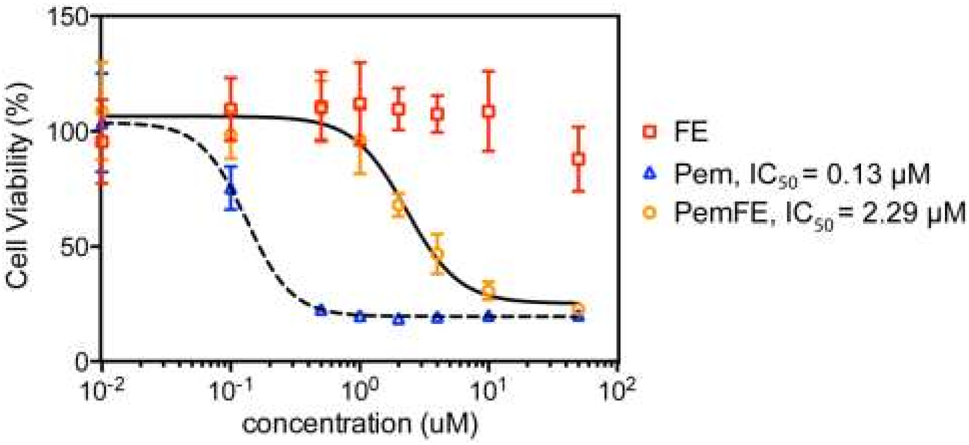

Figure S3. *In vitro* dose-response relationship study of the **PemFE**, **FE**, and free pemetrexed molecules against mouse glioma GL-261 cells.

References

(1) Siegel, R. L.; Miller, K. D.; Jemal, A. *Ca-Cancer J Clin* 2015, *65*, 5-29.

(2) Lee, S.; Xie, J.; Chen, X. Y. *Current Topics in Medicinal Chemistry* 2010, *10*, 1135-1144.

(3) Chen, J.; Liu, T. W. B.; Lo, P. C.; Wilson, B. C.; Zheng, G. *Bioconjugate Chem* 2009, *20*, 1836-1842.

(4) Allen, T. M.; Cullis, P. R. *Science* 2004, *303*, 1818-1822.

(5) Duncan, R. *Nat Rev Cancer* 2006, *6*, 688-701.

(6) *Nanoscience and nanotechnologies : opportunities and uncertainties*; The Royal Society & The Royal Academy of Engineering, 2004.

(7) Ashoori, R. C. *Nature* 1996, *379*, 413-419.

(8) Michalet, X.; Pinaud, F. F.; Bentolila, L. A.; Tsay, J. M.; Doose, S.; Li, J. J.; Sundaresan, G.; Wu, A. M.; Gambhir, S. S.; Weiss, S. *Science* 2005, *307*, 538-544.

(9) Resch-Genger, U.; Grabolle, M.; Cavaliere-Jaricot, S.; Nitschke, R.; Nann, T. *Nat Methods* 2008, *5*, 763-75.

(10) Jun, Y. W.; Huh, Y. M.; Choi, J. S.; Lee, J. H.; Song, H. T.; Kim, S.; Yoon, S.; Kim, K. S.; Shin, J. S.; Suh, J. S.; Cheon, J. *J Am Chem Soc* 2005, *127*, 5732-5733.

(11) Dubertret, B.; Calame, M.; Libchaber, A. J. *Nat Biotechnol* 2001, *19*, 365-370.

(12) Li, H. X.; Rothberg, L. J. *Anal Chem* 2004, *76*, 5414-5417.

(13) Chow, E. K. H.; Ho, D. *Sci Transl Med* 2013, *5*.

(14) Templeton, N. S.; Lasic, D. D.; Frederik, P. M.; Strey, H. H.; Roberts, D. D.; Pavlakis, G. N. *Nat Biotechnol* 1997, *15*, 647-652.

(15) Lian, T.; Ho, R. J. Y. *J Pharm Sci* 2001, *90*, 667-680.

(16) Martina, M. S.; Fortin, J. P.; Menager, C.; Clement, O.; Barratt, G.; Grabielle-Madelmont, C.; Gazeau, F.; Cabuil, V.; Lesieur, S. *J Am Chem Soc* 2005, *127*, 10676-10685.

(17) Torchilin, V. P. *Nat Rev Drug Discov* 2005, *4*, 145-160.

(18) Oerlemans, C.; Bult, W.; Bos, M.; Storm, G.; Nijsen, J. F. W.; Hennink, W. E. *harm Res-Dordr* 2010, *27*, 2569-2589.

(19) Lavasanifar, A.; Samuel, J.; Kwon, G. S. *Adv Drug Deliver Rev* 2002, *54*, 169-190.

(20) Medina, S. H.; El-Sayed, M. E. H. *Chem Rev* 2009, *109*, 3141-3157.

(21) Longmire, M.; Choyke, P. L.; Kobayashi, H. *Current Topics in Medicinal Chemistry* 2008, *8*, 1180-1186.

(22) Maeda, H.; Nakamura, H.; Fang, J. *Adv Drug Deliver Rev* 2013, *65*, 71-79.

(23) Prabhakar, U.; Maeda, H.; Jain, R. K.; Sevick-Muraca, E. M.; Zamboni, W.; Farokhzad, O. C.; Barry, S. T.; Gabizon, A.; Grodzinski, P.; Blakey, D. C. *Cancer Res* 2013, *73*, 2412-2417.

(24) Moghimi, S. M.; Hunter, A. C.; Murray, J. C. *Pharmacol Rev* 2001, *53*, 283-318.

(25) Choi, H. S.; Liu, W.; Misra, P.; Tanaka, E.; Zimmer, J. P.; Ipe, B. I.; Bawendi, M. G.; Frangioni, J. V. *Nat Biotechnol* 2007, *25*, 1165-1170.

(26) Decuzzi, P.; Lee, S.; Bhushan, B.; Ferrari, M. *Ann Biomed Eng* 2005, *33*, 179-190.

(27) Ferrari, M. *Small* 2008, *4*, 20-25.

(28) Peer, D.; Karp, J. M.; Hong, S.; FaroKHzad, O. C.; Margalit, R.; Langer, R. *Nat Nanotechnol* 2007, *2*, 751-760.

(29) Bertrand, N.; Wu, J.; Xu, X.; Kamaly, N.; Farokhzad, O. C. *Adv Drug Deliv Rev* 2014, *66*, 2-25.

(30) Kirpotin, D. B.; Drummond, D. C.; Shao, Y.; Shalaby, M. R.; Hong, K. L.; Nielsen, U. B.; Marks, J. D.; Benz, C. C.; Park, J. W. *Cancer Res* 2006, *66*, 6732-6740.

(31) Bhattacharyya, S.; Khan, J. A.; Curran, G. L.; Robertson, J. D.; Bhattacharya, R.; Mukherjee, P. *Adv Mater* 2011, *23*, 5034-5038.

(32) Pasqualini, R.; Koivunen, E.; Ruoslahti, E. *Nat Biotechnol* 1997, *15*, 542-546.

(33) Roxin, A.; Zheng, G. *Future Med Chem* 2012, *4*, 1601-1618.

(34) Lopez-Otin, C.; Matrisian, L. M. *Nat Rev Cancer* 2007, *7*, 800-808.

(35) Lopez-Otin, C.; Bond, J. S. *Journal of Biological Chemistry* 2008, *283*, 30433-7.

(36) Egeblad, M.; Werb, Z. *Nat Rev Cancer* 2002, *2*, 161-174.

(37) Gialeli, C.; Theocharis, A. D.; Karamanos, N. K. *Febs J* 2011, *278*, 16-27.

(38) Mohamed, M. M.; Sloane, B. F. *Nat Rev Cancer* 2006, *6*, 764-775.

(39) Aggarwal, N.; Sloane, B. F. *Proteom Clin Appl* 2014, *8*, 427-437.

(40) Stuart, M. A. C.; Huck, W. T. S.; Genzer, J.; Muller, M.; Ober, C.; Stamm, M.; Sukhorukov, G. B.; Szleifer, I.; Tsukruk, V. V.; Urban, M.; Winnik, F.; Zauscher, S.; Luzinov, I.; Minko, S. *Nat Mater* 2010, *9*, 101-113.

(41) Roy, D.; Cambre, J. N.; Sumerlin, B. S. *Prog Polym Sci* 2010, *35*, 278-301.

(42) de la Rica, R.; Aili, D.; Stevens, M. M. *Adv Drug Deliver Rev* 2012, *64*, 967-978.

(43) Khan, A. R.; James, M. N. G. *Protein Sci* 1998, *7*, 815-836.

(44) Podgorski, I.; Sloane, B. F. *Biochem Soc Symp* 2003, *70*, 263-276.

(45) Zhong, Y. J.; Shao, L. H.; Li, Y. *Int J Oncol* 2013, *42*, 373-383.

(46) Dvorak, M.; Kopeckova, P.; Kopecek, J. *J Control Release* 1999, *60*, 321-332.

(47) Kopecek, J.; Kopeckova, P.; Minko, T.; Lu, Z. R. *Eur J Pharm Biopharm* 2000, *50*, 61-81.

(48) *Oncology-Ny* 2011, *25*, 904-+.

(49) Doronina, S. O.; Toki, B. E.; Torgov, M. Y.; Mendelsohn, B. A.; Cerveny, C. G.; Chace, D. F.; DeBlanc, R. L.; Gearing, R. P.; Bovee, T. D.; Siegall, C. B.; Francisco, J. A.; Wahl, A. F.; Meyer, D. L.; Senter, P. D. *Nat Biotechnol* 2003, *21*, 778-784.

(50) Weissleder, R.; Tung, C. H.; Mahmood, U.; Bogdanov, A., Jr. *Nat Biotechnol* 1999, *17*, 375-8.

(51) Glangchai, L. C.; Caldorera-Moore, M.; Shi, L.; Roy, K. *J Control Release* 2008, *125*, 263-272.

(52) Fuchs, S.; Otto, H.; Jehle, S.; Henklein, P.; Schluter, A. D. *Chem Commun* 2005, 1830-1832.

(53) Zhang, C. Y.; Pan, D. Y.; Luo, K.; Li, N.; Guo, C. H.; Zheng, X. L.; Gu, Z. W. *Polym Chem-Uk* 2014, *5*, 5227-5235.

(54) de la Torre, C.; Mondragon, L.; Coll, C.; Sancenon, F.; Marcos, M. D.; Martinez-Manez, R.; Amoros, P.; Perez-Paya, E.; Orzaez, M. *Chem-Eur J* 2014, *20*, 15309-15314.

(55) Kim, C. J.; Lee, D. I.; Kim, C.; Lee, K.; Lee, C. H.; Ahn, I. S. *Anal Chem* 2014, *86*, 3825-3833.

(56) Ducry, L.; Stump, B. *Bioconjugate Chem* 2010, *21*, 5-13.

(57) Shankar, R.; Samykutty, A.; Riggin, C.; Kannan, S.; Wenzel, U.; Kolhatkar, R. *Mol Pharmaceut* 2013, *10*, 3776-3788.

(58) Chowdhury, M. A.; Moya, I. A.; Bhilocha, S.; McMillan, C. C.; Vigliarolo, B. G.; Zehbe, I.; Phenix, C. P. *J Med Chem* 2014, *57*, 6092-6104.

(59) Whitesides, G. M.; Grzybowski, B. *Science* 2002, *295*, 2418-2421.
(60) Desiraju, G. R. *J Am Chem Soc* 2013, *135*, 9952-9967.
(61) Winfree, E.; Liu, F. R.; Wenzler, L. A.; Seeman, N. C. *Nature* 1998, *394*, 539-544.
(62) Kato, T. *Science* 2002, *295*, 2414-2418.
(63) Dobson, C. M. *Nature* 2003, *426*, 884-890.
(64) Fialkowski, M.; Bishop, K. J. M.; Klajn, R.; Smoukov, S. K.; Campbell, C. J.; Grzybowski, B. A. *J Phys Chem B* 2006, *110*, 2482-2496.
(65) Karsenti, E. *Nat Rev Mol Cell Bio* 2008, *9*, 255-262.
(66) Camazine, S. *Self-organization in biological systems*; Princeton University Press: Princeton, N.J., 2003.
(67) Timonen, J. V. I.; Latikka, M.; Leibler, L.; Ras, R. H. A.; Ikkala, O. *Science* 2013, *341*, 253-257.
(68) Velichko, Y. S.; Stupp, S. I.; de la Cruz, M. O. *J Phys Chem B* 2008, *112*, 2326-2334.
(69) Paramonov, S. E.; Jun, H. W.; Hartgerink, J. D. *J Am Chem Soc* 2006, *128*, 7291-7298.
(70) Collins, L.; Parker, A. L.; Gehman, J. D.; Eckley, L.; Perugini, M. A.; Separovic, F.; Fabre, J. W. *Acs Nano* 2010, *4*, 2856-2864.
(71) Fu, I. W.; Nguyen, H. D. *Biomacromolecules* 2015.
(72) Hartgerink, J. D.; Beniash, E.; Stupp, S. I. *P Natl Acad Sci USA* 2002, *99*, 5133-5138.
(73) Vauthey, S.; Santoso, S.; Gong, H. Y.; Watson, N.; Zhang, S. G. *P Natl Acad Sci USA* 2002, *99*, 5355-5360.
(74) Niece, K. L.; Hartgerink, J. D.; Donners, J. J. J. M.; Stupp, S. I. *J Am Chem Soc* 2003, *125*, 7146-7147.
(75) Cui, H. G.; Webber, M. J.; Stupp, S. I. *Biopolymers* 2010, *94*, 1-18.
(76) Silva, G. A.; Czeisler, C.; Niece, K. L.; Beniash, E.; Harrington, D. A.; Kessler, J. A.; Stupp, S. I. *Science* 2004, *303*, 1352-1355.
(77) Tysseling-Mattiace, V. M.; Sahni, V.; Niece, K. L.; Birch, D.; Czeisler, C.; Fehlings, M. G.; Stupp, S. I.; Kessler, J. A. *J Neurosci* 2008, *28*, 3814-3823.
(78) Schneider, J. P.; Pochan, D. J.; Ozbas, B.; Rajagopal, K.; Pakstis, L.; Kretsinger, J. *J Am Chem Soc* 2002, *124*, 15030-15037.
(79) Zhang, S. G. *Nat Biotechnol* 2003, *21*, 1171-1178.
(80) Zhang, S. G. *Biotechnol Adv* 2002, *20*, 321-339.
(81) Whitney, M. A.; Crisp, J. L.; Nguyen, L. T.; Friedman, B.; Gross, L. A.; Steinbach, P.; Tsien, R. Y.; Nguyen, Q. T. *Nat Biotechnol* 2011, *29*, 352-U181.
(82) Funovics, M.; Weissleder, R.; Tung, C. H. *Analytical and Bioanalytical Chemistry* 2003, *377*, 956-963.
(83) Jedeszko, C.; Sloane, B. F. *Biol Chem* 2004, *385*, 1017-1027.
(84) Duncan, R.; Cable, H. C.; Lloyd, J. B.; Rejmanova, P.; Kopecek, J. *Makromolekulare Chemie-Macromolecular Chemistry and Physics* 1983, *184*, 1997-2008.
(85) Rejmanova, P.; Kopecek, J.; Pohl, J.; Baudys, M.; Kostka, V. *Makromolekulare Chemie-Macromolecular Chemistry and Physics* 1983, *184*, 2009-2020.
(86) Pasut, G.; Veronese, F. M. *Prog Polym Sci* 2007, *32*, 933-961.

(87) Lowe, S. B.; Dick, J. A. G.; Cohen, B. E.; Stevens, M. M. *Acs Nano* 2012, *6*, 851-857.
(88) Galler, K. M.; Aulisa, L.; Regan, K. R.; D'Souza, R. N.; Hartgerink, J. D. *J Am Chem Soc* 2010, *132*, 3217-3223.
(89) Giano, M. C.; Pochan, D. J.; Schneider, J. P. *Biomaterials* 2011, *32*, 6471-6477.
(90) Hahn, M. E.; Gianneschi, N. C. *Chem Commun* 2011, *47*, 11814-11821.
(91) Levesque, S. G.; Shoichet, M. S. *Bioconjugate Chem* 2007, *18*, 874-885.
(92) Lutolf, M. P.; Lauer-Fields, J. L.; Schmoekel, H. G.; Metters, A. T.; Weber, F. E.; Fields, G. B.; Hubbell, J. A. *P Natl Acad Sci USA* 2003, *100*, 5413-5418.
(93) Ghadiali, J. E.; Stevens, M. M. *Adv Mater* 2008, *20*, 4359-4363.
(94) Hirst, A. R.; Roy, S.; Arora, M.; Das, A. K.; Hodson, N.; Murray, P.; Marshall, S.; Javid, N.; Sefcik, J.; Boekhoven, J.; van Esch, J. H.; Santabarbara, S.; Hunt, N. T.; Ulijn, R. V. *Nature Chemistry* 2010, *2*, 1089-1094.
(95) Gao, Y.; Shi, J.; Yuan, D.; Xu, B. *Nature Communications* 2012, *3*.
(96) Gao, Y.; Zhao, F.; Wang, Q. G.; Zhang, Y.; Xu, B. *Chemical Society Reviews* 2010, *39*, 3425-3433.
(97) Williams, R. J.; Smith, A. M.; Collins, R.; Hodson, N.; Das, A. K.; Ulijn, R. V. *Nat Nanotechnol* 2009, *4*, 19-24.
(98) Raeber, G. P.; Lutolf, M. P.; Hubbell, J. A. *Biophysical Journal* 2005, *89*, 1374-1388.
(99) Tyagi, S.; Kramer, F. R. *Nat Biotechnol* 1996, *14*, 303-308.
(100) Tyagi, S.; Bratu, D. P.; Kramer, F. R. *Nat Biotechnol* 1998, *16*, 49-53.
(101) Tan, W. H.; Wang, K. M.; Drake, T. J. *Current Opinion in Chemical Biology* 2004, *8*, 547-553.
(102) Zheng, G.; Chen, J.; Stefflova, K.; Jarvi, M.; Li, H.; Wilson, B. C. *P Natl Acad Sci USA* 2007, *104*, 8989-8994.
(103) Olson, E. S.; Jiang, T.; Aguilera, T. A.; Nguyen, Q. T.; Ellies, L. G.; Scadeng, M.; Tsien, R. Y. *P Natl Acad Sci USA* 2010, *107*, 4311-4316.
(104) Ghadiali, J. E.; Lowe, S. B.; Stevens, M. M. *Angewandte Chemie-International Edition* 2011, *50*, 3417-3420.
(105) Thurley, S.; Roglin, L.; Seitz, O. *J Am Chem Soc* 2007, *129*, 12693-+.
(106) Hartgerink, J. D.; Beniash, E.; Stupp, S. I. *Science* 2001, *294*, 1684-1688.
(107) Trent, A.; Marullo, R.; Lin, B.; Black, M.; Tirrell, M. *Soft Matter* 2011, *7*, 9572-9582.
(108) Yu, Y. C.; Berndt, P.; Tirrell, M.; Fields, G. B. *J Am Chem Soc* 1996, *118*, 12515-12520.
(109) Lowik, D.; Van den Heuvel, M.; Van Hest, J. *Journal of Peptide Science* 2010, *16*, 36-37.
(110) Vernille, J. P.; Kovell, L. C.; Schneider, J. W. *Bioconjugate Chem* 2004, *15*, 1314-1321.
(111) Hill, J. P.; Jin, W. S.; Kosaka, A.; Fukushima, T.; Ichihara, H.; Shimomura, T.; Ito, K.; Hashizume, T.; Ishii, N.; Aida, T. *Science* 2004, *304*, 1481-1483.
(112) Matmour, R.; De Cat, I.; George, S. J.; Adriaens, W.; Leclere, P.; Bomans, P. H. H.; Sommerdijk, N. A. J. M.; Gielen, J. C.; Christianen, P. C. M.; Heldens, J. T.; van Hest, J. C. M.; Lowik, D. W. P. M.; De Feyter, S.; Meijer, E. W.; Schenning, A. P. H. J. *J Am Chem Soc* 2008, *130*, 14576-14583.

(113) De Greef, T. F. A.; Smulders, M. M. J.; Wolffs, M.; Schenning, A. P. H. J.; Sijbesma, R. P.; Meijer, E. W. *Chem Rev* 2009, *109*, 5687-5754.

(114) Vives, E.; Brodin, P.; Lebleu, B. *Journal of Biological Chemistry* 1997, *272*, 16010-16017.

(115) Eijan, A. M.; Sandes, E. O.; Riveros, M. D.; Thompson, S.; Pasik, L.; Mallagrino, H.; Celeste, F.; Casabe, A. R. *Cancer* 2003, *98*, 262-268.

(116) Maguire, T. M.; Shering, S. G.; Duggan, C. M.; McDermott, E. W.; O'Higgins, N. J.; Duffy, M. J. *Int J Biol Marker* 1998, *13*, 139-144.

(117) Reinheckel, T.; Deussing, J.; Roth, W.; Peters, C. *Biol Chem* 2001, *382*, 735-741.

(118) Weissleder, R. *Science* 2006, *312*, 1168-1171.

(119) Willmann, J. K.; van Bruggen, N.; Dinkelborg, L. M.; Gambhir, S. S. *Nat Rev Drug Discov* 2008, *7*, 591-607.

(120) Kircher, M. F.; Hricak, H.; Larson, S. M. *Mol Oncol* 2012, *6*, 182-195.

(121) Weissleder, R.; Mahmood, U. *Radiology* 2001, *219*, 316-333.

(122) Massoud, T. F.; Gambhir, S. S. *Gene Dev* 2003, *17*, 545-580.

(123) Chen, K.; Chen, X. Y. *Current Topics in Medicinal Chemistry* 2010, *10*, 1227-1236.

(124) Leung, K.; Chopra, A.; Shan, L.; Eckelman, W. C.; Menkens, A. E. *Nanomedicine-Uk* 2012, *7*, 1101-1107.

(125) Wender, P. A.; Mitchell, D. J.; Pattabiraman, K.; Pelkey, E. T.; Steinman, L.; Rothbard, J. B. *Proc Natl Acad Sci U S A* 2000, *97*, 13003-8.

(126) Low, P. S.; Henne, W. A.; Doorneweerd, D. D. *Acc Chem Res* 2008, *41*, 120-9.

(127) Banerjee, S. R.; Pullambhatla, M.; Foss, C. A.; Nimmagadda, S.; Ferdani, R.; Anderson, C. J.; Mease, R. C.; Pomper, M. G. *J Med Chem* 2014, *57*, 2657-69.

(128) Agarwal, R.; Singh, V.; Jurney, P.; Shi, L.; Sreenivasan, S. V.; Roy, K. *Proceedings of the National Academy of Sciences* 2013, *110*, 17247-17252.

(129) Rejman, J.; Oberle, V.; Zuhorn, I. S.; Hoekstra, D. *Biochem J* 2004, *377*, 159-169.

(130) Zhang, S. L.; Li, J.; Lykotrafitis, G.; Bao, G.; Suresh, S. *Adv Mater* 2009, *21*, 419-+.

(131) Gao, H. J.; Shi, W. D.; Freund, L. B. *P Natl Acad Sci USA* 2005, *102*, 9469-9474.

(132) Liu, J.; Sun, Y. D.; Drubin, D. G.; Oster, G. F. *Plos Biol* 2009, *7*.

(133) Geng, Y.; Dalhaimer, P.; Cai, S. S.; Tsai, R.; Tewari, M.; Minko, T.; Discher, D. E. *Nat Nanotechnol* 2007, *2*, 249-255.

(134) Gratton, S. E. A.; Ropp, P. A.; Pohlhaus, P. D.; Luft, J. C.; Madden, V. J.; Napier, M. E.; DeSimone, J. M. *P Natl Acad Sci USA* 2008, *105*, 11613-11618.

(135) Jiang, W.; Kim, B. Y. S.; Rutka, J. T.; Chan, W. C. W. *Nat Nanotechnol* 2008, *3*, 145-150.

(136) Kolhar, P.; Anselmo, A. C.; Gupta, V.; Pant, K.; Prabhakarpandian, B.; Ruoslahti, E.; Mitragotri, S. *P Natl Acad Sci USA* 2013, *110*, 10753-10758.

(137) Lowik, D. W. P. M.; Garcia-Hartjes, J.; Meijer, J. T.; van Hest, J. C. M. *Langmuir* 2005, *21*, 524-526.

(138) Pashuck, E. T.; Cui, H. G.; Stupp, S. I. *J Am Chem Soc* 2010, *132*, 6041-6046.

(139) Missirlis, D.; Chworos, A.; Fu, C. J.; Khant, H. A.; Krogstad, D. V.; Tirrell, M. *Langmuir* 2011, *27*, 6163-6170.

(140) Missirlis, D.; Teesalu, T.; Black, M.; Tirrell, M. *Plos One* 2013, *8*.

(141) Bai, S.; Pappas, C.; Debnath, S.; Frederix, P. W. J. M.; Leckie, J.; Fleming, S.; Ulijn, R. V. *Acs Nano* 2014, *8*, 7005-7013.
(142) Kuang, Y.; Du, X. W.; Zhou, J.; Xu, B. *Adv Healthc Mater* 2014, *3*, 1217-1221.
(143) Rubio, J.; Alfonso, I.; Burguete, M. I.; Luis, S. V. *Chem Commun* 2012, *48*, 2210-2212.
(144) Furuya, T.; Kiyota, T.; Lee, S.; Inoue, T.; Sugihara, G.; Logvinova, A.; Goldsmith, P.; Ellerby, H. M. *Biophysical Journal* 2003, *84*, 1950-1959.
(145) Han, S. Y.; Cao, S. S.; Wang, Y. M.; Wang, J. Q.; Xia, D. H.; Xu, H.; Zhao, X. B.; Lu, J. R. *Chem-Eur J* 2011, *17*, 13095-13102.
(146) Nelson, R.; Sawaya, M. R.; Balbirnie, M.; Madsen, A. O.; Riekel, C.; Grothe, R.; Eisenberg, D. *Nature* 2005, *435*, 773-778.
(147) Balbirnie, M.; Grothe, R.; Eisenberg, D. S. *P Natl Acad Sci USA* 2001, *98*, 2375-2380.
(148) Duncan, R.; Cable, H. C.; Lloyd, J. B.; Rejmanova, P.; Kopecek, J. *Makromolekulare Chemie-Macromolecular Chemistry and Physics* 1983, *184*, 1997-2008.
(149) Lock, L. L.; Cheetham, A. G.; Zhang, P. C.; Cui, H. G. *Acs Nano* 2013, *7*, 4924-4932.
(150) Vieira, E. P.; Hermel, H.; Mohwald, H. *Bba-Proteins Proteom* 2003, *1645*, 6-14.
(151) Stine, W. B.; Dahlgren, K. N.; Krafft, G. A.; LaDu, M. J. *Journal of Biological Chemistry* 2003, *278*, 11612-11622.
(152) Colella, R.; Casey, S. F. *Biotech Histochem* 2003, *78*, 101-108.
(153) Colella, R.; Jackson, T.; Goodwyn, E. *Biotech Histochem* 2004, *79*, 121-127.
(154) Fernandez, P. L.; Farre, X.; Nadal, A.; Fernandez, E.; Peiro, N.; Sloane, B. F.; Shi, G. P.; Chapman, H. A.; Campo, E.; Cardesa, A. *Int J Cancer* 2001, *95*, 51-55.
(155) Miyake, H.; Hara, I.; Eto, H. *Anticancer Res* 2004, *24*, 2573-2577.
(156) Szpaderska, A. M.; Frankfater, A. *Mol Biol Cell* 1999, *10*, 347a-347a.
(157) Szpaderska, A. M.; Frankfater, A. *Cancer Res* 2001, *61*, 3493-3500.
(158) Podgorski, I.; Linebaugh, B. E.; Sameni, M.; Jedeszko, C.; Bhagat, S.; Cher, M. L.; Sloane, B. F. *Neoplasia* 2005, *7*, 207-223.
(159) Chen, L.; McCrate, J. M.; Lee, J. C.; Li, H. *Nanotechnology* 2011, *22*, 105708.
(160) Verma, A.; Stellacci, F. *Small* 2010, *6*, 12-21.
(161) Ter-Avetisyan, G.; Tuennemann, G.; Nowak, D.; Nitschke, M.; Herrmann, A.; Drab, M.; Cardoso, M. C. *Journal of Biological Chemistry* 2009, *284*, 3370-3378.
(162) Steinman, R. M.; Silver, J. M.; Cohn, Z. A. *J Cell Biol* 1974, *63*, 949-969.
(163) Hong, S. P.; Leroueil, P. R.; Janus, E. K.; Peters, J. L.; Kober, M. M.; Islam, M. T.; Orr, B. G.; Baker, J. R.; Holl, M. M. B. *Bioconjugate Chem* 2006, *17*, 728-734.
(164) Chen, J. M.; Hessler, J. A.; Putchakayala, K.; Panama, B. K.; Khan, D. P.; Hong, S.; Mullen, D. G.; DiMaggio, S. C.; Som, A.; Tew, G. N.; Lopatin, A. N.; Baker, J. R.; Holl, M. M. B.; Orr, B. G. *J Phys Chem B* 2009, *113*, 11179-11185.
(165) Sovadinova, I.; Palermo, E. F.; Huang, R.; Thoma, L. M.; Kuroda, K. *Biomacromolecules* 2011, *12*, 260-268.
(166) Asati, A.; Santra, S.; Kaittanis, C.; Perez, J. M. *Acs Nano* 2010, *4*, 5321-5331.
(167) Hemmerich, P. H.; von Mikecz, A. H. *Plos One* 2013, *8*.
(168) Zinchuk, V.; Zinchuk, O.; Okada, T. *Acta Histochem Cytoc* 2007, *40*, 101-111.
(169) Duffy, M. J. *Clin Exp Metastasis* 1992, *10*, 145-55.

(170) Joyce, J. A.; Baruch, A.; Chehade, K.; Meyer-Morse, N.; Giraudo, E.; Tsai, F. Y.; Greenbaum, D. C.; Hager, J. H.; Bogyo, M.; Hanahan, D. *Cancer Cell* 2004, *5*, 443-53.

(171) Choi, K. Y.; Swierczewska, M.; Lee, S.; Chen, X. *Theranostics* 2012, *2*, 156-78.

(172) Pearce, T. R.; Shroff, K.; Kokkoli, E. *Adv Mater* 2012, *24*, 3803-3822.

(173) Chen, Z. P.; Zhang, P. C.; Cheetham, A. G.; Moon, J. H.; Moxley, J. W.; Lin, Y. A.; Cui, H. G. *J Control Release* 2014, *191*, 123-130.

(174) Gao, Y.; Shi, J. F.; Yuan, D.; Xu, B. *Nature Communications* 2012, *3*.

(175) Adams, J. *Cancer Cell* 2004, *5*, 417-21.

(176) Tong, R.; Tang, L.; Ma, L.; Tu, C. L.; Baumgartner, R.; Cheng, J. J. *Chemical Society Reviews* 2014, *43*, 6982-7012.

(177) Tang, L.; Yang, X.; Yin, Q.; Cai, K.; Wang, H.; Chaudhury, I.; Yao, C.; Zhou, Q.; Kwon, M.; Hartman, J. A.; Dobrucki, I. T.; Dobrucki, L. W.; Borst, L. B.; Lezmig, S.; Helferich, W. G.; Ferguson, A. L.; Fan, T. M.; Cheng, J. *P Natl Acad Sci USA* 2014, *111*, 15344-15349.

(178) Tong, R.; Cheng, J. *Angewandte Chemie-International Edition* 2008, *47*, 4830-4834.

(179) Lin, Y. A.; Cheetham, A. G.; Zhang, P. C.; Ou, Y. C.; Li, Y. G.; Liu, G. S.; Hermida-Merino, D.; Hamley, I. W.; Cui, H. G. *Acs Nano* 2014, *8*, 12690-12700.

(180) Razgulin, A.; Ma, N.; Rao, J. H. *Chemical Society Reviews* 2011, *40*, 4186-4216.

(181) Bremer, C.; Tung, C. H.; Weissleder, R. *Nat Med* 2001, *7*, 743-748.

(182) Drake, C. R.; Miller, D. C.; Jones, E. F. *Curr Org Synth* 2011, *8*, 498-520.

(183) Zhang, P.; Cheetham, A. G.; Lock, L. L.; Li, Y.; Cui, H. *Current opinion in biotechnology* 2015, *34C*, 171-179.

(184) Zhu, L.; Ma, Y.; Kiesewetter, D. O.; Wang, Y.; Lang, L. X.; Lee, S.; Niu, G.; Chen, X. Y. *Acs Chem Biol* 2014, *9*, 510-516.

(185) Nitiss, J. L. *Nat Rev Cancer* 2009, *9*, 338-350.

(186) Liu, T. W. B.; Chen, J.; Zheng, G. *Amino Acids* 2011, *41*, 1123-1134.

(187) Qiu, L. P.; Wu, C. C.; You, M. X.; Han, D.; Chen, T.; Zhu, G. Z.; Jiang, J. H.; Yu, R. Q.; Tan, W. H. *J Am Chem Soc* 2013, *135*, 12952-12955.

(188) Wang, H.; Yang, R. H.; Yang, L.; Tan, W. H. *Acs Nano* 2009, *3*, 2451-2460.

(189) Santra, S.; Kaittanis, C.; Santiesteban, O. J.; Perez, J. M. *J Am Chem Soc* 2011, *133*, 16680-16688.

(190) Gondi, C. S.; Rao, J. S. *Expert Opin Ther Tar* 2013, *17*, 281-291.

(191) Hwang, J. H.; Lee, K. H.; Lee, K. Y.; Ryu, J. K.; Kim, Y. T.; Yoon, Y. B.; Lee, H. S. *J Gastroen Hepatol* 2006, *21*, A429-A429.

(192) Krepela, E.; Vicar, J.; Cernoch, M. *Neoplasma* 1989, *36*, 41-52.

(193) Li, C. S.; Chen, L. W.; Wang, J. L.; Zhang, L. Y.; Tang, P. Z.; Zhai, S. Q.; Guo, W. W.; Yu, N.; Zhao, L. D.; Liu, M. B.; Yang, S. M. *Oncol Rep* 2011, *26*, 869-875.

(194) Wu, D.; Wang, H. J.; Li, Z. N.; Wang, L. H.; Zheng, F. Y.; Jiang, J.; Gao, Y. T.; Zhong, H. F.; Huang, Y.; Suo, Z. H. *Histol Histopathol* 2012, *27*, 79-87.

(195) Fonseca, S. B.; Pereira, M. P.; Kelley, S. O. *Adv Drug Deliver Rev* 2009, *61*, 953-964.

(196) Zhang, K.; Fang, H.; Chen, Z.; Taylor, J.-S. A.; Wooley, K. L. *Bioconjugate Chem* 2008, *19*, 1880-1887.

(197) Kurtoglu, Y. E.; Mishra, M. K.; Kannan, S.; Kannan, R. M. *Int J Pharmaceut* 2010, *384*, 189-194.

(198) Eckford, P. D.; Sharom, F. J. *Chem Rev* 2009, *109*, 2989-3011.
(199) Dubikovskaya, E. A.; Thorne, S. H.; Pillow, T. H.; Contag, C. H.; Wender, P. A. *P Natl Acad Sci USA* 2008, *105*, 12128-12133.
(200) Lindgren, M.; Rosenthal-Aizman, K.; Saar, K.; Eiriksdottir, E.; Jiang, Y.; Sassian, M.; Ostlund, P.; Hallbrink, M.; Langel, U. *Biochem Pharmacol* 2006, *71*, 416-425.
(201) Aroui, S.; Brahim, S.; De Waard, M.; Kenani, A. *Biochem Bioph Res Co* 2010, *391*, 419-425.
(202) Leriche, G.; Budin, G.; Darwich, Z.; Weltin, D.; Mely, Y.; Klymchenko, A. S.; Wagner, A. *Chem Commun* 2012, *48*, 3224-3226.
(203) Linder, K. E.; Metcalfe, E.; Nanjappan, P.; Arunachalam, T.; Ramos, K.; Skedzielewski, T. M.; Marinelli, E. R.; Tweedle, M. F.; Nunn, A. D.; Swenson, R. E. *Bioconjugate Chem* 2011, *22*, 1287-1297.
(204) Zhang, P. C.; Cheetham, A. G.; Lock, L. L.; Cui, H. G. *Bioconjugate Chem* 2013, *24*, 604-613.
(205) Zhang, P. C.; Lock, L. L.; Cheetham, A. G.; Cui, H. G. *Mol Pharmaceut* 2014, *11*, 964-973.
(206) Nakase, I.; Niwa, M.; Takeuchi, T.; Sonomura, K.; Kawabata, N.; Koike, Y.; Takehashi, M.; Tanaka, S.; Ueda, K.; Simpson, J. C.; Jones, A. T.; Sugiura, Y.; Futaki, S. *Mol Ther* 2004, *10*, 1011-1022.
(207) Futaki, S.; Nakase, I.; Taclokoro, A.; Takeuchi, T.; Jones, A. T. *Biochem Soc T* 2007, *35*, 784-787.
(208) Gottesman, M. M.; Fojo, T.; Bates, S. E. *Nat Rev Cancer* 2002, *2*, 48-58.
(209) Fojo, A. T.; Ueda, K.; Slamon, D. J.; Poplack, D. G.; Gottesman, M. M.; Pastan, I. *P Natl Acad Sci USA* 1987, *84*, 265-269.
(210) Schmidt, N.; Mishra, A.; Lai, G. H.; Wong, G. C. L. *Febs Lett* 2010, *584*, 1806-1813.
(211) Lin, R.; Zhang, P.; Cheetham, A. G.; Walston, J.; Abadir, P.; Cui, H. *Bioconjug Chem* 2015, *26*, 71-7.
(212) Kisiday, J.; Jin, M.; Kurz, B.; Hung, H.; Semino, C.; Zhang, S.; Grodzinsky, A. J. *P Natl Acad Sci USA* 2002, *99*, 9996-10001.
(213) Matson, J. B.; Stupp, S. I. *Chem Commun* 2012, *48*, 26-33.
(214) Holmes, T. C.; de Lacalle, S.; Su, X.; Liu, G. S.; Rich, A.; Zhang, S. G. *P Natl Acad Sci USA* 2000, *97*, 6728-6733.
(215) Black, K. A.; Lin, B. F.; Wonder, E. A.; Desai, S. S.; Chung, E. J.; Ulery, B. D.; Katari, R. S.; Tirrell, M. V. *Tissue Eng Pt A* 2015, *21*, 1333-1342.
(216) Haines-Butterick, L.; Rajagopal, K.; Branco, M.; Salick, D.; Rughani, R.; Pilarz, M.; Lamm, M. S.; Pochan, D. J.; Schneider, J. P. *P Natl Acad Sci USA* 2007, *104*, 7791-7796.
(217) Amdursky, N.; Gazit, E.; Rosenman, G. *Adv Mater* 2010, *22*, 2311-2315.
(218) Wall, B. D.; Diegelmann, S. R.; Zhang, S. M.; Dawidczyk, T. J.; Wilson, W. L.; Katz, H. E.; Mao, H. Q.; Tovar, J. D. *Adv Mater* 2011, *23*, 5009-5014.
(219) Messmore, B. W.; Hulvat, J. F.; Sone, E. D.; Stupp, S. I. *J Am Chem Soc* 2004, *126*, 14452-14458.
(220) Altunbas, A.; Lee, S. J.; Rajasekaran, S. A.; Schneider, J. P.; Pochan, D. J. *Biomaterials* 2011, *32*, 5906-5914.
(221) Tang, C.; Miller, A. F.; Saiani, A. *Int J Pharmaceut* 2014, *465*, 427-435.

(222) Li, J. Y.; Kuang, Y.; Gao, Y.; Du, X. W.; Shi, J. F.; Xu, B. *J Am Chem Soc* 2013, *135*, 542-545.
(223) Tu, R. S.; Tirrell, M. *Adv Drug Deliver Rev* 2004, *56*, 1537-1563.
(224) Bowerman, C. J.; Liyanage, W.; Federation, A. J.; Nilsson, B. L. *Biomacromolecules* 2011, *12*, 2735-2745.
(225) Kokkoli, E.; Mardilovich, A.; Wedekind, A.; Rexeisen, E. L.; Garg, A.; Craig, J. A. *Soft Matter* 2006, *2*, 1015-1024.
(226) Nagai, Y.; Unsworth, L. D.; Koutsopoulos, S.; Zhang, S. G. *J Control Release* 2006, *115*, 18-25.
(227) Liang, G. L.; Yang, Z. M.; Zhang, R. J.; Li, L. H.; Fan, Y. J.; Kuang, Y.; Gao, Y.; Wang, T.; Lu, W. W.; Xu, B. *Langmuir* 2009, *25*, 8419-8422.
(228) Wang, J.; Wang, B. A.; Schwendeman, S. P. *J Control Release* 2002, *82*, 289-307.
(229) Zong, X. H.; Kim, K.; Fang, D. F.; Ran, S. F.; Hsiao, B. S.; Chu, B. *Polymer* 2002, *43*, 4403-4412.
(230) De Jong, W. H.; Borm, P. J. A. *Int J Nanomed* 2008, *3*, 133-149.
(231) Zhao, F.; Ma, M. L.; Xu, B. *Chemical Society Reviews* 2009, *38*, 883-891.
(232) Vemula, P. K.; Wiradharma, N.; Ankrum, J. A.; Miranda, O. R.; John, G.; Karp, J. M. *Current opinion in biotechnology* 2013, *24*, 1174-1182.
(233) Longmire, M.; Choyke, P. L.; Kobayashi, H. *Nanomedicine-Uk* 2008, *3*, 703-717.
(234) Heldin, C. H.; Rubin, K.; Pietras, K.; Ostman, A. *Nat Rev Cancer* 2004, *4*, 806-813.
(235) Lammers, T.; Kiessling, F.; Hennink, W. E.; Storm, G. *Mol Pharmaceut* 2010, *7*, 1899-1912.
(236) Chakravarty, R.; Hong, H.; Cai, W. B. *Mol Pharmaceut* 2014, *11*, 3777-3797.
(237) Seymour, L. W.; Ferry, D. R.; Anderson, D.; Hesslewood, S.; Julyan, P. J.; Poyner, R.; Doran, J.; Young, A. M.; Burtles, S.; Kerr, D. J.; Clin, C. R. C. P. I.-I. *J Clin Oncol* 2002, *20*, 1668-1676.
(238) Harrington, K. J.; Mohammadtaghi, S.; Uster, P. S.; Glass, D.; Peters, A. M.; Vile, R. G.; Stewart, J. S. W. *Clin Cancer Res* 2001, *7*, 243-254.
(239) Viglianti, B. L.; Ponce, A. M.; Michelich, C. R.; Yu, D. H.; Abraham, S. A.; Sanders, L.; Yarmolenko, P. S.; Schroeder, T.; MacFall, J. R.; Barboriak, D. P.; Colvin, O. M.; Bally, M. B.; Dewhirst, M. W. *Magn Reson Med* 2006, *56*, 1011-1018.
(240) Langereis, S.; Geelen, T.; Grull, H.; Strijkers, G. J.; Nicolay, K. *Nmr Biomed* 2013, *26*, 728-744.
(241) Bohmer, M. R.; Klibanov, A. L.; Tiemann, K.; Hall, C. S.; Gruell, H.; Steinbach, O. C. *Eur J Radiol* 2009, *70*, 242-253.
(242) Ward, K. M.; Aletras, A. H.; Balaban, R. S. *J Magn Reson* 2000, *143*, 79-87.
(243) Liu, G. S.; Song, X. L.; Chan, K. W. Y.; McMahon, M. T. *Nmr Biomed* 2013, *26*, 810-828.
(244) Terreno, E.; Stancanello, J.; Longo, D.; Delli Castelli, D.; Milone, L.; Sanders, H. M. H. F.; Kok, M. B.; Uggeri, F.; Aime, S. *Contrast Media Mol I* 2009, *4*, 237-247.
(245) McMahon, M. T.; Gilad, A. A.; DeLiso, M. A.; Berman, S. D. C.; Bulte, J. W. M.; van Zijl, P. C. M. *Magn Reson Med* 2008, *60*, 803-812.

(246) Liu, G. S.; Liang, Y. J.; Bar-Shir, A.; Chan, K. W. Y.; Galpoththawela, C. S.; Bernard, S. M.; Tse, T.; Yadav, N. N.; Walczak, P.; McMahon, M. T.; Bulte, J. W. M.; van Zijl, P. C. M.; Gilad, A. A. *J Am Chem Soc* 2011, *133*, 16326-16329.
(247) McVicar, N.; Li, A. X.; Goncalves, D. F.; Bellyou, M.; Meakin, S. O.; Prado, M. A. M.; Bartha, R. *J Cerebr Blood F Met* 2014, *34*, 690-698.
(248) Zhou, J. Y.; Payen, J. F.; Wilson, D. A.; Traystman, R. J.; van Zijl, P. C. M. *Nat Med* 2003, *9*, 1085-1090.
(249) Yang, X.; Song, X. L.; Li, Y. G.; Liu, G. S.; Banerjee, S. R.; Pomper, M. G.; McMahon, M. T. *Angewandte Chemie-International Edition* 2013, *52*, 8116-8119.
(250) Longo, D. L.; Dastru, W.; Digilio, G.; Keupp, J.; Langereis, S.; Lanzardo, S.; Prestigio, S.; Steinbach, O.; Terreno, E.; Uggeri, F.; Aime, S. *Magn Reson Med* 2011, *65*, 202-211.
(251) Chen, L. Q.; Howison, C. M.; Jeffery, J. J.; Robey, I. F.; Kuo, P. H.; Pagel, M. D. *Magn Reson Med* 2014, *72*, 1408-1417.
(252) Chen, L. Q.; Randtke, E. A.; Jones, K. M.; Moon, B. F.; Howison, C. M.; Pagel, M. D. *Mol Imaging Biol* 2015, *17*, 488-496.
(253) Longo, D. L.; Sun, P. Z.; Consolino, L.; Michelotti, F. C.; Uggeri, F.; Aime, S. *J Am Chem Soc* 2014, *136*, 14333-14336.
(254) Desmond, K. L.; Moosvi, F.; Stanisz, G. J. *Magn Reson Med* 2014, *71*, 1841-1853.
(255) Hazarika, M.; White, R. M.; Johnson, J. R.; Pazdur, R. *Oncologist* 2004, *9*, 482-488.
(256) Cheetham, A. G.; Zhang, P. C.; Lin, Y. A.; Lock, L. L.; Cui, H. G. *J Am Chem Soc* 2013, *135*, 2907-2910.
(257) Lin, R.; Cheetham, A. G.; Zhang, P. C.; Lin, Y. A.; Cui, H. G. *Chemical Communications* 2013, *49*, 4968-4970.
(258) Frohlich, E. *Int J Nanomed* 2012, *7*, 5577-5591.
(259) Gazit, E. *Faseb J* 2002, *16*, 77-83.
(260) Guo, C.; Luo, Y.; Zhou, R. H.; Wei, G. H. *Acs Nano* 2012, *6*, 3907-3918.
(261) Langer, R. *Nature* 1998, *392*, 5-10.
(262) Schroeder, A.; Heller, D. A.; Winslow, M. M.; Dahlman, J. E.; Pratt, G. W.; Langer, R.; Jacks, T.; Anderson, D. G. *Nat Rev Cancer* 2012, *12*, 39-50.
(263) Li, S. D.; Huang, L. *Mol Pharmaceut* 2008, *5*, 496-504.
(264) Torchilin, V. P. *Adv Drug Deliver Rev* 2006, *58*, 1532-1555.
(265) Kataoka, K.; Harada, A.; Nagasaki, Y. *Adv Drug Deliver Rev* 2001, *47*, 113-131.
(266) Duncan, R. *Nat Rev Drug Discov* 2003, *2*, 347-360.
(267) Haag, R.; Kratz, F. *Angewandte Chemie-International Edition* 2006, *45*, 1198-1215.
(268) Nel, A. E.; Madler, L.; Velegol, D.; Xia, T.; Hoek, E. M. V.; Somasundaran, P.; Klaessig, F.; Castranova, V.; Thompson, M. *Nat Mater* 2009, *8*, 543-557.
(269) Discher, D. E.; Eisenberg, A. *Science* 2002, *297*, 967-973.
(270) Lee, C. C.; MacKay, J. A.; Frechet, J. M. J.; Szoka, F. C. *Nat Biotechnol* 2005, *23*, 1517-1526.
(271) Patri, A. K.; Kukowska-Latallo, J. F.; Baker, J. R. *Adv Drug Deliver Rev* 2005, *57*, 2203-2214.

(272) Ghosh, P.; Han, G.; De, M.; Kim, C. K.; Rotello, V. M. *Adv Drug Deliver Rev* 2008, *60*, 1307-1315.
(273) Paciotti, G. F.; Myer, L.; Weinreich, D.; Goia, D.; Pavel, N.; McLaughlin, R. E.; Tamarkin, L. *Drug Delivery* 2004, *11*, 169-183.
(274) Euliss, L. E.; DuPont, J. A.; Gratton, S.; DeSimone, J. M. *Chemical Society Reviews* 2006, *35*, 1095-1104.
(275) Cabral, H.; Nishiyama, N.; Kataoka, K. *Accounts of Chemical Research* 2011, *44*, 999-1008.
(276) Aida, T.; Meijer, E. W.; Stupp, S. I. *Science* 2012, *335*, 813-817.
(277) Jolivet, J.; Cowan, K. H.; Curt, G. A.; Clendeninn, N. J.; Chabner, B. A. *New England Journal of Medicine* 1983, *309*, 1094-1104.
(278) Ozaki, Y.; King, R. W.; Carey, P. R. *Biochemistry* 1981, *20*, 3219-3225.
(279) Szakacs, Z.; Noszai, B. *Electrophoresis* 2006, *27*, 3399-3409.
(280) Lucock, M. *Molecular Genetics and Metabolism* 2000, *71*, 121-138.
(281) Low, P. S.; Henne, W. A.; Doorneweerd, D. D. *Accounts of Chemical Research* 2008, *41*, 120-129.
(282) Ciuchi, F.; Dinicola, G.; Franz, H.; Gottarelli, G.; Mariani, P.; Bossi, M. G. P.; Spada, G. P. *J Am Chem Soc* 1994, *116*, 7064-7071.
(283) Gottarelli, G.; Mezzina, E.; Spada, G. P.; Carsughi, F.; DiNicola, G.; Mariani, P.; Sabatucci, A.; Bonazzi, S. *Helv Chim Acta* 1996, *79*, 220-234.
(284) Bonazzi, S.; Demorais, M. M.; Gottarelli, G.; Mariani, P.; Spada, G. P. *Angew Chem Int Edit* 1993, *32*, 248-250.
(285) Kato, T.; Matsuoka, T.; Nishii, M.; Kamikawa, Y.; Kanie, K.; Nishimura, T.; Yashima, E.; Ujiie, S. *Angewandte Chemie-International Edition* 2004, *43*, 1969-1972.
(286) Kamikawa, Y.; Nishii, M.; Kato, T. *Chem-Eur J* 2004, *10*, 5942-5951.
(287) Kamikawa, Y.; Nishii, M.; Kato, T. *Mol Cryst Liq Cryst* 2005, *435*, 755-765.
(288) Kanie, K.; Nishii, M.; Yasuda, T.; Taki, T.; Ujiie, S.; Kato, T. *J Mater Chem* 2001, *11*, 2875-2886.
(289) Atluri, R.; Hedin, N.; Garcia-Bennett, A. E. *J Am Chem Soc* 2009, *131*, 3189-+.
(290) Chakraborty, P.; Roy, B.; Bairi, P.; Nandi, A. K. *J Mater Chem* 2012, *22*, 20291-20298.
(291) Cui, H. G.; Pashuck, E. T.; Velichko, Y. S.; Weigand, S. J.; Cheetham, A. G.; Newcomb, C. J.; Stupp, S. I. *Science* 2010, *327*, 555-559.
(292) Hamley, I. W.; Krysmann, M. J.; Castelletto, V.; Noirez, L. *Adv Mater* 2008, *20*, 4394-4397.
(293) Lowik, D.; van Hest, J. C. M. *Chemical Society Reviews* 2004, *33*, 234-245.
(294) Gao, Y.; Kuang, Y.; Guo, Z. F.; Guo, Z. H.; Krauss, I. J.; Xu, B. *J Am Chem Soc* 2009, *131*, 13576-+.
(295) Rana, S.; Nissen, F.; Lindner, T.; Altmann, A.; Mier, W.; Debus, J.; Haberkorn, U.; Askoxylakis, V. *Mol Imaging* 2013, *12*.
(296) Li, X. M.; Kuang, Y.; Xu, B. *Soft Matter* 2012, *8*, 2801-2806.
(297) Peeters, E.; Delmotte, A.; Janssen, R. A. J.; Meijer, E. W. *Adv Mater* 1997, *9*, 493-&.
(298) Pommier, Y. *Nat Rev Cancer* 2006, *6*, 789-802.
(299) Zhu, J. H.; Zhang, S. Y.; Zhang, F. W.; Wooley, K. L.; Pochan, D. J. *Advanced Functional Materials* 2013, *23*, 1767-1773.

(300) Cui, H. G.; Chen, Z. Y.; Wooley, K. L.; Pochan, D. J. *Macromolecules* 2006, *39*, 6599-6607.

(301) Cui, H. G.; Chen, Z. Y.; Zhong, S.; Wooley, K. L.; Pochan, D. J. *Science* 2007, *317*, 647-650.

(302) Reneker, D. H.; Geil, P. H. *Journal of Applied Physics* 1960, *31*, 1916-1925.

(303) Goodsell, D. S. *Stem Cells* 1999, *17*, 314-315.

(304) Cubberley, M. S.; Iverson, B. L. *J Am Chem Soc* 2001, *123*, 7560-7563.

(305) Goux, W. J.; Kopplin, L.; Nguyen, A. D.; Leak, K.; Rutkofsky, M.; Shanmuganandam, V. D.; Sharma, D.; Inouye, H.; Kirschner, D. A. *Journal of Biological Chemistry* 2004, *279*, 26868-26875.

(306) Chari, R. V. J.; Miller, M. L.; Widdison, W. C. *Angewandte Chemie-International Edition* 2014, *53*, 3796-3827.

(307) Wang, A. Z.; Farokhzad, O. C. *J Nucl Med* 2014, *55*, 353-356.

(308) Zhang, X. J.; Zhang, J.; Ma, Y. Y.; Pei, X. Y.; Liu, Q. M.; Lu, B.; Jin, L.; Wang, J. C.; Liu, J. *Int J Biochem Cell B* 2014, *46*, 1-8.

(309) Zhang, X. X.; Eden, H. S.; Chen, X. Y. *J Control Release* 2012, *159*, 2-13.

(310) Varghese, B.; Vlashi, E.; Xia, W.; Lopez, W. A.; Paulos, C. M.; Reddy, J.; Xu, L. C.; Low, P. S. *Mol Pharmaceut* 2014, *11*, 3609-3616.

(311) Vaitilingam, B.; Chelvam, V.; Kularatne, S. A.; Poh, S.; Ayala-Lopez, W.; Low, P. S. *J Nucl Med* 2012, *53*, 1127-1134.

(312) Haddley, K. *Drugs Today (Barc)* 2013, *49*, 701-15.

(313) Perini, G. F.; Pro, B. *Biol Ther* 2013, *3*, 15-23.

(314) Haubner, R.; Wester, H. J.; Burkhart, F.; Senekowitsch-Schmidtke, R.; Weber, W.; Goodman, S. L.; Kessler, H.; Schwaiger, M. *J Nucl Med* 2001, *42*, 326-336.

(315) Garanger, E.; Boturyn, D.; Dumy, P. *Anti-Cancer Agent Me* 2007, *7*, 552-558.

(316) Corti, A.; Curnis, F.; Arap, W.; Pasqualini, R. *Blood* 2008, *112*, 2628-2635.

(317) Garde, S. V.; Forte, A. J.; Ge, M.; Lepekhin, E. A.; Panchal, C. J.; Rabbani, S. A.; Wu, J. J. *Anti-Cancer Drug* 2007, *18*, 1189-1200.

(318) Lee, T. Y.; Lin, C. T.; Kuo, S. Y.; Chang, D. K.; Wu, H. C. *Cancer Res* 2007, *67*, 10958-10965.

(319) Chang, D. K.; Chiu, C. Y.; Kuo, S. Y.; Lin, W. C.; Lo, A.; Wang, Y. P.; Li, P. C.; Wu, H. C. *Journal of Biological Chemistry* 2009, *284*, 12905-12916.

(320) Laakkonen, P.; Akerman, M. E.; Biliran, H.; Yang, M.; Ferrer, F.; Karpanen, T.; Hoffman, R. M.; Ruoslahti, E. *P Natl Acad Sci USA* 2004, *101*, 9381-9386.

(321) Song, X. L.; Yang, X.; Banerjee, S.; Pomper, M. G.; McMahon, M. T. *Contrast Media Mol I* 2015, *10*, 74-80.

(322) Terreno, E.; Barge, A.; Beltrami, L.; Cravotto, G.; Castelli, D. D.; Fedeli, F.; Jebasingh, B.; Aime, S. *Chem Commun* 2008, 600-602.

(323) Zhao, J. M.; Har-El, Y. E.; McMahon, M. T.; Zhou, J.; Sherry, A. D.; Sgouros, G.; Bulte, J. W. M.; van Zijl, P. C. M. *J Am Chem Soc* 2008, *130*, 5178-5184.

(324) Jeong, W. J.; Lim, Y. B. *Bioconjugate Chem* 2014, *25*, 1996-2003.

(325) Gudlur, S.; Sukthankar, P.; Gao, J.; Avila, L. A.; Hiromasa, Y.; Chen, J. H.; Iwamoto, T.; Tomich, J. M. *Plos One* 2012, *7*.

(326) Greenfield, N. J. *Nat Protoc* 2006, *1*, 2876-2890.

(327) Staack, A.; Badendieck, S.; Schnorr, D.; Loening, S. A.; Jung, K. *BMC Urol* 2006, *6*, 19.

(328) Para, G.; Hamerska-Dudra, A.; Wilk, K. A.; Warszyński, P. *Colloids and Surfaces A: Physicochemical and Engineering Aspects* 2010, *365*, 215-221.
(329) Al-Soufi, W.; Piñeiro, L.; Novo, M. *Journal of Colloid and Interface Science* 2012, *370*, 102-110.
(330) Buttle, D. J.; Murata, M.; Knight, C. G.; Barrett, A. J. *Archives of Biochemistry and Biophysics* 1992, *299*, 377-380.
(331) Rodriguez-Franco, E. J.; Cantres-Rosario, Y. M.; Plaud-Valentin, M.; Romeu, R.; Rodriguez, Y.; Skolasky, R.; Melendez, V.; Cadilla, C. L.; Melendez, L. M. *Plos One* 2012, *7*.
(332) Meixenberger, K.; Pache, F.; Eitel, J.; Schmeck, B.; Hippenstiel, S.; Slevogt, H.; N'Guessan, P.; Witzenrath, M.; Netea, M. G.; Chakraborty, T.; Suttorp, N.; Opitz, B. *J Immunol* 2010, *184*, 922-930.

Curriculum Vitae

Personal Information

Name : Lye Lin Lock

Date of Birth : 20 March 1987

Location of Birth : Kuantan, Pahang, Malaysia

Country of Nationality : Malaysia

Johns Hopkins University

Department of Chemical and Biomolecular Engineering

3400 North Charles Street; Croft Hall rm 368; Baltimore MD, 21218, USA

Email Address : lyelin87@gmail.com

Mobile Phone : (716) 566-0779

Educational History

2015 Doctor of Philosophy
Johns Hopkins University, Baltimore, MD
Program in Chemical and Biomolecular Engineering
Advisor : Honggang Cui, Ph.D.

2010 Bachelor of Science
University at Buffalo, State University of New York, Buffalo, NY
Program in Chemical Engineering

Professional Experience

August 2010 – August 2015

Graduate Research Assistant
Department of Chemical and Biomolecular Engineering
Johns Hopkins University, Baltimore, MD
My doctoral thesis explores peptide-based supramolecular nanostructures for cancer diagnostics and therapeutics.

January 2013 – May 2013

Graduate Teaching Assistant

Course : Current Topics in Functional Molecular Assembly
Department of Chemical and Biomolecular Engineering
Johns Hopkins University, Baltimore, MD
Prepared course materials and instructed several class sessions.

January 2012 – May 2014

Graduate Teaching Assistant
Course : Kinetics Processes
Department of Chemical and Biomolecular Engineering
Johns Hopkins University, Baltimore, MD
Assisted lectures, conducted recitations to facilitate students in understanding course materials.

May 2009 – May 2010

Undergraduate Research Assistant
Department of Chemical and Biological Engineering
University at Buffalo, State University of New York, Buffalo, NY
Assessed the feasibility of expressing GPCR in yeast as a high throughput screening system for drug discovery process.

Patents

- "Instant Encapsulation of Small Molecule Drugs and Biologics Using Peptide Nanofiber Hydrogels", *submitted on March 2015*
  Inventors : **Lye Lin Lock** and Honggang Cui
- "Supramolecular Nanobeacon Imaging Agents As Protease Sensors", *US Patent Application # 14/059974, filed on October 2013*
  Inventors : **Lye Lin Lock**, Andrew G. Cheetham, and Honggang Cui

Publications

1. **Lock, L. L.**; Li, Y.; Mao, X. Bai, R.; Liu,G.; Cui, H., "An anticancer drug-based controlled release nanofiber hydrogel system with inherent MRI signals", *in preparation.*
2. **Lock, L. L.**; Mao, X.; Cui, H., "Instant encapsulation of small molecule drug and biologics using self-assembling peptide nanofibers", *in preparation.*

3. **Lock, L. L.**; Reyes, C.; Zhang, P.; Cui, H., “Shape- and charge-dependent cellular internalization of self-assembling supramolecular nanobeacons by cancer cells”, *to be submitted.*
4. **Lock, L. L.**; Tang, Z.; Keith, D.;Reyes, C.; Cui, H., “Enzyme-specific doxorubicin drug-beacon as multidrug-resistant theranostic molecular probes”, ***ACS Macro Letters,*** 2015, 4, 552-555.
5. Zhang, P.; Cheetham, A. G.; **Lock, L. L.**; Li, Y.; Cui, H., “Activatable Nanoprobes for Biomolecular Detection”, ***Current Opinion in Biotechnology*****,** 2015, 34, 171-179.
6. Wang, J.; Mao, W.; **Lock, L. L.**; Tang, J.; Sui, M.; Sun, W.; Cui, H.; Xu, D.; Shen, Y., The role of micelle size in tumor accumulation, penetration, and treatment, ***ACS Nano***, 2015,*ASAP,* DOI: 10.1021/acsnano.5b02017
7. Pastuszka, M.; Wang, X.; **Lock, L. L.**; Mohd Janib, S.;Cui, H.; DeLeve, L. D.; MacKay, J. A., “An amphipathic alpha-helical peptide from Apolipoprotein A1 stabilizes protein polymer nanoparticles”, ***Journal of Controlled Release*****,** 2014,191,15-23.
8. Mohd Janib, S.; Gustafson, J.; Minea, R. O.; Swenson, S. D.; Liu, S.; Pastuszka, M. K.; **Lock, L. L.**; Cui, H.; Markland Jr., F.S.; Conti, P. S.; Li, Z.; MacKay, J. A., “Multimeric disintegrin protein polymer fusions that target tumor vasculature”, ***Biomacromolecules***, 2014, 2014, 15 (7), 2347–2358.
9. Zhang, P.; **Lock, L. L.**; Cheetham, A. G.; Cui, H., “Enhanced cellular entry and efficacy of Tat conjugates by rational design of the auxiliary segment”, ***Molecular Pharmaceutics***, 2014, 11 (3), 964-973.
10. Zhang, P.; Cheetham, A. G.; Lock, L. L.; Cui, H., “Cellular uptake and cytotoxicity of drug-peptide conjugates regulated by conjugation site”, ***Bioconjugate Chemistry,*** 2013, 24 (4), 604-613.
11. **Lock, L.L.**; Cheetham, A. G.; Zhang, P.; Cui, H., “Design and construction of supramolecular nanobeacons for enzyme detection”, ***ACS Nano***, 2013, 7 (6), 4924-4932.
12. **Lock, L. L.**; LaComb, M.; Schwarz, K.; Cheetham, A. G.; Lin, Y.-A.; Zhang, P.; Cui, H., “Self-assembly of natural and synthetic drug amphiphiles into discrete supramolecular nanostructures”, ***Faraday Discussions***, 2013, 166, 285-301.
13. Cheetham, A. G.; Zhang, P.; Lin, Y.-A.; **Lock, L. L.**; Cui, H., “Supramolecular nanostructures formed by anticancer drug assembly”, ***Journal of the American Chemical Society*****,** 2013, 135 (8), 2907-2910.

Awards and Honor

- ChemBE Graduate Research Award, March 2014

  Johns Hopkins University, Baltimore, MD

Department of Chemical and Biomolecular Engineering

- INBT Nano-Bio Symposium Poster Award, May 2012
  Johns Hopkins University, Baltimore, MD
  Institute for NanoBioTechnology
- CBE Academic Excellence Award, August 2010
  State University of New York at Buffalo, Buffalo, NY
  School of Engineering and Applied Sciences
- Undergraduate Research Prize, April 2010
  State University of New York at Buffalo, Buffalo, NY
  University Libraries